EPFL

Thèse n° 9538

2D MoS_2 Nanopores: Wafer-scale Fabrication and Monolayer Stability for Long-term Single-Molecule Sensing

Présentée le 4 novembre 2022

Faculté des sciences et techniques de l'ingénieur
Laboratoire de biologie à l'échelle nanométrique
Programme doctoral en microsystèmes et microélectronique

pour l'obtention du grade de Docteur ès Sciences

par

Mukeshchand THAKUR

Acceptée sur proposition du jury

Prof. L. G. Villanueva Torrijo, président du jury
Prof. A. Radenovic, directrice de thèse
Prof. M. Wanunu, rapporteur
Prof. F. Montel, rapporteur
Prof. Ph. Renaud, rapporteur

École polytechnique fédérale de Lausanne

2022

Nature has billions of years of evolutionary experience. To mimic such a complex system would take more than one PhD thesis.
It's a collective effort and I play a small part in such an effort...

Acknowledgements

First and foremost, I am grateful to **Aleksandra** for providing me with excellent PhD experience and a learning environment at her laboratory. She is one of THE best PI one could hope for. Her curiosity and enthusiasm has always kept me up throughout my PhD in all ups and downs. I have always felt motivated after we have meetings, and that is a good sign of a leader! Thanks a lot for all the guidance and support all the way. Hvala!

I extend my gratitude to **Andras** for allowing me to use various instruments at LANES and for scientific advice at the meetings. I also want to thank **Jens Gundlach** and **Andrew Laszlo** for being an awesome company for a year which I will cherish my whole life. Also, Jens's burgers are the best! But apart from that, you have inspired a lot of young researchers like me not give up on science.

Next, from the "Three pore guys" gang – **Michael** and **Martina**. These were not only my mentors but also my gurus at the lab. Thanks for being with me and always keeping me on the right path. All the food, hikes, and for the deep conversations about the "last sun of the year!" You both have been like an elder brother and sister to me! **Michael** has been a source of inspiration for me. You inculcated confidence in me and I learnt a lot from you, thanks for being there. I owe you unlimited beers! **Martina**!! So many memories and discussions (from super crazy to super serious), science and life. You have always supported me and your genuine guidance has always helped me. Hvala! **Bruna**!! Thanks for being an awesome company and keeping our nerdy life balanced during the stressful times. Obrigada! I want to thank **Mukesh Tripathi** (my another brother) from LANES. Apart from sharing our first name, we also share lot of things. You were my eyes to the 2D materials I have transferred and imaging the best images of our nanopores. Again, needless to mention all the stuff we have cherished over the past few years and many more to come.

I also want to extend my thanks to **Lely** for helping me out right from the first day in the lab and always inviting me to all our commune aperos. Next, I want to thank **Sanjin**, **Seb** and **Michal** for all the fun discussion, cricket game, and a memorable trip in Israel. Also, Michal has been my MoS_2 dealer since the beginning and I am grateful to him. Cheers to our large-area

collaboration and thanks for opening your “large-area” heart to me. **Evgenii**, my volleyball star, thanks a lot for all the fun over years inside and outside the lab. I enjoyed sharing organization tips as president of our respective Indian and Russian-speaking association at EPFL. I am always indebted to you for introducing me to dear Gera (may her soul rest in peace). I am grateful to so many people that have created a sense of safe zone in the lab – **Vytautas**, **Jochem**, **Miao**, **Arielle** and so many others for supporting me in the lab. Shout out to **Andrey**! He has been a very kind and helpful to me and an awesome collaborator all the way until the end. Your substrates are the best! Thanks for making my PhD smooth as it wouldn't have been possible without your microfabrication support. Spasibo!
Now come to new peeps who joined our lab - **Nianduo**, **Yunfei**, **Vasily**, **Theo**, **Wayne**, **Eveline**, **Nathan**, **Simon**, **Khalid**, and **Helena**. You have been awesome in the lab and I wish you all the best times ahead. Thanks for all the pleasant memories and company in Croatia. How can I forget Prof. **Yunfei**! We have shared a lot of memories in a past one year and gone through a share of ups and downs. I wish you all the best luck from my side and may you excel in your life. I am sure you will, I will be around. Thanks for being a partner for eating all the spiciest Chinese cuisine in Europe (especially sharing our famous poison dish!). **Nianduo** has been a very awesome student-cum-collaborator and I am glad to have had worked with you. I am sure you will do awesome in your PhD! **Bart**- my Taiwan ally, thanks for all the creative discussion in the lab and showing me how to make Chinese dumplings. Xie Xie! I also want to thank LANES guys – **Guilherme** (maregaaa!), **Yanfei** for providing me with her MoS_2 samples. **Cheol-Yeon** for competing with me at the drinks, and other members from LANES.

I want to extend a very special thanks to Livit (my residence) guys –**Ankit, Rasool, Shankha, Santhanu, Shreyas, Richa, Ashutosh, Nihar, Arya, Bhushan, Harshvardhan, Moulik, Pruthvi** and so many others who has been a support for me all the way along. Most of them were also a part of YUVA-Indians community at EPFL and I extend my gratitude to all of them. Special thanks to **Ankit, Rasool and Nihar** for sharing all the science/political/bollywood dancing/cooking and being around during the stressful time of Covid-19! Shout-out "with a melodious voice" to **Shreyas** for his chai! **Santhanu** and **Nihar**, I am eagerly waiting for your breakthrough on qubits and fantastic algorithm in future. Thanks to I want to thank **Akshay** and **Mounika** for always welcoming me to their house for food and trips. I can write pages-long blogs for each of them. If I am missing someone my apologies.

I would like to acknowledge my thesis mentors, **Prof. Carlotta Guiducci** and **Prof. Georg Fantner** for suggestions in my candidacy exam. Special thanks to my thesis jury: **Prof. Meni Wanunu**, **Prof. Fabien Montel**, **Prof. Phillpe Renaud** and my jury president **Prof. Guillermo Villanueva** for their encouraging comments on my work. I also want to thank **Martine Truan** and **Lucie Auberson** for the administrative support and all the help with my organization at EPFL.

I would like to acknowledge my friends in the Republic of India - **Rajesh**, **Vijay**, and **Prashant** for the longest friendship. I want to thank **Mukesh Kumawat**, **Mukesh Dhanka**, **Dev Thacker**,

Pritam and **Amit Sharma** back from IIT Bombay days for always inspiring me to take one step forward. I wish to extend special thanks to **Prof. Madhuri Sharon**, late **Prof. Maheshwar Sharon** and **Prof. Rohit Srivastava** for believing in me and supporting me in science. The list is long and surely I will forget many.

I won't miss my mom and dad though! Usually, I don't speak my heart out to them an probably they won't read this. Since my memories go back I have seen all their life sacrifices and struggles with selfless intentions and for one particular reason – "Educate me and have a better life for myself". I am lucky to be your child and promise to have a better life for ourselves. I am happy that my brother is taking care of you guys, and at some point I will buy him a nice Swiss watch. I want to thank my new family - **Gauri**, my in-laws, and other **Gangapurwala** members for embracing me into your family and "allowing" Gauri to be mine. No words that exist in the history of language to express how Gauri has been a spectrum of life from a dear friend to a life companion. Thanks for being with me from my worst to not so worse.

Lastly, there are so many people who have diverted me to where I am today. I am glad I met them on the journey of life so far. Thanks for catalysing me at throughout.

Lausanne, 29 September 2022 (post-corona era) Mukeshchand Thakur

Abstract

Biologically inspired solid-state nanopores are artificial openings or apertures in thin membranes similar to natural protein ion channels in a lipid bilayer of cell membranes. In solid-state nanopores, a thin insulating membrane with single or multiple pores separates two conductive salt solutions. When an electric field is applied across this membrane, electrically charged species such as ions pass through these nanopore(s), generating a nanopore ion current. In essence, nanopores are single-molecule sensors and valuable tools for studying biophysics. For instance, an intrinsically charged biomolecule such as DNA can be electrophoretically threaded through the nanopore, transiently blocking the ionic current. Such change in the ionic signal is a characteristic of the molecule passing through the pore. Hence nanopore-sensing is an attractive, low-cost, and label-free single-molecule sensing technology.

In principle, the thinner the nanopore membrane, the more ions can flow through the pore, and the more sensitive the nanopore sensing will be. With progress in two-dimensional (2D) materials, the marriage of nanopores with 2D materials - "2D nanopores" have emerged as a new class of ultra-thin membrane solid-state nanopores. Molybdenum disulfide (MoS_2) is a 2D material with an atomic thickness (0.7 nm) that approaches the inter-base distance of two DNA bases, and unlike graphene, the DNA tends to stick less to MoS_2. Naturally, it was a lucrative 2D material for the DNA sequencing application. However, there are inherent challenges and bottlenecks with using MoS_2 as 2D nanopores due to sensitive fabrication and inherent challenges of the 2D materials leading to low device yield. In this thesis, I will demonstrate ways to improve high-throughput production and the development of more reliable and durable nanopore devices.

In the second chapter, I will introduce MoS_2 material as a 2D nanopore system and elaborate fabrication of nanopore substrates. I will discuss various problems and issues related to substrate fabrication, transfer, nanopore-creation, and nanopore measurements. Finally, I list a step-by-step protocol and troubleshooting guide for early-stage 2D nanopore researchers. In the third chapter, I specifically focus on "chip-scale" transfer strategies for MoS_2 grown using chemical vapor deposition (CVD). I introduce two transfer approaches - direct-transfer and stamp-assisted- with just water as a medium. I will demonstrate these transfer approaches and discuss their advantages and limitations. Furthermore, I discuss hydrocarbon contamination with 2D materials and their implications in nanofluidics.

In the fourth chapter, I demonstrate a scalable transfer from chip-scale to a larger "wafer-scale" for batch fabrication of nanopore substrates for single-molecule DNA sensing. With PDMS-based polymer, I will demonstrate 3-inch monolayer MoS_2 transfer on nanopore substrates with 128 nanopore devices with high transfer efficiency (>70%). Moreover, the technique is etchant-free, and growth substrates are recyclable after transfer.
In the fifth chapter, I show experimental evidence of delamination of monolayer MoS_2 from nanopore substrates. I study and correlate delamination effects with ionic current through MoS_2 nanopore and transmission electron microscopy (TEM). Further, I discuss the oxidation of MoS_2 as another major issue while using MoS_2 nanopores in an aqueous buffer solution in standard operating conditions in nanopore sensing. I investigate the chemical oxidation of the monolayer MoS_2 membrane and nanopores using aberration-corrected high-resolution electron microscopy and photoluminescence spectroscopy in aqueous conditions. I address the delamination issue by chemically modifying the silicon nitride substrates with an organosilicon that increases the adherence of monolayer MoS_2 layers. This surface pre-treatment helped reinforce 2D layer attachment to the substrate, increasing the nanofluidic devices' durability. Further, we show that the nanopore enlargement due to dissolved oxygen in an aqueous solution can be considerably reduced in a low dissolved oxygen concentration in solution. These strategies improved MoS_2 nanopore stability for long-term DNA sensing measurements, a significant improvement for 2D nanopore stability. Our surface modification can be extended to other 2D materials and applications where delamination is often an issue for device failure.

Key words: solid-state nanopore, nanopore, 2D nanopore, 2D materials, molybdenum disulfide, transition-metal dichalcogenide, monolayer, membrane, transfer, chip-scale, wafer-scale, PMMA, PDMS, polymer-free, nanofluidics, transmission electron microscopy, oxidation, stability, single-molecule, translocation, biosensing, OpenNanopore

Résumé

Les nanopores artificiels d'inspiration biologique sont des ouvertures contrôlées dans des membranes minces, semblables aux canaux ioniques naturels des protéines dans la bicouche lipidique des membranes cellulaires. Dans les nanopores artificiels, une fine membrane isolante à pores simples ou multiples sépare deux solutions salines conductrices. Lorsqu'un champ électrique est appliqué à travers cette membrane, des espèces chargées électriquement, telles que des ions, passent à travers ces nanopores, générant un courant ionique. Par essence, les nanopores sont des capteurs monomoléculaires et des outils précieux pour étudier la biophysique. Par exemple, une biomolécule intrinsèquement chargée, comme l'ADN, peut être introduite par électrophorèse dans le nanopore, ce qui bloque transitoirement le courant ionique. Cette modification du signal ionique est une caractéristique de la molécule qui traverse le pore. La détection par nanopore est donc une technologie de détection de molécules uniques attrayante, peu coûteuse et sans marqueur.
En principe, plus la membrane du nanopore est fine, plus les ions peuvent circuler à travers le pore, et plus la détection par nanopore est sensible. Avec les progrès réalisés dans le domaine des matériaux bidimensionnels (2D), le mariage des nanopores et des matériaux 2D - les "nanopores 2D" - est apparu comme une nouvelle catégorie de nanopores artificiels à membrane ultrafine. Le disulfure de molybdène (MoS_2) est un matériau 2D dont l'épaisseur atomique (0,7 nm) se rapproche de la distance inter-bases de deux bases d'ADN, et contrairement au graphène, l'ADN a tendance à moins coller au MoS_2. Naturellement, il s'agissait d'un matériau 2D lucratif pour l'application de séquençage de l'ADN. Cependant, l'utilisation du MoS_2 comme nanopores 2D présente des défis inhérents à la fabrication impliquant des matériaux 2D, ce qui entraîne un faible rendement des dispositifs. Dans cette thèse, je démontrerai les moyens d'améliorer la production à haut débit et le développement de dispositifs de nanopores plus fiables et durables.
Dans le deuxième chapitre, je présenterai le matériau MoS_2 comme un système de nanopores 2D et j'élaborerai la fabrication de substrats des nanopores. Je discuterai de divers problèmes et questions liés à la fabrication du substrat, au transfert, à la création de nanopores et aux mesures des nanopores. Enfin, j'énumère un protocole étape par étape et un guide de dépannage pour les chercheurs débutants en nanopores 2D.
Dans le troisième chapitre, je me concentre sur les stratégies de transfert à l'échelle de la puce pour le MoS_2 obtenu par dépôt chimique en phase vapeur (CVD). Je présente deux approches

de transfert - le transfert direct et le transfert assisté par tampon - avec seulement de l'eau comme milieu. Je ferai la démonstration de ces approches de transfert et discuterai de leurs avantages et de leurs limites. En outre, je discute de la contamination par les hydrocarbures avec les matériaux 2D et de leurs implications en nanofluidique.
Dans le quatrième chapitre, je démontre un transfert évolutif de l'échelle de la puce à une plus grande "échelle de la tranche" pour la fabrication par lots de substrats de nanopores pour la détection d'ADN à l'échelle de la molécule unique. Avec un polymère à base de PDMS, je démontrerai le transfert d'une monocouche de MoS_2 de 3 pouces sur des substrats nanopores avec 128 dispositifs nanopores avec une efficacité de transfert élevée (>70%). De plus, la technique est sans décapage et les substrats de croissance sont recyclables après le transfert.
Dans le cinquième chapitre, je démontre expérimentalement la délamination de la monocouche de MoS_2 des substrats de nanopores. J'étudie et corrèle les effets de délamination avec le courant ionique à travers le nanopore MoS_2 et la microscopie électronique à transmission (TEM). En outre, je discute de l'oxydation du MoS_2 comme un autre problème majeur lors de l'utilisation de nanopores de MoS_2 dans une solution tampon aqueuse dans des conditions d'exploitation standard dans la détection de nanopores. J'étudie l'oxydation chimique de la membrane monocouche de MoS_2 et des nanopores en utilisant la microscopie électronique haute résolution corrigée des aberrations et la spectroscopie de photoluminescence dans des conditions aqueuses. J'aborde le problème de la délamination en modifiant chimiquement les substrats de nitrure de silicium avec un organosilane qui augmente l'adhérence des couches de MoS_2 monocouche. Ce prétraitement de surface a permis de renforcer l'attachement de la couche 2D au substrat, augmentant ainsi la durabilité des dispositifs nanofluidiques. De plus, nous montrons que l'élargissement des nanopores dû à l'oxygène dissous dans une solution aqueuse peut être considérablement réduit dans une solution à faible teneur en O2 dissous. Ces stratégies ont permis d'améliorer la stabilité des nanopores MoS_2 pour des mesures de détection d'ADN à long terme, une amélioration significative pour la stabilité des nanopores 2D. Notre modification de surface peut être étendue à d'autres matériaux 2D et à des applications où la délamination est souvent un problème résultant en la défaillance du dispositif.

Mots clefs : nanopore à l'état solide, nanopore, nanopore 2D, matériaux 2D, disulfure de molybdène, dichalcogénure de métal de transition, monocouche, membrane, transfert, échelle de la puce, échelle de la tranche, PMMA, PDMS, sans polymère, nanofluidique, microscopie électronique à transmission, oxydation, stabilité, molécule unique, translocation, biodétection, OpenNanopore.

Contents

List of Figures

List of Tables

1 Introduction

1.1 Nanopores and their brief history with time

The biological system has evolved for over a billion years and the story of the pores dates to the time (unknown) when the cell learns to exchange nutrients, communicate with neighboring cells, and finally developed complex transport systems within itself. The concept of separation and compartmentalization was perhaps one of the major evolution milestones that would enable complex cellular processes.

Logarithmically fast forward to a countable history, in the context of today's perception of nanopore technology, maybe it is reasonable to start from 1953 when Wallace H. Coulter patented a resistive pulse technique to count and size blood cells.[1] His idea was quite simple: A micrometer-sized hole in a membrane (cellophane at that time), separating two chambers filled with saline solution. The application of pressure or an electric field can then drive suspended particles (such as blood cells) through the orifice. Measuring the ionic current during this process reveals current blockages with amplitudes corresponding to the size of the particle. With this simple invention, Coulter had a significant impact on the clinical world for decades to come.[2] Obviously, the size of the aperture defined the type of analyte one could detect. Moving from relatively large blood cells to viruses, DNA molecules, or individual proteins each needed substantial technological advances.

It was only in the 1990s that the orifice size shrunk to the nanometer scale by using lipid bilayers and natural protein pores. This reduction in size allowed the possibility of the sensing of single polynucleotide strands.[3] After this, the nanopore technology flourished and evolved over years with new variations of nanopores entering the game. Now I will walk you through those classes of nanopores as we proceed further.

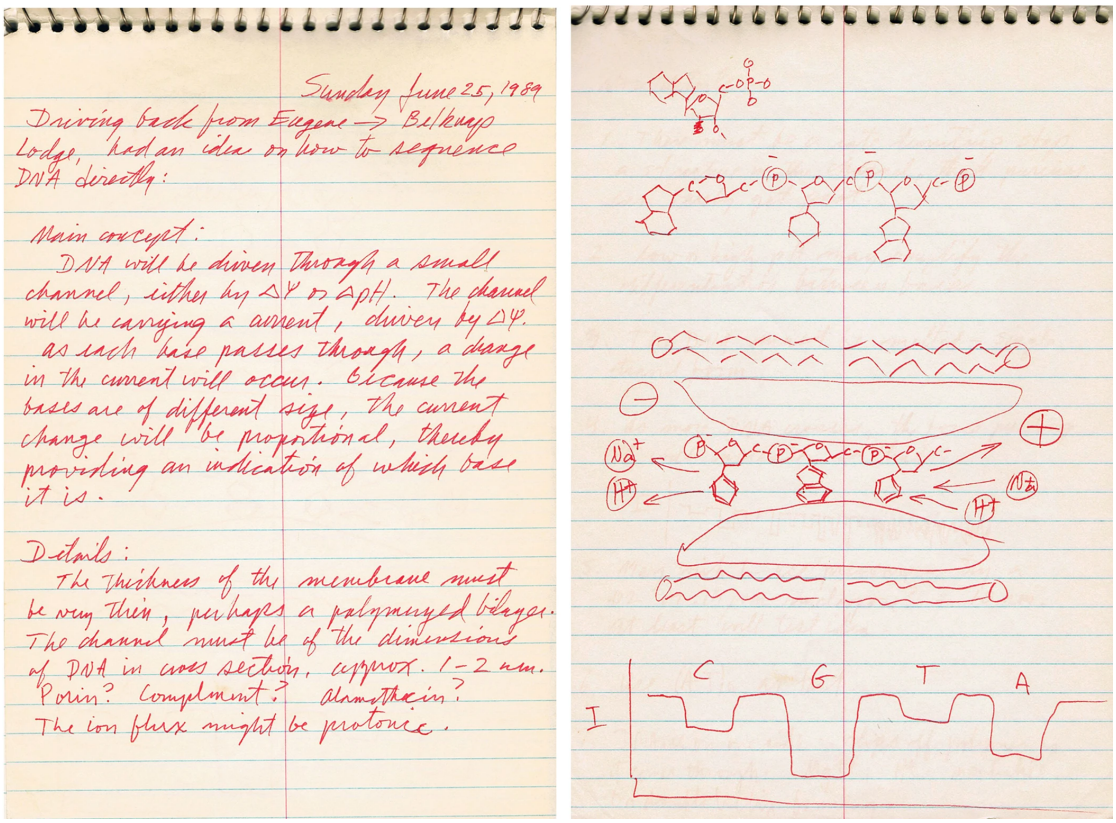

Figure 1.1: Notebook sketch from David Deamer illustrating nanopore sequencing (dated 25 June 1989). This Figure was published in Deamer et al.[4] and obtained with permission of Springer Nature publishing group.

1.2 Biological pores to engineered solid-state pores

Biological nanopores are protein pores (transmembrane proteins) embedded in a lipid bilayer. In the context of nanopores, the first biological pore studied was the α-hemolysin pore that started in the 1980s. A notebook sketch from David Deamer's notebook (Fig.1.1), back in 1989, demonstrates the early notion of a nanopore-based DNA translocation.[4] Initial work on translocation of single-stranded (ss) DNA was shown by using α-hemolysin pore in the seminal paper back in 1996.[3] In addition, one of the critical experiments related to this biological pore was the gating problem that would spontaneously switch the pore to a non-conducting state which Kasianowicz and others addressed by having at least one open channel in his lipid membranes.[3, 5] This early-stage work was a pioneering start to the "nanopore sensors" field.

The notion of nanopores as sensors sparked attention toward individual nucleotide identification and sequencing. Around the same time, nanopore-based DNA sequencing was one of the proposed genomic approaches toward low-cost rapid human genome sequencing for less than $1,000.[6] However, one significant issue still was the speed of translocating molecules through the pore and resolving the individual nucleobases. The ssDNA would go through

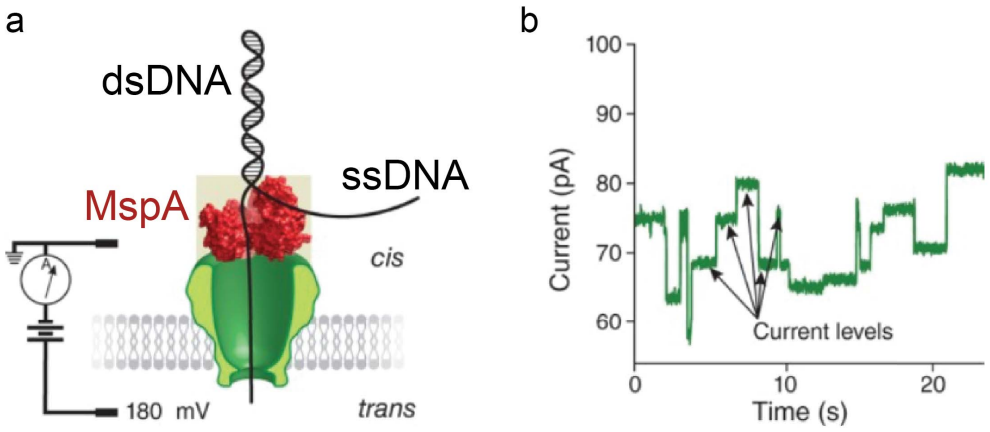

Figure 1.2: (a) Electrophoretic transport of dsDNA (black) unwound by helicase (red) into ssDNA is threaded into the MspA pore (green). (b) Representative ionic current time trace that shows different current levels as the ssDNA translocates through the MspA pore. Each level corresponds to the individual nucleotide passing through the pore. This Figure was published in Deamer et al.[4] and obtained with permission of Springer Nature publishing group.

with a speed of one nt s^{-1}, about three orders of magnitude higher than the ideal speed (1 nt ms^{-1}) for DNA sequencing application. Consequently, new strategies for slowing down the speed using phi29 DNA polymerases[7, 8] and MspA pore[8, 9] (Fig.1.2) were demonstrated. Meanwhile, Oxford Nanopore Technologies (ONT) was founded in 2005 with their first device as, MinION which would open doors to nanopore-based DNA sequencing.[4]

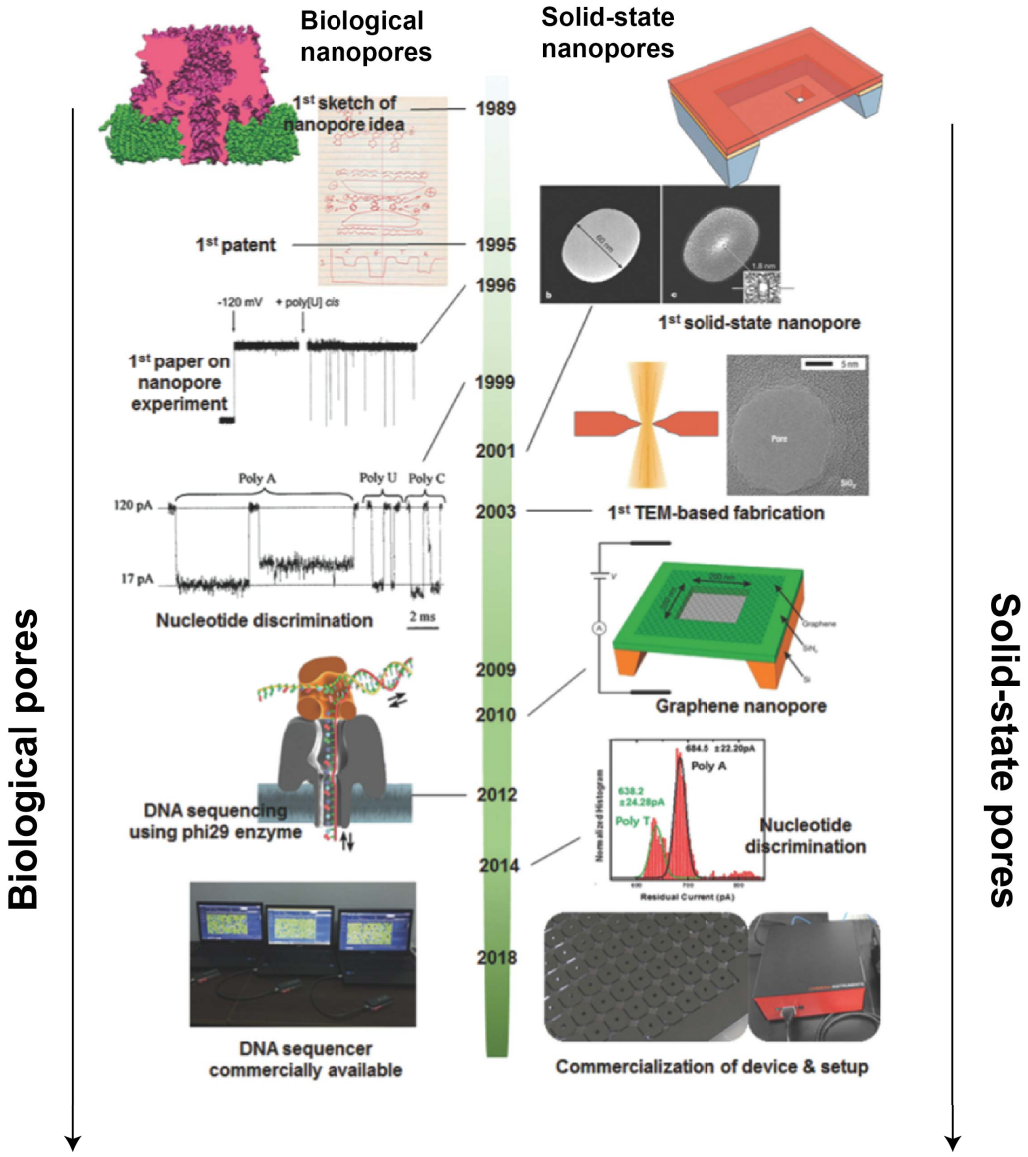

Figure 1.3: Historical timeline showing development in the field of nanopores (until 2018). On the left panel, is the development milestones in biological nanopores while on the right we see solid-state nanopores. This Figure was published in Lee et al.[10] and obtained with permission of John Wiley and Sons publishing group.

These studies are considered early-stage milestones that would set the stage for new development in nanopore sensors, nicely illustrated (Fig.1.3) by Lee et al.[10]

By this time, nanopores were about to diverge into biological nanopores and solid-state nanopores.[10–14] Figure.1.4 shows a thickness comparison of some well-known biological pores and solid-state nanopores. The first solid-state nanopore for DNA detection was devel-

oped[15] by ion-beam sculpting a silicon nitride (SiN_x) membrane. Meanwhile, biological pores took off to sequence DNA[16] and revolutionized the sequencing market.[17] Following the list, Cees Dekker's group showed nanopores in SiO_2 using e-beam lithography and etching.[18] Typically, silicon-based SiN_x membranes are used in solid-state nanopores. This is mainly due to the well-developed processes in microfabrication: silicon nitride acts as a stop layer for the anisotropic wet-etching process of silicon using potassium hydroxide (KOH), which made it the material of choice for fabricating freestanding membranes. Low-stress silicon nitride (LS SiN_x) can achieve stable membranes as thin as 3 nm,[19] while the typical thicknesses range from 20-30 nm. The material has electrically insulating properties and can thus be used to separate aqueous salt solutions.

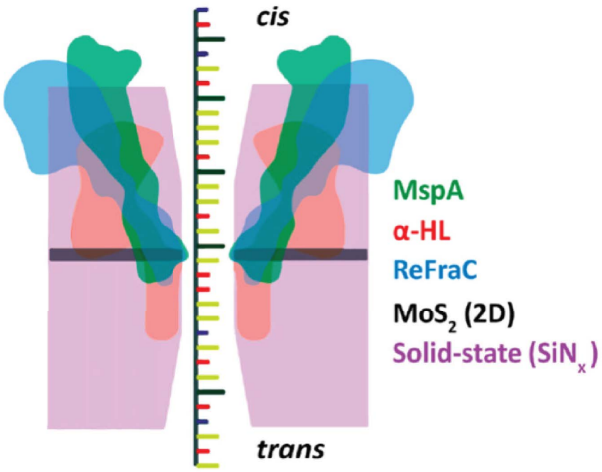

Figure 1.4: Illustration showing superimposition of various nanopores and their thicknesses with a ssDNA threading through the pore. Originally by Carson and Wanunu[11] and adapted by Fragasso.[20] This Figure was published in Fragasso et al.[20] Copyright (2020) American Chemical Society.

To measure any ionic conductance, a nanopore needs to be engineered in the material to provide a connection between the two reservoirs. To date, there are many methods such as e-beam lithography with reactive ion etching (RIE), ion beam milling,[15] dielectric breakdown,[21] drilling with a transmission electron microscope (TEM)[22] or the very recently introduced laser beam fabrication.[23, 24]

1.3 Comparison of biological nanopores and solid-state nanopores

Being proteins, where the structure dictates the molecule's function, the biological pores have a crucial advantage of shape and size reproducibility over the solid-state nanopores. They also possess advantages in measurement reliability as well as lower membrane noise than solid-state nanopores. There is a known issue of batch-to-batch variation in solid-state pores, a major limitation that depends on the sensitivity of the fabrication technology.

The solid-state nanopores offer many advantages compared to biological ones, such as robustness, tunable pore size, stability over a wide range of voltages and concentrations, and the possibility of direct integration with the electronics. This is because the biological lipid membrane is inherently fragile and sensitive to voltages applied during the translocation experiment (<200 mV). This has been addressed using mechanically stable polymers and engineering membranes support. Figure 1.4 shows a thickness comparison from commonly studied nanopores.

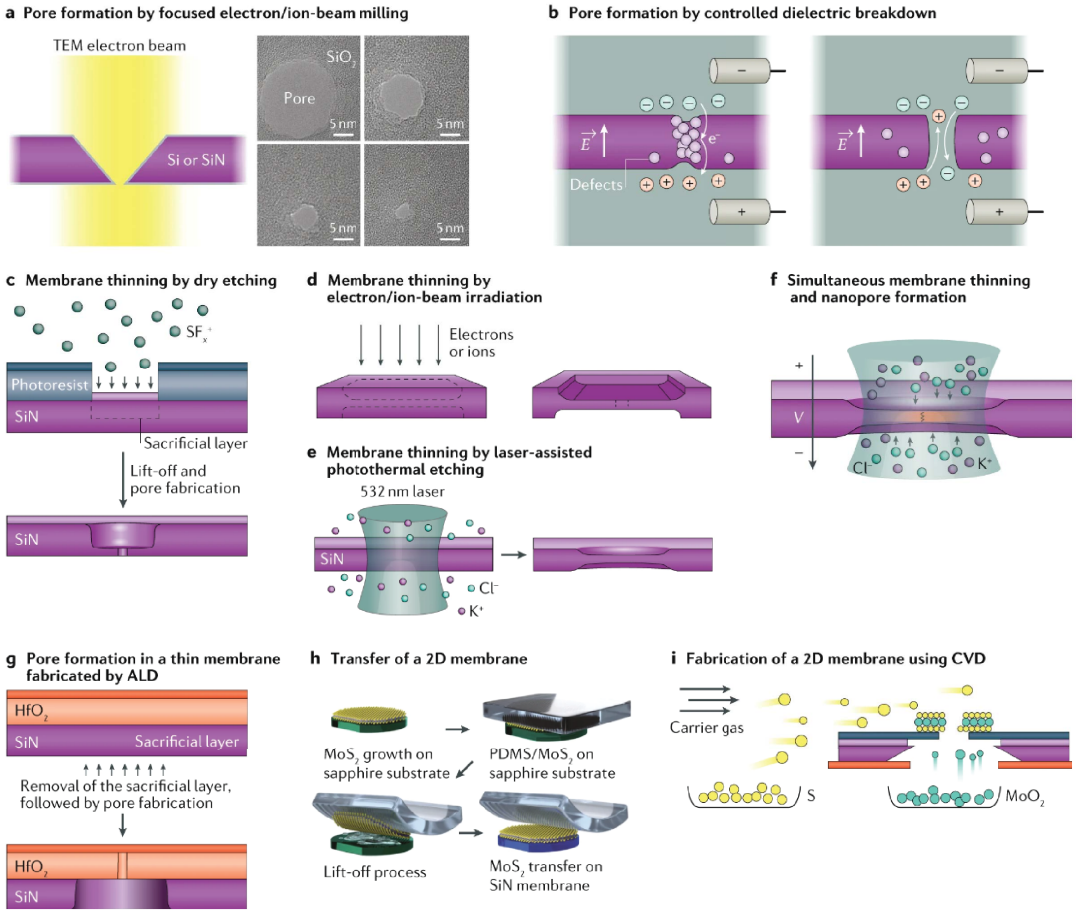

Figure 1.5: Illustration showing solid-state nanopores fabrication. This Figure was published in Xue et al.[13] and obtained with permission of Springer Nature publishing group.

1.4 Solid-state nanopore fabrication

With an idea to mimic biological pores, about two decades ago[25] solid-state nanopores were fabricated in thin silicon-based substrates. Since then, solid-state nanopores have been used to distinguish ss- and dsDNA,[26] different polynucleotides[27] and detect DNA folding[28] and even knots.[29] Furthermore, they have also been shown to detect proteins,[30] to understand the dynamics of protein folding,[31–33] going as far as to extract the protein's shape in real-time.[34] A solid-state nanopore device architecture involves a thin free-standing membrane, a few nanometers in thickness, and a suitable size of a nanopore in the free-standing membrane. Additionally, in the case of a 2D nanopore, another layer of atomically thin 2D material is transferred onto a free-standing membrane and then a nanopore is fabricated in the membrane. I will now summarize and discuss some well-known methods to fabricate these structures to make solid-state nanopore devices.

Figure.1.5 summarize conventional methods and techniques involved in the fabrication of

solid-state nanopores. At the early stages of solid-state nanopores, a focused ion beam (FIB)[15, 35] or electron beam[18] was used to drill as well as real-time monitoring of the changes in the nanopore size and shape. The single-digit nanopore sizes that can be achieved using this technique are down to the sub-nanometer level. However, for single nanopores, the process was not high throughput as it relies on manual pore fabrication using an expensive tool such as TEM. Following this, other inexpensive techniques such as controlled dielectric breakdown (CDB)[19, 21] was introduced that rely on high voltage to generate about 1-2 nm pore sizes in situ. The process is low-cost and nanopore sizes can be tuned but suffer from a limitation of multiple nanopore formation. Unlike drilled nanopores, as it is fabricated in situ, the pores are wet in the fabrication process and do not require an additional wetting step.

For high-throughput solid-state nanopore fabrication, thinning down by membrane etching has been demonstrated.[13, 36–40] In the context of 2D nanopores, atomically thin 2D material is either exfoliated[41] or grown using state-of-the-art techniques such as chemical vapor deposition (CVD).[42] The 2D materials such as MoS_2 can either be grown directly on the membrane[43] or transferred from the growth substrate to the nanopore substrate.[44, 45]

1.5 Two-dimensional Nanopores: the quest to go atomically thin

The solid-state nanopore field has seen tremendous advances in recent years, but these nanopores typically lack the single-nucleotide resolution that is needed to achieve DNA sequencing. With the emergence of graphene in 2004, several research groups reported DNA translocation experiments through this ultra-thin 2D material.[46–48] The hope was that the ultra-thin nature of these materials, which approaches the inter-base distance in a DNA strand, will provide the spatial resolution needed to achieve DNA sequencing. However, although in ultra-thin nanopores the resistance of the channel is greatly reduced, and access resistance still represents an obstacle that keeps the sensing length substantially large compared to the membrane thickness.[49] Furthermore, graphene for DNA translocations was hindered because the DNA sticks to the hydrophobic surface.[50] In 2011, molybdenum disulfide (MoS_2), a semiconducting, three-atom-thick transition metal dichalcogenide (TMD) was introduced as a promising material for field-effect transistors.[51] Soon after, its viability as a membrane for DNA translocation experiments has been tested.[52] The hydrophobic interaction between DNA and graphene that made it difficult to translocate DNA through graphene nanopores was not observed in MoS_2 nanopores. Furthermore, in the case of graphene, the sensitivity regarding signal-to-noise ratio was improved compared to conventional SiN_x membranes. By changing the customary potassium chloride (KCl) electrolyte pair to a gradient of room temperature ionic liquids (RTIL) and KCl allowed for the detection and discrimination of single nucleotides.[53] Not only is the MoS_2 membrane suitable for biomolecule detection, but its ultrathin nature and relatively high surface potential in liquid provide a perfect platform for an ion-selective membrane that can be used to desalinate salt water[54] or generate power through osmotic pressure.[55] Furthermore, due to its semiconducting properties, a translocating biomolecule can also act as a gate for a nanopore-field-effect transistor device.[56]

For nanopore fabrication, electrochemical reaction (ECR),[44, 57] can be utilized which greatly reduces the costs and increases the throughput of nanopore fabrication. Another way toward large-scale nanopores production using high-throughput focused-ion beam (FIB) to make sub-nanometers pores in 2D materials.[58–60] Focusing on the fabrication of 2D nanopores, let us enter the next section where I specifically discuss "transfer" of 2D materials - one of the crucial step in materials science and device fabrication. Following are various techniques demonstrated so far towards the transfer of 2D materials, especially MoS_2.

1.6 Layer Transfer technologies

Since the isolation of graphene by Geim and Novosolev back in 2004,[61] with a simple 'scotch tape technique' marked the onset of 2D materials research that later led them to win the Nobel Prize in Physics in 2010. This was also the first 2D material transfer technique that involve the use of a peeling technique to exfoliate graphene from a bulk graphite crystal. Since then, there has been tremendous advancement in the field of 2D materials - including TMDs films such as MoS_2[51] as a semiconductor material and so did various layer transfer technologies that are on par with scalable growth. Transfer of 2D TMDs comprises "wet–transfer" and "dry–transfer" modalities and resembles controlled placement of these atomically thin materials to the desired location "deterministic" without changing the properties of the material. Historically, the exfoliation-mediated transfer was developed, while over time various transfer developments followed as the research on the growth of CVD-based 2D materials took off. Now I will discuss various transfer techniques pertaining to TMDs that are more relevant to my research work and highlight their developments and challenges.

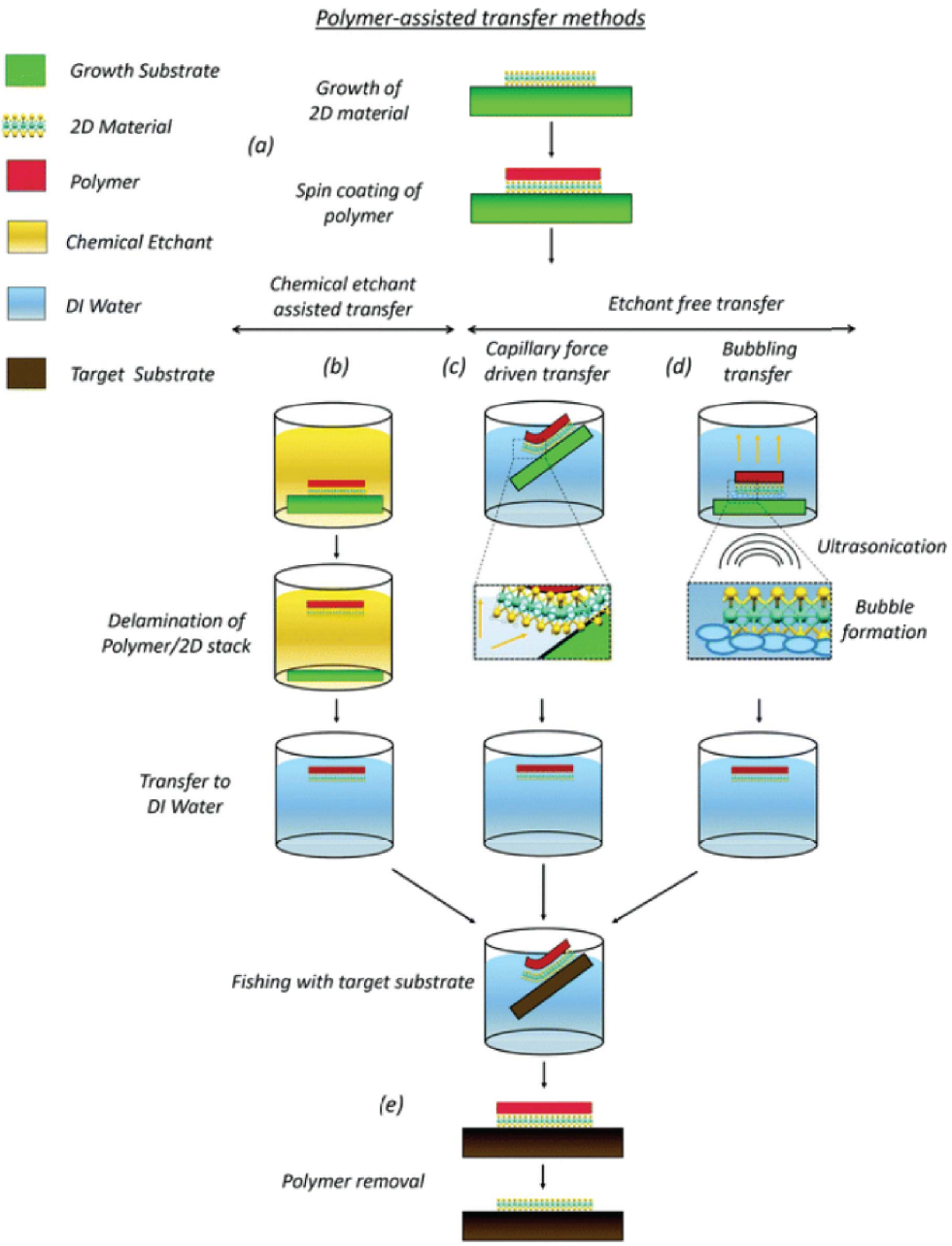

Figure 1.6: Schematic showing mechanically assisted wet-transfer methods for 2D materials. This Figure was published in Schranghamer et al.[62] and obtained with permission from the Royal Society of Chemistry.

1.6.1 Mechanical support-assisted transfer

Basically, a mechanical support-assisted transfer comprises a polymer layer such as polymethyl methacrylate (PMMA)[63] that is applied on the 2D surface and delaminated along with the 2D material from the growth substrate. The delamination of the 2D material is either facilitated by etching the underlying substrate or capillary force. Following this, the delaminated polymer along with the 2D material is then fished on the target substrate, and the polymer layer is then removed by dissolution in organic solvents (acetone, toluene). Figure 1.6 shows a schematic of the mechanical support-assisted wet-transfer method.

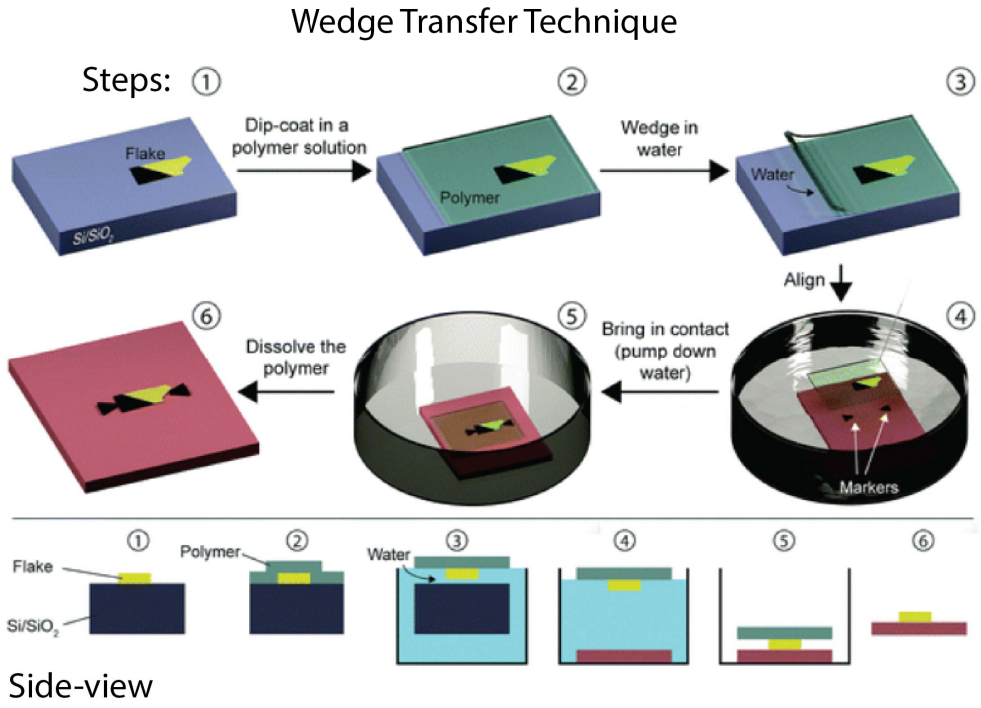

Figure 1.7: Wedging transfer method for transferring 2D flakes. This Figure was published in Frisenda et al.[64] and obtained with permission from the Royal Society of Chemistry.

An example of such transfer was demonstrated by Schneider[65] developed a so-called 'wedging transfer' method, where a hydrophobic polymer is spin-coated on an exfoliated 2D material and delaminated using capillary forces followed by transfer. The whole process is summarized in Figure 1.7. However, this technique suffers from the limitation of folding, buckling, and blister formation due to trapped bubbles after the drying process. One major advantage of this technique is that it can 'conform' to any arbitrary flexible or curved substrates.

Yet another transfer type of transfer method is a deterministic transfer method using a polydimethylsiloxane (PDMS)[41] as shown in Figure 1.8. This technique relies on the viscoelastic properties of PDMS and is a dry technique as it does not require any wet solvent step. The advantage of this process is a faster transfer speed and an ability to optically align the 2D

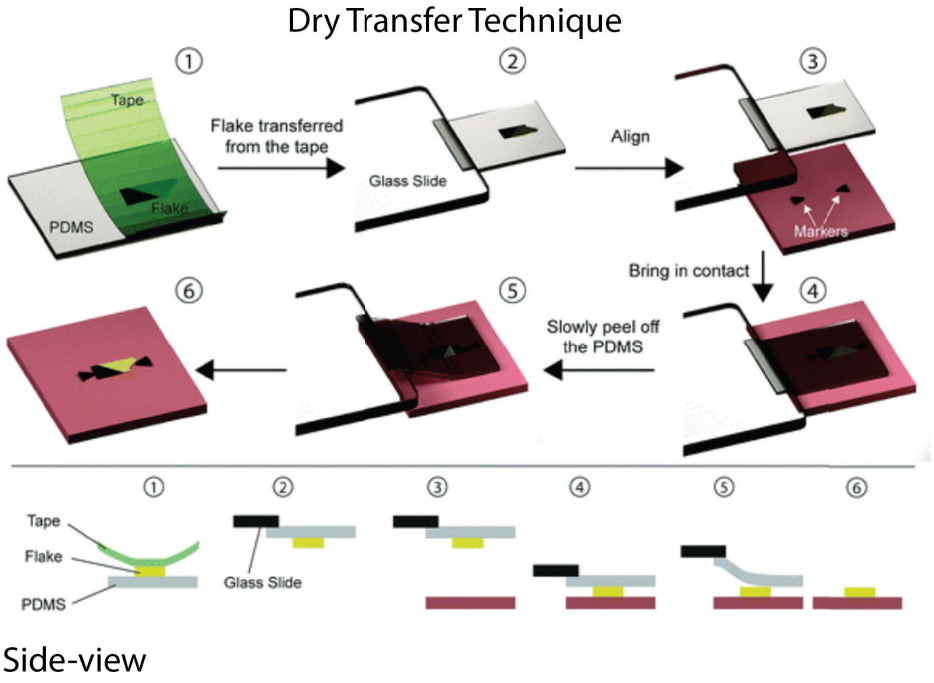

Figure 1.8: Dry transfer method using PDMS stamp. This Figure was published in Frisenda et al.[64] and obtained with permission from the Royal Society of Chemistry.

material on the target substrate.

1.6.2 Polymer-free transfer

The polymer residues after transfer using mechanically assisted transfer methods are one of the major limitations for device failure due to unwanted effects such as doping, deterioration of the device characteristics, and finally lead to low device yield.[44, 66, 67] Efforts toward polymer-free transfer system (Fig.1.9) led to approaches such as water-soluble layers or the use of thermal release tape (TRT).[62, 68] For instance, the use of a sacrificial layer of salt[69] was demonstrated to transfer MoS_2 films. Briefly, a water-soluble layer is coated on the 2D material growth substrate followed by wedging it in the water. As the film dissolves in an aqueous solution, the film floats on the water and is then transferred to the target substrate. Another recent example is the mechanically-assisted free transfer,[67] within a few centimeter-scale with a claim of residue-free transferred films, albeit a more detailed morphological analysis of the films needs to be performed.

So far, all these approaches are demonstrated on a “chip-scale” or up to centimeter-scale substrates. There is a need for large area or wafer-scale transfer strategy that facilitates and complements high-throughput applications. In the next section, I will discuss some wafer-scale transfer strategies for atomically thin materials.

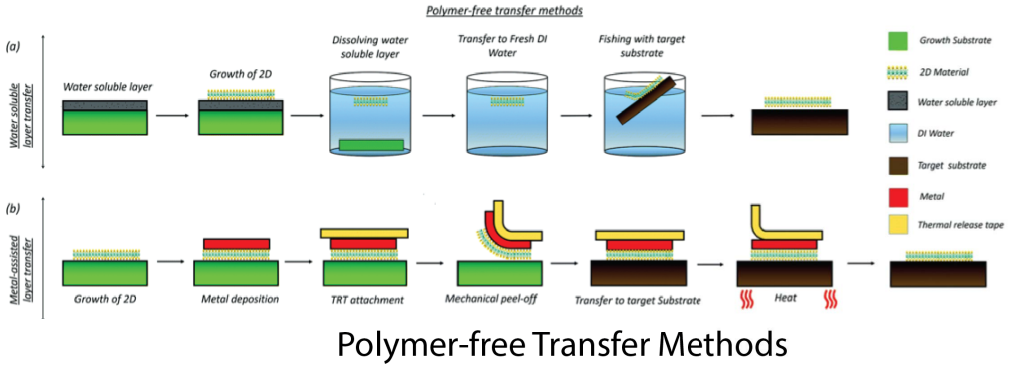

Figure 1.9: Two variants of polymer-free transfer techniques. This Figure was published in Schranghamer et al.[62] and obtained with permission from the Royal Society of Chemistry.

1.6.3 Large-area transfer

One of the advantages of large-area or wafer-scale transfer[45, 70–72] is that compared to the chip-scale deterministic transfer methods,[41, 44, 65] the technique does not require any precise optical alignment step. While PMMA has also been demonstrated for large-area transfer,[70] the process can lead to buckling and folding during transfer and reduce the transfer efficiency. Wafer-scale transfer using PDMS is demonstrated, as PDMS polymer is significantly thicker (1-2 mm), but still flexible and optically transparent, providing better mechanical stability during the transfer process.[41, 44] With PDMS-based wafer-scale transfer, a large number of nanopore devices (n=128) were fabricated with 70% transfer efficiency.[45] This transfer process is robust and reproducible and has a scalability potential. While the wafer-scale transfer process can lead to improved device yield, the actual success of the solid-state nanopore devices will depend upon practical limitations that one has to address, which will be discussed further.

1.7 Practical challenges in 2D Nanopore Devices

Solid-state nanopores including 2D nanopores suffer from certain bottlenecks that limit their commercial application as medical diagnostic sensors or even DNA sequencers. The most fundamental problems include nanopore noise,[10, 20] temporal resolution due to fast translocation,[11, 73] and molecular motion of polymer inside the nanopore.[74, 75] Specifically, practical limitations of 2D nanopore membranes and devices include low device yield,[44, 58]stability of the nanopore membranes and pores,[22, 36, 76] 2D material oxidation,[77, 78]pore contamination, wetting and clogging in nanopores.[36, 79]

1.8 Structure and content of the thesis

This thesis will focus on scalable fabrication and addresses practical bottlenecks in 2D MoS_2 nanopores and devices as nanopore sensors. The thesis is divided into five sections:

2D MoS_2 nanopores device fabrication Chapter 2 describes a detailed discussion about nanopores in MoS_2, its substrate fabrication process, nanopore drilling, and potential issues related to the manufacturing of devices. One can always refer to detailed step-by-step protocol given at the end of the thesis.

Chip-scale transfer of 2D MoS_2 film/s In Chapter 3, I present two chip-scale transfer methods – the direct transfer approach and a stamp-based transfer approach. Apart from transfer techniques, we learn new insights regarding hydrocarbon contamination.

Wafer-scale transfer and nanopore production In Chapter 4 (summarized in Figure 1.10), I demonstrate a large-area semi-automated wafer-scale transfer technique capable of transferring about 128 nanopore devices with 70% transfer efficiency.

2D Nanopore instability in aqueous solution In Chapter 5, I present observations and some experimental evidence that the cause of 2D nanopores' instability arises due to membrane delamination and oxidation of the 2D material in an aqueous solution. I address the membrane instability issue with surface functionalization that led to stabilized membrane devices. Further, we perform long-term biosensing by prolonging the lifetime of the MoS_2 nanopore by abrogating oxidation issues in the buffer.

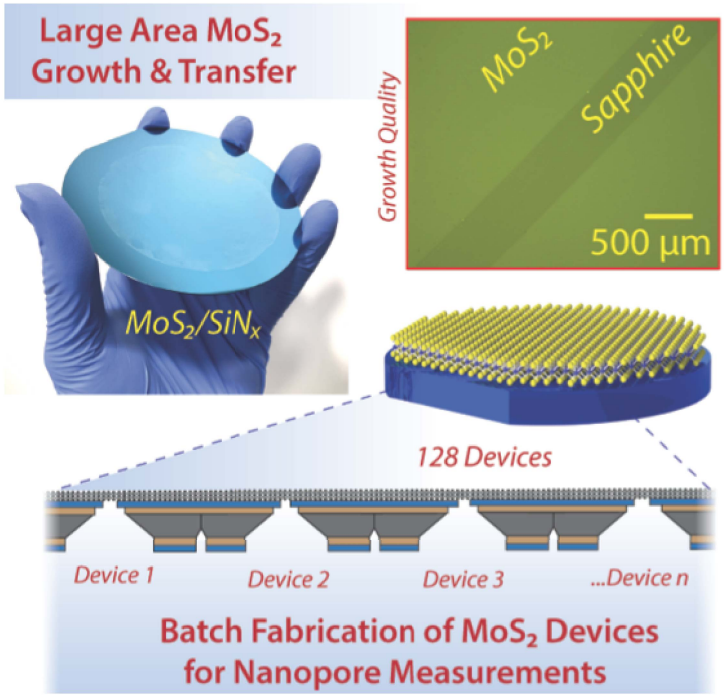

Figure 1.10: Wafer-scale growth and transfer for the batch production of MoS_2 nanopore devices. This Figure was published as graphical abstract in Thakur et al.[45] and obtained with permission of John Wiley and Sons publishing group.

2 Two-Dimensional MoS_2 Nanopores Device Fabrication

This chapter is a post-print version from following publication:

> Michael Graf[1], Martina Lihter[1], **Mukeshchand Thakur**[1], Vasileia Georgiou, Juraj Topolancik, B. Robert Ilic, Ke Liu, Jiandong Feng, Yann Astier and Aleksandra Radenovic. Fabrication and Practical Applications of Molybdenum Disulfide Nanopores. Nature Protocols, 14 (2019).

M.G., M.L., and M.T. contributed equally.[1] K.L. and J.F. performed initial work on device fabrication, MoS_2 transfer and pore characterization. M.G., J.T., V.G., and B.R.I developed the substrate fabrication process, V.G. fabricated the substrates. Y.A. supervised the substrate fabrication process. J.F., K.L., and A.R. developed the ECR pore drilling method. M.G. built the transfer microscope set-up, M.G. and M.L. developed PMMA transfer method and optimized MoS_2 cleaning procedure, M.T. developed PDMS transfer method, M.L. and M.G. performed TEM characterization, M.L. and K.L. optimized the TEM pore drilling method. M.G. developed the translocation data acquisition and analysis software. M.G., M.L., and M.T. fabricated the devices. M.G. performed the translocation experiments presented. M.G., M.L., M.T., J.T., and A.R. wrote the manuscript.

2.1 Short Overview

In this section, we briefly summarize the procedure of making 2D MoS_2 devices. We divided the process flow into three parts: Substrate preparation, MoS_2 transfer, and nanopore creation. A graphical overview of all the involved steps is illustrated in Figure 2.1. In order to make a large number of devices at once, as many steps as possible should be performed on a wafer-scale. For technical reasons, the fabrication of the substrates is done on a wafer, while the material transfer and nanopore fabrication are processed at a chip-scale. Developing wafer-scale MoS_2 growth and transfer methods will allow more efficient device fabrication in the future.

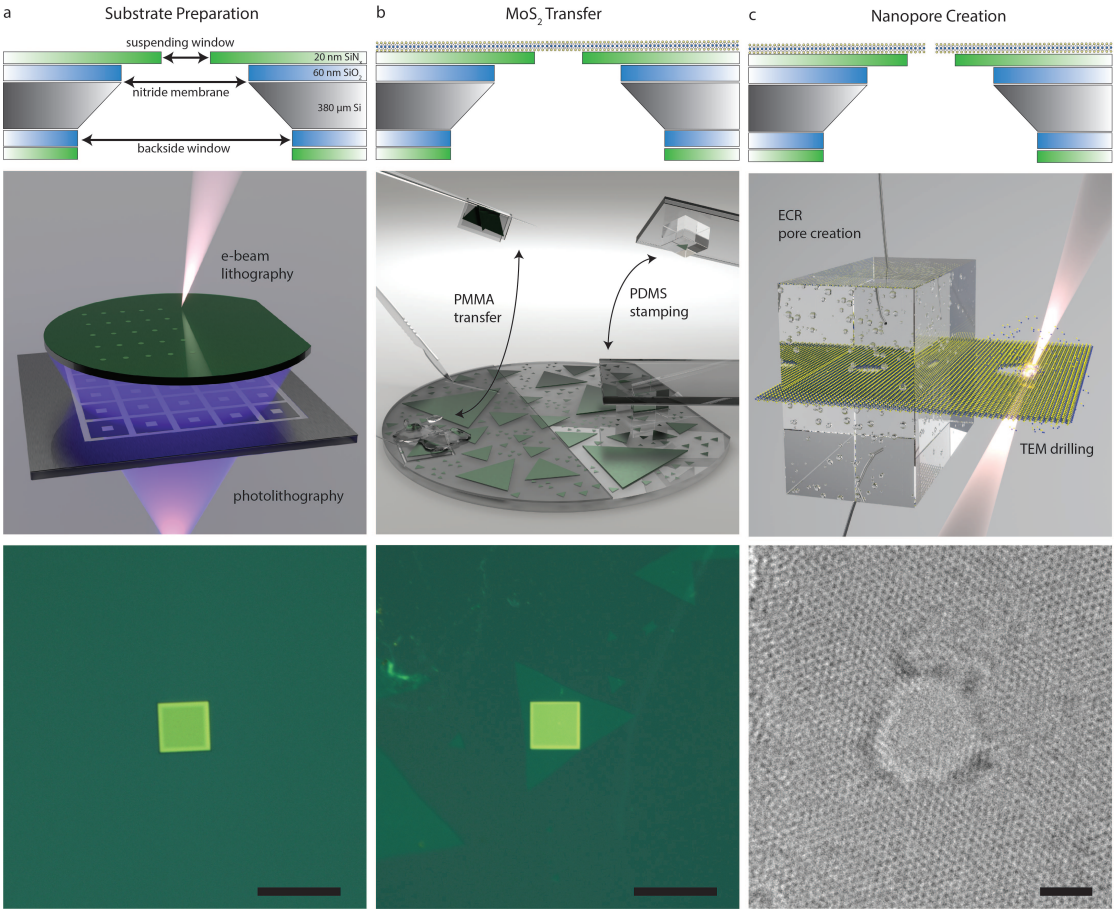

Figure 2.1: Overview of the fabrication process. (a) Substrate preparation. Top: A schematic of the finished device. Middle: Illustration of the involved methods: E-beam lithography is used to pattern the suspending opening, whereas photolithography is used to create the backside opening for KOH etching. Bottom: An optical micrograph of the resulting freestanding silicon nitride membrane. Scale bar 20 μm. (b) Transfer of MoS_2. Top: A schematic of the device when MoS_2 has been transferred. Middle: An illustration of the two options of transferring the material: PMMA or PDMS-assisted lift- off and alignment on the target substrate Bottom: An optical micrograph of a single crystal MoS_2 (triangle) transferred to the silicon nitride membrane. Scale bar 20 μm. (c) Drilling of a nanopore. Top: A schematic of the finished device. Middle: Illustration of the two nanopore creation methods available to users: TEM drilling and ECR pore creation. Bottom: A TEM image of a drilled nanopore. Scale bar, 2 nm.

We need to fabricate substrates used to suspend the monocrystalline material. The starting point is a 4-inch silicon wafer, where both sides contain a thin layer of SiO_2 and SiN_x. E-beam lithography is then used to write nanometer-sized circles on the front-side resist. Each of these will later serve as one thin suspending window on the chip. A reactive ion etching step then transfers this pattern to the wafer by etching away the SiO_2 and SiN_x layers. On the backside of the wafer, we use photolithography to create openings that serve for KOH wet-etching of the silicon. In this step, it is important that the backside square is perfectly aligned with

the previously written supporting window. By exposing the backside to KOH the silicon gets etched leaving a suspended SiN_x membrane with a nanometer-sized opening. After dicing the wafer, we can start to transfer the MoS_2. In order to be able to transfer MoS_2 one needs to obtain exfoliated or CVD grown material, best on a sapphire substrate, but other substrates such as SiO_2 or SiN_x might also work. Commensurability of the sapphire lattice with the single-crystal domain of MoS_2 ensures large grain sizes and relatively low number of defects compared to the growth on other substrates. The material now needs to be transferred and aligned from the sapphire substrate to the suspending window in the SiN_x membrane. There are several possible strategies to transfer the monocrystalline MoS_2 which are discussed in the Transfer Methods section. Briefly, a polymer such as poly(methyl methacrylate) (PMMA) or polydimethylsiloxane (PDMS) is used to lift a part of the MoS_2 material from the growth substrate. The different methods have their own advantages and disadvantages which will be discussed in detail further. Once the material is transferred, we need to create a nanopore of a suitable size. Two options are available, depending on the accessible equipment: One option is TEM drilling, where we carefully focus the electron beam to an extremely small spot size. The material is very unstable under electron beam irradiation. Therefore we will provide the best strategies for getting the desired results by inducing the least amount of damage to the material. Furthermore, we show how to assess the quality and cleanliness of the material best. The second option to create nanopore is an electrochemical reaction process,[30] which offers a fine control on the pore size by simple means of a voltage source and a current amplifier. Also, we will provide strategies for a proper flow cell design, how to reduce noise in the system and how to properly wet the nanopore.

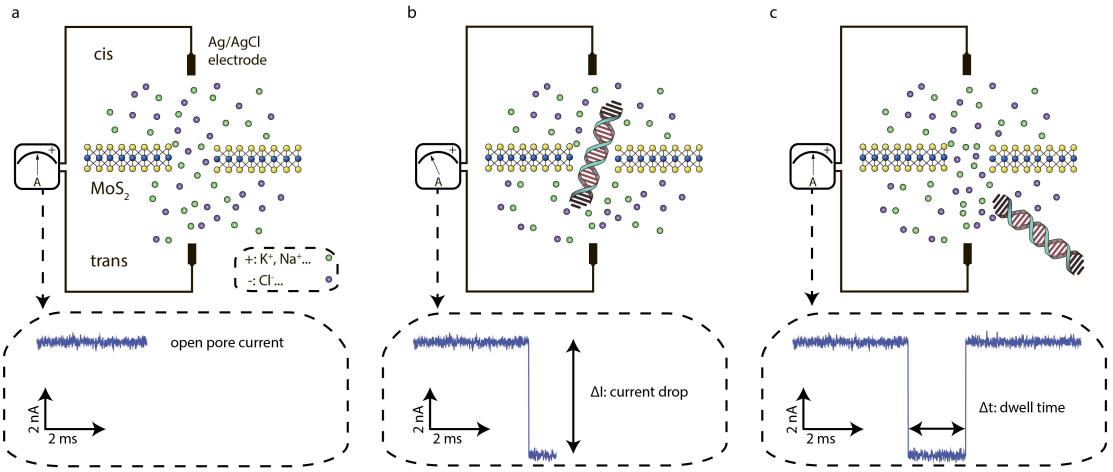

Figure 2.2: Nanopore Sensing Principle. (a) Open pore current caused by ions migrating in the electric field created by the Ag/AgCl electrodes. (b) The negatively charged double-stranded (ds) DNA gets pushed through the nanopore by the high electric field at this location. Consequently, the current drops with a magnitude of ΔI, proportional to the size of the molecule. (c) The dsDNA molecule exits the pore and the current level returns to the open pore value. The dwell time extracted from this translocation event is proportional to the length of the molecules. MoS_2 thickness and DNA molecules are not to scale.

Devices produced according to this protocol can be used to detect biomolecules such as DNA. The detection of DNA is probably the most promising application since the thickness of the MoS_2 membrane is approaching the inter-base distance in DNA, paving the way for sequencing. In 2014, the first DNA translocations in MoS_2 membranes had shown that high signal-to-noise ratios can be achieved and strong sticking of DNA to the membrane as observed in graphene is not an issue, improving translocation rate substantially.[52] The sensitivity to discern individual nucleotides using MoS_2 nanopores has been shown in 2015, using a viscosity gradient to slow the single nucleotides.[53] DNA translocations in other 2D transition metal dichalcogenides (TMDs), such as WS_2 have also been shown.[80] We have tested WSe_2 as well, of course, any other 2D material, stable in water and with a membrane thickness close to the inter-base distance in DNA can be used. Figure2.2 shows a schematic representation of a dsDNA molecule translocating through a MoS_2 nanopore in a highly concentrated salt solution. During the passage of the negatively charged polymer such as DNA, the ionic current is blocked. The amplitude of the blockage, ΔI, is determined by the number of excluded ions, which generally corresponds to the size of the molecule, whereas the length of the polymer correlates with the dwell time Δt. The electric field drop is concentrated at the nanopore and extends as a function of the applied voltage spherically into the chamber. In other words, the molecules are only captured once they diffuse into this capture radius. This dependence on free diffusion results in a correlation between the molecular concentration and the capture rate (the number of translocations per unit time).

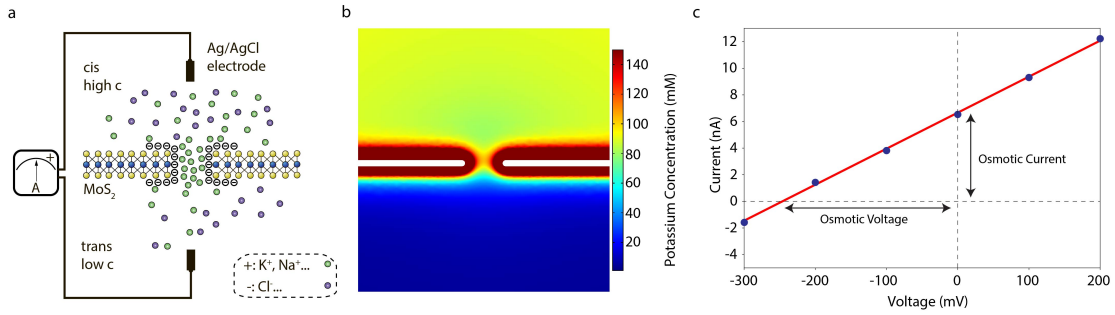

Figure 2.3: Osmotic power conversion. (a) Schematic of the experimental set-up. A salt concentration gradient provides chemical energy which is converted to electrical energy by a net current of ions through the cation-selective nanopore. (b) Finite element model simulation of the potassium distribution at the charged wall of a 6 nm nanopore. (c) Current-voltage relationship of a concentration gradient of 1000 using a 6 nm pore.

Besides translocation of biomolecules, 2D membranes are attractive candidates for water desalination and osmotic power generation (a schematic is provided in Figure 2.3a). Due to their very small thickness, the resistance to the ionic current is reduced and the power output increased. A MoS_2 membrane in solution acquires a surface charge due to deprotonation at active sites such as sulfur vacancies. It is estimated that the surface charge of a MoS_2 membrane is about -50 to -100 mC/m^2 at neutral pH.[55] This negative charge and the fact that the electrical double layer overlaps in small nanopores renders this system ion-selective,

i.e., negatively charged ions such as chloride are electrostatically repelled, whereas the cations are attracted (for illustrative purposes, Figure 2.3b shows a simulated distribution of potassium ions around a 6 nm pore). A salt-concentration-gradient pushes the ions from the more concentrated side to the less concentrated side. In combination with the ion selectivity of the pore, this results in a net current which can be converted to electrical current at the electrodes. A typical current-voltage response of such a system is shown in Figure 2.3c. The current at zero voltage is the osmotic current, whereas the voltage needed to zero the current is the osmotic voltage.[55]

2.2 Substrate Fabrication

While designing the device layout one should consider the mechanical stability of the chip, the membrane and especially the 2D material. Choosing the appropriate materials and optimizing the geometry one can substantially reduce the noise and improve the performance of the device.

The substrates used to suspend MoS_2 are typically silicon-based because of the microfabrication technology developed for the electronics industry. The main element of the chip is a thin membrane (in our case 20 nm) which has the role of supporting the 2D material. It is made of low-stress SiN_x, a good dielectric material with high mechanical strength. In order to insulate the membrane from the underlying silicon substrate, a 70 nm SiO_2 layer is deposited between the silicon and the nitride.

Additionally, this configuration also reduces the total capacitance of the chip.[81, 82] Silicon can be sculpted by the very well-established anisotropic etching with KOH or tetramethylammonium hydroxide (TMAH). The etch rate is strongly dependent on the surface orientation yielding a much faster etch in the *(100)* direction than *(111)*. This results in a pyramidal pit in silicon. The SiN_x etching rate is orders of magnitude slower than the rate of silicon which ensures that SiN_x membranes stay intact until the Si/SiO_2 layers get completely removed. Moreover, the thicknesses of the SiN_x (20 nm) and SiO_2 (70 nm) layers define the contrast of the monolayer when observed through an optical reflection microscope due to constructive/destructive interferences,[83] which is important for characterization and alignment.

However, silicon is a semiconducting material with resistivity depending on the doping level. A large surface of the silicon is exposed to the ionic solution through the etched pyramidal channel. This high capacitance system typically adds an order of magnitude higher noise compared to biological nanopores.[84]

2.2.1 Noise in nanopores

The detection of molecule translocations, especially in DNA sequencing, relies on a good signal-to-noise ratio. In order to improve the performance of the device, one should minimize

the background noise mainly coming from the nanopore chip and the interface with the electronics. The overall noise can be presented as power spectral density (PSD) as a function of frequency and generally contains several components: flicker (pink) noise, thermal (white) noise, dielectric (blue) noise and capacitive (purple) noise.

Flicker noise, or *1/f* noise, dominates the low-frequency part of the spectrum and influences the stability of the measurements. The source of this type of noise in solid-state nanopores is not well understood, but it mainly originates from the movement of ions at the pore-electrolyte interface and their convective flow in the bulk.[85] It depends on the pore size, salt concentration,[86] pH,[85, 87] and surface related effects such as charge fluctuations,[87] hydrophobic-hydrophilic interactions, and nanobubble formation.[88] An additional increase of *1/f* noise in 2D nanopores can come from mechanical vibrations of 2D material.[89, 90]

Thermal noise is frequency independent and originates from thermal fluctuations of charge carriers inside the nanopore. Dielectric and capacitive noise dominate at 1-10 kHz and >10 kHz, respectively, and are closely related to dielectric loss (heat dissipation) and the coupling of amplifier's noise with the capacitances[91–93] in the system. Since the DNA translocation events in solid-state nanopores generally have dwell times on the order of microseconds, their readout will be profoundly affected by this high-frequency noise. For that reason, reducing the capacitance is very important. The capacitance, C, of each layer in the chip can be described by $C = \epsilon_0 \epsilon_r \mathrm{A/L}$ where ϵ_0 is permittivity of vacuum, ϵ_r relative permittivity of the particular dielectric layer, A surface exposed to solution on, L the thickness of particular layer. Reducing the noise can be done by carefully choosing the substrate and membrane material such as a glass substrate[93] or low-doped silicon.[94]

Since different layers on top of each other act as capacitors in series, the total capacitance will be dominated by the layer with the lowest capacitance. Adding a thicker layer of dielectric material in the chip structure, such as SiO_2 [81, 82] or glass,[92] thus also reduces the noise.

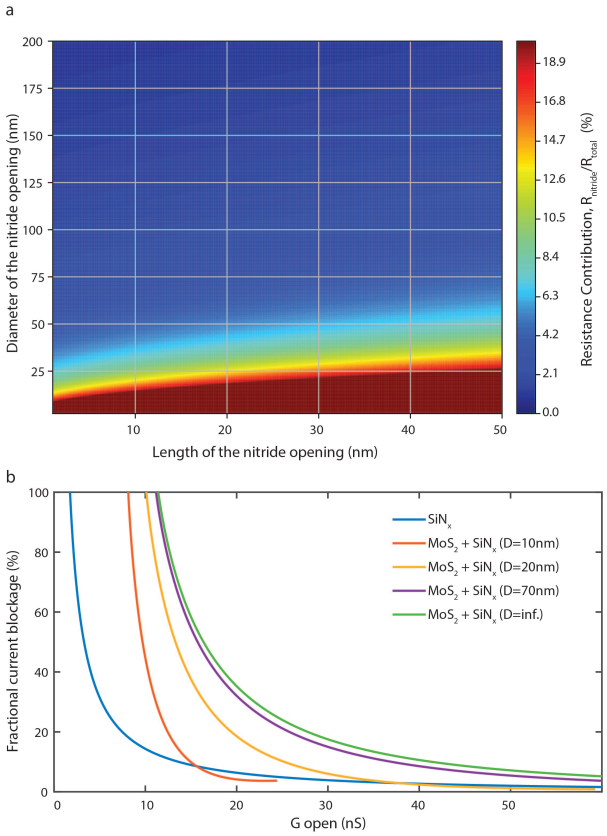

Figure 2.4: Diameter and thickness of the supporting opening. (a) The contribution of the supporting opening $R_{nitride}$ to the total resistance of the system R_{total} (= R_{MoS_2} + $R_{nitride}$). is estimated by comparing its resistance to the resistance of a 2.5nm hole in monolayer MoS_2 suspended on the supporting opening. The color-coded values are percentages of this supporting window resistance and are cut-off at 20% (red colour) for visibility. (b) The expected fractional current blockage due to DNA translocation is plot as a function of the conductance of the device and different substrate geometries. The blue curve represents the expected fractional current blockage of a pore in a silicon nitride membrane without suspended MoS_2. The green curve represents a MoS_2 membrane that is not suspended (D=Inf.) to illustrate the theoretically best configuration. The other curves show a pore suspended on a nitride opening of variable size (10 nm, 20 nm, 70 nm), which illustrates the influence of the size of the suspending hole. The thickness of SiN_x was set to 20nm whereas the effective thickness of MoS_2 was set to 1.6 nm. This can be helpful to estimate the influence of the suspending opening on observed translocation traces.

Another approach to reduce the noise is to increase the SiN_x membrane thickness (L) and decreasing the surface area of the membrane and the opening. A thicker supporting membrane of small dimension provides better robustness and reduces the capacitance. The suspending-opening should also be as small as possible to restrict the part of the 2D material that is exposed to the solution leading to better mechanical stability and thus lowering the 1/f noise.[89] However, increasing the thickness while reducing the opening could lead to a channel-like

configuration where the total ionic resistance is not governed by the 2D nanopore but by the SiN_x opening instead (Figure 2.4a).

2.2.2 Electrical Discharge

Although reducing the noise of the system sounds promising, it can cause other serious technical problems such as 2D material damage due to electrical discharges.[95] Especially during wetting of the device, charges can be built up in the flow cell and can lead to discharges when an electrical path is created by the ionic solution. The amplitude of this discharge is highly dependent on the capacitance of the device. A high capacitance device ($\approx$1 nF) can create an electrical field up to 0.1V/nm whereas a low capacitance device (< 80 pF) can create an electrical field of 1V/nm.[95] This emphasizes the potential problem occurring when using atomically thin membranes suspended on low capacitance substrates such as glass.

2.2.3 Coating

Coating the chips using silicone elastomer has been proven so far to be a safe option to reduce the noise substantially. Painting the surface exposed to the liquid outside the SiN_x membrane improves dielectric properties[84] of the substrate and reduces the capacitance. The coating needs to be resistant to the solution used in experiments. The type of coating we describe in this protocol is not compatible with organic solvents and room temperature ionic liquids (RTILs).[53]

2.2.4 Leakage

Defects in the low-stress SiN_x/SiO_2 thin-film bilayer such as charge traps and pin-holes provide additional paths for current flow, thereby affecting the current leakage through the membrane into the substrate. Such defects are introduced during film growth and sample handling during membrane fabrication, nanopore formation, and MoS_2 transfer. Current leakage can significantly impact ionic current measurements during DNA translocation through MoS_2 nanopores. While some leakage seems to be necessary for charge dissipation to ensure structural stability of the membranes (well-insulated membranes with 200 nm-thick SiO_2 underlayer proved to be highly unstable), excessive leakage is not desirable because it increases the background signal and reduces the signal-to-noise ratio.

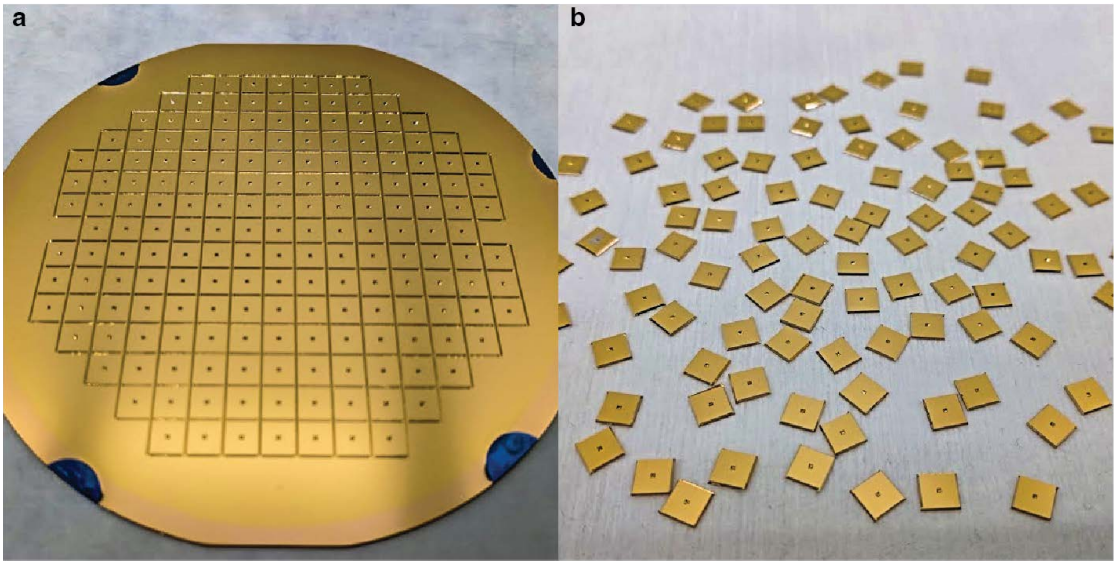

Figure 2.5: Gold-plating the test chips. (a) Test wafer with an array of membranes. (b) isolated chips with single membranes.

To assess fabrication-induced damage and to quantify variation of current leakage across a 4" substrate, an array of membranes was defined. Nanopores and electron beam lithography (EBL) alignment markers were not patterned on these substrates. Additional defects can be introduced while defining these features in fully-built devices. Since it is difficult to measure the current leakage in hundreds of devices in a fluidic cell, the test wafer was covered on both sides with 50 nm-thick layers of Au deposited at an angle of 45° by biased target deposition (BTD) (4Wave IBD/BTD Cluster Sputter Deposition System). The BTD technique, which is traditionally used in the fabrication of tunnel junctions was utilized to ensure a good sidewall coverage in the KOH etched vias and to prevent interface mixing and formation of defects in SiN/SiO_2 layers. Individual 5×5mm chips supporting single membranes were carefully isolated by cleaving without damaging the metalized surfaces, effectively creating 180 large-area metal-insulator-metal (MIM) junctions. The substrate side of a 4" wafer with an array of etched vias and trenches covered with Au and separated single-membrane devices are shown in Figure 2.5.

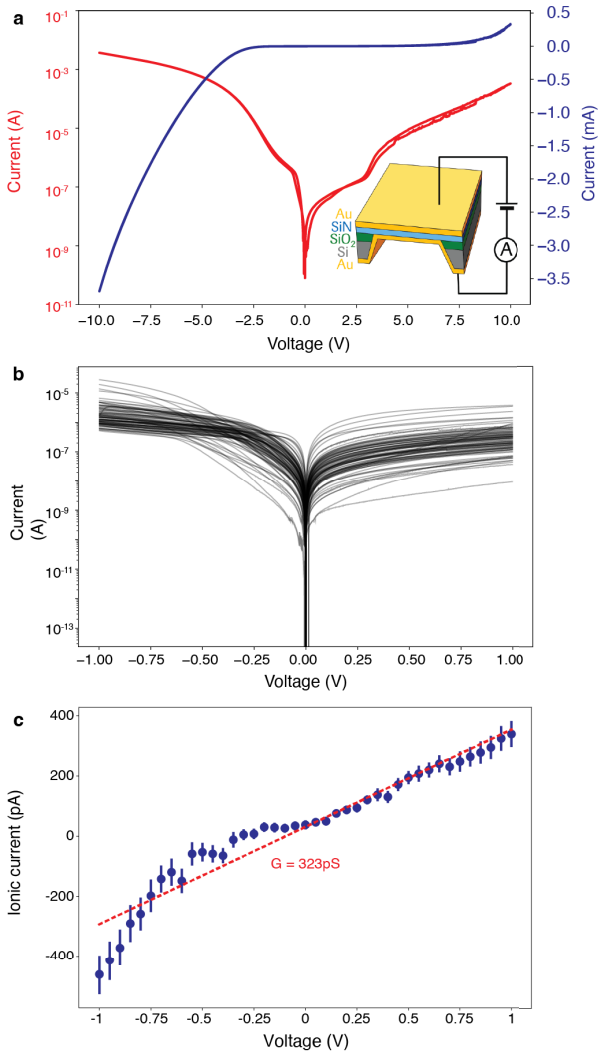

Figure 2.6: Leakage tests. (a) I–V curve of MIM junctions from the test wafer plotted on a logarithmic scale to emphasize the rapid current changes around 0 V. The right axis (blue) shows the same data on a linear scale to emphasize the observed asymmetry. Inset: a schematic of the leakage current measurement. (b) I–V curves of 90 MIM junctions. (c) I–V curve in 1 M KCl of a SiN_x membrane without an aperture. The linear fit was to extract the conductance value and the deviation from the linearity in this case is due to membrane leakage. The I–V curve itself was generated by fitting the current trace of each voltage change to a single exponential decay function (capacitive decay due to membrane charging); the error bars represent the uncertainty of this fit.

We measure current leakage in the MIM junctions at voltages ranging from –10 to 10 V using a parameter analyzer (Keithley 4200A SCS). Typical I–V curves of the measured devices are presented in Fig.2.6a. The curve is nonlinear and highly asymmetric, which is unusual for a symmetric MIM junction and is more characteristic of a metal–semiconductor junction. This suggests that current leakage through the Si substrate is probably a substantial contributor to

charge transport. Figure 2.6b shows the measured I–V curves of 90 MIM junctions showing leakage current variations at a small bias from –1 to 1 V. The plot indicates that there is an order-of-magnitude variation in leakage current across the wafer, which can be attributed to nonuniform distribution of defects. This approach is useful in assessing the general quality of the SiN_x layer, but overestimates the leakage because current paths on the whole chip surface are taken into account. In addition, the metal coating provides a low-resistance contact for the SiN_x membrane, facilitating the electron transfer.

In a nanopore experiment, only the vicinity of the membrane is in contact with the electrolyte. Furthermore, the charge transfer of ions to the SiN_x surface is much more limited than in the case of a metal contact and is typically associated with trap-assisted tunneling of electrons.[21] To further investigate the integrity of our devices in the experimental environment, we measure I–V curves in 1 M KCl. We find a much lower leakage conductance of only ≈323 pS (Fig.2.6c). Compared with typical conductances of small nanopores (>10 nS), this leakage current is not an important contribution. Note that the leakage current is highly dependent on the surface area of the SiN_x membrane, growing when the membrane size is increased. Therefore, it is critical to design the membrane as small as possible.

2.3 MoS_2 Sources and transfer

The easiest way of obtaining single-layer MoS_2 crystals is to exfoliate them mechanically from a bulk MoS_2 crystal using the scotch-tape method.[61, 96] In this process, the tape is used to peel off a thin flake from the crystal. By repeating this process many times on the cleaved flake, one can obtain layers of different thicknesses, including monolayers, which then can be transferred to the future device surface by pressing the tape down and peeling it off. However, the yield in obtaining monolayers in this way is low, and one needs to spend much time identifying single-layer flakes under a microscope. This method has several limitations: As exfoliation is a random process, the probability to obtain a single layer directly on the location of the membrane is very low, requiring a more efficient transfer process to the future device or a fabrication process that is personalized for each device.

A better way of obtaining large quantities of single-layer crystals is the direct crystalline thin-film growth on different dielectric or semiconductor surfaces such as sapphire, SiO_2 and SiN_x by chemical vapor deposition (CVD) method.[96, 97] In this method, the 2D material is grown in a reacting chamber at a well-controlled temperature and pressure condition from molybdenum and sulfur precursors. A more specific type of CVD method is metalorganic chemical vapor deposition (MoCVD)[98] in which the metalorganic precursors are typically introduced into the reacting chamber as ultrapure gases.

The material used for nanopore devices needs to have good quality, to produce a uniform monolayer with low defect density resulting in high mechanical and chemical stability. Minimizing grain boundaries during the growth increases the probability of having a uniform layer above the suspending window. Furthermore, the monocrystalline region needs to be large

enough to be easily aligned with the substrate.

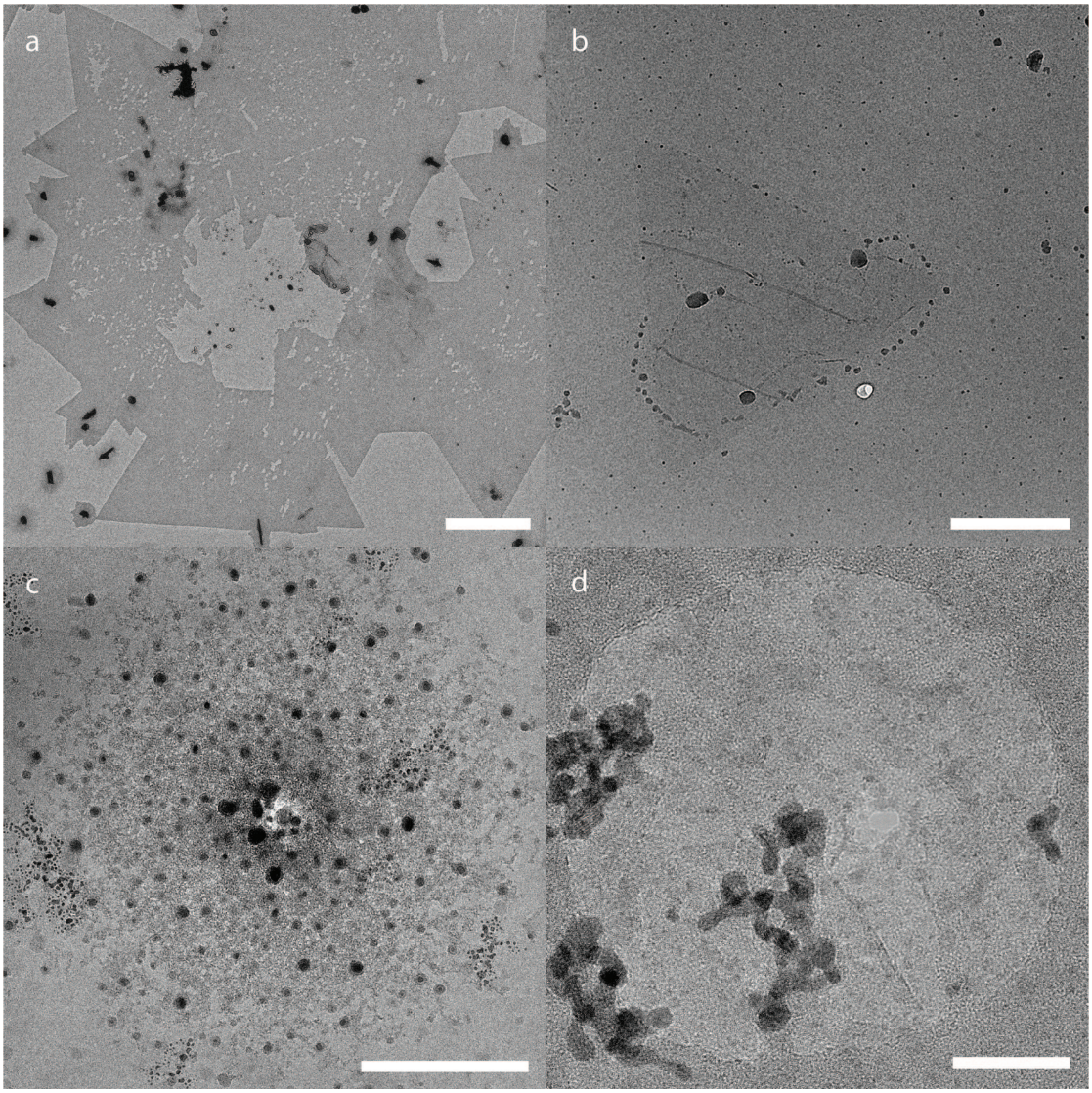

Figure 2.7: Troubleshooting MoS_2 transfer. TEM images (Talos microscope, 80 kV). (a) Detachment of a transferred MoS_2 from the SiN_x aperture area after experiments in solution. Scale bar, 5 μm. (b) MoS_2 monocrystal misaligned with respect to the opening. Scale bar, 1 μm. (c) Contaminated SiN_x aperture. Scale bar, 200 nm. (d) PMMA contamination of a freestanding MoS_2 monolayer. Scale bar, 20 nm.

2.3.1 Summary of Transfer Methods

Although a direct growth of MoS_2 over a silicon substrate opening has been shown before,[43] it is quite challenging to achieve a uniform monolayer grown over an aperture. The transfer of the material from the growth substrate to the SiN_x aperture is an alternative and reliable way of obtaining a 2D monocrystal over the opening. However, in addition to the quality of the

MoS_2, one of the most critical issues in nanopore fabrication in 2D materials is the transfer. If the suspended MoS_2 region is damaged or detached (Fig.2.7a), misaligned with respect to the aperture (Fig. 2.7b) or too contaminated (Fig. 2.7c,d), the devices are generally unusable. Appropriate transfer methods, including the cleaning procedure, will ensure a good transfer of the MoS_2 material from one substrate to the other without compromising quality. Here, we describe two methods, both of which depend on water penetration between the MoS_2 layer and the underlying substrate, usually sapphire. Owing to different surface energies of these materials (MoS_2 is hydrophobic, whereas sapphire is hydrophilic), the MoS_2 detaches from its growth substrate.[65, 99, 100]

PMMA – MoS_2 Transfer Method

PMMA is deposited as a few hundreds of nanometers thick film by spin-coating onto the substrate carrying the MoS_2. To perform multiple transfers using a single growth substrate, the spin-coated PMMA layer can be cut into small patches (such as 0.25 mm^2) using a sharp razor blade. An individual patch can be lifted-off by placing a water droplet near the edge and slightly poking the flake by a needle which enhances the water penetration between the layer and the substrate. Once the PMMA starts floating on the water droplet, it can be picked up with a glass microcapillary. At this point, the PMMA-MoS_2 layer folds around the microcapillary tip and can be transferred to another water droplet on the SiN_x chip. The layer evenly unfolds once it touches the water. The position of the layer can then be precisely adjusted under a 50x long-working-distance objective on a reflection microscope. The layer is manipulated with a glass-microcapillary attached to the x-y-z stage while the chip is fixed by vacuum to a small heating platform. Heating up to 40-50°C enables faster water evaporation. If the MoS_2 is misaligned, it can be re-aligned by adding a water droplet, which detaches the layer from the surface and allows to repeat the alignment. If the SiN_x surface is very hydrophobic, the contact angle of the water droplet will be large, and the PMMA layer floating at the surface will be curved with respect to the chip surface. This can make it difficult to adjust the exact position of the monocrystals especially if they are relatively small. Instead of water, a non-polar organic solvent could be used as a transfer medium to circumvent this minor issue. It is important to note that exposing the SiN_x surface to oxygen plasma or piranha solution would make the surface hydrophilic and therefore facilitate better alignment using water as a transfer medium. However, in our experience, hydrophilic surfaces have poor adhesion to MoS_2 which can result in the layer detachment in solutions (Figure 2.7a). Any pre-treatment to render the SiN_x hydrophilic should, therefore, be avoided.

After the transfer, one should start the cleaning procedure (in case of PMMA-assisted transfer) as soon as possible to remove all the polymer successfully. The cleanliness of the 2D material is crucial for nanopore devices for many reasons: The polymer residues locally increase the thickness and make it difficult to drill through the material no matter which technique is used (Figure 2.7d). Enlarged thickness near the pore region decreases the conductance decreasing the apparent pore size and conductance blockage caused by DNA translocations. Flexible

polymer chains can disturb the flow of ions and DNA molecules, creating an unstable current baseline, and sometimes even gradual clogging of the hole. The cleaning protocol depends on the polymer used for the transfer procedure. The procedure can be divided into two parts: First, the majority of the polymer gets removed with several iterations of dissolving and diluting in hot acetone followed by rinsing in hot IPA and DI water. The second part is an annealing process at temperatures higher than 300°C in inert atmosphere where any residual PMMA chains are thermally degraded.

PDMS – MoS_2 Transfer Method

Transfer of MoS_2 using PDMS has been reported earlier[65, 72, 101, 102] on diverse substrates. The technique relies on the hydrophobic-hydrophilic property of the MoS_2 and substrate respectively. In our experiments, we use a small PDMS-stamp (1 mm^2) anchored to a glass slide (described in Figure 3.5) to lift-off mono-crystalline MoS_2 grown on a sapphire substrate using the capillary-force exerted by water. The PDMS stamps are hydrophobic, thin, flexible and optically transparent, they can be operated easily using a simple micro-manipulator to lift-off and perform the transfer of MoS_2 onto the SiN_x membrane with good precision (a transfer video is also available in the online version of this text).[44]

Briefly, the PDMS stamp (hydrophobic) is brought in physical contact with the MoS_2 (hydrophobic) surface which is grown on a sapphire substrate (hydrophilic). Following this, a water-droplet is placed around the edge of the PDMS/ MoS_2 /sapphire surface and using a micromanipulator the PDMS stamp is slowly lifted off (Z-direction). Due to the capillary action, the water penetrates between the sapphire and MoS_2 transferring MoS_2 directly onto the PDMS surface where it adheres by hydrophobic interaction. The PDMS stamp being optically transparent, allows precise alignment of the MoS_2 to the SiN_x membrane. The transfer is terminated by simply stamping the MoS_2 to the SiN_x membrane. The technique can be used to transfer multi-layer MoS_2 and can be extended to other hydrophobic TMDs grown on a hydrophilic substrate. No further cleaning steps are required in this technique.

2.3.2 Transfer Quality

Optical microscopy and photoluminescence can be used to quickly confirm if the 2D material was successfully grown, transferred and aligned onto the desired surface. Transmission electron microscopy (TEM) has become a standard tool not only for detailed inspection and nanopore imaging, but also for drilling nanopores. Ionic current measurements are routinely used for pore characterization in ionic solution and have the advantage of providing direct information on the pore size at any time during the experiment. In combination with the electrochemical reaction (ECR) process[57] for creating nanopores, it is possible to avoid the use of TEM altogether thereby enabling a low-cost and simple nanopore fabrication.

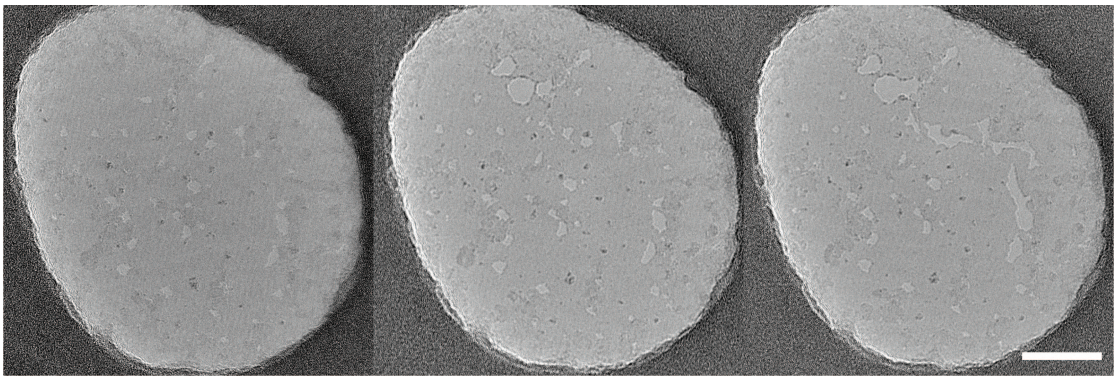

Figure 2.8: Beam damage. (Left to right) Successive damage of an MoS_2 monolayer by an electron beam. Scale bar, 20 nm.

TEM characterization

High-resolution TEM (HR-TEM) is a technique with subnanometer resolution and gives the best insight into the quality and cleanliness of 2D material at the atomic level. The imaging of 2D crystals is extremely challenging since the electron beam can induce damage in the structure of the crystal. In the case of MoS_2 the main mechanism can be described as a "knock-on" damage where the atom is ejected from the crystal due to inelastic scattering of the incident electrons.[103] Since the lighter atoms need less energy to be displaced, the S atoms will be more easily ejected (the knock-on threshold voltages for Mo and S are 560 kV and 80 kV, respectively).[104, 105]

In order to prevent material damage, the imaging needs to be performed at a low acceleration voltage and in a high vacuum environment to avoid any excess of moisture and gaseous molecules. We perform imaging with 80 kV acceleration voltage while keeping the electron current density below 0.05 pA/nm^2. However, even at this condition sulfur vacancy defects can still be introduced and can lead to layer-cracking over time (Figure 2.8). As mentioned earlier, the regions exposed to the electron beam should have as little contamination as possible since residues can migrate and contaminate the clean parts. Selected area diffraction can give information about the crystal structure of the material and verify if the transfer was successful. Since commercial TEM holders are usually made for 3-mm diameter TEM grids, it may be necessary to design a custom-made holder that fits the nanopore chip.

2.4 Nanopore Drilling and Ionic Measurements

2.4.1 Nanopore creation by TEM drilling

The drilling can be performed in the same mode (HR-TEM bright field, 80 kV) as the imaging. The beam should be set to the smallest spot size, enabling better precision during pore creation. First, the area of interest is placed in the center of the field of view. The beam is then quickly

contracted to the smallest spot in the center of that area. If the layer is clean, within a second, one will notice local damage of the layer. During the pore growth process, the beam spot can be continuously increased up to the desirable pore size to monitor the process more easily. Once the pore is grown to the desired size, the beam should be blanked immediately to stop further damage to the layer. After spreading the beam, it is safe to unblank the beam and image the nanopore. In this approach, the critical step for making small pores is fast beam contraction. During the contraction time, the current density markedly increases, which sometimes causes the layer to be damaged before reaching the smallest possible beam size.

In our experience, creating nanopores <2 nm with TEM is not very controllable, and extreme care must be taken because it is very easy to destroy the sample. Furthermore, the TEM technique is expensive, time consuming (only one sample can be inspected at a time) and requires a skillful operator.

2.4.2 Nanopore creation by Electrochemical Reaction (ECR)

Nanopores can also be created in ionic solution by applying a high potential difference across the membrane, thereby triggering an ECR on the surface of the material. There are two variations of this technique: application of a series of short high-voltage pulses[106] and a stepwise increase of voltage until a certain threshold value is reached.[57] We use the second approach, which enables us to create pores <2 nm with high precision. We start with a low voltage (200 mV), which we slowly increase in steps of 100 mV. The leakage current is usually constant for a certain voltage value. Once the critical voltage is reached, the current starts increasing more dramatically, indicating pore growth. One can monitor the growth process by observing the current level and can terminate the process when the pore has reached the conductance corresponding to the desired size. The threshold value highly depends on the number of active sites in the material (i.e., defects), the thickness of the material and cleanliness.

From our experience, the threshold voltage can vary between 0.8 V and 2.5 V. The advantages of this method are several: (i) The pore creation can be done in situ, avoiding contamination from the TEM. (ii) The drilling can technically be done with the same nanopore setup, which makes it a low-cost, simple and accessible technique compared to TEM. (iii) A big advantage comes from the fact that this process is scalable, enabling parallel nanopore fabrication.

2.5 Ionic Current Measurements

Due to their simplicity, ionic current measurements represent the primary characterization method in the nanopore field, providing quick information on the nanopore size. By varying the measurement conditions such as pH, one can get insights into more specific material properties such as the membrane capacitance or the surface charge density. Comparing to TEM imaging this is an easier and cheaper way of nanopore size characterization, but

unfortunately, it does not provide any information about the cleanliness and the number of pores.

The ionic conductance of the nanopore, G, can be expressed by:

$$G = \sigma \left[\frac{4L}{\pi d^2} + \frac{1}{d} \right]^{-1} \tag{2.1}$$

where σ is the conductivity of the solution, L the MoS_2 membrane thickness, and d the pore diameter.[49, 107] The first term in the brackets is related to the resistance of a nanopore channel that depends on the pore area and thickness. The second one is linked to the access resistance, a resistance that is caused by convergence from bulk to a confined area. The access resistance depends mainly on the diameter of the constriction and can be visually presented as two semi-cupola regions, one at each side of the pore, which influence the nanopore conductance. The pore 'senses' not only what is translocating through the channel, but also everything that can be found in the region in front of the pore. This is even more pronounced in 2D pores that have a high aspect ratio, d/L, where the access resistance dominates over the channel resistance and increases the sensing length significantly. This simple and practical geometric model does not take into account many electro-osmotic effects such as the surface charge of the material near the pore, a local gradient of concentration, irregular pore geometry or functional groups at the pore rim, which all affect the conductance as well.[52, 108]

Experimentally, the value of G can be measured by recording the ionic current baseline at a specific voltage. Due to asymmetric charge distributions, pore geometries or improper wetting, the current-voltage dependence is not always linear, so it is more accurate to record the current at different values of voltages. The value G can then be easily extracted from the slope of the linear I-V dependence. While recording the ionic current, it is important to acquire enough data since the current is exponentially dropping or increasing, respectively, within the first few seconds after the voltage switch. This happens because the voltage changes cause charging (or discharging) of the capacitors in the system. The real baseline current value can thus be fitted exponentially from this decay region, or linearly from the points after the decay where the current is stabilized. Due to their fine structure 2D-material pores are very susceptible to electrochemical reactions and voltages applied, so in order to reduce the risk of pore enlargement, it is better to stay below +/-400 mV, or even less depending on the conditions and the quality of the material. Exposure to laser light,[80] high level of oxygen in solution or the presence of reactive species can enhance the degradation of 2D material. If the material has a large number of defects, it will be also more prone to electrochemical reactions.[57]

Molecule translocations and pore-size estimation. While passing through the pore a molecule is blocking the flow of ions which causes a conductance drop ΔG:

$$\Delta G = \frac{G(d) - G(d_{\text{eff}})}{G_{(\text{d})}} \tag{2.2}$$

where G(d) is an open pore conductance and G(d_{eff}) the conductance of a partially blocked pore. The effective pore diameter, d_{eff}, denotes the diameter that corresponds to a pore with the same conductance as the blocked pore. It can be expressed by: $d_{\text{eff}} = \sqrt{(d^2 - {d_{\text{mol}}}^2}$, where d and d_{mol} are the diameters of the pore and the translocating molecule, respectively.

Due to the access resistance, a detected current signal does not necessarily need to be caused by a translocation through the channel. A drop in conductance can be provoked when a molecule temporarily resides inside the pore sensing region, partially enters or just probes the access resistance.[22, 109] The dwell-time and the current drop of a translocation event highly depends on the applied voltage. Consequently, recording current traces at different voltages should indicate if a certain current trace is a translocation. If the pore size is known, it is advantageous to calculate the expected conductance drop based on the diameter of the molecule and compare it with the experimental values. Since the blockage contains information on how big the pore diameter is with respect to the diameter of the translocating molecule, one can use DNA as a molecular ruler to extract the pore diameter from the conductance drop of DNA.[89, 107, 110] This is particularly useful when the pore is created in situ by dielectric breakdown or electrochemical reaction[21, 53] In general, it is better to use dsDNA because it is more rigid than ssDNA[107] and consequently tends to fold less. For the size estimation of relatively small pores (smaller than ≈6 nm) one should avoid using very long DNA (>10k bases) since it can easily fold and clog the pore.

Influence of multiple pores: In the case that one has more than one pore which are far away from each other and do not influence each other's conductance, the DNA blockage would be higher than predicted due to the contribution of access resistance.[57] However, by increasing the number of pores and by reducing the distance between them, the total conductance should scale sub-linearly, meaning that the conductance per pore strongly decreases with the number of pores.[111]

2.6 Experimental Set-Up for Nanopore measurements

2.6.1 Amplifiers Set-Up

A low noise current amplifier is used to measure the current generated at the Ag/AgCl electrodes. Historically, the patch-clamp amplifier Axopatch 200B (Molecular Devices, San Jose, California, United States) has been widely used in nanopore experiments due to its excellent noise performance and simplicity of use. The maximal achievable bandwidth is set to 100kHz, which is enough for most purposes, but might not be sufficient for small molecule translocations, such as proteins, where typical dwell times are in the order of a few microseconds.[30]

Table 2.1: A selection of current amplifiers used in nanopore experiments. *Analog-to-digital-converter unit available separately.

Amplifier	Bandwidth	Current limits	DAQ	Voltage limits	Company
Axopatch 200B	100 kHz	200 nA	No*, BNC	1 V	Molecular Devices
Chimera VC100	1 MHz	20 nA	Yes, USB3	1 V	Chimera Instruments
Femto DLPCA-200	<500 kHz	30 mA	No, BNC	10 V	Femto Messtechnik
eONE	100 kHz	20 nA	Yes, USB2	380 mV	Elements
EPC 10 USB	60–100 kHz	2 μA	Yes, USB2	2 V	HEKA Elektronik

Furthermore, the Axopatch 200B can apply a maximum voltage of 1V, which might not be sufficient for all applications such as ECR or dielectric breakdown.[21]

Amplifiers with larger bandwidths up to 1MHz especially created for nanopore experiments such as the Chimera Instruments VC100 (New York, NY, USA) are available but suffer from drawbacks such as small current ranges (e.g. ± 20 nA). Furthermore, in order to take advantage of the larger bandwidth, the devices need to be very low-noise, i.e. glass nanocapillaries or membranes fabricated on glass substrates.[93]

To alleviate the need to apply higher voltages and potentially measure higher currents than possible with an Axopatch 200B or a Chimera VC100, we use the variable gain low-noise amplifier Femto DLPCA-200 (FEMTO Messtechnik, Berlin, Germany). This flexible instrument allows measuring anything from the pA to mA range. A selection of available current amplifiers useful for nanopore experiments can be found in Table 2.1.

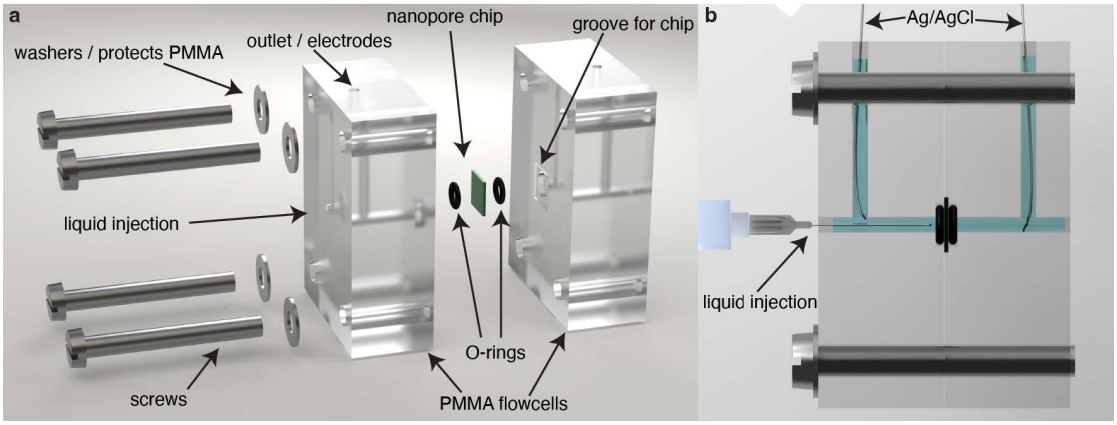

Figure 2.9: Flow Cell Design. (a) Parts of the flow cell assembly. b, Side-view of the assembled system. A syringe is used to inject the liquid to the horizontal channels. (b) The vertical channels act as an outlet for the liquid and a place for the Ag/AgCl electrodes.

2.6.2 Flow Cell

The function of the flow cell is to safely secure the nanopore chip and to properly seal the chip to the chamber in order to avoid unwanted current leakage. All materials used need to

be electrically insulating. Disposable flow cells using PDMS can be prepared by designing appropriate molds (machined or photolithography). Here we describe a two-part flow cell based on computer-numerical-control (CNC)-machined PMMA. The advantage of using PMMA over other materials is its transparency after polishing. Transparency is crucial in order to detect bubbles during the filling process.

A rendering of a disassembled version of the proposed flow cell set-up can be found in Figure 2.9a. A 3D design of the proposed flow cell is available in Supplementary Data on the online version of this paper.[44] The flow cell is comprised of two PMMA blocks that can be screwed together. The nanopore chip is sandwiched by two rubber O-rings placed in the appropriate grooves in the PMMA blocks. To avoid breakage of the fragile silicon chip, a groove with dimensions matching the chip in one of the PMMA blocks can be added. This groove will fit the O-ring and the chip, so that the surface is leveled with the rest of the PMMA block. In such a configuration breakage of the device by screwing the parts together can be completely avoided (Figure 2.9b). The horizontal inlet is used to apply the liquid to the nanopore. Typically, we use 1ml insulin syringes with needles slightly shorter than the inlet length to avoid contact and breakage of the chip. The second, vertical channel acts as an outlet during liquid injection and washing. Furthermore, it allows to insert the Ag/AgCl electrodes. In order to prevent evaporation of the buffer solution, the channels can be sealed by glass slides or PDMS plugs. Since these flow cells are reusable, a good cleaning strategy is needed in order to completely remove analyte residues. For this purpose, we use an ultrasonic bath in diluted soap (RBS 25 solution), followed by several DI-water washes and rinsing in ethanol.

2.6.3 Device Handling

To mitigate the problem of breaking MoS_2 due to electrical discharges, a few simple preventive measures should be introduced: (1) Wear antistatic gloves and a grounded wrist strap at all times when handling the flow cells. (2) Perform all work on a grounded anti static table mat. Additionally, any charge build-up can be neutralized using an Ag/AgCl connection between the two sides of the membrane during wetting and handling of the flow cell.

2.6.4 Pore Wetting

Ethanol and DI-water at a 1:1 (vol:vol) ratio is used to wet the pore Step 38B(i-ix) due to its lower surface tension. In our experience, the ultrathin membrane wets very rapidly (a few minutes) rendering lengthy soaking unnecessary. Usually, salt solutions buffered with tris(hydroxymethyl)aminomethane (Tris) and ethylenediaminetetraacetic acid (EDTA) adjusted to pH 7.4. are injected after the wetting step. EDTA is added for the purpose of DNA translocations since this chelating agent binds divalent cations and prevents DNA from coagulating. Degassing the buffers is very important since nanobubbles can form at the nanopore and block the ionic current.

2.6.5 Electrodes

In nanopore measurements, conventional reference Ag/AgCl/KCl electrodes are used. Besides having a stable electrode potential they are also nonpolarizable, which means there is no need to overcome an overpotential in order for the current to flow. In other words, in this way the potential difference across the membrane is equal to the potential difference that is applied. If the experiments are performed in chloride-based solutions and the measured currents are low (nA), electrodes can be made simply by chlorinating a silver wire and inserting them directly into sample solution. The chlorination is usually done by leaving the silver wire in a bleach solution or electrochemically by applying a positive potential to the silver wire inserted into a KCl solution. In this way one gets a greyish AgCl coating which should be thick enough to ensure stable current measurements. Since AgCl is photosensitive,[112] electrodes need to be freshly prepared before each experiment and stored in the dark.

Table 2.2: A selection of available nanopore data analysis software.

Name	Functions	Language	Lab
Open Nanopore	Event extraction, multilevel fitting and statistics	MATLAB	LBEN, EPFL
PythIon	Trace viewer, event extraction	Python	Wanunu lab, Northeastern University
MOSAIC	Multistate nanopore data, highly extensible	Python	National Insititute of Standards and Technology (NIST)
Transalyzer	Event detection, statistics	MATLAB	Dekker lab, Delft University of Technology, The Netherlands
Nanopore Analysis	Event detection, statistics	MATLAB	Long lab, East China University of Science and Technology, Shanghai, China
Chimera Software	Acquisition, event filter and automatic I–V curve creation	Python	LBEN,EPFL
Pypore	Event detection, Event analysis	Python	Drndić Lab, University of Pennsylvania

2.7 Signal Processing and Data Analysis

2.7.1 Data Acquisition

Solid-state nanopore data is typically acquired at bandwidths of about 10kHz due to the fairly high noise in silicon-based nanopore devices. Reducing the noise level of the nanopore chip using glass substrates made it possible to push the bandwidth to 1MHz.[93] Typically, the data is acquired through an analog-to-digital converter running at an appropriate sampling frequency. The data can then be saved as received by the card or a specialized software is used to save only the frames that contain the signal of interest while discarding the rest. In simple terms, the software analyzes the currently received signal frame and detects by a simple thresholding method whether a translocation event occurred or not. In the case of a detected translocation event, the software saves the current frame. If no event is detected the frame is discarded. This strategy allows to keep the file-sizes to reasonable values (this is especially important at high bandwidths) and facilitates the subsequent analysis.

A carefully designed acquisition software with automation features should help the experimenter to save time and improve reproducibility. We will discuss a few key elements that can help to improve the productivity:

1. Automatic voltage sweep. The user should be able to select the voltage range and the time spent at each point (dwell time). In order to avoid unilateral charging of the membrane the sweeps should be done in alternating polarity, i.e. 0, 100, -100, 200, -200mV...
2. Digital low-pass. Depending on the acquisition bandwidth used, the signal needs to be digitally filtered in order to lower the noise and make translocation events visible.
3. Signal detection. At low voltages the translocation rate might be very small, making it crucial to record only when translocations occur. This can be achieved by implementing a live translocation detection. For example, a simple threshold can be defined as: $y(t) < \mu_y - Sx\sigma_y$ current signal, μ_y the signal mean and σ_y, the standard deviation of the signal. S is a parameter chosen by the user to set the sensitivity of the detection. Once the condition is satisfied, the current sequence can be saved.
4. Automatic Zap. This function applies a negative voltage of chosen amplitude and duration. This is useful to unclog the nanopore.
5. Feedback Loop. Automatic voltage reset (0V) when the device reaches a predefined conductance value. This is especially useful for the ECR method where the controlled growth of the nanopore should be stopped at a certain conductance.

Typically, LabView (National Instruments, Austin TX, USA) provides an easy to use environment for developing the acquisition software. Depending on the devices used, other programming languages such as Python can be powerful tools.

2.8 Data Analysis

In this part, we provide a very broad overview of the data-analysis flow.

2.8.1 I-V Relationships

Ideally, the recorded file should contain current and voltage data. The data is then segmented into piecewise constant voltage values. Due to the high capacitance of the nanopore device, a short decay of the current is observed when the voltage switches. The current in each segment should then be fitted to an exponential decay function: $y(t) = Y_0 e^{-\frac{t}{\tau}} + Y$, where where Y is the current at infinite time, corresponding to the current of interest in the I–V characteristic; $Y_0 + Y$ is the initial current of the decay and τ the decay rate. Extracting Y and plotting it for all voltages V will lead to the I–V curve. The slope of this curve corresponds to the conductance S (=1/R).

2.8.2 Translocation Data Analysis

The first step in analyzing translocation data is to find the location in the trace, where the event occurs. One way to detect these abrupt current changes is to create a mean and variance trace which, combined, provide a thresholding condition for detecting the current drops. These detection algorithms can be implemented using appropriate digital filters and are widely implemented in existing nanopore software (see Table 2.2) coordinates of the events are found, the internal structure of the translocation might be of interest. Other algorithms such as the CUSUM[113] are summarized in a statistically more meaningful way. Typically, scatter plots and histograms of the current drop versus the dwell time are built in order to reveal subpopulations linked to the molecules structure during the translocation. during the translocation.

2.8.3 A selection of available software

Many research groups have developed their own software to handle nanopore data and often made it publicly available. The general requirement for such a software is first to extract translocation events from the noisy signal. Once the locations of the translocation events have been found, the software fits the amplitude and dwell time of the event. Not all programs can handle multi-level events. The amplitude and dwell time are fitted using different methods, in some cases the effects due to filter distortions are considered, for other it is not. From all the software listed in Table 2.2, MOSAIC is probably the most comprehensive, but likely the one with the steepest learning curve.

2.9 Comparison with other methods

There are many advantages of the fabrication procedure described in this protocol over previously published procedures. First, the substrates are fabricated at the wafer scale using e-beam lithography and RIE etching to achieve the suspending window. In similar work, the suspending opening have been done using FIB,[48] which typically requires chip-per-chip alignment, limiting the throughput and producing additional costs. Furthermore, using ECR, we describe an alternative way of producing the nanopores which greatly reduces the costs and increases the throughput. It would be straightforward to expand this technique to the wafer scale by using individually addressable microfluidic channels and customized software.

In terms of material, MoS_2 provides some advantages over the better-known graphene monolayers. First of all, DNA is less sticky to the surface of MoS_2, whereas in graphene significant stickiness is observed.[50] Other TMDs or alternative ultra-thin 2D materials might provide equal or better properties than MoS_2. So far only WS_2[80] and hexagonal boron nitride (hBN)[110] have been investigated as alternative membrane materials. We have tried WSe_2 as well, but no advantage was found. Therefore, more explorative work is needed to evaluate the large number of possible candidate materials available.[114]

In terms of 2D material transfer, most of the existing transfer methods rely on polymers which are spin-coated on exfoliated or CVD-grown MoS_2 and then detached from the substrate using an etching solution such as KOH or NaOH.[102, 115, 116] This might induce defects in the MoS_2 which is highly problematic for nanopore devices application. These methods are also limited by residual contamination by the etchants, demanding additional cleaning steps. Moreover, many methods usually involve large-scale transfer of materials,[70, 72, 99, 100] which lacks the precision in aligning the micron-sized 2D monocrystals over the specific membrane area. Since the suspended area is quite small, large area transfer also results in a waste of material especially if one has a limited supply.

The PMMA-assisted transfer is based on the wedging transfer method[65] which employs water-assisted lift-off. The published method enables a microscale precision by manual alignment under the microscope and repositioning of the same layer many times. In our approach, we cut the PMMA pieces down to 0.25 mm^2 and it is possible to manipulate them by a microcapillary on a water droplet.

Deterministic transfer of 2D materials by using PDMS has been demonstrated.[41] However, while this is a method suitable for exfoliated material, it represents a challenge in the case of CVD-grown monolayer since it cannot be easily detached from the growth substrate. We address this issue by using PDMS stamps (up to 1 mm^2) in combination with water assisted lift-off. The PDMS transfer methods are attractive since they require fewer steps of post-transfer cleaning, however, the flake repositioning is not possible in this case in contrast to PMMA-assisted approach. Both methods are etchant-free, which reduces the number of steps and retains the quality after the transfer. In summary, the transfer can be done highly precisely, fast, economic and can be extended to other 2D materials.

In terms of performance, devices made in MoS_2 were predicted to achieve single-base resolution due to their small thickness. MoS_2 is thicker than graphene, but is believed to capture the ionic current better, since the ions are actually larger than the thickness of graphene membranes.[50] Furthermore, interesting electrical properties, in particular the intrinsic band-gap, allow the creation of more sophisticated devices and pave the way for exploring alternative sensing mechanisms.[56]

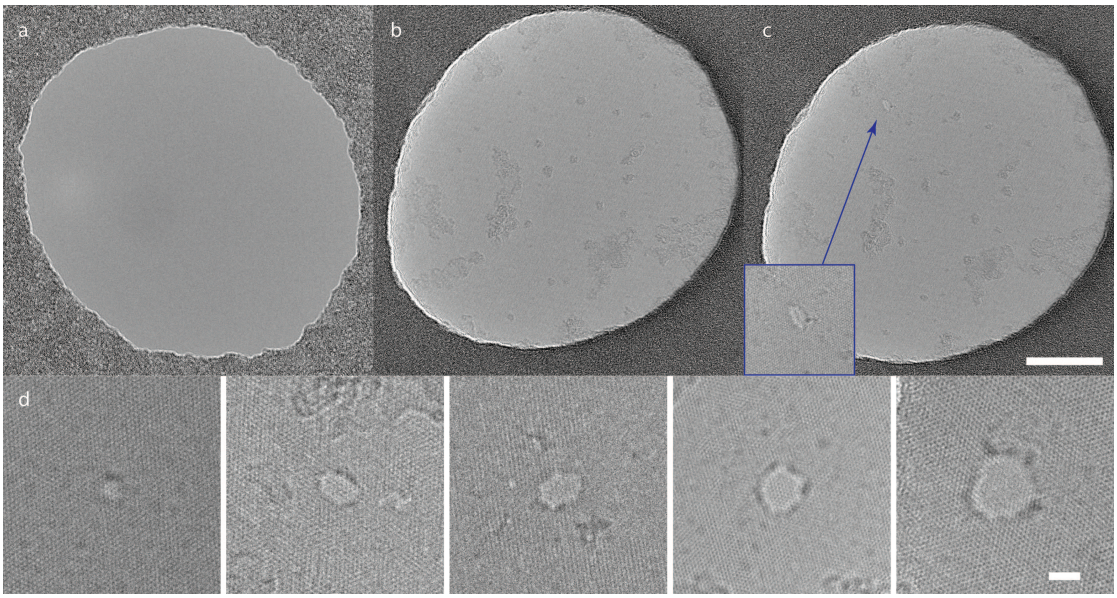

Figure 2.10: TEM images (Talos microscope, 80 kV). (a) A clean, successfully etched SiN_x aperture. (b) A clean MoS_2 monolayer suspended over the SiN_x aperture. (c) The same area as in b after drilling the nanopore (inset) with an electron beam. Scale bar, 20 nm (inset, 5 nm). (d) Nanopores of different sizes created by an electron beam. Scale bar, 2 nm.

2.10 Anticipated Results

2.10.1 Chip Fabrication

There are two key components in assessing the success of the substrate fabrication. First, the size of the resulting membrane can be assessed using an optical microscope (in reflection configuration). Typically, membranes are slightly larger than theoretically predicted due to imprecision in alignment of the pattern to the crystal axis of the silicon substrate. Second, the success of creating the suspending opening using e-beam lithography and RIE can be assessed by TEM. Figure 2.10a shows a TEM image of a successful opening in MoS_2. The size and shape of the opening can be compared to the designed patterns. These holes tend to be roughly 20 % larger than designed, which is probably due to backscattering of electrons during the e-beam lithography. Another common problem is that these holes are only partially open, it is thus imperative that the fabricated substrates are checked in a TEM. Alternatively, if no TEM is available, the fabricated chip can be placed in a flow cell and the conductance can be

measured to estimate opening size.

After MoS_2 transfer, the most reliable method of checking the cleanliness and success of the transfer is TEM. Figure 2.10b shows an intact and clean monolayer of MoS_2 suspended over the opening in the SiN_x membrane. Condensing the electron beam on that same sample allows the creation of MoS_2 nanopore (Figure 2.10c). The time during which the condensed beam irradiates the spot defines the pore size. Figure 2.10d shows a collection of different pore-sizes ranging from 1 nm to 4 nm in diameter that are achievable using TEM irradiation. Of course, bigger pore size are always possible by shifting the beam or the sample to irradiate the intact parts of the monolayer membrane.

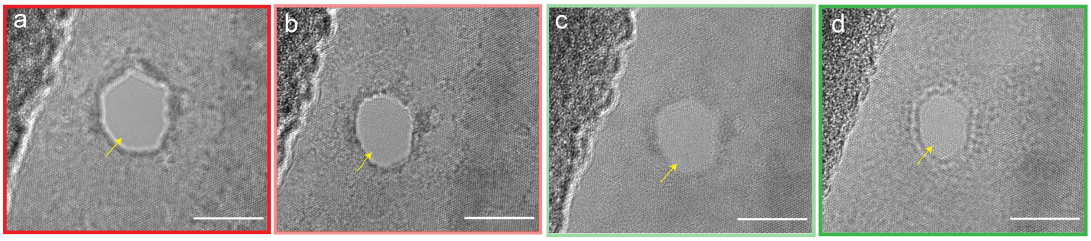

Figure 2.11: TEM image of a 10 nm MoS_2 nanopore with different Fresnel contrast at defocus values (± 100 nm). Scale bar, 10 nm. Overfocused (a,b), focused (c), and underfocused (d). The yellow arrows show evolution of interference spots.

It is worth mentioning that often there are periodic patterns on MoS_2 nanopore images from TEM. This is due to delocalisation and aberrations due to focusing. The periodic contrast moves with different defocus as seen in Figure 2.11 called Fresnel fringes of the same 10 nm MoS_2 nanopore. Underfocused, white fringes (2.11a,b) at -100 nm, -50 nm, at focus (2.11c) with least contrast and overfocused (2.11d) with black fringes. The yellow arrow shows the changes in the interference patterns with different defocus. The image is a composition of both transmitted and diffracted electron beam from the 2D material. The effect is because of different scattering of beams from the edges of the pores.

Another cause that one should be careful is related to the post-processing of the TEM images by Z-stacking multiple frames used for sensitive materials that drift while image acquisition. In this case, the stacked image can yield a final image with the interference patterns inside the nanopore.

2.10.2 DNA Translocations

In the subsequent chapter, Figure 3.7 we will summarize the DNA translocation data obtained with a device fabricated according to this protocol. We used the PDMS transfer method and applied ECR to generate the nanopore. A voltage of 900 mV was sufficient to induce a steady

current increase (Figure 3.7a, at 40 s). The voltage is then reset to zero. An IV response was then recorded between -200 mV and 200 mV and yielded a conductance of 10.3 nS. The pore size can thus be estimated to be about 2 nm. We then exchanged the cis-side buffer with buffer containing 2000 base pair long double-stranded DNA at a concentration of 10 ng/μL. This DNA was translocated at transmembrane voltages of 200, 300, 400 and 500 mV.

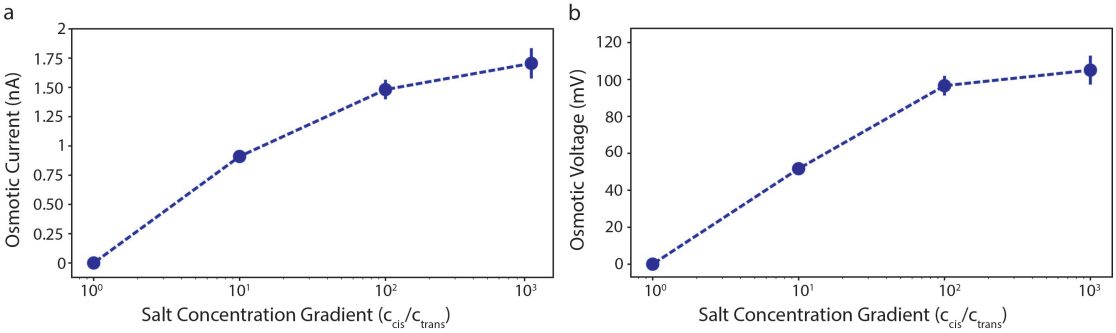

Figure 2.12: Anticipated Results: Osmotic Power Generation. All datapoints are extracted from a linear fit to the IV. The error bars are calculated by propagating the measurement error. (a) Osmotic current as a function of the salt concentration gradient (osmotic pressure). The osmotic current is defined as the net current at zero voltage generated by the osmotic pressure. (b) The osmotic voltage as a function of the osmotic pressure. The osmotic voltage is defined as the voltage needed to counteract the osmotic current, i.e. the voltage at which the current is zero.

2.10.3 Osmotic Power Generation

The application of MoS_2 nanopores for power generation relies on a salt concentration gradient. Substrate fabrication and the flow cell set-up are identical to biomolecule detection experiments. After verifying the nanopore size at symmetrical 1 M/1 M KCl condition, the current was set to zero (no osmotic pressure present). The trans-side was washed, and the buffer was replaced by 1mM KCl to create a 1:1000 concentration ratio. The first thing to notice is that the previously zeroed current is now non-zero value. A net current from the more concentrated to the less concentrated side was thus established. IV-curves taken in this condition show a prominent current offset. The electrode potential was then subtracted from the obtained value to retrieve the component due to osmotic pressure. Figure 2.12 shows the expected osmotic current (a) and voltage (b) values of a 5 nm MoS_2 nanopore. Typically, there is a saturation of the achievable osmotic power at a 1:100 concentration gradient, i.e. increasing the concentration gradient further does not significantly change the osmotic power generated.

2.11 Fabrication limitations and outlook

The main drawback of solid-state 2D MoS_2 nanopores and 2D material in general is their stability. Compared to nanopores made in thin SiN_x, MoS_2 nanopores are more prone to widening and damage, especially in solution. Also, the noise level is higher mainly due to mechanical and charge fluctuations of the suspended material. Eventual chemical modification could solve this issue. With the PMMA and PDMS transfer methods described here, there is still a risk of having unwanted polymer residues as contamination on a suspended 2D material which can affect the pore creation and translocation signals.

Nanopore fabrication by using electron beam is time consuming and expensive and not reproducible for very small pores. ECR overcomes this limitation but on the other hand it is possible to create multiple pores.[117] So far, only the substrate fabrication is done on the wafer scale all the other steps are done chip by chip. Wafer-scale growth and transfer of 2D material together with individually addressed microfluidic channels and ECR could lead toward nanopore parallelization that will enable high throughput of translocation data, as well as the upscaling of nanopore power generation. However, in terms of DNA sequencing, there are still fundamental limitations related to translocation speed that need to be resolved.[74, 118, 119]

3 Chip-scale Transfer of 2D MoS_2 film/s

The first part of this chapter: M.T. developed and characterized the polymer-free transfer method. M.T. performed bright-field TEM imaging and Raman measurements on the polymer-free transferred MoS_2 devices. The aberration-corrected STEM imaging was done by M. Tripathi and elemental analysis was performed by M.T. The second section (Section 3.4) of this chapter is a post-print version of the following publication:

> Michael Graf[1], Martina Lihter[1], **Mukeshchand Thakur**[1], Vasileia Georgiou, Juraj Topolancik, B. Robert Ilic, Ke Liu, Jiandong Feng, Yann Astier and Aleksandra Radenovic. Fabrication and Practical Applications of Molybdenum Disulfide Nanopores. Nature Protocols 14 (2019).

M.G., M.L., and M.T. contributed equally. K.L. and J.F. performed initial work on device fabrication, MoS_2 transfer and pore characterization. M.G., J.T., V.G., and B.R.I developed the substrate fabrication process, V.G. fabricated the substrates. Y.A. supervised the substrate fabrication process. J.F., K.L., and A.R. developed the ECR pore drilling method. M.G. built the transfer microscope set-up, M.G. and M.L. developed PMMA transfer method and optimized MoS_2 cleaning procedure. M.T. modified and developed PDMS transfer method, M.L., M.G. and M.T. performed TEM characterization, M.L. and K.L. optimized the TEM pore drilling method. M.G., M.L., and M.T. fabricated the devices for DNA translocation. M.G. performed the translocation experiments presented. M.G., M.L., M.T., J.T., and A.R. wrote the manuscript.

3.1 Summary

In this chapter, I will guide you through two chip-scale transfer techniques I developed in the lab during the initial period of my PhD. With emerging 2D material growth methods, exciting applications were boosted, especially biosensors based such as nanopores. Transfer is a critical step in 2D nanopores fabrication as it bridges high-quality growth and device integration. The transfer process is very sensitive and could directly affect the success rate of the devices. The first chip-scale technique I demonstrate in this chapter is a direct film transfer method without

the use of any mechanical support and provides insights into hydrocarbon contamination residues (since no polymer is used) that is currently one of the major challenges in the 2D materials and nanofluidics community. In the second method, I additionally demonstrate a polymer-based technique that is especially compatible with MOCVD-grown MoS_2 film(s) without the use of any etching solvent (KOH) which was otherwise common with conventional transfer methods.[62] With this technique, the transfer process is simple, deterministic, and more precise. I will discuss and conclude with comparisons of chip-scale transfer methods. Finally, I show biosensing applications using nanopore substrates.

3.2 Introduction

Atomically thin two-dimensional (2D) materials offer many opportunities to study fundamental science as well as exciting miniaturization potential. With the discovery of monocrystalline graphene in 2004[61] from its bulk crystal marked the onset of the field of 2D materials, and ever since it has been central to materials science and technology. Atomically thin 2D layered materials owing to their thickness, offer many exciting opportunities in fundamental science as well as exciting applications. Apart from graphene, other 2D materials such as transition metal dichalcogenides (TMDs) with general formula - MX_2, where M represents the transition metal atom (Mo, W, or Pb), and X is a chalcogen atom (S, Se, or Te). Of these TMDs, MoS_2[51] is most common and widely studied 2D semiconductor in nanoelectronics.

Tremendous amount of research has been conducted in the field of growth of 2D materials (graphene, TMDs) to achieve high-quality, crystalline, scalable large-area defect-free synthesis. In the interest of application with 2D materials there is a need to transfer as grown 2D materials from the initial growth or 'donor' substrate (typically SiO_2, sapphire) to the final or 'target' substrate. In essence, the transfer technology bridges 2D materials growth, device manufacturing as well as integration. The 2D material transfer without damaging the underlying donor substrate is one of the important key technologies for fabrication of devices that also enables recycling of the donor substrate for further growth.

Transfer technology bridges 2D materials growth and device manufacturing. Several important key experimental technologies had to follow to catch up with an advancement in the field of 2D materials. These technologies include – growth of high-quality crystals, large-area defect-free, and facile transfer of 2D materials with minimum changes to its original structure. Wafer-scale growth of atomically thin 2D materials on a large-area substrates opened opportunities toward scalable device manufacturing and flexible electronic devices. Hence there is a need toward a transfer technology that is simple, reproducible, and reliable. Structural damage of the 2D material such as folds, cracks and wrinkles are common limitations with various transfer processes. Polymers are one of the major problematic sources of contamination in 2D materials, especially after transfer even after cleaning processes. However, it is rarely reported that these contamination sources might arise not only from residual polymer (that is used as a mechanical support) but also from hydrocarbon (air-borne) sources.

Herein, I demonstrate two chip-scale transfer techniques in the context of nanopore devices. The two methods facilitate either polymer-assisted or without any polymer transfer of monolayer to few-layer MoS_2 from the growth substrate to the target substrate. Hydrocarbon-based contamination is often observed either in the form of completely covering the suspended 2D films or covering it in the patches. Often these 'residues' are attributed to the polymer (used as a mechanical support) in the transfer process. Using polymer-free technique as I will discuss below, we can see that most of the residues are contributed are inherent to the samples and arise from the air-exposure. Further, I also demonstrate a second technique which is PDMS polymer-based technique which is compatible with MoS_2 monocrystals grown on sapphire substrate with only solvent – water. The technique is very simple, easily configured using simple lab equipment and most importantly, enables recycling of the sapphire substrate as it does not involve corrosive etching of the growth substrates unlike other methods. Using this method, nanopore devices were used for DNA biosensing.

For nanopore applications requiring nanoscale 2D material thickness, there is a need towards simple, faster, and reduced contamination transfer approach. Here I demonstrate two 'chip-scale' transfer approaches:

(1) In the first part a direct transfer approach is demonstrated that is completely polymer-free, mechanical support-free and the transfer is achieved only using water as a solvent (i.e., without chemical etchants).

(2) In the second part of this chapter, I show another chip-scale stamp-based transfer process that is specially developed for MOCVD grown 2D TMD material. The method is precise and deterministic and compatible with a variety of planar nanopore substrates such as SiN_x, SiO_2, etc. In this work we used SiN_x as most common substrate for nanopore experiments.

These two methods are demonstrated using MoS_2, although it can be extended to other 2D materials.

3.3 Results and Discussion

3.3.1 Direct Transfer Approach

Large-area MoS_2 films were grown on a sapphire substrate using MOCVD method reported previously. Figure 3.1 shows the steps involved in the direct transfer process on a SiN_x surface. First, the MoS_2 films detach from the sapphire substrate due to capillary force-mediated entry of water between MoS_2 film and sapphire substrate (Fig.3.1a). Subsequently, the films spontaneously detach (≈1 min) and float on the air-water interface (Fig.3.1b). Here, we use a SiN_x substrate to transfer floating films on the nanopore aperture. The substrate is brought in close contact with the 2D films and gently removed and gradually dried on a hot plate (≈120°C, 5 min). This ensures the removal of the residual water and enhances the attachment of the films on the substrate.

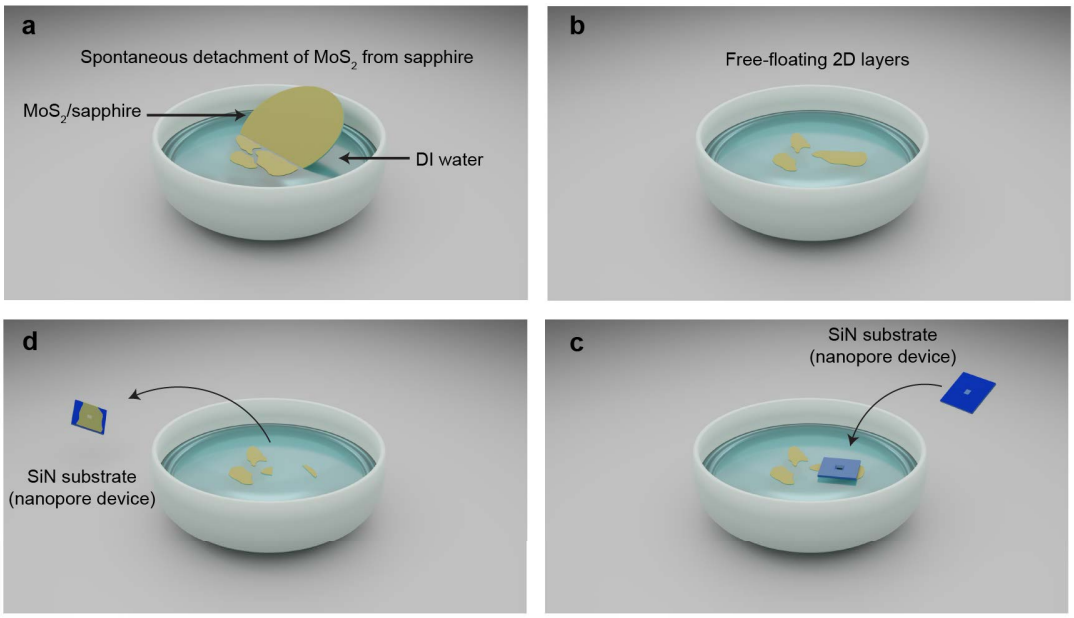

Figure 3.1: Direct transfer of MoS_2 from sapphire (growth) substrate to the SiN_x (target) nanopore substrate. (a) Water-assisted detachment of mono-few-layers MoS_2 from the sapphire substrate. (b) Free-floating 2D layers of MoS_2 without any mechanical support. (c) Transfer of the floating 2D layers onto the SiN_x substrate. (d) Transfer of 2D MoS_2 over the SiN_x nanopore substrate.

3.3.2 TEM characterization

Figure 3.2a shows an optical micrograph of typical as-transferred MoS_2 layers on a SiN_x TEM substrate. Further, we set out to investigate the transferred MoS_2 samples using TEM. As seen from the image (Fig. 3.2a), the transferred films show voids and folding post-transfer on SiN_x substrate. One of the representative suspended MoS_2 image is shown in Figure 3.2b. Bright-field TEM images of suspended MoS_2 surface with occasional contamination patches or residues on the surface (Fig. 3.2b). Further, the suspended MoS_2 layers were either monolayer or multilayer form observed as Moiré pattern in Figure 3.2c. Aberration-corrected scanning TEM images show high-resolution images of monolayer and bilayer interface with hydrocarbon residues (Fig. 3.2d). We did not observe any e-beam induced deposition while imaging the sample suggesting the persistent nature of these residues (Fig. 3.2e). Inherent single vacancy defects are shown in Figure 3.2f.

In a quest to clean or remove these residues, we treated the as-transferred samples with hot acetone (90°C, 3 h) and cleaned them with IPA. Following this, the samples were annealed in vacuum at 350°C for 8h. This process is typical for cleaning PMMA-transferred MoS_2 samples to remove contamination that might arise due to the transfer process. Figure 3.3 shows TEM images of MoS_2 samples with (Fig.3.3 a-d) and without (Fig.3.3 e-h) annealing process. It is observed that these hydrocarbon residues persist after the cleaning process. This suggests

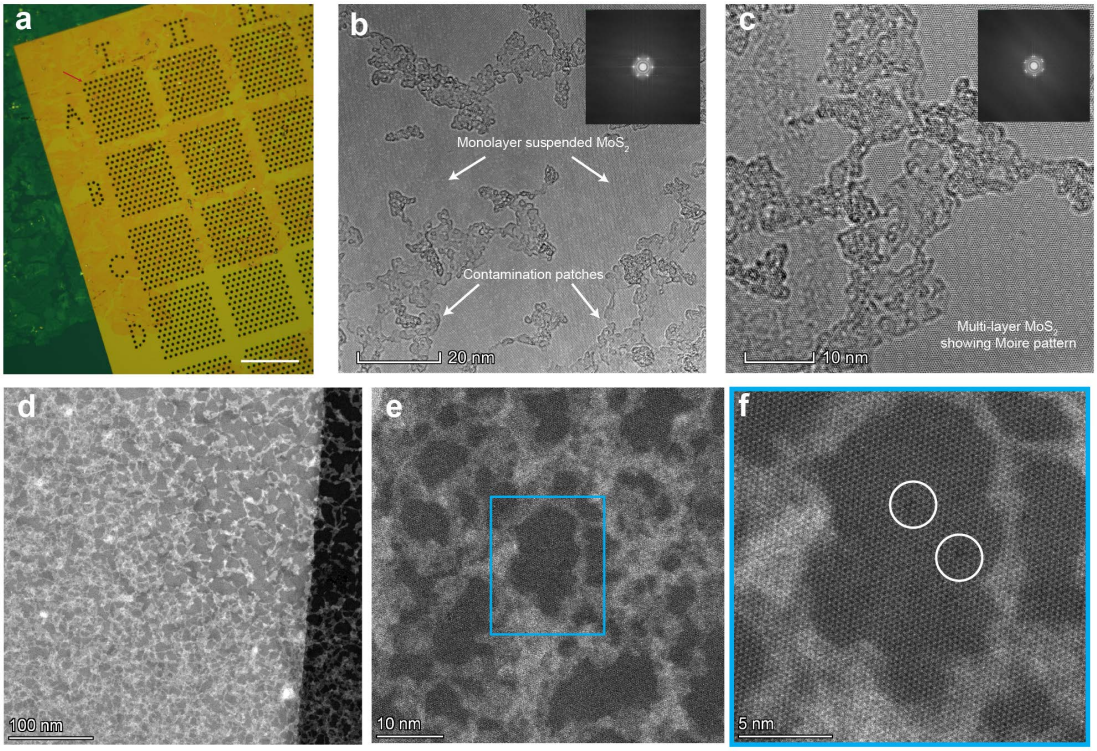

Figure 3.2: Microscopic characterization of MoS_2 films via direct transfer technique. (a) As-transferred MoS_2 on TEM grid with 200 nm thick SiN_x and each aperture size 2 μm. For TEM imaging, the suspended part of the MoS_2 is marked (red arrow). Scale bar, 500 μm. (b) Bright-field TEM image of suspended MoS_2 showing clean areas with occasional contamination patches (or residues). Inset shows FFT image showing monolayer MoS_2. (c) TEM image showing a Moiré pattern formed by MoS_2 layers, due to imperfectly aligned multi-layers as seen in the FFT image. (de) Aberration-corrected scanning TEM images of large-area suspended MoS_2 film. (f) Zoomed-in image of monolayer MoS_2 film with marked circle showing single vacancy defect.

that hydrocarbon residues are very persistent in nature and resistant to the cleaning process.

3.3.3 Raman spectroscopy of MoS_2 films

To evaluate the transfer quality and film thickness, we measure Raman spectra of the transferred MoS_2 films on the SiN_x substrates after transfer. Figure 3.4 shows three spots of MoS_2/SiN_x measured on the same sample after transfer. The difference in the Raman peaks show variable thicknesses as seen in spot 1, monolayer ($\approx$19 cm^{-1}) and multilayers spot 2 and spot 3 with peak differences as $\approx$323.8 cm^{-1}, 24 cm^{-1}, respectively. Typically, Raman spectra of MoS_2 reveal two vibration modes: E^1_{2g}, an in-plane vibration mode and A_{1g}, an out-of-plane vibration mode. The former peak appears at $\approx$380 cm^{-1} and the latter at $\approx$405 cm^{-1}. The difference in these peaks correlate to the number of MoS_2 layers. Figure 3.4b shows Raman

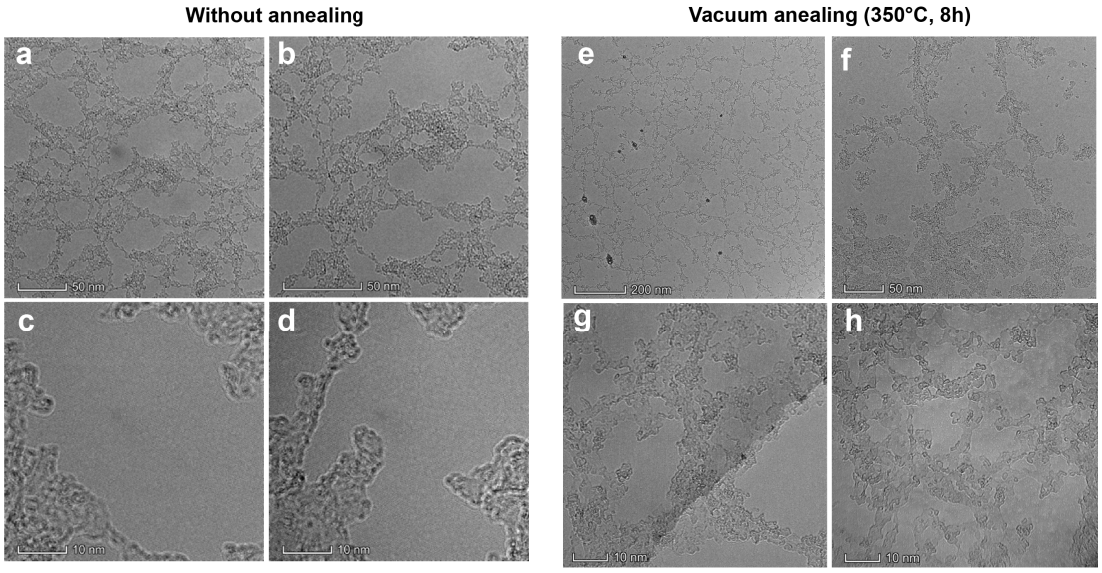

Figure 3.3: TEM image showing hydrocarbon residues are resistant to high temperature annealing process. TEM images of a suspended region of MoS_2 film after direct transfer without any treatment (a-d), and with vacuum annealing at high temperature and stored in vacuum until imaging. This cleaning process is typical for polymer-based transfer processes (e-h). The residues are still persistent after cleaning process. Scale bars: a-b: 50 nm, c-d: 10 nm, e: 200 nm, f: 50 nm, g-h: 10 nm

peak differences before and after transfer in different samples. The film thicknesses increase to ≈2-3 layers post-transfer (Fig. 3.4b). The peak differences show that the direct transfer approach renders film folding post-transfer and therefore increasing the width in the peaks as revealed in Raman spectra.

Table 3.1: Comparison of chip-scale 2D material transfer techniques.

Characteristics	Direct Transfer	PDMS Stamp Transfer	PMMA-assisted Transfer
Hydrocarbon residues	Present	Present	Present
Folding	Mostly	Occasionally	No
Scalability	Not scalable	+++	++
Transfer time per device	1-2 min	10 min	15min and 8h (cleaning)
Device yield	+	+++	+++
Solvent	DI water	DI water	DI water

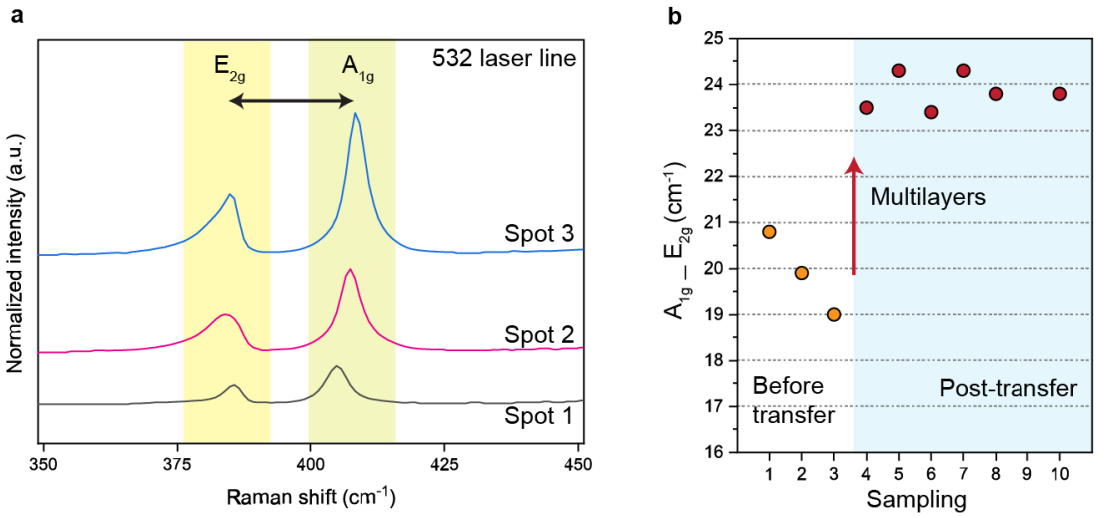

Figure 3.4: Raman characterization of MoS_2 films transferred by direct transfer approach using 532 nm laser on SiN_x substrate. (a) Raman spectra at three different locations showing two peaks corresponding to $E^1{}_{2g}$ and A_{1g} stretching modes in 2D MoS_2. The difference between the stretching modes varies at different spots on the sample. Three representative spots are shown. (b) Changes in the layer thickness is observed due to folding aberrations during the direct transfer process.

3.4 Stamp Transfer for CVD-grown substrates

Although a direct growth of MoS_2 over silicon substrate opening has been shown before,[43] it is quite challenging to achieve a uniform monolayer grown over a suspended area. The transfer of the material from the growth substrate to the SiN_x opening is an alternative and reliable way of obtaining 2D monocrystal over the opening. In general, the comparison of transfer methods is shown in Table 3.1.

Besides the quality of the MoS_2, one of the most critical steps in nanopore fabrication in 2D materials is the transfer. If the suspended MoS_2 region is damaged, contaminated or misaligned with respect to the opening, the devices are generally unusable. Appropriate transfer methods, including the cleaning procedure, will ensure a good transfer of the MoS_2 material from one substrate to the other without compromising the inherent quality.

3.4.1 Results and Discussion

Here we describe stamp transfer method that depend on water penetration between the MoS_2 layer and the underlying substrate, usually sapphire. Due to different surface energies of these materials (MoS_2 is hydrophobic, while sapphire is hydrophilic) the MoS_2 detaches from its growth substrate.[65, 99, 100] Transfer of MoS_2 using PDMS has been reported earlier[101, 102, 120] on diverse substrates. The technique relies on the hydrophobic-hydrophilic property of

the MoS_2 and substrate, respectively.

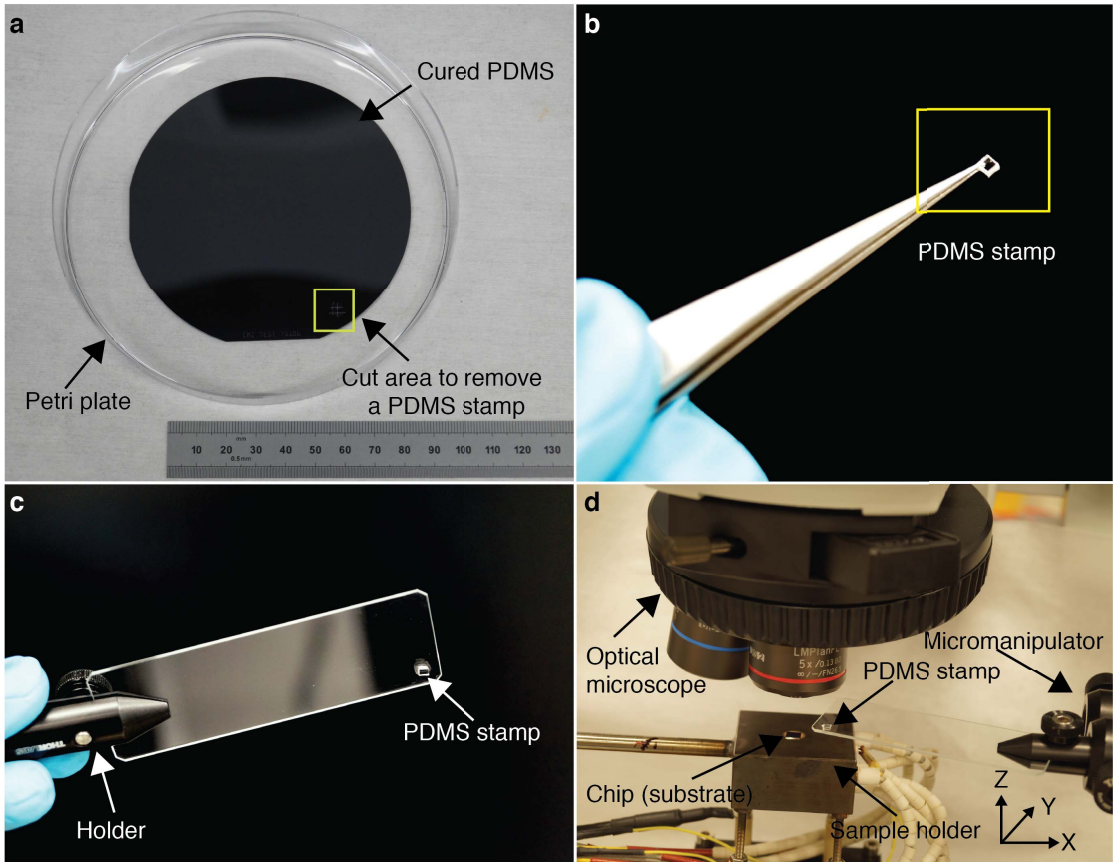

Figure 3.5: PDMS-assisted selective transfer of MoS_2 - an overview. (a) PDMS is baked on a clean blank silicon wafer inside a petri dish and the highlighted area point the place where a small stamp is dissected using a scalpel and (b) highlighting a single PDMS stamp cut from (a). (c) PDMS stamp mounted on a clean glass slide with a micromanipulator holder. The holder is fixed on a micromanipulator stage for MoS_2 transfer. (d) MoS_2 transfer experiment set-up containing a micromanipulator stage equipped with XYZ axes control with a holder for glass slide with PDMS stamp. The sample holder stage comprises of a substrate placement area equipped with a vacuum suction for stabilizing the substrate in addition to XYZ axes and yaw motions. The whole process of transfer is monitored using an optical microscope with a 5X and 50X objectives.

In our experiments, we use a small PDMS-stamp (1 mm^2) anchored to a glass slide to lift-off mono-crystalline MoS_2 grown on a sapphire substrate using the capillary-force exerted by water (Fig. 3.5). The PDMS stamps are hydrophobic, thin, flexible and optically transparent, they can be operated easily using a simple micro-manipulator to lift-off and perform the transfer of MoS_2 onto the SiN_x membrane with good precision. Briefly, the PDMS stamp (hydrophobic) is brought in physical contact with the MoS_2 (hydrophobic) surface which is grown on a sapphire substrate (hydrophilic). Following this, a water-droplet is placed

around the edge of the PDMS/ MoS_2 /sapphire surface and using a micromanipulator the PDMS stamp is slowly lifted off (Z-direction). Due to the capillary action, the water penetrates between the sapphire and MoS_2 transferring MoS_2 directly onto the PDMS surface, where it adheres by hydrophobic interaction. The PDMS stamp being optically transparent, allows precise alignment of the MoS_2 to the SiN_x membrane. The transfer is terminated by simply stamping the MoS_2 to the SiN_x membrane. The technique can be used to transfer multi-layer MoS_2 and can be extended to other hydrophobic TMDs grown on a hydrophilic substrate. No further cleaning steps are required in this technique.

3.4.2 TEM characterization of MoS_2 transferred using PDMS-stamp technique

The imaging of 2D crystals is extremely challenging since the electron beam can induce damage in the structure of the crystal. In the case of MoS_2 the main mechanism can be described as a "knock-on" damage where the atom is ejected from the crystal due to inelastic scattering of the incident electrons.[103] Since the lighter atoms need less energy to be displaced, the S atoms will be more easily ejected (the knock-on threshold voltages for Mo and S are 560 kV and 80 kV, respectively). In order to prevent material damage, the imaging needs to be performed at a low acceleration voltage and in a high vacuum environment to avoid any excess of moisture and gaseous molecules. We perform imaging with 80kV acceleration voltage while keeping the electron current density below 0.05 pA/nm^2. However, even at this condition sulfur vacancy defects can still be introduced and can lead to layer-cracking over time.

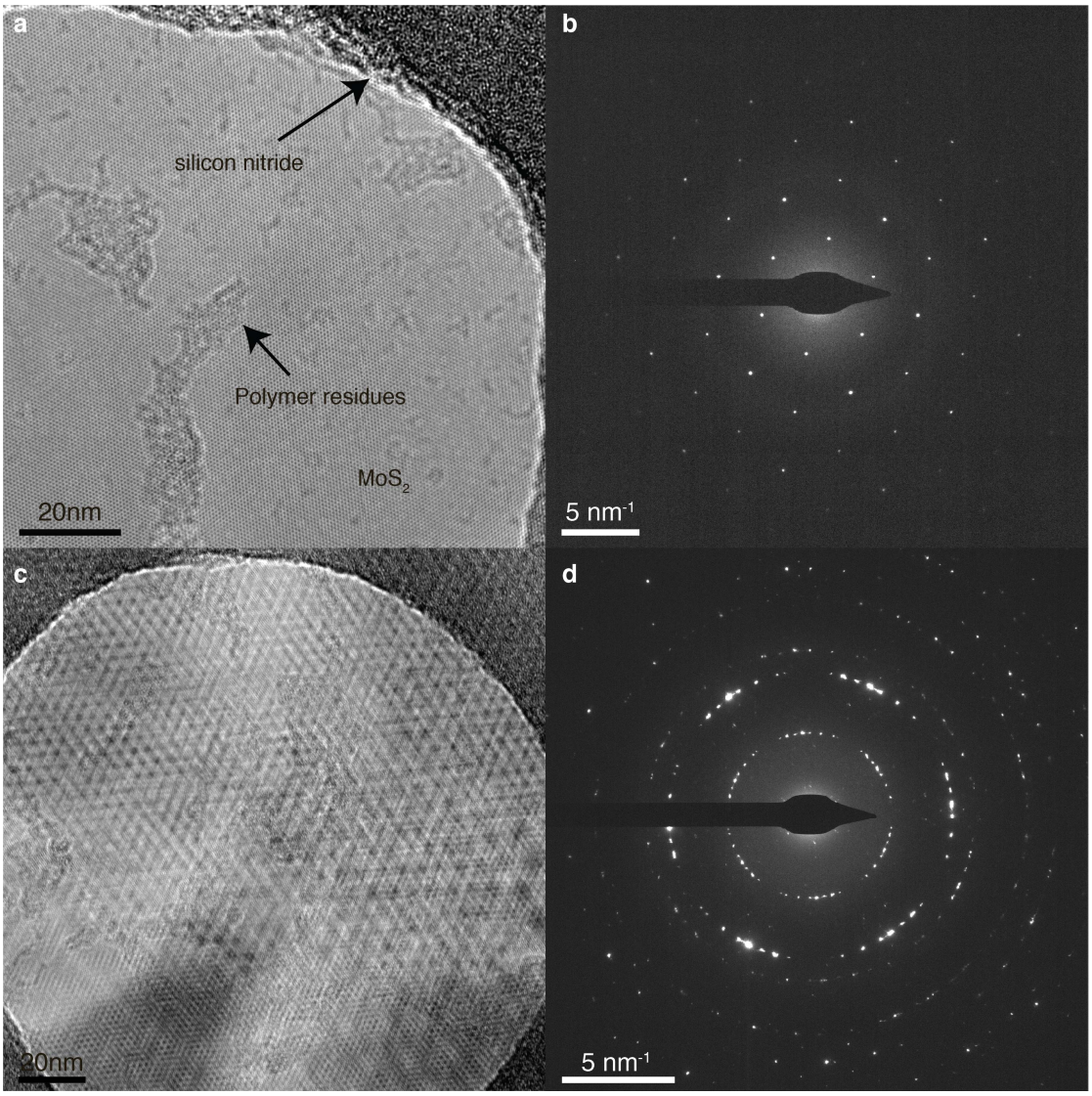

Figure 3.6: TEM characterization of MoS_2 film using PDMS-stamp technique. (a) TEM image of suspended 2-layer MoS_2. The arrow indicates the edge of the SiN_x opening. Residues of PDMS polymer are shown as well. Scale bar 20 nm. (b) Diffraction image of, a. Scale bar 5 nm^{-1}. The double layer cannot be resolved due to perfect alignment of the two layers. The high contrast in a points towards a double layer membrane. If more than one layer is present and the layers are not perfectly aligned, the final image produces Moiré patterns (c). Scale bar 20 nm. The diffraction image can then be used to identify the orientation and number of layers (d). Scale bar 5 nm^{-1}.

Figure 3.6a shows a suspended MoS_2 double layer over the opening in SiN_x. Polymer residues can be seen as amorphous patches and chains which can interact with the beam causing hydrocarbon deposition. As mentioned earlier, the regions exposed to the electron beam should have as little contamination as possible since residues can migrate and contaminate the clean parts. Selected area diffraction can give information about the crystal structure of

the material and verify if the transfer was successful. Figure 3.6b shows a diffraction pattern characteristic for 2H-phase MoS_2. Due to specific growth conditions sometimes there could be more than one crystalline layer stacked on top of each other. In bright-field imaging mode, the layers rotated at a certain angle with respect to each will give specific Moiré patterns. Figure 3.6c shows the opening area with the regions where the layers with different orientations are overlapping. In this case the diffraction pattern consists of many signals coming from individual layers rotated respectively to each other (Figure 3.6d). The information about the crystal structure can also be obtained from the Fast Fourier Transform of the bright field image.

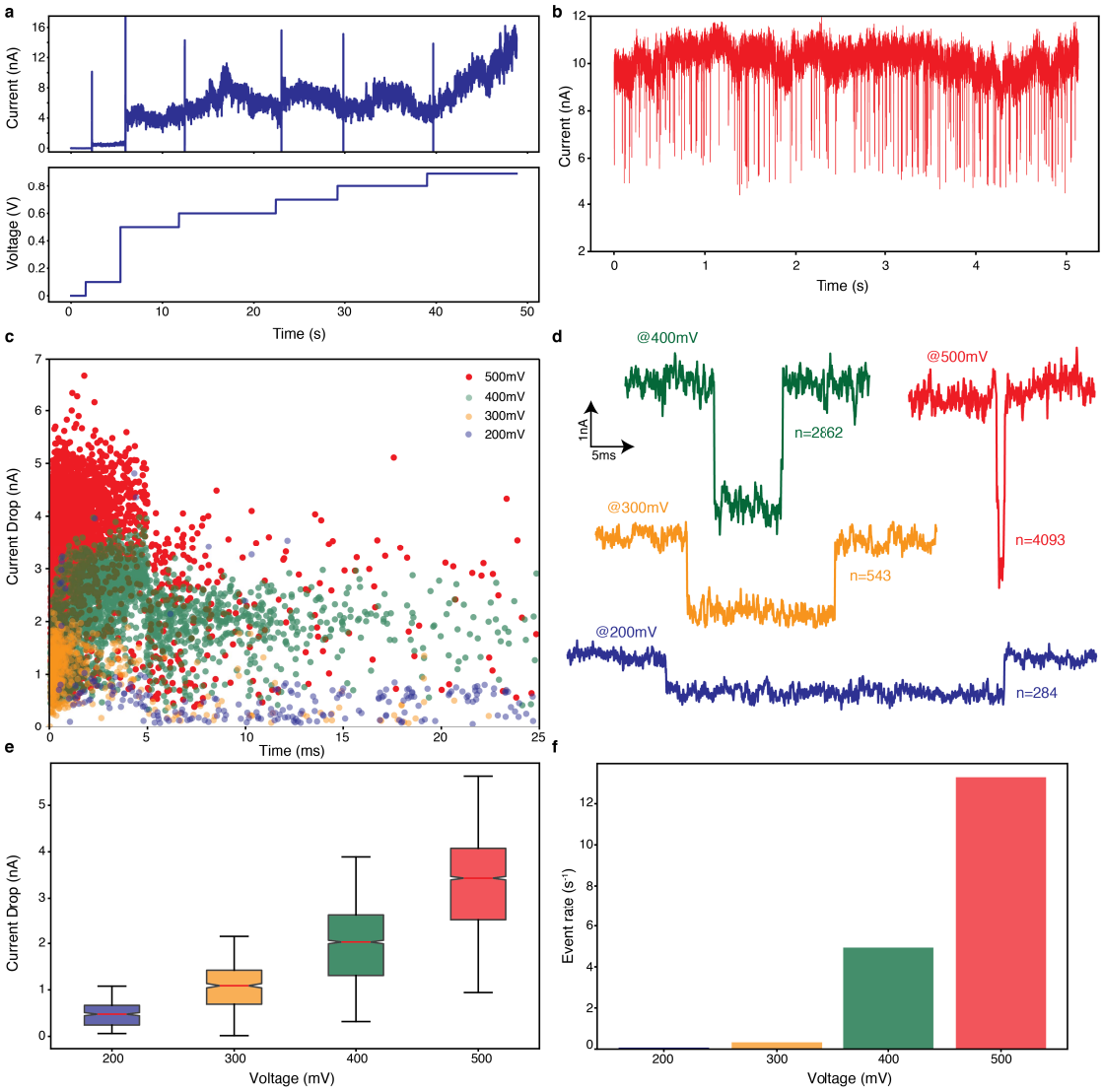

Figure 3.7: DNA translocation from nanopore device when used for translocations transferred using PDMS-stamp technique. (a) The ECR trace used to create a nanopore. The sudden increase of the current at 0.9 V is associated with a pore generation. (b) A typical translocation trace in a 2 nm large pore recorded at a voltage of 500 mV. (c) Scatter plot of current drop versus dwell time for different translocation voltages (color-coded). (d) Example of a representative event for each voltage. The number of recorded translocations for each condition is reported next to trace. (e) Boxplot of the current drops reported in c. The current drop increases linearly with the applied voltage. The red line indicates the median values, the upper and lower ends of the box denote the upper and lower quartile, whereas the whiskers encompass the rest of the data points. This is typically used to confirm that the observed events are translocations. (f) Translocation rate calculated by dividing the number of events for each voltage by the acquisition time. The translocation rate increases exponentially with voltage.

3.4.3 DNA Translocations

In Figure 3.7, we summarize the data obtained with a device fabricated according to this protocol. We used the PDMS transfer method and applied ECR to generate the nanopore. A voltage of 900 mV was sufficient to induce a steady current increase Figure 3.7a, at 40 s). The voltage is then reset to zero. An IV response was then recorded between -200 mV and 200 mV and yielded a conductance of 10.3 nS. The pore size can thus be estimated to be about 2 nm. We then exchanged the cis-side buffer with buffer containing 2000 base pair long double-stranded DNA at a concentration of 10 ng/μL. This DNA was translocated at transmembrane voltages of 200, 300, 400 and 500 mV. An extract of the current trace at 500 mV can be found in Figure 3.7b. A scatter plot of the current drop and dwell time is shown Figure 3.7c. Representative translocation events for each voltage are shown in Figure 3.7d. Typically, the current drop depends linearly on the voltage applied (Figure 3.7e), i.e., the conductance change induced by the dsDNA is roughly constant as a function of the applied voltage range.[26] As shown in Figure 3.7f, small nanopores, where the dsDNA capture is governed by an energy barrier, show an exponentially increasing event rate.[121]

3.5 Conclusion

In terms of 2D material transfer, most of the existing transfer methods rely on polymers which are spin-coated on exfoliated or CVD-grown MoS_2 and then detached from the substrate using an etching solution such as KOH or NaOH.[102, 115, 116] This might induce defects in the MoS_2 which is highly problematic for nanopore devices application. These methods are also limited by residual contamination by the etchants, demanding additional cleaning steps. Moreover, many methods usually involve large-scale transfer of materials,[70, 72, 99, 100] which lacks the precision in aligning the micron-sized 2D monocrystals over the specific membrane area). Since the suspended area is quite small, large area transfer also results in a waste of material especially if one has a limited supply.

The polymer-free direct transfer technique is a low-cost straightforward method, it is not economical. However, thanks to this technique, the residues referred to as polymer contamination in typical transfer processes. Direct transfer method helps to address a long-time debate and suggests accounting the presence of hydrocarbons in 2D materials. Although, this direct transfer approach is a relatively easy and facile method to transfer MoS_2 films, introduction of voids and film folding limit the film quality and throughput of transfer process suggesting a need for new transfer methods. This technique is useful for applications where devices are not compatible with harsh solvent cleaning and demand multi-layer 2D transfer.

Deterministic transfer of 2D materials by using PDMS has been demonstrated.[41] However, while this is a method is only suitable for exfoliated 2D material, it represents a challenge in the case of CVD-grown monolayer since it cannot be easily detached from the growth

substrate. We address this issue by using PDMS stamps (up to 1 mm^2) in combination with water assisted lift-off. The PDMS transfer methods are attractive since they require fewer steps of post-transfer cleaning. The processed method is etchant-free, which reduces the number of steps and retains the quality after the transfer. In summary, the transfer can be done highly precisely, fast, economic and can be extended to other 2D materials.

4 Wafer-Scale Fabrication of Nanopore Devices for Single-Molecule DNA Biosensing using MoS_2

The following section is a post-print version of:

Mukeshchand Thakur,[1] Michal Macha,[1] Andrey Chernev, Michael Graf, Martina Lihter, Jochem Deen, Mukesh Tripathi, Andras Kis, and Aleksandra Radenovic. "Wafer-Scale Fabrication of Nanopore Devices for Single-Molecule DNA Biosensing using MoS_2." Small Methods, 4 (2020).

M.T and M.M contributed equally to this work. M.M. developed the large-scale growth method and performed the Raman, AFM, SEM, and optical characterization. Nanopore substrates were fabricated by A.C. M.T developed a large-area built transfer setup and performed a wafer-scale transfer of MoS_2. M.T and M.L performed brightfield TEM imaging and biosensing experiments on nanopore devices. M. Tripathi performed STEM imaging. J.D. and M.G. developed nanopore-sensing software. All authors provided constructive comments on the manuscript.

4.1 Summary

Atomically thin (two-dimensional - 2D) nanoporous membranes are an excellent platform for a broad scope of academic research. Their thickness and intrinsic ion selectivity (demonstrated for example in MoS_2) make them particularly attractive for single-molecule biosensing experiments and osmotic energy harvesting membranes. Currently, one of the major challenges associated with the research progress and industrial development of 2D nanopore membrane devices is small scale thin-film growth and small-area transfer methods. To address these issues, we demonstrate a large-area protocol including a wafer-scale monolayer MoS_2 synthesis, Si/SiN_x substrate fabrication and wafer-scale material transfer. Firstly, we introduce the 3-inch wafer scale MOCVD growth yielding homogenous monolayer MoS_2 films. Secondly, we fabricate a large number of devices in one batch by employing the wafer-scale thin-film transfer method with high transfer efficiency (>70% device yield). The growth, the transfer quality and cleanliness were investigated using transmission electron microscopy,

atomic force microscopy and Raman spectroscopy. Finally, the applicability and robustness of our large-area protocol was demonstrated by performing a set of double-stranded DNA translocation experiments through as-fabricated MoS_2 nanopore devices. We believe that the shown approach will pave the way towards wafer-scale, high-throughput use of 2D nanopores in various applications.

4.2 Introduction

Nanopore-based sensing is attractive in the field of single-molecule detection as it offers low-cost, label-free and high-throughput analysis. In general, a nanopore device is a small nanometric aperture separating two compartments filled with ionic solutions. When a bias voltage is applied, an electrically charged molecule (e.g. DNA) electrophoretically threads through the nanopore. This process generates a transient resistive pulse in the ion current, which can be used to study the translocation of a single molecule.

Based on their composition, nanopores are categorized as biological, silicon- or polymer-based solid-state pores or DNA-origami pores.[14, 122, 123] One of the promising applications of nanopore devices is DNA sequencing, often regarded as the fourth-generation sequencing technology. So far, only biological nanopores have been used for commercial sequencing applications.[9, 124] Since the functional unit of these biological nanopores are protein channels, their stability in the lipid-bilayer is limited by the ionic strength of the electrolyte, the voltage that can be applied, chemical, mechanical and thermal stability. In contrast, solid-state nanopores are more mechanically and chemically robust, providing flexibility in working with higher voltages, ionic concentrations and temperatures. Their size can be precisely tuned for a desired application and on top of that, they can be fabricated in sizable arrays, potentially improving the sensing efficiency.

To improve the spatial and temporal resolution of detection, for biopolymers such as DNA, the thickness and the pore diameter of the sensing membrane needs to be comparable with the lateral diameter of the biopolymer. In this regard, two-dimensional (2D) materials such as graphene,[46, 47] hexagonal boron nitride,[110] and TMDs materials such as tungsten disulfide (WS_2)[80] and MoS_2[40, 43, 44, 52, 53, 56] were explored as 2D solid-state nanopores. MoS_2, in particular, is interesting since it is composed of three-atoms (≈0.65 nm).[51] In addition to the thickness, the presence of hydrophilic molybdenum atoms at the pore facilitates the base differentiation. Furthermore, DNA tends to interact less with the membrane surface when compared to graphene.[50] And lastly, the signal-to-noise ratio in MoS_2 is higher than in other 2D materials.[50, 52] All these reasons make MoS_2 an attractive and widely studied 2D material for DNA biosensing application. Experimentally, using a gradient of room temperature ionic liquids and KCl solution, monolayer MoS_2 nanopore devices have achieved single-nucleotide differentiation.[53] Furthermore, monolayer MoS_2 nanopore devices are becoming promising tools for emerging scientific applications in defect-engineering research[58, 125–128] and highly-efficient blue energy harvesting.[55, 129, 130]

One of the most crucial bottlenecks of monolayer device fabrication is the thin film synthesis and its processing scale. Most reported applications rely on a relatively small monolayer substrate size which enforces a single-chip transfer and fabrication of a single device a time.[41, 44, 52, 80] This approach is highly time consuming and cost ineffective, especially if the application requires a significant number of devices. Likewise, even if a uniform thin film growth is performed on a large substrate area, without an easy and repeatable large-scale transfer method the same problem remains. Hence, a large-scale approach towards the production of robust, low-cost and scalable nanopore devices is paramount to ensure high research yield and scientific progress in this field. Currently, the major challenges associated with 2D MoS_2 nanopore devices are their high-quality and defect-free synthesis, sensing noise associated with device architecture, and variability in the fabricated devices in terms of pore size, pore geometry and thickness. These problems, usually occurring with applications requiring 2D materials requiring a clean large-scale microfabrication process.

In this work, we address these challenges by growing large-area continuous MoS_2 films on a 3-inch sapphire substrate with subsequent wafer-scale transfer using PDMS. The growth process is based on metalorganic chemical vapor deposition (MOCVD). By using the c-plane sapphire substrates, high-purity gaseous phase precursors and an alkaline salt as a growth catalyst, we obtain the reproducible and highly efficient synthesis of continuous mono- to few-layer MoS_2 films. For the transfer of MoS_2 films, we use PDMS as a supporting polymer along with water, avoiding any hazardous etchants (e.g. KOH) or additional etching steps during transfer. The transfer process is less labour intensive and does not need any additional expensive instruments usually used in existing deterministic transfer methods.[41, 44] Furthermore, the MoS_2 growth substrate is recyclable thereby reducing the substrate costs. In combination with PDMS transfer, we demonstrate cost-effective and time-efficient method for large-scale nanopore-device fabrication (a total of 128 devices per batch) with successful transfer yield (>70%). The 2D material quality and cleanliness of the wafer-scale transferred MoS_2 was evaluated with high-resolution transmission electron microscopy (HRTEM) and aberration-corrected scanning transmission electron microscopy (STEM) imaging. We have found that transfer quality is comparable to the well established, small-scale PMMA-based techniques[44, 58] and can be adapted to other polymer materials.

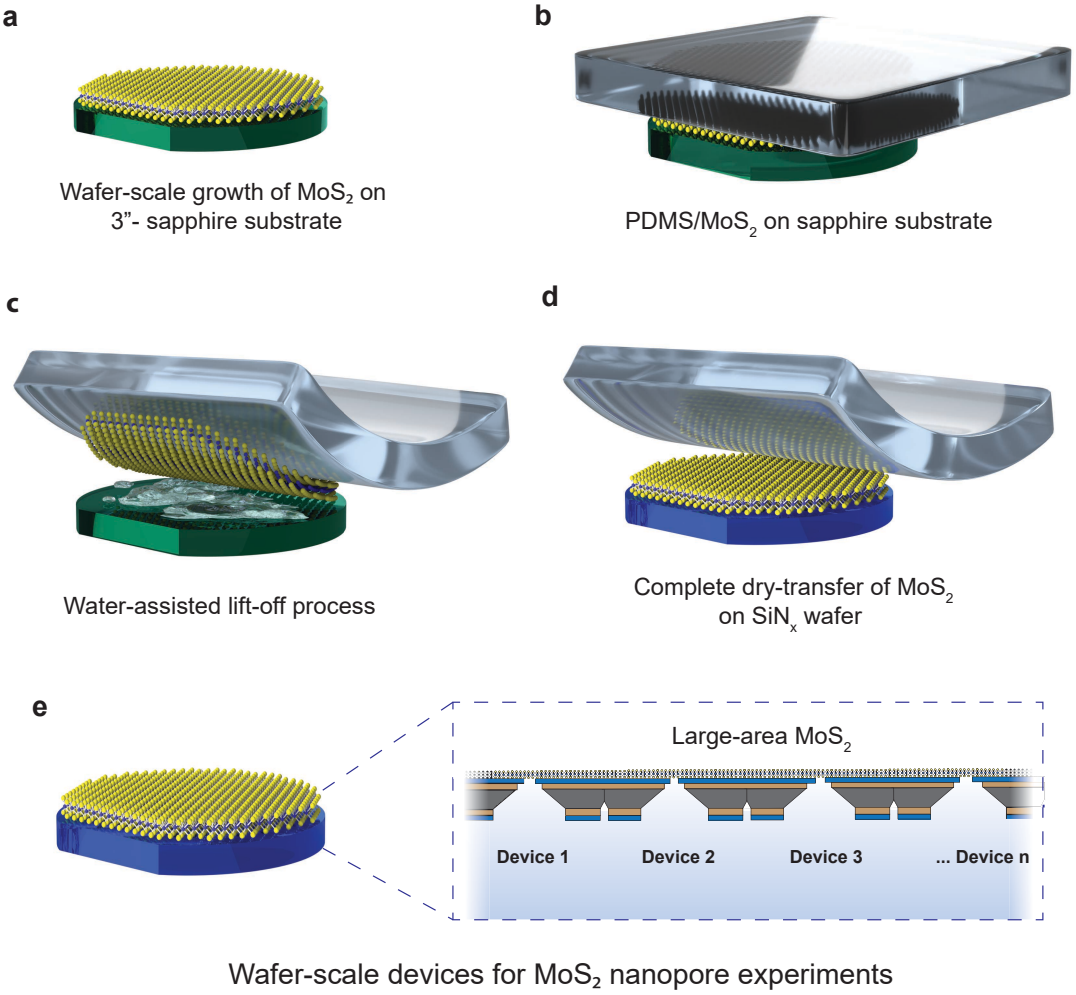

Figure 4.1: Illustration showing the wafer-scale PDMS-transfer of MoS_2 from a 3-inch sapphire wafer to a silicon substrate containing an array of SiN_x membranes with apertures. The objects are not to scale. (a) Large-area MoS_2 on the growth substrate. (b) The PDMS stamp is aligned to the MoS_2/sapphire substrate. (c) Lift-off process where the water penetrates the interface between sapphire and MoS_2, while using a step-motor the PDMS/MoS_2 is lifted off. (d) Dry transfer of large-area MoS_2 on the SiN_x wafer achieved by stamping using PDMS. (e) Large-area MoS_2 transferred to the target substrate now containing devices that can be used for the nanopore experiments. This figure was published in Small Methods, 2020, Thakur et al.[45]

4.3 Results and Discussion

4.3.1 Wafer-scale MoS_2 growth and transfer

For the 2D material synthesis, we have used a modified and upscaled methodology based on a combination of two different approaches. The first one uses the metalorganic precursor (molybdenum hexacarbonyl $Mo(CO)_6$) and diethyl sulfide (DES) as molybdenum and

sulfur sources,[131] respectively. The second one relies on the addition of spin-coated liquid-phase growth promoters, sodium molybdate (Na_2MoO_4) and alkaline salt, prior to the growth phase,[42, 132] Using a spin-coated Na_2MoO_4 solution both to ensure uniform seeding and as an additional molybdenum source during growth step yields highly homogenous, large 2D crystals of MoS_2, leading to continuous monolayer formation under proper process parameters. The use of alkaline salts as a crystal growth catalyst is a common practice in the MoS_2 synthesis protocols,[96, 98, 133] which lowers the density of nucleation sites and the melting point of the solid-state precursors. This results in an increase of the final crystal size by orders of magnitude. In particular, NaCl is an advantageous addition to the growth. Under elevated temperature, it can form intermediate ternary species with molybdenum acting as planar, cyclic seeding promoters both suppressing the nucleation and increasing lateral crystal growth rate on the target substrate.[98]

Taking advantage of both of these approaches, we have used a spin-coated mixture of both Na_2MoO_4 and NaCl as a continuous growth promoter. Prior to the growth, annealed and hydrophilized c-plane sapphire wafers (3-inch) were coated with promoter solution to achieve a uniform layer. Typical growth step is performed in a homemade MOCVD, hot-wall, vertical furnace for 30 min at 850°C under the flow of 210 sccm of Ar, 1 sccm of O2, 4 sccm of H_2 (Figure S4.1). In contrast to previous publications,[42, 98, 132] we are adding several new elements and improvements to our process. First, we use separate bubblers for $Mo(CO)_6$ and DES, which increases the control in delivering the gases into the chamber, and 12 sccm of Ar is flowing through a bubbler filled with, $Mo(CO)_6$, and 3 sccm of Ar through separate DES bubbler. Second, the sapphire substrate is placed vertically to achieve uniform exposure to the gases and homogeneous reaction conditions. The combination of the metal-organic gaseous precursor, the sulfur-rich atmosphere, and the Na_2MoO_4 solution uniformly coated on the substrate, ensures a uniform seeding of MoS_2 across the whole substrate and a steady supply of Mo mass, promoting large-scale, continuous film formation with a high degree of control. The addition of NaCl to the spin-coating solution ensures a high reaction rate and a low nucleation density, which as a result increases the overall grain size, visible through merged, extruded grain boundaries, and single crystals on the edges of the substrate. A moderate amount of hydrogen is necessary to help decomposing the DES and $Mo(CO)_6$ ligands and to prohibit carbon containing reaction products from depositing on the substrate. Lastly, we are introducing small amounts of oxygen to the process, which ensures smooth grain mergers, decreases the probability of a secondary layer formation, and further limits the nucleation density due to local etching of unsteady nuclei.[132] The thickness of the continuous MoS_2 film can be controlled both with the concentration ratio of Na_2MoO_4/NaCl and the flow of O_2 (Figure S4.2), and can range from single flakes to continuous multilayer. As a result, this method allows to repeatedly and efficiently produce large area mono- and multilayer MoS_2 alike.

The substrate fabrication process is detailed in the methods section and Figure S4.3. Each fabricated silicon wafer results in >120 devices where each device has one single aperture in a thin SiN_x membrane. In order to assess the variability of these apertures, we have characterized

the apertures from different parts of the wafer using TEM. The size of the aperture is ≈75 nm within 5% error (Figure S4.4).

The next step is the large-scale transfer of MoS_2 to the Si/SiN_x wafer. Figure 4.1 depicts the steps involved in this process. The lift-off step is based on a surface-energy assisted transfer of MoS_2 using water[44, 120, 134, 135] accompanied with a step-controlled translating stage. The material transfer is performed by aligning the PDMS onto the as-grown MoS_2 growth substrate (Figure 4.1a-b). The next step comprises of manually placing of MoS_2/PDMS layer in a container with water and lifting-off as water penetrates at the interface between the MoS_2 and the sapphire substrate (Figure 4.1c). Due to the surface interaction between MoS_2/PDMS (hydrophobic) and sapphire (hydrophilic), the water preferentially penetrates between MoS_2 and the sapphire substrate enabling the surface-energy based lift-off of MoS_2.[99, 134] In the absence of water, the MoS_2 does not attach to the PDMS completely. Subsequently, MoS_2 is manually stamped on the SiN_x surface completing the large-area transfer.[99, 101] It must be noted that during the transfer steps, we used the lift-off and stamping speed in the range of 5-10 μm/s (Figure 4.1c-d). One of the advantages of wafer-scale transfer is that unlike deterministic transfer methods,[44, 70] this approach is simple and does not require any precise optical alignment setup. While wet-etching based wafer-scale transfer using polymers such as poly(methyl methacrylate) (PMMA) was recently demonstrated for MoS_2,[70] it requires surface modification of the growth substrate and an additional substrate etching step which may deteriorate the thin 2D material due to the harsh etchants used (e.g. KOH). In addition, PMMA coating was shown to have a time-dependant corrosive effect on the coated 2D materials, which can lead to poor device performance.[136] Furthermore, due to the thickness of thin PMMA films (several hundreds of nanometers), the wet transfer processes are prone to unwanted crumbling of the material, decreasing the transfer efficiency.[137] The PDMS, being significantly thicker (1-2 mm), but still flexible and optically transparent, provides a better mechanical stability, increasing transfer efficiency.[64, 99, 138] Previous reports have demonstrated small-scale deterministic transfer of TMDs using a both PDMS and PMMA.[44, 70, 99, 138]

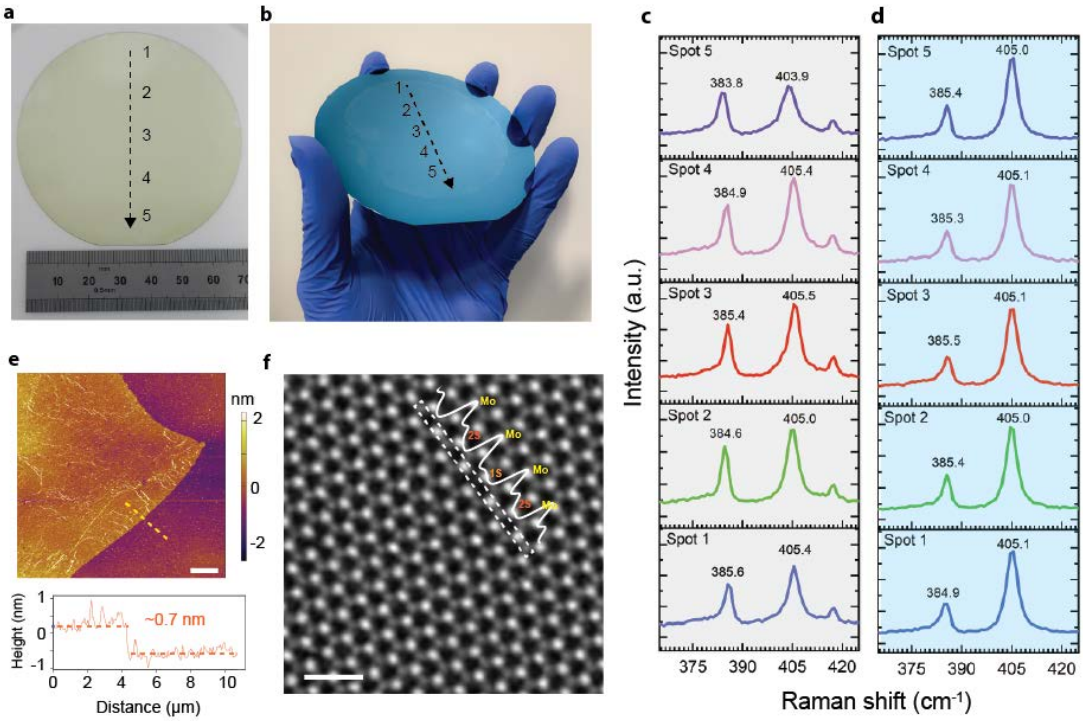

Figure 4.2: Characterization of large-area MoS_2 films. (a) Continuous MoS_2 film grown on a sapphire substrate. (b) Large-area wafer-scale transfer of MoS_2 over a silicon wafer with 128 SiN_x membranes containing apertures. The blue contrast of the MoS_2 transferred from the growth substrate is visible on the SiN_x surface. (c-d) Raman spectroscopy from the same region of the wafer before (gray panel) and after the transfer (blue panel) of the MoS_2 films (unmarked peak around 420 $^{-1}$ on a before transfer spectra is a signature peak of the Al_2O_3 substrate used for the MoS_2 synthesis). (e) AFM analysis showing monolayer MoS_2 post-transfer with ≈0.7 nm height profile. Scale bar, 6 μm. (f) Double Gaussian filtered STEM image after transfer showing a clean MoS_2 lattice structure. Due to its Z-contrast dependency, the lattice structure can be directly inferred from the molybdenum atom (brighter) and the sulfur atom (darker) contrasts. A few intrinsic sulfur-vacancies can be directly observed in the image (inset: Intensity peak profile along the line for selected atoms showing one sulfur vacancy). Scale bar, 1 nm. This figure was published in Small Methods, 2020, Thakur et al.[45]

4.3.2 Characterization of MoS_2 films

Optical images of as-grown MoS_2 (Figure S4.5) show a uniform layer of film with rare secondary nucleation spots. Using sapphire as a substrate ensures epitaxial connection on the MoS_2/sapphire interface due to crystal lattice match.[96] However, Na-based compounds assisting the MoS_2 growth were reported to diminish such an epitaxial interface due to Na-intercalation under the grown film large-area epitaxial monolayer.[139] Indeed, optical images (Figure S4.5) reveal rare spots of extruded grain boundaries, which suggests imperfect grain stitching. Nonetheless, for our application, we have not observed any odd grain boundaries nor low-quality suspended areas on fabricated membrane devices. In our case, the sap-

phire substrate was (depending on the batch) ≈90-100% covered with continuous mono- to few-layer films (Figure 4.2a) which were transferred to the SiN_x substrates (Figure 4.2b).

To further inspect the large-scale growth quality and uniformity, Raman spectroscopy was performed across the whole wafer pre- and post-transfer of MoS_2 (Figure 4.2c-d). The relative distance between in-plane $E^1{}_{2g}$ and out-of-plane A_{1g} acoustic phonon modes is an indicator of MoS_2 thickness.[41, 70] In our case, the average separation between $E^1{}_{2g}$ and A_{1g} peaks remains in the range of 19.5 cm^{-1} to 20.5 cm^{-1}, suggesting a uniform monolayer character of the film across the entire substrate. The absence of a peak separation difference between the spectra before and after the transfer is an indication of the non-destructive character of the transfer method. We observe, however, a small increase in $E^1{}_{2g}/A_{1g}$ intensity ratios after the transfer, which can be due to changes in exciton-phonon interaction with the supporting substrate[140] or doping by charge transfer.[141] Additionally, to analyse the uniformity or the quality of the MoS_2 films, photoluminescence (PL) measurements were performed at the similar regions (labelled in Figure 4.2a-b) before and after the transfer (Figure S4.6). The PL peaks did not show any significant shift (< 5 nm) before and after transfer process indicating that the crystal quality of the layers did not deteriorate after the transfer.[70, 142] These results are in corroboration with the Raman measurements. This may be attributed to the mild conditions used in the water-assisted transfer process that avoids the use of any harsh etchants, preserving the quality of the MoS_2 films.[70] The AFM surface characterization reveals ≈0.7 nm thick layers after the transfer, corresponding to the thickness of monolayer MoS_2 (Figure 4.2e).[51]

Aberration-corrected STEM is a well-established method to characterize the structural uniformity at atomic scale in low-dimensional materials including MoS_2, h-BN and graphene.[105, 143, 144] The STEM image (Figure 4.2f) shows the crystal lattice structure of a monolayer MoS_2 film. Due to the annular dark field contrast dependency, the intensity of the atomic columns can be directly interpreted since it is directly proportional to $Z^{1.6\text{-}2.0}$ (where Z is the atomic number of the element).[143] Thus, Mo-atomic sites appear brighter in intensity than the sites where two sulfur atoms are on top of each other. The intensity profile along the line shows the peak positions of the Mo-atoms and S-atoms, respectively. To avoid electron-beam induced knock-on damage, a low acceleration voltage (80 kV) was used during the imaging.[143] A few intrinsic S-vacancies can be observed in the image,[105] further confirming the high-quality growth of our MoS_2 films (also shown in the line profile in Figure 4.2f). Furthermore, to assess the cleanliness of the suspended transferred MoS_2 regions, larger areas were analysed where large-area clean regions with MoS_2 films can be observed with some polymer contamination (see Figure S4.7). Due to advancements of aberration-correction, a smaller sized electron-beam probe (full width half maximum, FWHM, ≈0.1 nm) in STEM can be intentionally placed on the clean MoS_2 regions to create nanopores with tunable sizes in a controlled way by sputtering the atoms, for instance Panel 4 in Figure S4.7 shows a nanopore (≈2 nm) formed by the electron-probe.

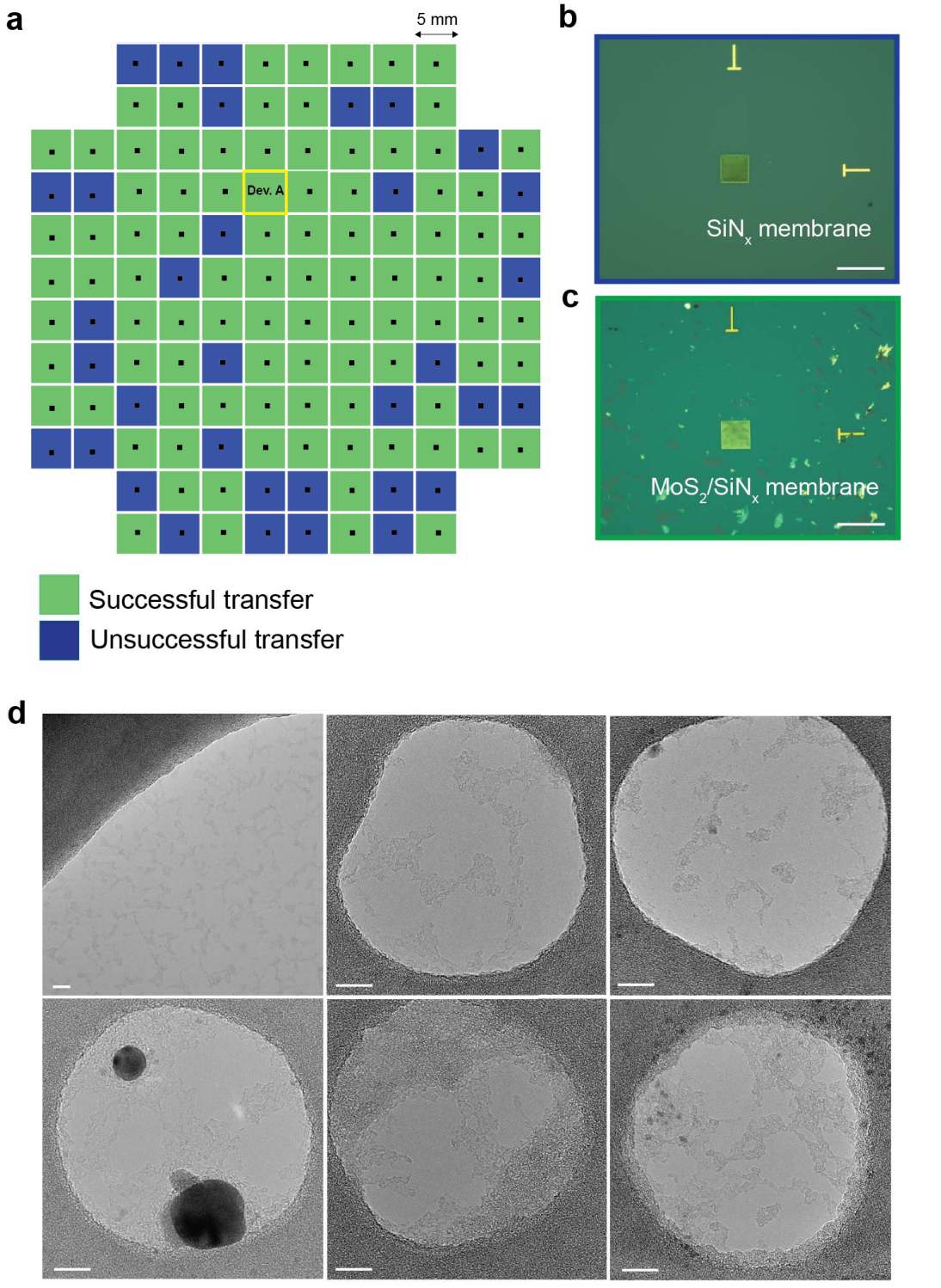

Figure 4.3: Transfer efficiency. (a) Color-map showing the wafer-scale transfer efficiency of MoS_2 over the SiN_x membrane using PDMS. The devices and their transfer is represented as complete (n = 94, green) or unsuccessful transfer (n = 34, blue). (b) A representative substrate before transfer and (c) after transfer to the SiN_x membrane. All scale bars are 50 μm. (d) TEM imaging of suspended MoS_2 after transfer. The devices show MoS_2 regions with few polymer residues after transfer. All scale bars are 10 nm. This figure was published in Small Methods, 2020, Thakur et al.[45]

4.3.3 Wafer-scale transfer efficiency

The wafer-scale MoS_2 transfer efficiency of >70% device yield was calculated as the percentage of devices that have an aperture fully covered with MoS_2 (Figure 4.3a). Variation from batch to batch is shown in a Table 4.1. Two optical images of devices without MoS_2 (Figure 4.3b) and with MoS_2 (Figure 4.3c) show large-area MoS_2 transferred over the SiN_x membrane. A successful transfer is calculated by the number of devices with a MoS_2 flake transferred on the membrane and the devices without are regarded as unsuccessful transfer. Representative devices analysed by TEM imaging are shown in Figure 4.3d. For devices, where the transfer process was unsuccessful, it is possible to use a chip-scale deterministic transfer method[44] to increase the device yield. The transfer efficiency can be enhanced by a slow lift-off process and a high monolayer coverage of the MoS_2 on the growth substrate. One of the biggest challenges is to obtain residue-free transfer, since it affects the electronic properties of 2D materials. This surface contamination originate from the transfer methods using sacrificial polymer coatings (e.g. PDMS or PMMA).[44, 145]

During the transfer, polymer layer is in direct contact with the MoS_2 which inevitably leads to residual surface contamination on the monolayer film.[146] Additional contamination source are airborne hydrocarbon contaminants adsorbing on the MoS_2 layers when exposed to air.[147, 148] The device cleanliness can be improved by transfer strategies, which avoid the use of polymers.[144] However, such methods are not compatible with the large-area transfer because the thin 2D material films without polymer support can cause uncontrolled transfer, leading to large cracks or folding in the transferred material. Another approach is to develop strategies that allow the direct growth of MoS_2 over the SiN_x aperture, as demonstrated by Waduge et al.[43] where the approach indeed promises scalability and avoids any further contamination with polymer arising from the transfer step. However, growing over apertures is not trivial and typically yields a mix of single and multilayer MoS_2 films. Thus, currently, polymer-based wafer-scale transfer for device fabrication is preferred.[70]

Another challenge is the lack of an efficient nanopore fabrication method that could be employed for wafer scale fabrication while maintaining pore size reproducibility and distribution. Among all the state-of-art techniques, ion beam irradiation[127] and lithography-based fabrication[149, 150] are the most promising. However, they are still facing a number of technical problems which make them not suitable for batch fabrication of single nanopore devices. Ion beam methods are generally used for pore fabrication at a large scale and lack precise pore definition. The lithographic approach on the other hand requires additional steps involving polymer coatings, leading to further, otherwise avoidable, surface contamination. For these reasons, we have used an electrochemical reaction (ECR)-based pore drilling method.[57]

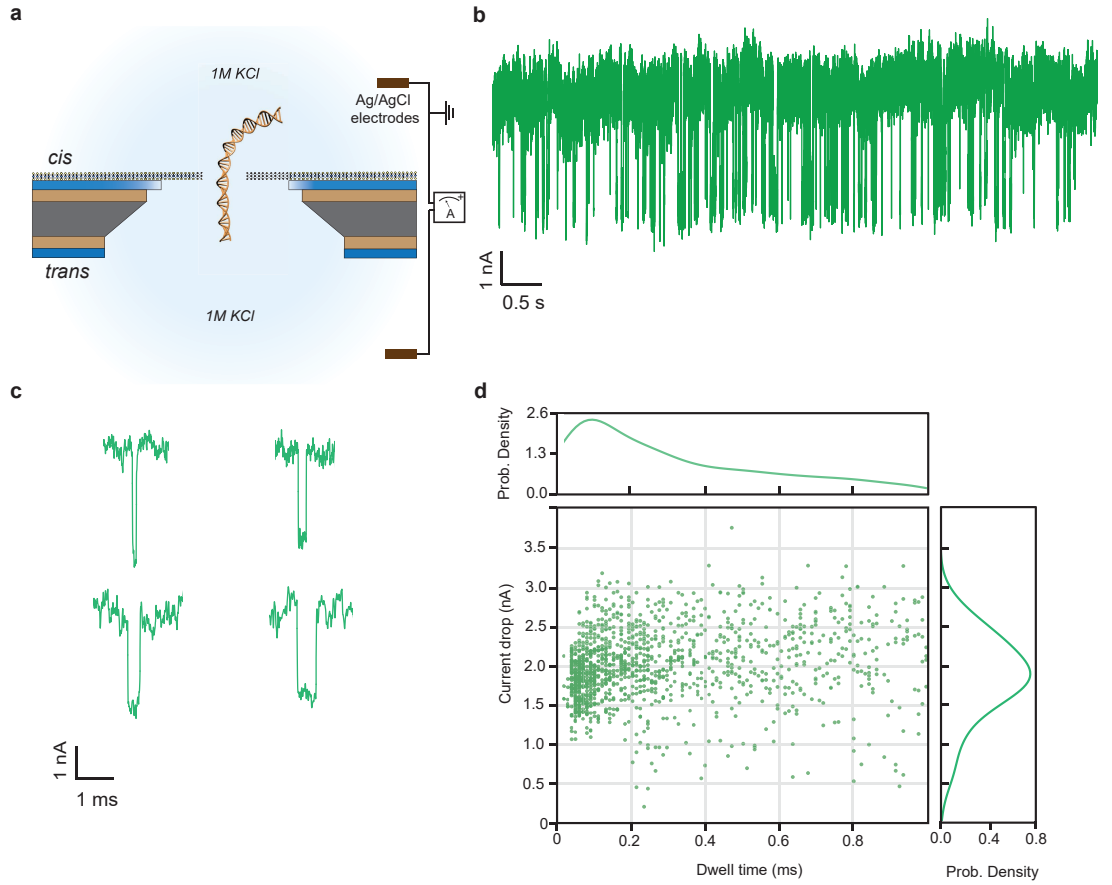

Figure 4.4: Short double-stranded (ds)DNA translocations through a MoS_2 nanopore (Device A). (a) Schematic showing the setup for the translocation experiment (not to scale). (b) Concatenated 10-s trace of 100 bp dsDNA recorded in 1M KCl. The mean open-pore current here is 12.6 ±0.2 nA. The data was recorded at 500 mV, low-pass filtered at 10 kHz, and digitized at 100 kHz. (c) Representative events from the trace shown in (b). (d) All-point scatter-plot and probability density estimation of the current drop versus dwell time (n = 1266). This figure was published in Small Methods, 2020, Thakur et al.[45]

4.3.4 Short DNA translocations

To demonstrate the applicability of the MoS_2 nanopores, we performed DNA translocations from representative MoS_2 nanopore devices made using the reported growth and transfer method. Figure 4.4a shows the schematic of the experimental setup. The MoS_2 membrane separates the cis and trans chambers (1M KCl-Tris EDTA) of the flow cell. We chose two MoS_2 devices from different sites from the wafer and fabricated a single nanopore in each device using our previously reported ECR method.[57] In this method, a nanopore is induced by applying a voltage across the membrane to electrochemically etch the MoS_2 at defect sites. The I-V measurement of Device A in 1M KCl are shown in Figure S4.10. The pore size obtained was ≈3.6 nm which is typically calculated from the open pore conductance using

the well established conductance model for cylindrical pores.[107] However, differences in ion mobilities of K^+ and Cl^- can affect the estimation of the nanopore sizes for sub 5 nm pores in MoS_2.[151] Since in our case, the nanopore sizes are below 5 nm, our nanopore diameter using the estimation proposed by Perez et al.[151] is ≈3.9 nm.

We then set out to measure short DNA translocations through this nanopore. No translocation signals occur in the absence of DNA (negative control) in any of these devices. We then added 100 bp dsDNA (a final concentration of 20 nM) to the cis-compartment (1M KCl, TE-buffer, pH 7.5) and electrophoretically translocated the DNA molecules through the nanopore. The translocations were performed at 500 mV at room temperature (≈24°C). We recorded a total number of 1266 events which were fitted using a CUSUM algorithm.[113] A representative 10s concatenated current-time trace showing 100 bp DNA translocations at 500 mV is shown in Figure 4.4b. The ion-current baseline fluctuations are associated with charge interactions occurring at the rim of the nanopore[20] as well as the mechanical fluctuations of the thin suspended 2D material.[152] A few representative events from the trace are shown in Figure 4.4c. Figure 4.4d shows a scatter plot of all the fitted events obtained from Device A at 500 mV with a MoS_2 nanopore. We observed a relative current blockade of ≈20-25%, which corresponds well to the expected fractional current blockade (≈25%) of dsDNA.[44] Most of the recorded events for 100 bp DNA show an average dwell time less than 200 μs, while some events span over a millisecond. The bandwidth of our system is about 10 kHz, which can lead to distortions of events shorter than ≈50 μs.[153] The dwell time distribution is associated with the limited bandwidth of the measurement, leading to the invisibility of fast translocation events.[154] The longer dwell time for the events seen in Figure 4.4c-d can arise from interaction of the DNA with MoS_2 around nanopore surface before completely threading through the pore. Both ssDNA and dsDNA are known to interact with MoS_2 surface albeit with different affinities[56, 155] which might increase their residence time in the pore thereby increasing their dwell time. The nucleobases of the ssDNA are exposed which is in contrast to dsDNA. These exposed nucleobases interact with the MoS_2 surface via van der Waals (vdW) interactions.[155, 156] These nucleobases possess differential affinity towards transition metal dichalcogenides (e.g. MoS_2 and WS_2) and they interact via vdW forces.[157] The vdW interaction for adsorption is facilitated by a large electronegativity difference between Mo-atoms and S-atoms of MoS_2. Molecular dynamic simulations show that the MoS_2 nanopore edge also play an important role in the sticking behavior of both ssDNA and dsDNA.[50] The MoS_2 nanopore with higher Mo-atoms (hydrophilic) termination interacts less to the DNA (hydrophobic) in comparison to S-atom (hydrophilic) termination. In solid-state SiN_x pores, it has been observed that due to interaction with the nanopore, the fluctuations of the DNA is stabilized.[75] Thus the residence time of the DNA can be influenced by the interaction with the nanopore edges as well as the surface of the material. Furthermore, we show 100 bp translocation at lower voltages in another MoS_2 nanopore Device B from different batch with similar pore diameter (≈4 nm) fabricated using the same ECR method (the details of this experiment are shown in Figure S4.11).

4.4 Conclusion

In conclusion, we demonstrated large-area manufacturing of MoS_2 nanopore devices by wafer-scale growth, fabrication and transfer of MoS_2 films. We show that the fabrication of 128 devices on a single 4-inch wafer can be performed with >70% efficiency. With the current technique, it is possible to further scale-up by using higher density of devices and transfer of large-area 2D materials. The MoS_2 quality and the nanopore devices were clean at the atomic scale as confirmed by TEM and STEM imaging. The single-nanopores were created by the ECR method. Unlike TEM-based nanopore drilling, by electrically isolating each device from each other, this method has the potential for simultaneous creation of nanopores in-situ making it a scalable method of single nanopores production on the same wafer. In the end, we showed the applicability of our devices for biosensing of short 100 bp DNA molecules. In principle, these devices can be used for other exciting applications involving wafer-scale flexible electronics[70, 158–160] as well as highly efficient osmotic energy harvesting cells[129] or recently emerged extension of nanopore sequencing – a nanopore field-effect transistors enabling both ionic and transverse current based biomolecule detection.[56, 127, 161, 162] We believe that further integration and parallelization of nanopore based membrane devices will lead to high-throughput usage and in turns will encourage new, emerging, commercial applications of this technology.

4.5 Experimental section

4.5.1 Wafer-scale growth of MoS_2

Prior to the growth, 3-inch c-plane sapphire wafers (MTI) were cleaned with IPA, acetone and DI, annealed in 1000°C for 6 h to obtain an atomically smooth surface, treated with potassium hydroxide solution (Sigma Aldrich, 99.0%) for 30 min, rinsed with DI water, dried, and finally spin-coated with a growth promoter in aqueous solution of 0.03 M Na_2MoO_4 (Sigma Aldrich, 98.0%) and 0.1 M NaCl (Sigma Aldrich, 99.5%). MoS_2 film synthesis was performed in a 4-inch hot-wall tube furnace (MTI OTF-1200X-II). For carrier and process gases we used ultra high purity Ar (Carbagas, 99.999%), H2 (Vici DBS NM Plus 100 Hydrogen Generator, purity 99.999%), and O2 (Carbagas, 99.9%). Molybdenum hexacarbonyl ($MoCO_6$, Sigma Aldrich, 99.9%) and diethyl sulphide ($C_2H_6S_2$, Sigma Aldrich, 98.0%) were used for metalorganic precursor and reaction gas respectively, and were kept in separate bubblers maintained at stable 17°C and room pressure. Spin-coated sapphire substrates were then loaded vertically in a quartz boat placed inside the reactor tube. This position ensures perpendicular exposure to the gas flow, thus ensuring axial growth uniformity. Furnace was then filled with Ar, ramped up to 120°C and held under carrier Ar flow of 210 sccm for 30 min to dry the reactor walls of adsorbed water molecules. After this step, the reactor was ramped to 850°C at a rate of 20°C per min. The growth step was initiated by injecting 4 sccm of H_2, 1 sccm of O_2 and precursor gases. With an argon flow of 12 sccm for $Mo(CO)_6$ and 3 sccm for DES through both bubblers, the actual mass flow of $Mo(CO)_6$ and DES at 17°C and at ambient pressure was 4.4 x 10^{-4} sccm

and 2.5 x 10^{-1} sccm, respectively. After the growth step, the furnace was cooled down to room temperature naturally. To avoid MoS_2 deterioration, samples were kept in a dry atmosphere between all of the subsequent transfer and characterization steps.

4.5.2 Nanopore substrate fabrication

Double-side polished 100 mm (100) undoped Si-wafers (produced by Active Business Company) were covered with 60 nm of SiO_2 and 20 nm low-stress SiN_x from both sides (done by supplier). Photolithography and dry etching were done to open apertures in the back side SiN_x layer for the subsequent wet etching process required for SiN_x membrane formation on the front-side. Front-side e-beam lithography and dry etching were performed to form 80 nm-diameter apertures in SiN_x membranes with the following parameters: 100kV e-beam voltage, polymethyl methacrylate (PMMA, molecular weight 495K, 4% in anisole) as e-beam resist (EBR) and CHF_3/O_2 gas mixture for dry etching. As a final step acid piranha cleaning was done to achieve clean surface of the target nanopore substrate prepared for the further MoS_2 transfer.

4.5.3 MoS_2 transfer

We used PDMS-assisted transfer of 3-inch MoS_2 films from the sapphire wafer to the SiN_x wafer assisted by water.[72] The PDMS base reagent and curing agent were mixed in a 10:1 ratio and cured on a 4-inch Si-wafer for 4 h at 80°C. The PDMS was then cut, peeled off, and attached to a custom-made translation stage (MTS25A-Z8, Thorlabs) motorized by a DC Servo. For the complete lift-off process, one edge of the PDMS is attached to the translation stage while the PDMS is carefully placed on MoS_2/sapphire substrate. During this step a special care should be taken to avoid any air gaps or dust on the polymer/substrate interface. The PDMS/MoS_2/sapphire is then placed in a clean container and filled with pre-filtered (20 nm) DI-water. To preserve an entire 3-inch area of MoS_2 and ensure complete delamination we have used a slow, controlled lift-off speed of 5-10 μm/s. As a result, the PDMS slowly lifts off MoS_2 from the sapphire as the water penetrates below the MoS_2, enabling the attachment of MoS_2 to the PDMS surface. Further, we manually place PDMS/MoS_2 onto the SiN_x wafer in an all dry-transfer stamping technique. The PDMS is then peeled off with the translation motor to complete the transfer of MoS_2 on SiN_x wafer. After the transfer process is complete, the SiN_x wafer is annealed at 250°C (8 h) in argon and hydrogen (100 sccm and 10 sccm, respectively) environment.

4.5.4 Characterization

Atomic force microscopy was performed on the Asylum Research Cypher AFM system with tapping mode. Raman and PL spectroscopy were done with a Renishaw inVia Confocal Raman Microscope with a 532 nm laser beam at a low power (<0.3 mW) to avoid defect

nucleation and substrate damage. A diffraction grating of 3000 mm-1 was used for good spatial resolution. Transmission electron microscopy was performed on a FEI TEM Talos at 80 kV acceleration voltage in high-resolution TEM (HRTEM) mode. Prior to imaging, we performed moderate substrate heating in air (160°C for 30min) to minimize contamination and unwanted electron beam induced deposition of hydrocarbons. Scanning transmission electron microscopy imaging experiments were conducted using an aberration-corrected (with double Cs corrector) FEI Titan Themis TEM 60-300 kV, equipped with Schottky X-FEG electron source and a monochromator to reduce the effect of chromatic aberrations. To avoid sample damage, a low acceleration voltage (80 kV) was used for all the experiments, which is below the electron-beam induced knock-on damage of MoS_2. The typical electron probe current was 18 pA. Images were acquired with a Gatan high angle annular dark field (HAADF) detector with angular range (49.5-198 mrad) using 185 mm camera length. To highlight the relevant detail, the image was processed using the "double-Gaussian filtering" method.[163]

4.5.5 DNA Translocations

The MoS_2 devices were assembled in a customized PMMA flow cell. The flow cell design and assembling steps are explained in detail elsewhere.[44] We then filled the flow cell with 1M KCl, 10 mM Tris and 100 mM EDTA buffered at pH = 7.5 (20 nm filtered, degassed) and the nanopores in MoS_2 were made by the ECR technique.[57] Once the desired pore size was obtained, the translocation measurements were performed. NoLimits 100 bp DNA Fragment (Thermo Fisher Scientific, USA) was briefly preheated at 65-70°C followed by cooling down to room temperature prior to the experiment to ensure proper dispersion of the DNA molecules in the buffer and helps to avoid clogging of the nanopore.[29, 164] The 100 bp DNA was then added to the cis-compartment of the flow cell and a voltage was applied to electrophoretically translocate DNA through the nanopore. The data acquisition was performed using an Axopatch 200B (Axon Instruments, USA) low-pass filtered at 10 kHz and recorded at a 100 kHz sampling rate. The data analysis, event detection and plotting was done using the Python-based OpenNanopore toolkit (https://www.epfl.ch/labs/lben/opennanopore-python).

4.6 Supplementary Data for Chapter 4

All the following figures are a part of the supplementary file published in SmallMethods, 2020, Thakur et al.[45]

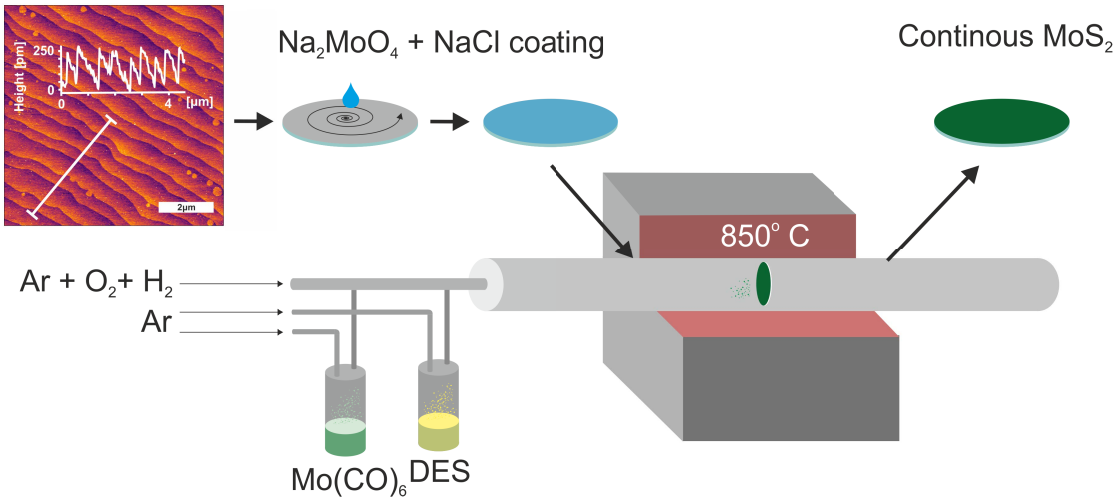

Figure S4.1: Schematic of the custom-made MOCVD setup for the MoS_2 monolayer synthesis. The annealed c-plane sapphire 3-inch wafer is spin-coated with growth promoter (mixture of Na_2MoO_4 and NaCl) and placed in a tube furnace. Growth step is performed in ambient pressure and at 850°C.

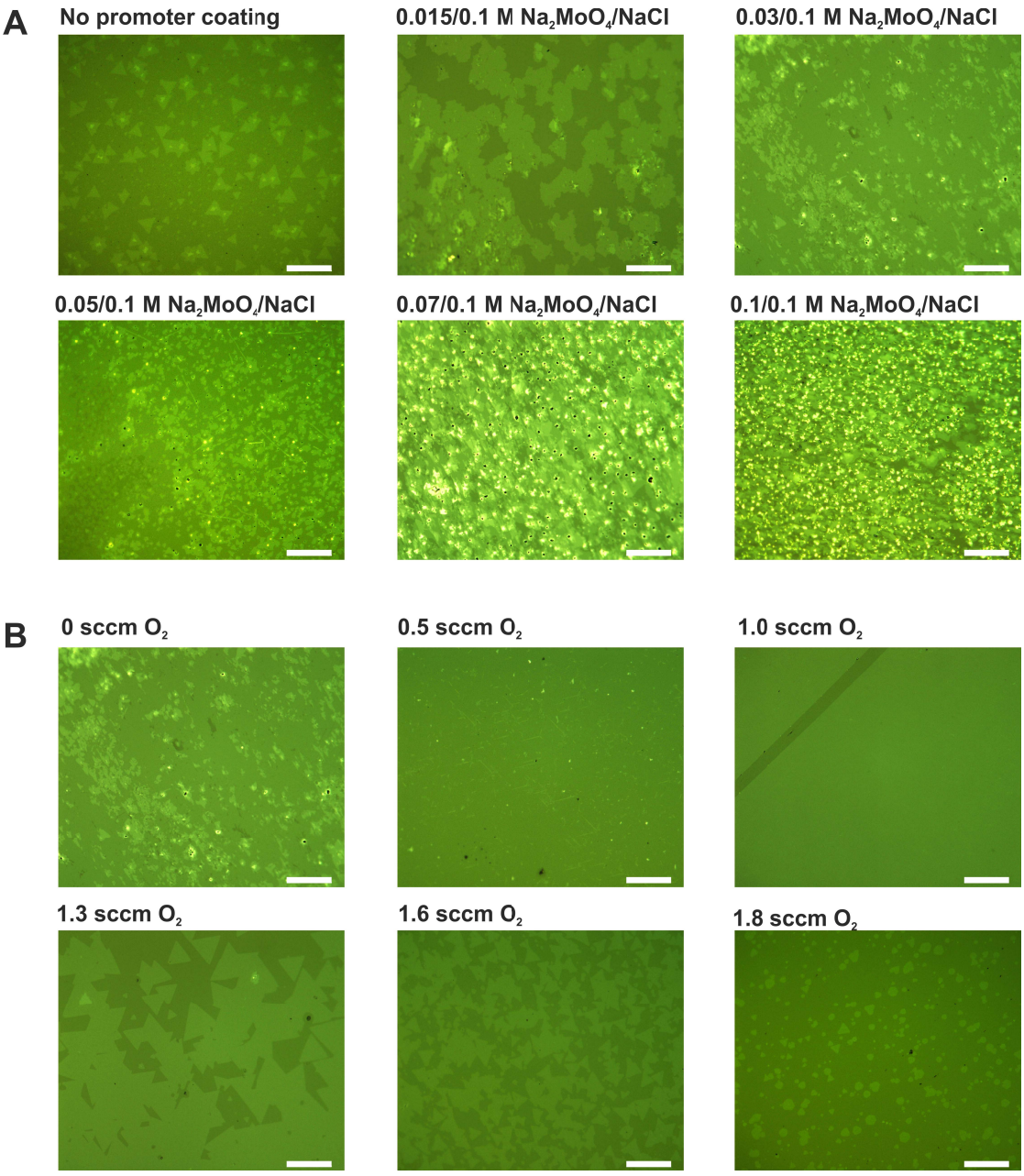

Figure S4.2: Optical images of a MoS_2 grown under different process conditions showing (a) an impact of precursor solution concentration ratio over a growth thickness. The growth process was done at 210 sccm of Ar, 3 sccm of diethyl sulphide, 12 sccm of $Mo(CO)_6$, 4 sccm of H_2 and 0 sccm of O_2 at 850°C for 30min. (b) a growth results influenced by the addition of slight O_2 flow to the reaction. The growth conditions were the same as in (a) with a constant precursor concentration of 0.03 M / 0.1 M and varying oxygen flow. All scale bars are 50 μm.

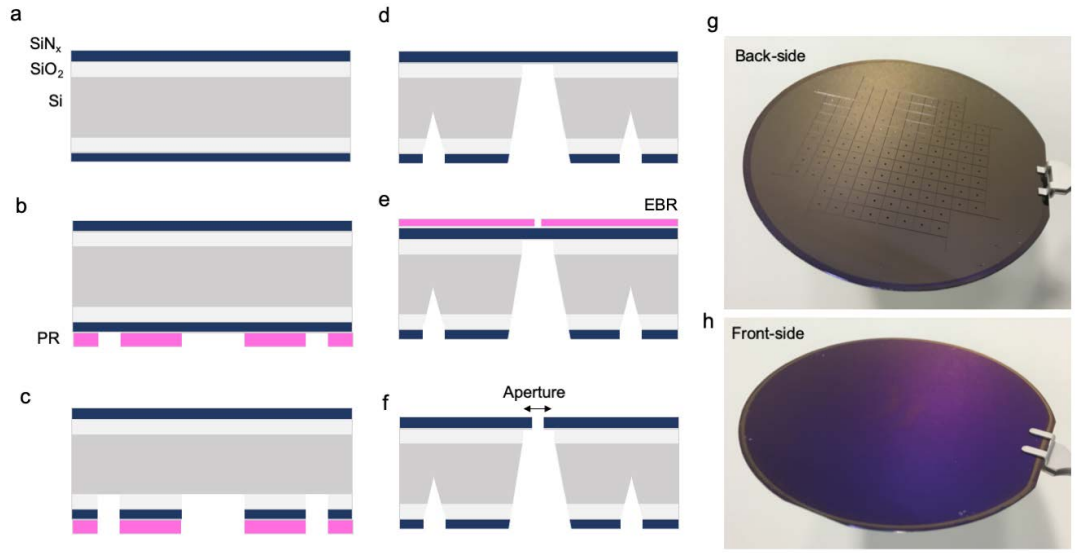

Figure S4.3: Substrate fabrication. Wafer-scale process of the supporting SiN_x chips preparation is explained step by step: double side polished 380 μm thick Si (100) 100 mm diameter wafer (darker grey) with 60 nm of SiO_2 (lighter grey) and 20 nm of SiN_x (dark blue) on each side (a) is being processed with back-side photolithography, pink for photoresist (PR) layer (b) and the pattern is transferred using dry etching (c). The aperture is exposed to 25% wt KOH to form the SiN_x membranes and dicing lines (d). The ≈80 nm apertures in the middle of each membrane are being formed using e-beam lithography, pink for e-beam resist (EBR) layer (e) and a consequent dry etching (f). The resulting wafer design is shown from the back side (g) and the front side (h).

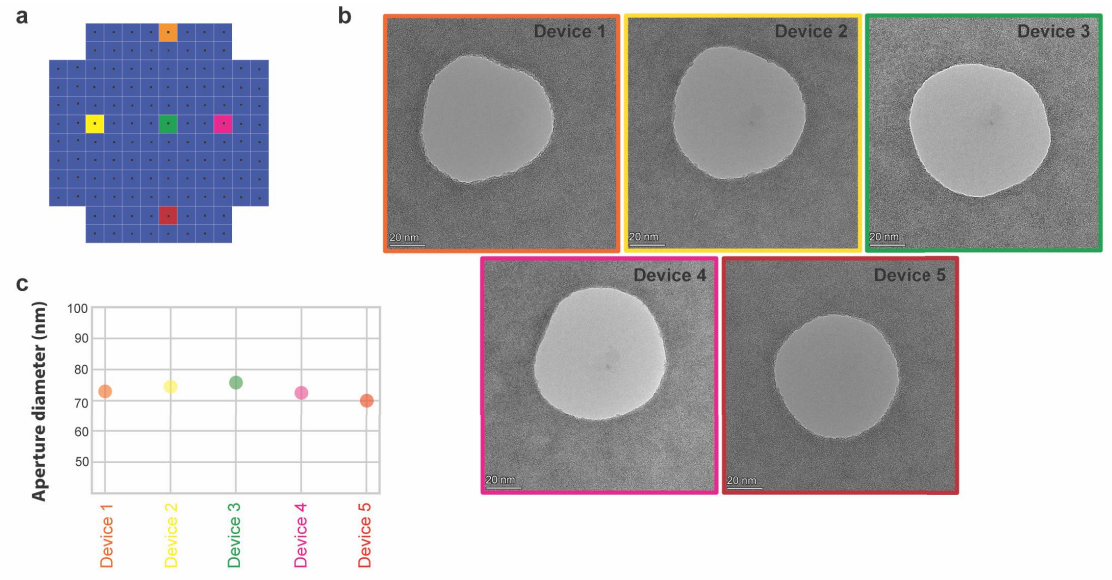

Figure S4.4: Substrate aperture variability and quality characterization. (a) Representative sites on the wafer from where five devices are used to characterize their aperture size and cleanliness before transfer. Presence of bulky residues around the aperture causes blister formation after the transfer of MoS_2. (b) TEM images of respective devices show the aperture openings and showed clean surface. All scale bars, 20 nm. (c) The aperture diameter was ≈75 nm showing similar sizes and very low substrate variation (<5% error), estimated using Image J.[165]

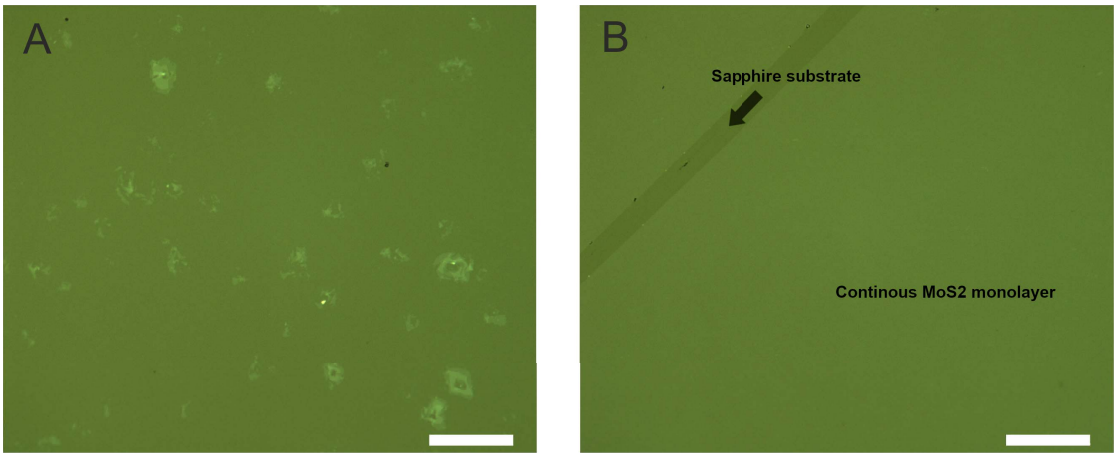

Figure S4.5: Optical images of a MoS_2 monolayer film grown over a large area from the same batch. (a) with visible extruded grain boundaries and secondary nucleation sites where the spin-coated solution was the thickest (around the edges of the substrate) representing roughly ≈10% of the substrate area, and (b) with a clean, continuous monolayer surface visible on the remaining area. Scale bars, 50 μm.

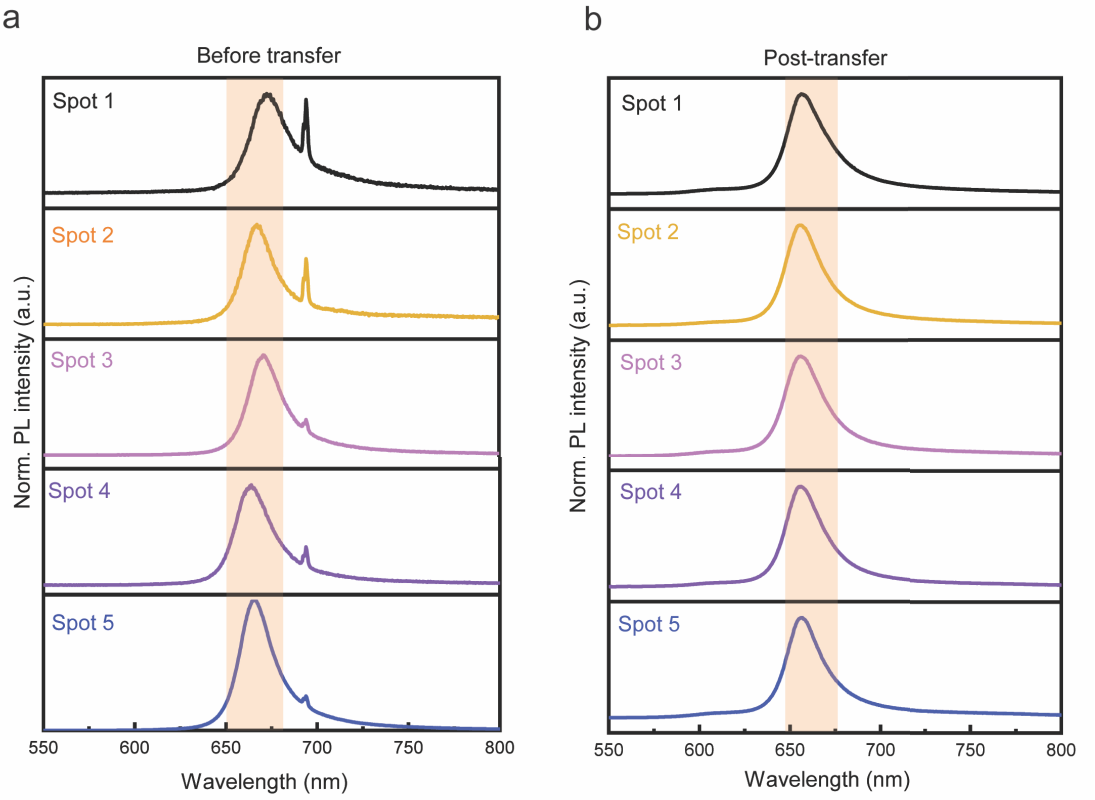

Figure S4.6: Photoluminescence measurements. (a) As-grown MoS_2 on the sapphire substrate from five different spots (shown in Figure 4.2a-b in the manuscript) before and (b) after the transfer on SiN_x surface. The shaded region in the graphs is a guide to the eye showing the peaks corresponding to the MoS_2.

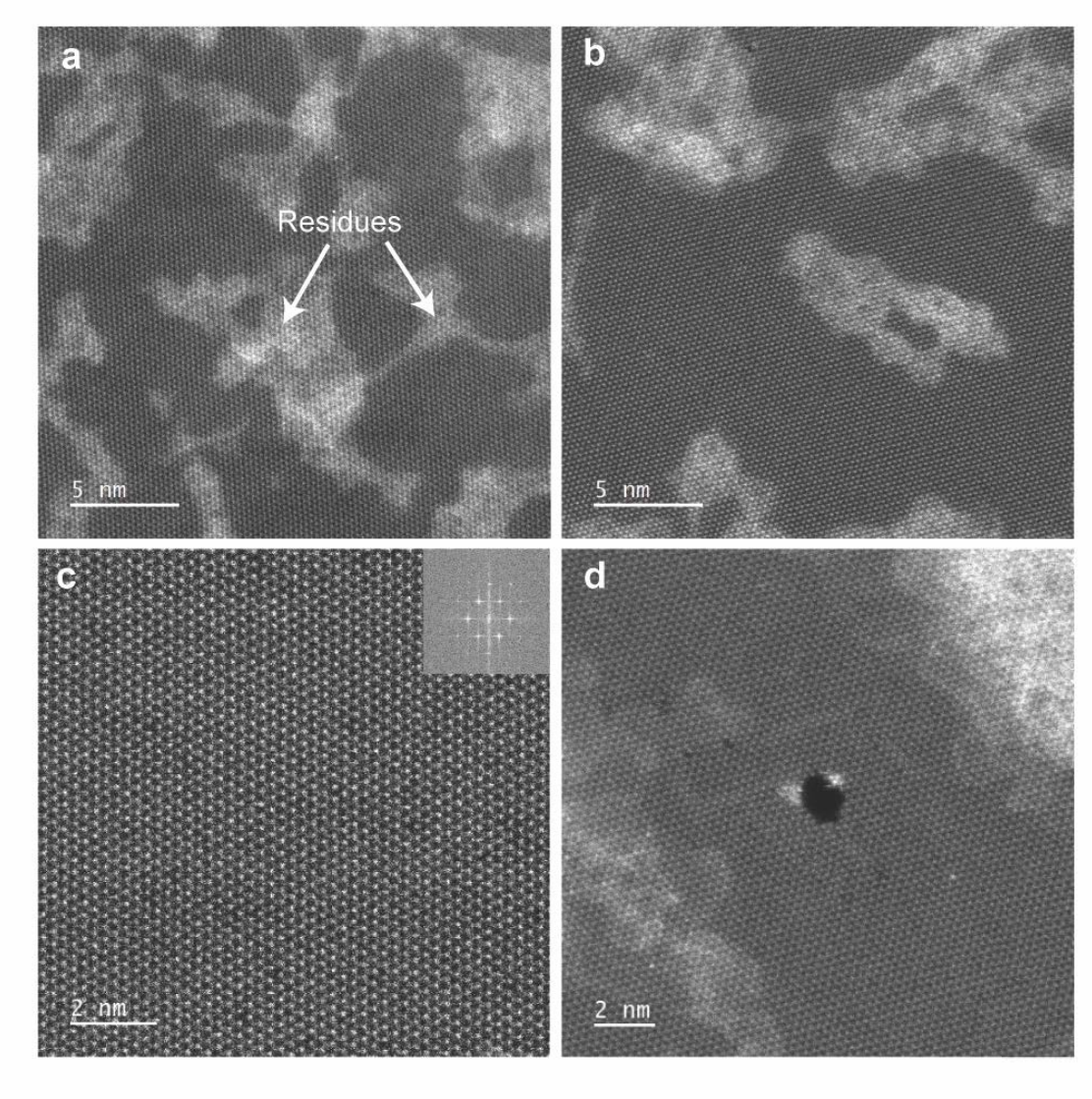

Figure S4.7: Raw STEM/HAADF images show a large-field of view (FOV) of continuous MoS_2 lattice transferred by PDMS. (a, b) Representative MoS_2 areas with residues (brighter contrast on the panels). (c) High magnification STEM image shows the perfect lattice structure of monolayer MoS_2. The inset image shows the Fast Fourier transform, which further confirms the monolayer structure. (d) A nanopore (≈2 nm) in the center of the image, formed by the electron-beam probe in STEM.

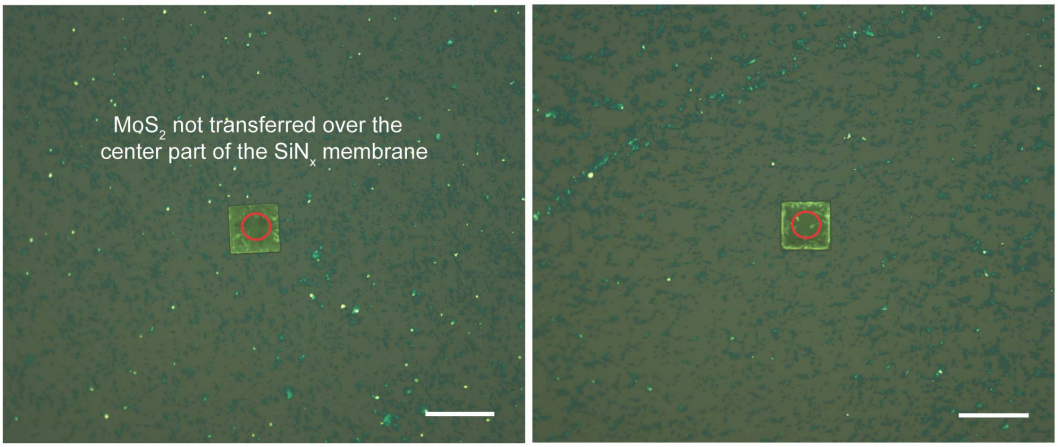

Figure S4.8: Optical images showing examples of unsuccessful transfer of MoS_2 over the highlighted region where the aperture is located. All scale bars are 50 μm.

Table 4.1: Comparison of wafer-scale transfer efficiency of MoS_2 using PDMS among different batches of substrates. From these wafer-scale transfer, the average transfer efficiency is 70.13±2.4 %. Batch C is shown in Figure 4.3.

Batch	**Total chips**	**Successful transfer**	**Unsuccessful transfer**	**Broken SiN_x membrane post-transfer**	**Transfer efficiency (%)**
Batch A	120	83	36	1	69.1
Batch B	128	87	41	0	67.9
Batch C	128	94	34	0	73.4

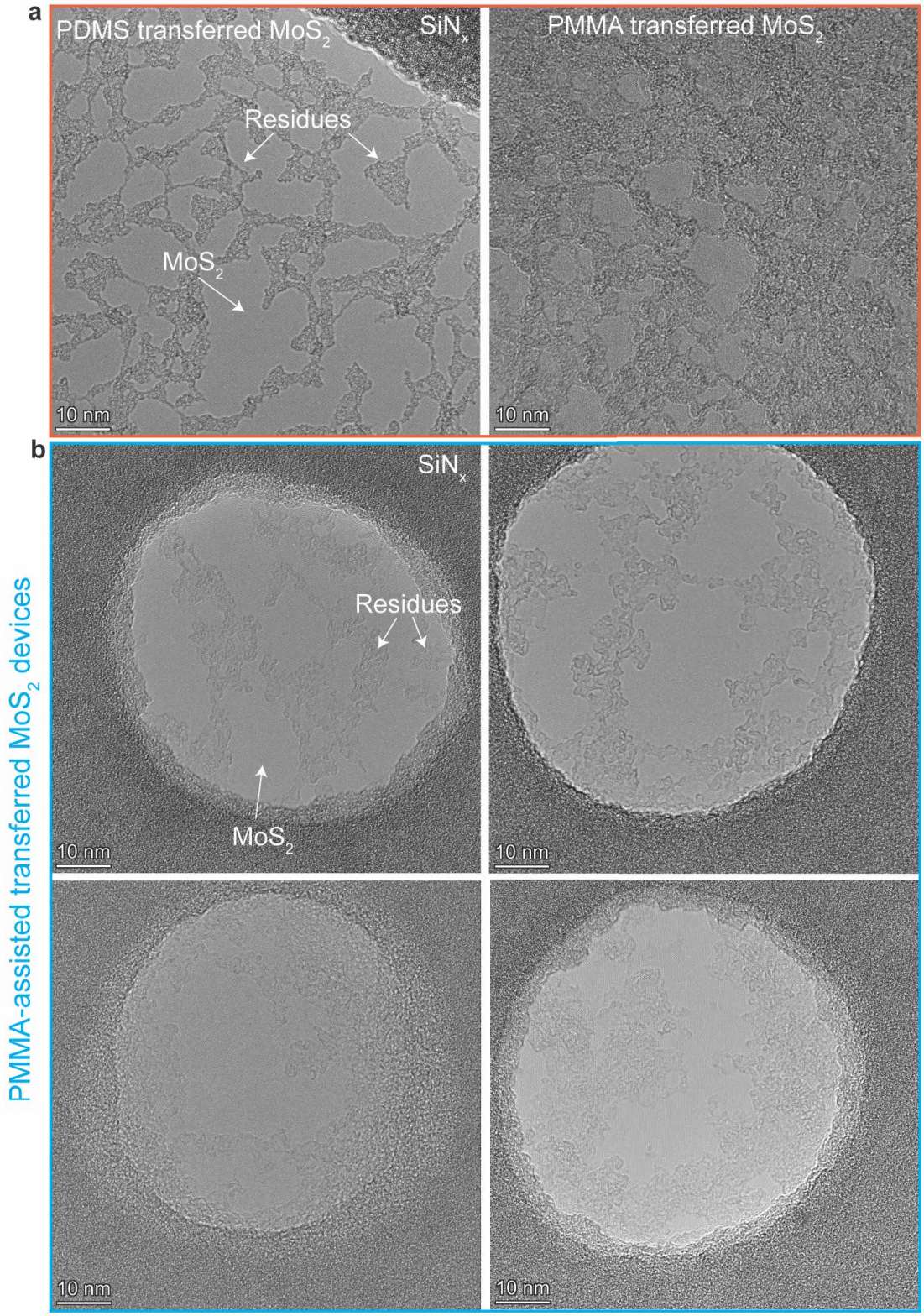

Figure S4.9: Comparison and cleanliness variation among samples of MoS_2 imaged using TEM. (a) TEM images showing suspended MoS_2 post-transfer using PDMS and PMMA polymers on SiN_x TEM grids. The calculated clean area MoS_2 (without residues) with traditional PMMA was ≈20% while with PDMS (current method) was ≈50% clean area on the respective MoS_2 samples. The clean regions were calculated using Image J.[165] (b) Representative devices with MoS_2 transferred using traditional PMMA polymer showing variation in cleanliness. These devices show comparable cleanliness with MoS_2 devices transferred using PDMS polymer (Figure 4.3b in main text).

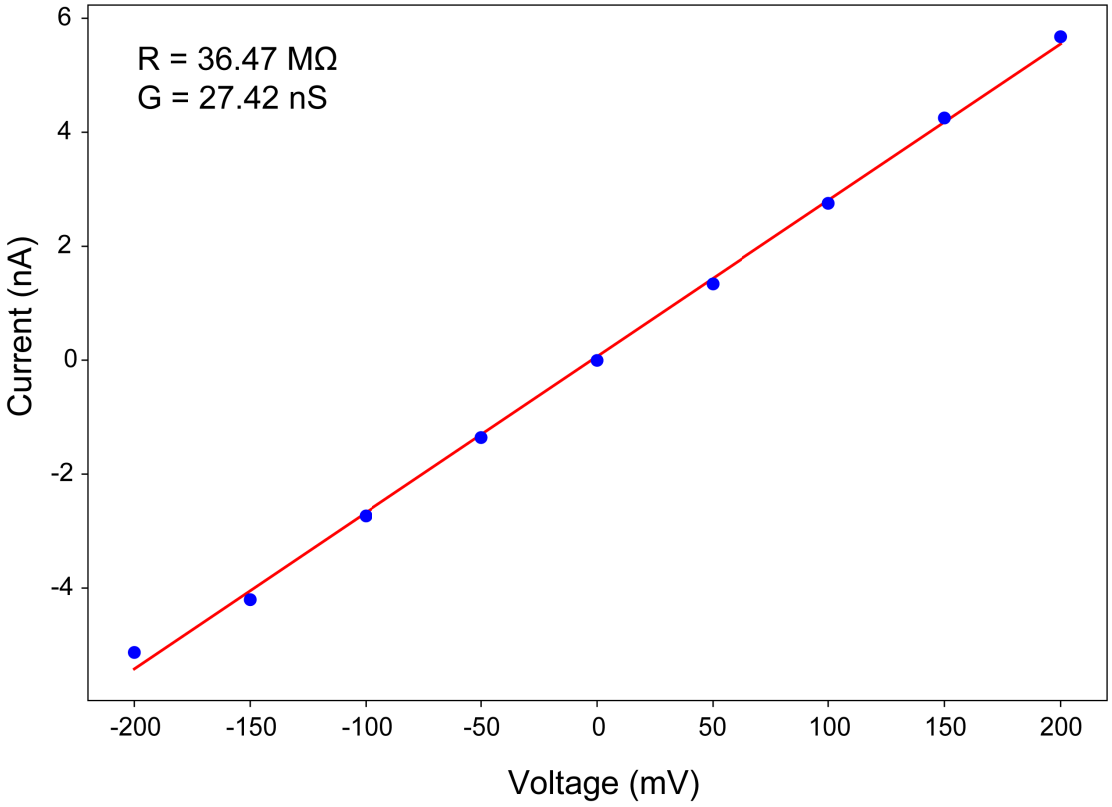

Figure S4.10: I-V characteristics (Device A). The location of Device A is highlighted in 4.3a. The I-V response for the MoS_2 nanopore was measured in 1M KCl by sweeping the voltage in the range between -200 mV and +200 mV.

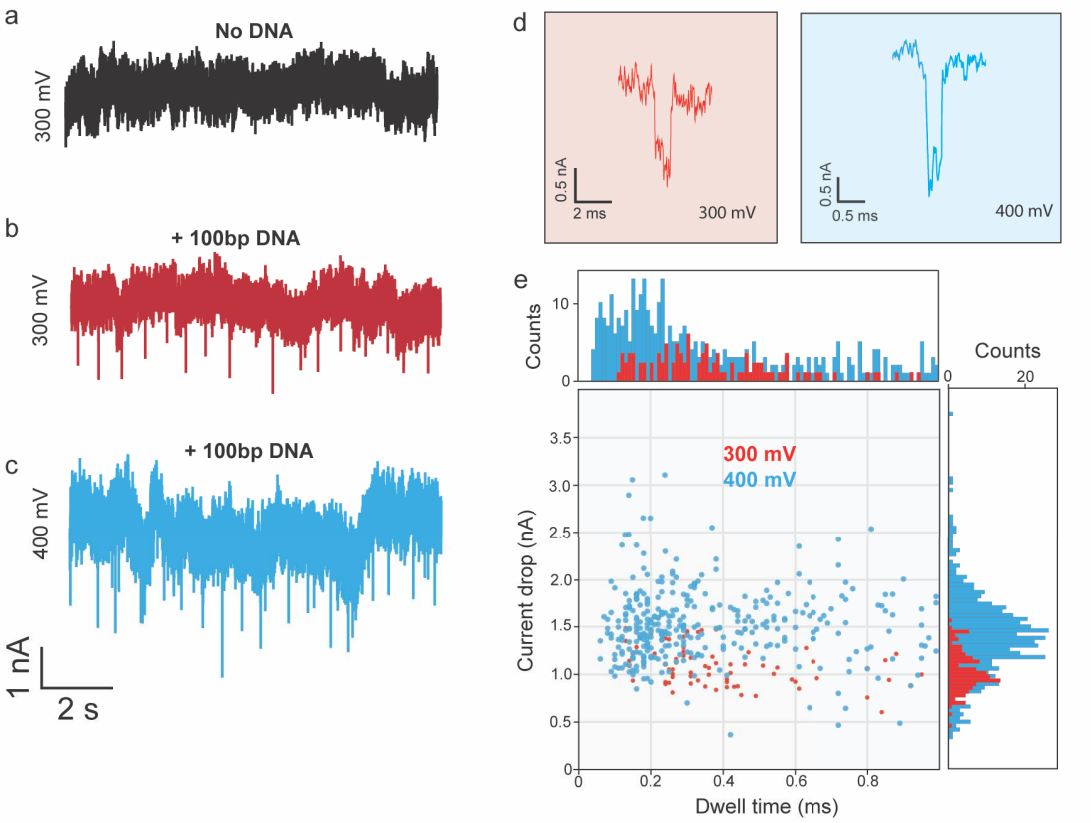

Figure S4.11: DNA translocation using ≈4 nm MoS_2 nanopore (Device B, from a batch number 2 of the wafer transfer) in 1M KCl. (a) Negative control: open-pore current trace at 1M KCl prior addition of DNA. The baseline current noise is a consequence of charge fluctuations occurring at the rim of the MoS_2 nanopore typically causing a dominant low-frequency noise.[20] Another reason could also be the mechanical fluctuations of the thin free-standing 2D membrane contributing additionally to the baseline fluctuations.[152] The current trace showed no translocation spikes measured at 300 mV. Current trace (10s) after the addition of 100 bp DNA (10 nM) showing translocation spikes measured at (b) 300 mV and (c) 400 mV. (d) Representative events from the traces obtained in (b and c). (e) Scatter and histogram plots, respectively, of 100 bp DNA translocation events. The events were recorded at 300 mV and 400 mV, and show ≈20% current blockades.

5 On Stability and Durability of 2D Nanofluidic Devices

The following section is a part of following publication which is currently under-review:

> **Mukeshchand Thakur**, Nianduo Cai, Miao Zhang, Yunfei Teng, Andrey Chernev, Mukesh Tripathi, Yanfei Zhao, Michal Macha, Farida Elharouni, Martina Lihter, Liping Wen, Andras Kis, and Aleksandra Radenovic. High Durability and Stability of 2D Nanofluidic Devices for Long-term Single-Molecule Sensing (under revision)

Y.Z. and M.M. contributed to the growth of MoS_2 samples. Y.T. and A.C. fabricated SiN_x substrates. M. Thakur transferred MoS_2 samples. M. Thakur and N.C. prepared HMDS/SiN_x substrates, fabricated the nanopores, and measured ion transport. Monolayer layer detachment was studied by M. Thakur and M. Lihter. The aberration-corrected TEM imaging and defects quantification was performed by M. Tripathi. PL imaging of MoS_2 and oxidative analysis was done by M.Z and F.E. Pore expansion studies and DNA translocation measurements were performed by M. Thakur. A. R. supervised the work. All authors contributed to the writing and discussion of the manuscript.

5.1 Summary

Nanopores in two-dimensional (2D) membranes hold immense potential in single-molecule sensing, osmotic power generation, and information storage. Recent advances in 2D nanopores, especially on single-layer MoS_2, focus on the scalable growth and manufacturing of nanopore devices. However, there still remains a bottleneck in controlling the nanopore stability in atomically thin membranes. Here, we evaluate major factors responsible for the instability of the monolayer MoS_2 nanopores. We identify chemical oxidation and delamination of 2D monolayers from their underlying substrates as the major reasons for the instability of MoS_2 membranes and nanopores. In the second part of this chapter, we addressed delamination of MoS_2 layers from the SiN_x substrate. I will introduce ways to improve stability of 2D MoS_2 films as well nanopores. Surface modification of the substrate and reducing the dissolved oxygen from the measurement solution improves nanopore stability and increases their shelf-life.

Understanding nanopore growth and stability can provide insights into controlling the pore size and shape. Durable engineered nanopore devices with improved pore life can enable long-term DNA sensing.

5.2 Introduction

Nanopores in two-dimensional (2D) materials are a promising class of solid-state sensors and serve as a versatile tool for mimicking biological pores and channels in cells.[11, 73, 125, 129, 166] Most commonly studied 2D materials are graphene,[46–48, 73] MoS_2,[43, 44, 52, 59] WS_2,[80, 167] hBN,[110] and more recently MXenes.[73, 168, 169] A typical 2D nanopore device consists of a nanopore in a free-standing atomically thin membrane over a supporting aperture that separates two reservoirs. Electrically charged biopolymers such as DNA, RNA, or proteins are driven through the nanopore under an applied electrical field and generate distinct signals in ionic current that are characteristic of translocating molecules. The 2D nanopore devices have become an important tool for studying single-molecule biophysics, ion transport, and selectivity.

Solid-state nanopores in general have inspired many novel applications such as water desalination,[170, 171] solute and gas separation,[167, 172] osmotic energy,[129] and digital DNA readout.[173] Of all the variety of 2D nanopores reported so far, nanopores in monolayer MoS_2 have gained considerable attention, especially in biosensing applications. An ultrathin triatomic monolayer MoS_2 (≈0.65 nm), in principle, provides high spatial resolution approaching the physical size of two adjacent DNA bases (0.34 nm). Compared to the graphene membranes, the sticking of DNA bases to the MoS_2 is relatively low,[50] which makes it a lucrative tool to study at a single molecular level. Indeed, MoS_2 nanopores have been shown to detect DNA molecules down to single-nucleotide resolution23 and even differentiate topological variations on DNA.[53] More recently, Graf et al.[56] demonstrated the fabrication of a MoS_2 nanopore field-effect transistor capable of detecting DNA simultaneously in ionic as well as in transverse channel through MoS_2 featuring the versatility of MoS_2 in different sensor modalities. Currently, the solid-state nanopore technology is still limited to lab-scale research due to practical bottlenecks that hinder its commercial application.[73, 90, 174, 175]

The device yield, variability, stability, and reliability are important performance metrics for any solid-state sensors.[174, 175] The terms - reproducibility, variability, and reliability are interrelated and highlight the fabrication process and success of the nanopore devices. Reproducibility (or repeatability) is the variability in terms of measurements from the device under the same experimental conditions. Variability is the deviation from the set characteristics of the device while reliability is related to the time device operates under external stress (e.g. voltage, pressure) within predefined parameters. Merchant et al.[46] deposited a thin ≈5 nm TiO_2 layer on the graphene membrane to address the noise and robustness of the device. Although the devices showed improved noise compared to uncoated counterpart, the coating increased the overall thickness of the membrane. Unfortunately, the stability of 2D nanopore

devices is poorly reported or overlooked and needs to be addressed to realize their commercial potential as sensors. Recently, few groups have studied the stability of silicon-based solid-state nanopore devices.[76, 176] Progress in the growth of high-quality MoS_2, large-area wafer-scale substrate fabrication, and transfer has improved the scalability and efficiency of MoS_2 nanopore device fabrication.[45] However, challenges such as delamination of the 2D membrane,[177] oxidation of the 2D material,[78, 178–180] and nanopore expansion in standard experimental conditions need detailed examination.[175] These parameters are critical for the development of 2D nanopore devices as well as for the advancement of 2D materials research.

This chapter investigates and discusses major reasons for the instability of monolayer MoS_2 membranes and their nanopores, leading to low reliability and device failure. We show that the delamination of the monolayer MoS_2 from its substrate is the main reason for the instability of nanopore devices. Further in the next chapter we will see how increasing the hydrophobicity of the SiN_x substrate by organosilane coating prior to transferring MoS_2 strengthens MoS_2-SiN_x interfacial interaction and thereby reduces detachment. Furthermore, we also found that the chemical oxidation of the MoS_2 monolayer creates and enlarges defects in MoS_2, leading to pore expansion in an aqueous solution. We show that reducing the oxygen concentration level in the buffer improves the nanopore lifetime by slowing down the pore edge dissolution. Reinforcing MoS_2-SiN_x interaction and minimizing the MoS_2 oxidation process in the buffer facilitates a continuous long-time DNA sensing on the same pore (>3 h). Finally, we discuss and provide guidelines to address other phenomena that can potentially compromise 2D nanopore devices such as nanopore clogging, surface contamination, and electrostatic damage that routinely lead to device failure.

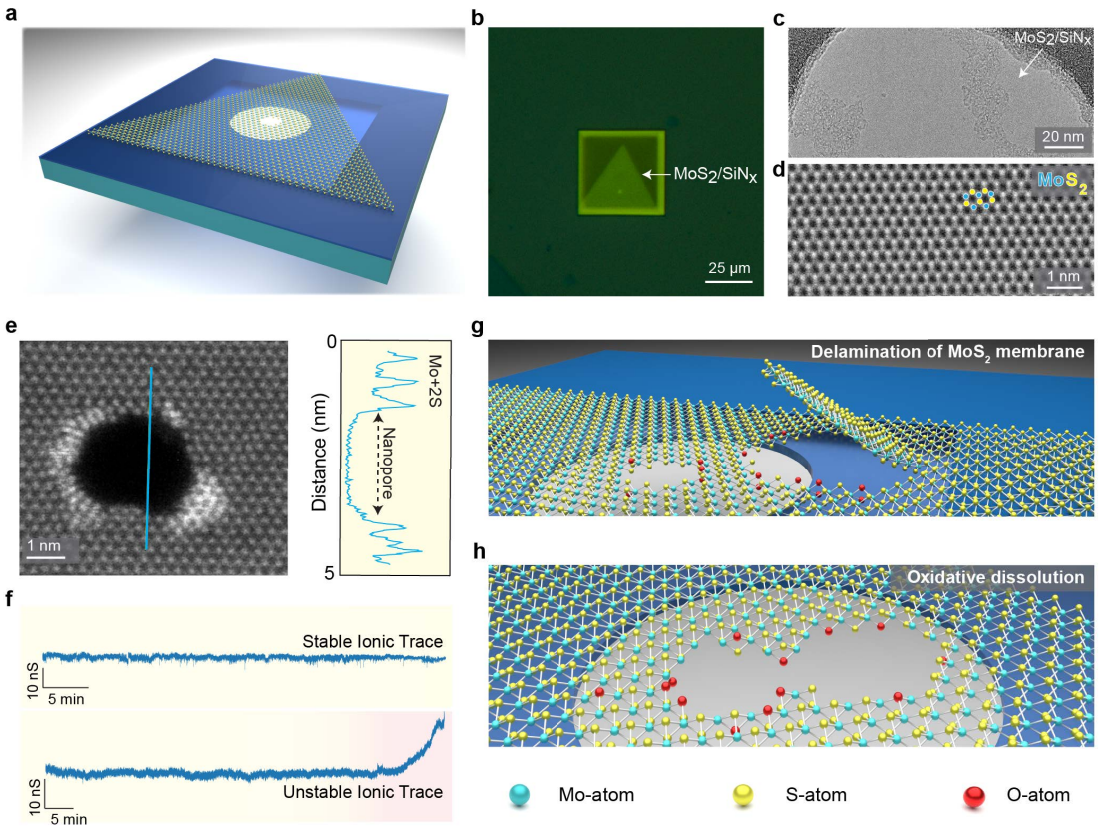

Figure 5.1: A 2D MoS_2 nanopore and nanopore instability. (a) Schematic showing a single crystal of monolayer MoS_2 transferred over a SiN_x membrane (≈20 nm thick). The crystalline monolayer MoS_2 is free-standing over a SiN_x aperture of ≈80 nm. A suitable nanopore is then created in the suspended part. (b) Optical micrograph of a 2D nanopore device after transfer of a monolayer MoS_2. (c) The bright-field TEM image of a clean suspended MoS_2 membrane and (d) an aberration-corrected ADFSTEM image of the membrane show perfect lattice with brighter Mo-atoms (indicated with blue circles) and relatively lighter S-atoms (indicated with yellow circles). (e) A nanopore (≈2.5 nm) drilled in ADF-STEM mode is shown with an intensity profile highlighting the Mo-atoms with a dangling bond at the edge of the nanopore. (f) Representative ionic current traces of two different nanopore devices that show stable and increasing open-pore current with time, respectively, emphasize the instability in 2D nanopores. (g, h) Schematic showing the mechanisms of device instability issues arising during the course of a nanopore experiment. The red color spheres represent oxygen atoms at the edges of the MoS_2 nanopore.

5.3 Results and Discussion

5.3.1 2D MoS_2 Nanopore: Device architecture and nanopore instability

A typical MoS_2 nanopore device comprises a suspended 2D material over a thin SiN_x substrate (Fig.5.1a). The SiN_x membrane (≈30 x 30 μm) is typically about 20 nm thick and consists of an

aperture of 80-100 nm in diameter defined by e-beam lithography (Fig.S5.1 and Fig. S5.2).[44, 45] A monolayer of MoS_2 is then deterministically transferred to the membrane (Fig.5.1b) such that there is a free-standing MoS_2 over the aperture (Fig.5.1c). See the Materials and Methods section for monolayer MoS_2 growth and transfer.

A 2D MoS_2 membrane is an atomically thin transition metal dichalcogenide that comprises two hexagonal planes of S-atoms and a hexagonal plane of Mo-atoms as shown in the aberration-corrected ADF-STEM image (Fig.5.1d). In a monolayer, the Mo-atom is covalently attached to the S-atoms in a trigonal prismatic geometry.[181] A nanopore is formed in the monolayer using either TEM-based method[44, 59] or in situ via the electrochemical-reaction (ECR) method.[57] Figure 5.1e shows a single MoS_2 nanopore with an approximate diameter (dTEM) is ≈2.5 nm drilled using STEM at 80 kV.[44] The nanopore in the monolayer MoS_2 shows edges terminated with mainly Mo-atoms. The brighter Mo-atoms are due to the heavier atom contrast of the Mo-atom compared to the S-atom. The nanopore device is then assembled into a custom-built flow cell[44] filled with an electrolyte (1M KCl), and the ionic current through the nanopore is measured by applying a voltage across the pore. Figure 5.1f shows an example ionic current time trace from two representative MoS_2 nanopore devices with stable (at 200 mV) and unstable current traces (300 mV) in 1M KCl. The majority of the issues related to the 2D nanopore devices are depicted in Figure.S5.3 . About ≈70% of the nanopore devices (n = 36 devices) showed unstable MoS_2 nanopore as a major reason for the device failure. This issue has also been observed before in graphene nanopores,[46] where ≈30% of the device failure is attributed to membrane damage. Indeed, 2D membrane and nanopore stability becomes of prime importance for the practical applications of the 2D nanopore sensors.

Figure 5.1g-h shows a schematic representation of two prime reasons for instability in 2D nanopores- (1) defects or leaky unstable membrane forming cracks and delamination, and (2) oxidative dissolution of a 2D nanopore in an air-saturated aqueous ionic solution.

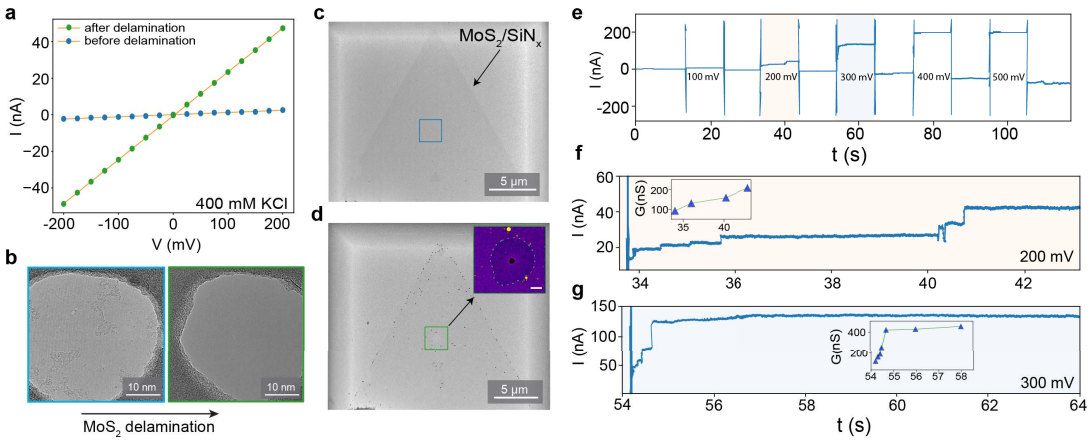

Figure 5.2: Delamination of monolayer MoS_2 from the SiN_x surface. (a) An IV curve from Device 1 measured in 400 mM KCl (pH 8) from MoS_2 nanopore with ≈13 nS in the beginning that increases to ≈225 nS (size of the SiN_x aperture). (b) Bright-field TEM images of Device 1, before and after the delamination. (c-d) A large field of view of Device 1 shows local delamination around the aperture area. Inset in (d) is a falsecolor zoom-in image with an area where the MoS_2 is completely detached (depicted as a dotted area) while the surrounding area retains MoS_2. Scale bar, 200 nm. (e) Measurements on Device 2 (d_{TEM} ≈2.5 nm). Experimental ionic traces show an unstable MoS_2 pore current probed at different voltages (range: ±500 mV, measured every 100 mV for 10s long). (f-g) Zoomed-in traces show an abrupt increase in the ionic current at low voltages: 200 mV and 300 mV. Insets in respective figures show a stepwise increase in the current.

5.3.2 Ionic measurements and delamination of monolayer MoS_2

To extract nanopore sizes from ionic current we used the general conductance model.[107] Figure 5.2a shows an I-V response of a small nanopore in the MoS_2 monolayer membrane. The device initially showed pore conductance (*Gopen*) as ≈13 nS (S = 4.12 S/m) which corresponds to the calculated nanopore diameter of ≈4.2 nm considering membrane thickness (L = 1 nm). After a few minutes of measurements, we observed an unstable ionic trace and the *Gopen* shoots up to ≈225 nS (≈72 nm, L = 25 nm). The *dcalc* corresponds to the open pore current of a bare aperture from the SiN_x membrane. For comparison, we measured the leakage conductance of the intact SiN_x membrane to be lower than ≈300 pS (Fig.S5.4). Indeed, bright-field TEM analysis of the same device reveals that the monolayer MoS_2 membrane got detached or delaminated from the aperture (Fig 5.2b). Figure 5.2c-d shows a large field of view TEM image of the same device with MoS_2 on the membrane before and after delamination near the aperture, respectively. The TEM image of MoS_2 delaminated from the aperture area on the membrane suggests weak interaction of MoS_2 to the underlying SiN_x surface (Fig. 5.2b green square and inset). A similar abrupt increase in the open pore ionic current was also observed with Device 2 which has a single MoS_2 nanopore of ≈2.5 nm fabricated by TEM drilling (Fig. S5.5). Figure 5.2e shows experimental ionic traces probed up to 500 mV measured in 1M KCl. The ionic current trace follows a similar pattern as Device 1, the current increases

in a stepwise manner starting at 200 mV and more. Figure 5.2f-g show zoomed current traces from two voltages: 200 mV and 300 mV where the current increases in discrete steps. We also observe the stepwise increase in the pore current up to *Gopen* ≈150 nS (200 mV) and even up to 400 nS (at 300 mV). This conductance is higher than the expected *Gopen* from this device which is around ≈25 nS (L = 1 nm, S = 11.5 S/m). We also observed unstable open pore ionic current and step-wise increase with voltage in different ionic strengths of the solution as shown in Figure S5.6.

Unstable ionic current trace or increase in ionic current several orders of magnitude more than expected can be attributed to one or more of the following reasons: the nanopore enlargement in size, or multiple nanopores formation at different defective sites in the 2D material,[58, 59] or delamination of 2D material.[44, 177] An abrupt increase in open-pore current has been observed before in 2D nanopores at higher voltages (>700 mV).[44, 58, 177] As shown in Figure 5.2e-f, the open-pore current at 300 mV shows more prominent increment steps compared to 200 mV indicating the delamination process is voltage-dependent. This corroborates well with studies on graphene pores transferred on hydrophilic SiN_x surfaces, and the extent of delamination is voltage-dependent.[177] The surface energy between MoS2 and SiNx surface is 250 mJ/m^2 similar to graphene-SiO_2 is 200 mJ/m^2 albeit this value depends on the substrate roughness and defects in the 2D material.[177] Delamination is related to the interaction energy of the 2D material with underlying support substrate. In the case of graphene on an oxidized SiN_x surface, experimentally a threshold voltage of ≈0.25V is observed. Delamination is characterized by an aberrant ionic conductance than expected due to decrease of the membrane resistance and enhanced intercalation of the ions between 2D membrane and SiN_x surface. This is facilitated especially when the SiNx surface is hydrophilic (O2 plasma- or piranha-treated treatment). Consequently, there is an alternate path for the ions to flow leading to higher current than expected. This results in a physical delamination of membrane starting from the aperture area until a crack or membrane edge that corresponds with the delaminated area.

Figure S5.7 shows examples from three different MoS_2 nanopore devices where a detachment of the monolayer was confirmed with TEM imaging. The 2D membrane instability via delamination can be influenced by an applied voltage and the adhesion strength between MoS_2 and SiN_x surfaces.

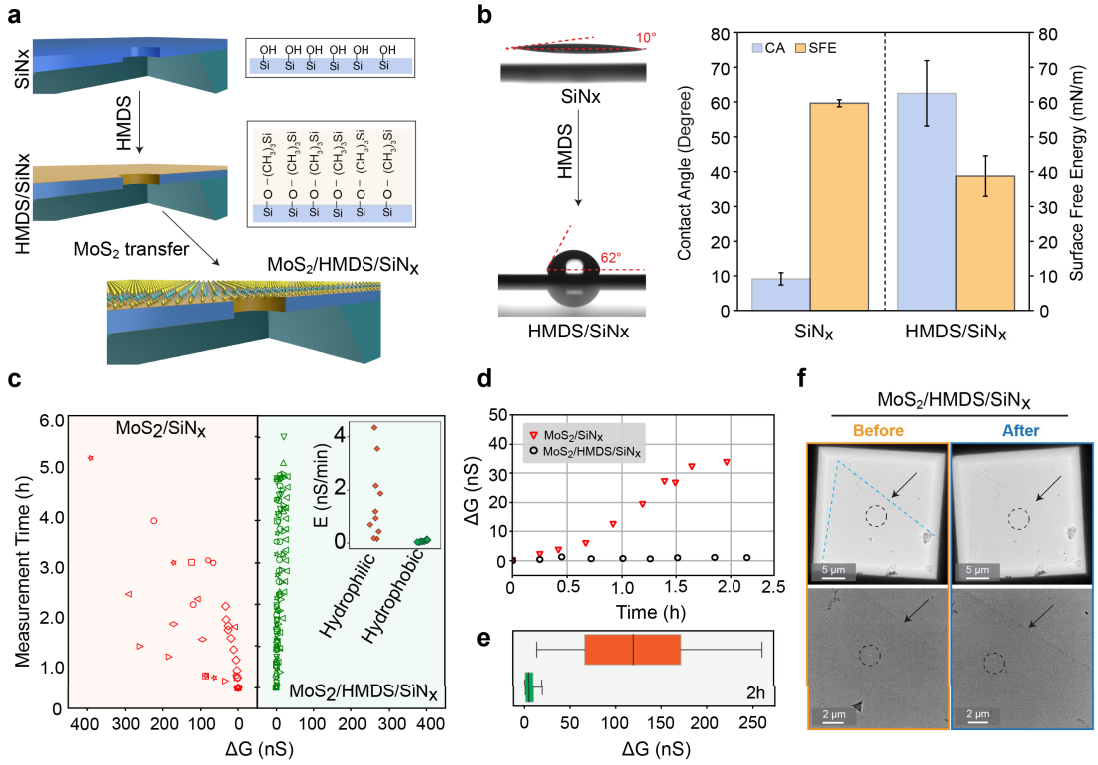

Figure 5.3: Enhanced extrinsic stability of MoS_2 membranes using HMDS-modified SiN_x substrates. (a) Schematic showing stepwise coating of the SiN_x surface with HMDS followed by transfer of monolayer MoS_2 over the membrane. (b) Characterization of HMDS-modified SiN_x substrates after HMDS-coating. The surface shows an increase in the contact angle (from ≈10°to ≈62°, n = 15) and a decrease in the free surface energy post-treatment (n = 11). (c) Stability analysis of MoS_2 nanopores transferred on hydrophilic substrates (n = 9) and hydrophobic substrates (n = 10). The increase in the open pore conductance (Δ G) is measured over time to indirectly correlate with the nanopore stability. Each marker represents ΔG from individual nanopore devices. Inset shows the rate of pore enlargement between all the pores. (d) A representative example of such two devices shows a drastic increase in conductance compared to the HMDS-modified substrate. (e) Box-plot showing a wide distribution of Δ G from unmodified hydrophilic substrates compared to a narrow distribution of modified substrates. (f) Bright-field TEM images of monolayer MoS_2 transferred on HMDS/SiN_x substrate show an intact membrane and no delamination.

5.3.3 Substrate modification and enhanced 2D membrane stability

One way to increase membrane stability of the MoS_2 layer on the SiN_x substrate is to reinforce the adhesion to the underlying substrate. To achieve this, we uniformly coat the SiN_x surface with HMDS and transfer MoS_2 to form MoS_2/HMDS/SiN_x interface (Fig.5.3a). We start with evaluating the effectiveness of HMDS treatment by assessing the change in wettability of the SiN_x surface. As shown in Figure5.3b, we calculate the contact angle (CA) and extract surface

free energy (SFE) of the HMDS/SiN_x surface using the Extended Fowkes method.[182]

Surface hydrophilicity is achieved through piranha solution treatment which is generally used to clean the nanopore devices. This treatment results in a formation of a dense and thin monolayer of hydroxyl groups (-OH) on the SiN_x surface.[44, 45] Additionally, the SiN_x surface is also exposed to O_2-plasma which renders the surface hydrophilic, with CA, ≈10° (Fig.5.3b). After HMDS treatment the contact angle increases up to ≈60°, due to the exposed methyl groups (-CH_3) being relatively more hydrophobic (Fig.5.3c). As plotted in Figure5.3b (right side), the SFE measurements show that HMDS-primed SiN_x surfaces(≈60 mN/m) have lower surface free energy compared to the bare SiN_x surface (≈40 mN/m), verifying successful HMDS-coating on the SiN_x surface.

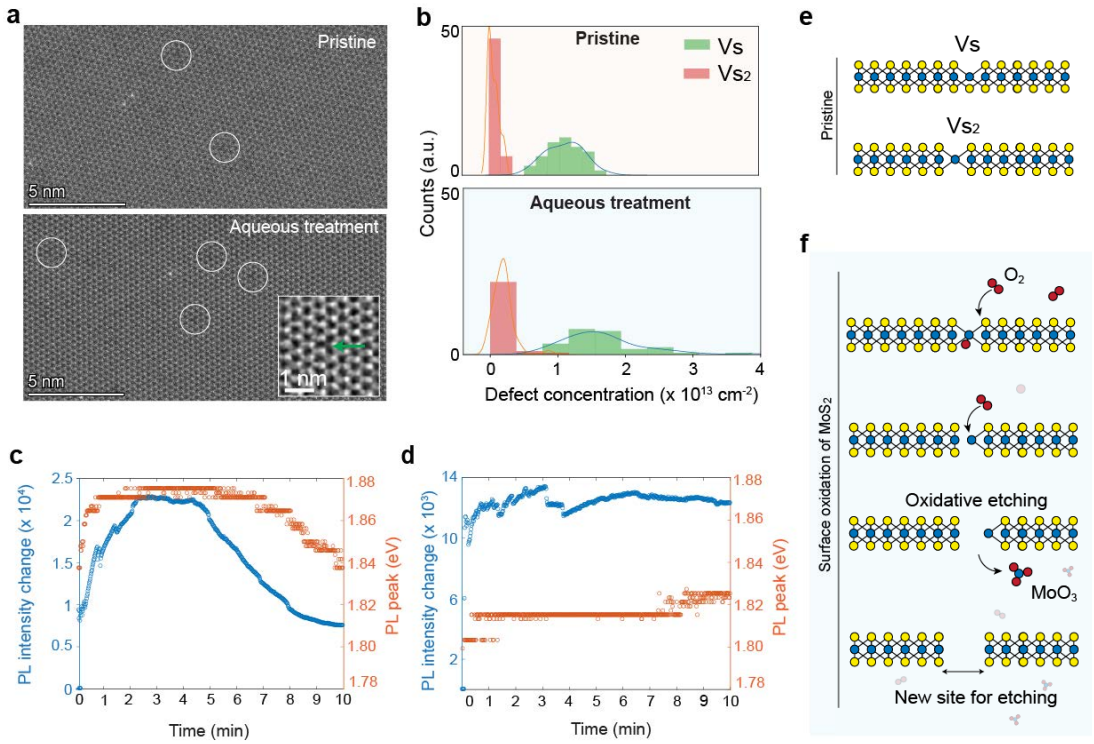

Figure 5.4: Quantification of surface defects and oxidation of monolayer MoS_2 in pristine and aqueous solution. (a) Aberration-corrected ADF-STEM image of monolayer MoS_2 in its pristine form and after incubation in aqueous solution. Marked circles show single sulfur vacancies in MoS_2 (Vs). Inset, an example of the marked circle, showing a single sulfur vacancy defect (green arrow). (b) Histogram and kernel density estimation analysis show two primary populations of defects (annotated as Vs and double sulfur vacancies, Vs2). There is a slight increase in the Vs concentration after treatment on the same order of magnitude at the same imaging conditions. Inset, an example of the marked circles from (a), showing a single sulfur vacancy defect (green arrow). PL spectrum of MoS_2 in aqueous solution the presence of oxygen (≈8 mg L-1) (c) and reduced oxygen level (≈1 mg L-1) (d). (e) Chemical structure of pristine MoS_2 showing sulfur vacancies in the basal plane. (f) Schematic of oxidative dissolution and etching of monolayer MoS_2 in airsaturated aqueous solution.

We then set out to study the MoS_2 nanopore stability by measuring the *Gopen* for all the devices over time. As shown in Figure5.3c, we compare the change in the *Gopen* (ΔG) from different MoS_2 nanopores devices transferred on the conventional hydrophilic SiN_x substrates with HMDS/SiN_x substrates. A general membrane stability improvement is observed for the HMDS-modified MoS_2 nanopore devices with low (ΔG) (<50 nS) compared to the unmodified devices where the (ΔG) increases more than 400 nS after 5 h of measurements. The inset shows a huge spread in the rate of change (E) in *Gopen* in unmodified SiN_x devices (up to 4 nS $min^{-}1$) compared to narrow distribution (<1 nS per min). Figure5.3d, shows two MoS_2 nanopore devices with ΔG increasing for MoS_2/SiN_x versus MoS_2/HMDS/SiN_x surface for 2h

of measurements. It is obvious that within the same measuring time interval, the conductance of the unmodified chip increases from 10 nS to around 40 nS, while that of the modified chip maintains stable conductance (≈12 nS). Figure5.3e shows a two-hour experiment variation in the distribution of ΔG in 1M KCl for all the devices. Occasional decrease of conductance is possible because of nanopore clogging that is common for 2D material nanopores, which can be caused by nanobubbles, hydrocarbons, and other impurities in the buffer solution.[44] In our experience with MoS_2 nanopores, generally such kind of clogging can be unclogged by applying an opposite voltage bias10 or re-flushing with a degassed and filtered salt solution.

The improvement in the stability after a surface modification indicates that 2D material-substrate interaction is of critical importance. Due to the enhanced van der Waals force between the hydrophobic MoS_2 layer and the HMDS-modified substrate, we observe a prolonged lifetime of the MoS_2 film on nanopore devices. Figure5.3f shows a TEM image of a device with an intact film of a monolayer MoS_2, before and after the experiment. The cleanliness and image of the nanopore are shown in FigureS5.8. For the MoS_2/HMDS/SiN_x device, the MoS_2 layer was intact as shown with arrows on the same area (Fig.5.3f). The MoS_2/HMDS/SiN_x interaction-related stability performance emphasizes the detachment of MoS_2 from the substrate is a major factor that causes device failure. Therefore surface modification strategies like HMDS-coating reinforces 2D layer interaction with the substrate and high membrane stability.

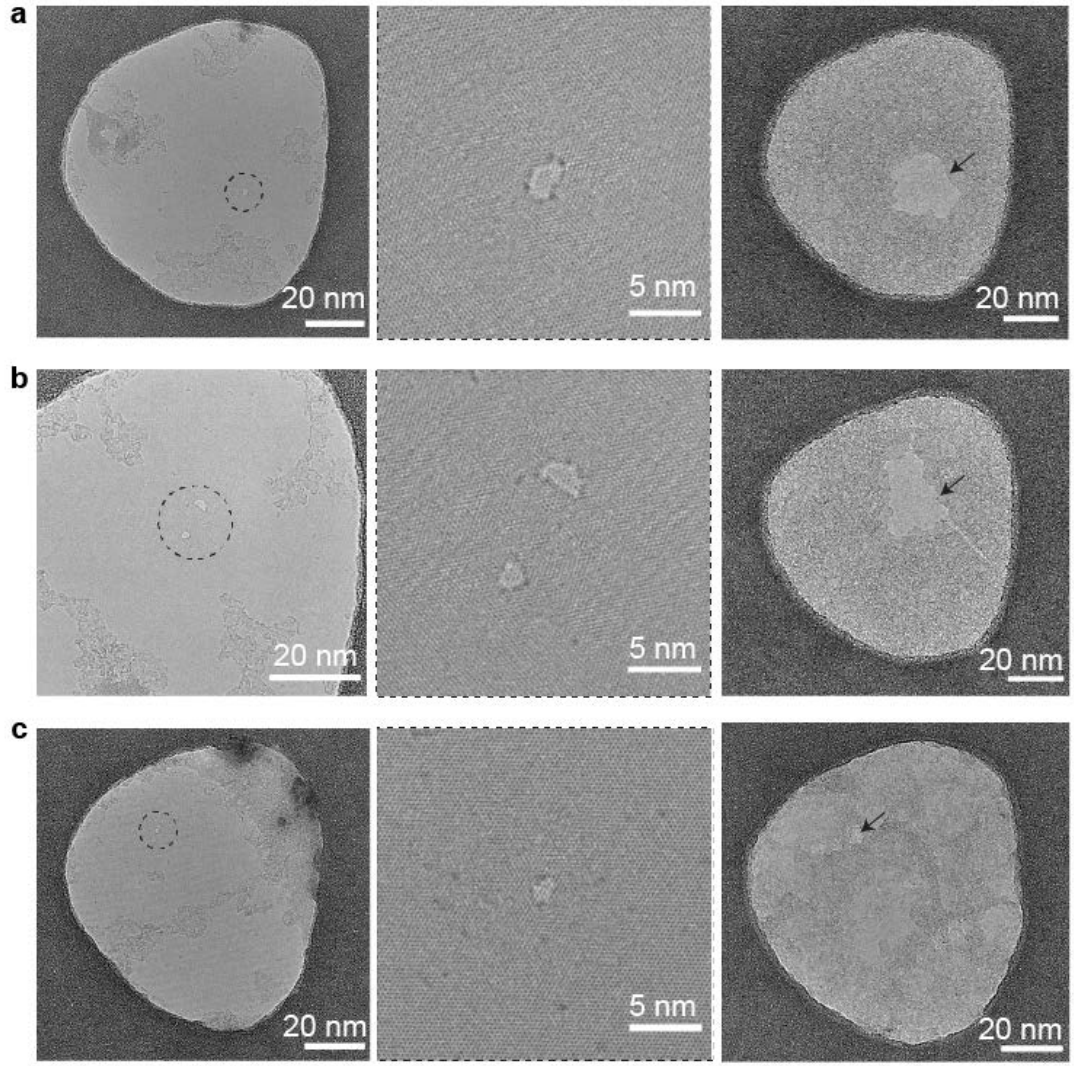

Figure 5.5: Bright-field TEM images of monolayer MoS_2 nanopores (single pore or double pores) drilled using TEM. The pores were incubated in 1M KCl aqueous buffer (10 mM TE-buffer, pH = 7.5) for 12 h at room temperature. The dissolved oxygen concentration was measured at ≈8 mg L^{-1} in panels (a-b) and maintained at 1 mg L^{-1} in panel (c). The dotted circles show the pore area and arrows point towards the same enlarged pore area.

5.3.4 Oxidation of MoS_2 and nanopore enlargement in aqueous solution

The aging of atomically thin materials due to oxidation is a major challenge in the field of 2D layered materials.[78, 183] Oxidation degrades the electronic and chemical properties of 2D TMDs and limits their application. It has been observed that in ambient conditions, the oxidation process of MoS_2 can start from the defects, edge planes, and grain boundaries resulting in the etching of the monolayer.[183] The oxidation process can occur by a thermodynamically more favorable reaction where the O-atom first adsorbs onto a S-atom from the

MoS_2 basal plane followed by a substitution reaction to form a Mo-O bond.[77] In comparison to the so-called 'air-sensitive' 2D materials,[179] monolayer MoS_2 is generally considered to be relatively stable as the basal plane faces a high energy barrier for oxygen molecules to diffuse in ambient conditions.[77] The high energy barrier (≈1.59 eV) protects the basal plane from molecular adsorption and substitution of S-atoms by O-atoms in pristine MoS_2. However, the barrier decreases to ≈0.8 eV in the presence of reactive sites such as vacancies or other defects.[77] Since the initial number of defects in the pristine MoS_2 can influence the rate of oxidation and degradation, we first set out to quantify pristine defects in our samples. We study 2D material quality both qualitatively and quantitatively in terms of the number of defects in the pristine monolayer MoS_2 (both monocrystalline or large-area grown MoS_2) used throughout the study.

Figure 5.4a shows the quantification of the defects of MoS_2 used for nanopore experiments. Detailed analysis of initial defect density calculation and quantification of defects in MOCVD large-area MoS_2 is shown in Figure S5.9 and Figure S5.10. We compare the sulfur defect concentration in pristine MoS_2 with the new defects introduced by incubation in an aqueous ionic solution (non-degassed 1M KCl, ≈12 h). Aberration-corrected TEM (Figure 5.4a, left panel) shows a representative TEM image of the same MoS_2 sample before and after an aqueous treatment (12 h). The total sulfur defect vacancies (Vs + Vs2) is estimated from ≈3500 nm^2 suspended area of monolayer MoS_2 either in pristine form or post incubation in aqueous solution. The sulfur defect concentration increased from 1.2 ± 0.3 x 10^{13} defects cm^{-2} to 1.9 ± 0.4 x 10^{13} defects cm^{-2} after incubation in aqueous solution with dissolved O_2 level (8 mg $L^{-}1$) (Figure 5.4b).

The dissolved oxygen in water plays an important role in the defect formation (0.7 x 10^{13} defects cm^{-2}) and could thereby influence the stability of the 2D MoS_2 in an aqueous environment.[78, 178] We study the accelerated oxidation process using photoluminescence spectroscopy (PL) on monolayer MoS_2. The MOCVD-grown MoS_2 was transferred on a clean glass substrate and the PL spectrum of MoS_2 is recorded in an aqueous solution. Figure 5.4c shows the changes in the PL spectrum of MoS_2 in water under laser excitation. After 4 min of laser illumination, the spectral peak intensity increases by more than 2 folds, and the photon energy blue-shifts by ≈35 meV. Such a spectral shift is corresponding to the transition from charged exciton emission to exciton emission that is caused by a reduction of free electrons in n-type MoS_2.[184] We suspect that the dissolved oxygen molecules in water (8 mg L^{-1}) react with MoS_2 under laser illumination as oxygen is an electron-withdrawing species. After the initial 4 min, a decay of PL intensity and spectral red-shift of MoS_2 is observed in the presence of dissolved oxygen (Fig. 5.4c).

A plausible cause could be a local material dissolution as similar spectral behaviors and mechanisms have been reported on MoS_2 exposed to air.[185, 186] To verify our hypothesis, we reduced the dissolved oxygen level in the water below 1 mg L^{-1} by argon gas purging and then performed the spectral measurement on MoS_2 in a sealed chamber. As can be seen in Figure 5.4d, the PL spectrum of MoS_2 is stable in both intensity and energy throughout

the measurement, implying neither photo-induced chemical reaction nor plausible material dissolution. This is in stark contrast with the spectral shift of MoS_2 in the presence of dissolved oxygen (8 mg L^{-1}). Figure 5.4e-f shows a schematic representation of single and double sulfur vacancies, and schematic representation of oxidation-induced etching of monolayer MoS_2, respectively.

Further, we study the oxidation-related stability and the dissolution by reducing the amount of oxidizing agents in the aqueous buffer. As shown in Figure 5.5, nanopores (single or double pores) in monolayer MoS_2 are fabricated in TEM, and the pore expansion is studied during incubation in an aqueous solution without applying the voltage. As seen in 5.5a,b, the nanopores enlarged in size when incubated in an air-saturated non-degassed 1M KCl TE-buffer (pH ≈7.5) at ambient temperature for 12 h. Whereas the single nanopore incubated at in low O_2-concentration (1 mg L^{-1}) buffer showed a slight increase in pore size (Fig. 5.5c). More statistics and images are shown in Figure S5.11.

Previously, bulk layered MoS_2 ($\approx 2\mu$m particles) has shown high stability to oxidation in an air-saturated aqueous solution.[77, 181, 187] While in 2D MoS_2 monolayers are more prone to oxidative degradation in an aqueous solution, especially at the nanopore sites as seen in Figure 5.5. Single nanopore from the same device grew in the air-saturated buffer and the double nanopores grew and merged to form a single larger nanopore (Fig. 5.5a,b). The aqueous oxidation of MoS_2 is typically caused by the presence of oxygen and hydroxyl ions in the aqueous solution that can etch MoS_2 via dissolution products such as MoO_3 and MoO_4^{2-} ions.[57, 77, 78, 186]

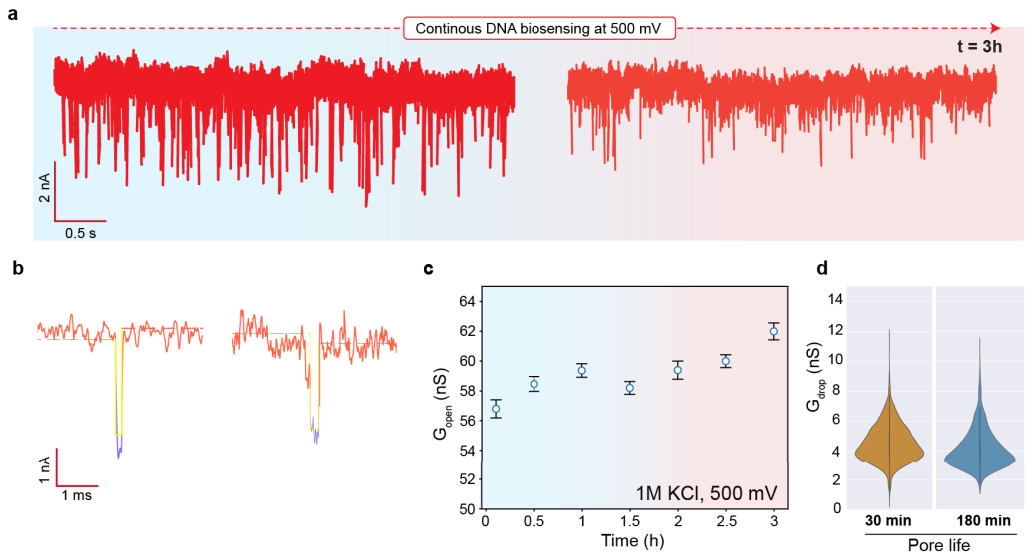

Figure 5.6: Long-term DNA sensing using a monolayer MoS_2 nanopore (d = 6.5 nm in 1 M KCl, pH 8). The flow cell is sealed during the experiment and the O_2-concentration in the buffer is less than 1 mg L^{-1}. (a) Translocation traces of 1kbp DNA at the beginning (number of events = 1832) and the end of the measurement (number of events = 1195) at 500 mV. (b) Example events from the traces in (a). The dotted line is a mean fit to open pore current and the yellow fit represents CUSUM-fit to the event. (c) Changes in the open pore conductance *(Gopen)* across different time points over the course of measurement. (d) Violin plots showing the distribution of conductance drop due to DNA molecules translocating through the pore at different time points.

5.3.5 Long term DNA sensing

With enhanced 2D membrane stability and by reducing aqueous oxidation of the monolayer MoS_2, we then set out to measure the stability of the nanopore in combination with DNA sensing. Single-molecule measurements using a molecular ruler, such as DNA, can be used as a tool to study changes in the nanopore conductance.[48, 52] Under an influence of an electric field, negatively charged DNA can be driven towards the pore and a successful passage through the pore generates a resistive pulse called an 'event'. Statistical measurements of conductance drop (*Gdrop*) of such events can indicate the membrane thickness as well as the size of the nanopore. Since for our study, we employ nanopore in a monolayer MoS_2, by considering a constant thickness, such statistical analysis of events can help us to probe the changes in the nanopore size throughout the experiment. This analysis is particularly useful in cases where the size of nanopore is comparable to the size of translocating molecule. The changes in *Gdrop* over time can indicate if the nanopore got enlarged, or also new nanopores have been created.

We perform continuous monitoring of the nanopore size using DNA translocations in monolayer MoS_2 nanopore fabricated using TEM drilling at 80 kV.[44] The TEM image of and the I-V

characteristics of the nanopore are shown in Figure S5.12. The flowcell was completely sealed and the 1 kbp double-stranded DNA is translocated on the same pore for >3 h at 500 mV in low dissolved O_2 concentration (<1 mg/L) buffer. The translocation events were analyzed using Open Nanopore (Python Package)[44] and events were further fitted using the cumulative sums (CUSUM) algorithm.[113] Only the CUSUM-fitted events were further used for analysis and plotting that represent individual translocations of DNA molecules.

In Figure 5.6a, a typical raw trace of a double-stranded DNA (1 kbp) translocation events from a MoS_2 nanopore of ≈6.5 nm diameter is estimated from the open pore current. The calculated open-pore conductance (*Gopen*) at the beginning of the measurement was ≈58 nS which increased to the *Gopen* of ≈62 nS towards the end of measurement at an expansion rate of 0.03 nS per min. Since monolayer MoS_2 was transferred for the experiment, we consider the thickness of the MoS_2 monolayer membrane as L = 1 nm (including the hydrodynamic layer) for our analysis. Figure 5.6b shows a single file translocation event from the respective traces. Figure 5.6c shows the mean *Gopen* from the nanopore over the course of the analysis. We observe that the *Gopen* of the nanopore grew by 4 nS (≈7%) over 3 h of measurement. The conductance blockades for the DNA (2.2 nm) are then extracted from each of these events and represented as conductance drops (Δ *Gdrop*). The Δ *Gdrop* was obtained from the same nanopore for traces at the beginning (t ≈ 0-30 min) and the end (t ≈ 150-180 min) of the measurement time. The translocation events (at least number of events = 1000) from these representative time frames are chosen to distinguish the nanopore size based on the Δ *Gdrop* obtained due to possible enlargement of the same nanopore. As shown in the violin plots in Figure 5.6d, the experimental value of the Δ *Gdrop* from an unfolded DNA is Δ *Gdrop* ≈3.9 nS (number of events = 1832 events) and Δ *Gdrop* of ≈3.5 nS (number of events = 1195 events) at 30 min and 180 min, respectively. These experimental values are closer to the expected Δ *Gdrop* values of ≈4.5 nS and ≈4.3 nS, respectively for a membrane thickness (L = 1 nm).[107] Previously, Larkin et al.[188] demonstrated the stability of nanopores in thin HfO_2 (2-7 nm) for continuous single-stranded DNA measurements. They also observed a *Gopen*<10% change in the conductance of a 1.4 nm diameter in HfO_2 at 350 mV. Indeed, despite being only three atoms thin, we observe similar stability in monolayer MoS_2 nanopore (≈6.5 nm) at 500 mV enabling long-term measurements. Long-term stability also emphasizes the absence of an opening of additional pores on the free-standing area, and good quality of our MOCVD-grown 2D material (fewer defects).[76] Although the latter is highly dependent on the quality of the 2D material and experimental condition. Additionally, as discussed above, a stable open pore current highlights the strong interaction of monolayer MoS_2 with HMDS-modified substrate.

5.4 Conclusion

We have studied major mechanisms of nanopore instability in 2D MoS_2 nanopores and demonstrated methods to avert them. We propose a device fabrication protocol that enhances stability of the monolayer MoS_2 membranes in ionic aqueous solution by introducing a layer of HMDS on the SiN_x surface, which improved the adhesion of MoS_2 to the substrate.

Further, we study the chemical oxidation in monolayer MoS_2 using PL, and examine the 2D nanopore enlargement in ionic solutions. We demonstrate the nanopore growth can be minimized by reducing the oxygen level in the ionic buffer in standard nanopore experimental conditions. Finally, we show continuous DNA translocation measurements on the same pore for hours with high stability. The stability of atomically thin free-standing 2D nanopores in ionic solutions is currently a major hurdle in the development of 2D nanopore sensors. With proposed stabilization methods, 2D nanopores can be used as reusable sensors and pave the way toward high-throughput long-term biosensors.

5.5 Experimental section

5.5.1 Nanopore Wafer-scale Substrate fabrication

Double-side polished 100 mm (100) undoped Si-wafers (Active Business) were covered with 60 nm of SiO_2 and 20 nm low-stress SiN_x from both sides. Photolithography and dry etching were done to open apertures in the back side SiN_x layer for the following wet etching process required for SiN_x membrane formation on the front side. Front-side e-beam lithography (Raith EBPG5000+) and dry etching were performed to form 120 nm-diameter apertures in SiN_x membranes with the following parameters: 100 keV e-beam, polymethyl methacrylate (PMMA, molecular weight 495 K, 4% in anisole) as e-beam resist and CHF_3/O_2 gas mixture for dry etching. As a final step, acid piranha cleaning and 300°C baking were applied to achieve a clean surface of the target nanopore substrate prepared for the transfer of MoS_2.

5.5.2 MoS_2 growth and transfer

The triangular shape monolayer MoS_2 crystal was grown via metal-organic chemical vapor deposition (MOCVD) in a 2-inch quartz tube furnace. The c-plane sapphire was used as the growth substrate and pre-annealed at 1000°C for 2 h in the air to create atomically smooth step terraces.[96] In order to suppress nucleation and promote large-area crystal growth, sodium chloride (NaCl) solution was spin-coated on the substrate prior to the growth,[98] as well as the introduction of oxygen during the growth.[189] The two gas precursors, molybdenum hexacarbonyl ($Mo(CO)_6$) and hydrogen sulfide (H_2S), carried by Ar gas, were mixed in the furnace with a flow rate ratio of 1:6028. The reaction took place at 850°C under subatmospheric pressure (850 mbar) and lasted for 30 min. After the growth, the $Mo(CO)_6$ precursor was immediately closed, while the H_2S was continuously supplied during the whole cooling process to prevent the sulfur vacancy formation. The large-area, continuous MoS_2 films that were used for initial defect density calculation were synthesized using the MOCVD method described elsewhere.[42, 45] Transfer of monolayer MoS_2 was performed using the PMMA-assisted transfer method described before.[44]

5.5.3 Surface modification and characterization

The surface of the SiN_x substrate was modified following oxygen plasma treatment (Tergeo Plasma Cleaner, PIE Scientific) and a standard Bis(trimethylsilyl)amine ($[(CH_3)_3Si]_2NH$, HMDS) priming process (OPTIhot VB20 HMDS unit, ATMsse). The oxygen plasma treatment was done to improve the HMDS priming efficiency by introducing more hydroxyl groups (-OH) on the SiN_x surface, with the following parameters: 35 W RF Power, 50 mtorr vacuum state, with 5.0 sccm O_2 gas flow for 20s. The standard HMDS priming process started with 10 min dehydration at 135°C in a vacuum chamber to remove the moisture. After dehydration bake, the surface was then exposed to the vapor HMDS for 60s. A monolayer of HMDS will be deposited on the SiN_x surface after the -OH groups on the wafer surface reacted with amino groups (-NH) from HMDS, and the surface was therefore terminated with methyl groups ($-CH_3$), which makes it hydrophobic. After the HMDS vapor exposure, several pumping, and N2 purging cycles were followed to remove the residual HMDS atmosphere. After the process was complete, substrates were removed from the chamber and after cooling down to room temperature, they were stored in a vacuum before the transfer process.

The contact angles (CA) and surface free energies (SFE) were obtained through a multi-dosing and imaging system (DSA-30E, Krüss) before and after the HMDS surface modification process to demonstrate the effectiveness of the priming process. The measurements started by depositing a drop of liquid on the sample surface, and the computation of CA was done on the live image or a captured frame by sequentially determining the baseline, extracting the liquid profile, and then calculating the angle. Three different liquids were used for the measurements with recommended doses, including water (3 μL), diiodomethane (2 μL), and ethylene glycol (2.5 μL). The CA values usually refer to measurement results from only water. SFE was also calculated on the system based on the CA values of three kinds of liquid using the Extended Fowkes method.[182]

5.5.4 TEM characterization and quantification of defects

Aberration-corrected annular dark-field scanning transmission electron microscopy (ADF-STEM) imaging was performed using a double Cs corrected FEI Titan Themis TEM 60–300 kV, equipped with Schottky X-FEG electron source and a Wein-type monochromator. All STEM were acquired using 21.2 mrad probe convergence angle, 185 mm camera length with corresponding 49.5-198 mrad collection angle, beam current of ≈18-20 pA, and 8 µs dwell time with 512×512 pixels for the faster scans. For the image series, all the images were aligned using Image J.[165] Intrinsic S defect concentrations were extracted from the linear fit extrapolation from defect concentration with respect to the accumulated e-beam dose rate.[190] To calculate the S defect concentrations in the histogram, different pristine regions were imaged and defects were calculated manually.

5.5.5 PL characterization

The PL spectrum of MoS_2 in water was measured on a custom-built confocal microscope. Briefly, the monolayer MoS_2 flakes grown by MOCVD in the batch as used in nanopore experiments were transferred on a coverslip.[44] The coverslip was then mounted on an air-tight fluidic chamber filled with Ultrapure MilliQ water with or without Ar gas purging. The fluidic chamber was then placed on top of the confocal microscope. A 561 nm laser (PicoQuant LDH-560) was focused on the MoS_2 surface through a water-immersion lens (Olympus CFI Plan Apo, IR 60xc WI) with a power density of 3×10^5 W/cm^2. The spectrum of MoS_2 was then measured by a fiber-coupled spectrometer (QE Pro from Ocean Optics). The dissolved oxygen level in water was measured in the fluidic chamber before and after spectrum measurement by a dissolved oxygen meter (Mettler Toledo InLab® OptiOx, part no. 51344621). All oxygen measurements were performed at ambient temperature.

5.5.6 DNA translocation and analysis

The MoS_2 nanopore chip was assembled onto a customized PMMA flowcell and details of which can be found here.[44] For pore size measurement and DNA translocations are performed in degassed and filtered 1M KCl in TE buffer (pH ≈8). Blank ionic traces were measured before checking artifacts or contaminants in the flowcell or from the substrate and the nanopore size using the conductance model.[107] We then add NoLimits 1 kbp DNA Fragment (50 nM, Thermo Fisher Scientific, USA) to the cis-compartment, and the flowcell is sealed. The DNA translocations are then recorded at a bias voltage of 500 mV. We exchange with fresh degassed buffer to avoid any salt evaporation effects on the open pore current. The oxygen concentration of the buffer was always monitored using a dissolved oxygen meter and reduced to less than 1 mg L^{-1}. The data acquisition was performed using an Axopatch 200B (Axon Instruments, USA) low-pass filtered at 10 kHz with a 100 kHz sampling rate. The event detection and fitting were performed using the Python-based OpenNanopore10 (https://www.epfl.ch/labs/lben/opennanopore-python).

5.6 Supplementary Data for Chapter 5

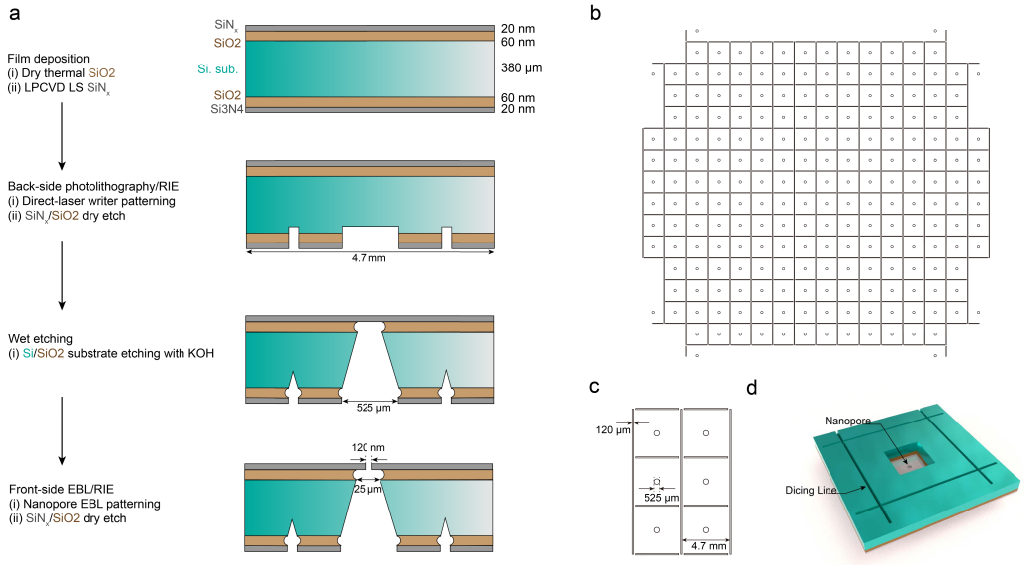

Figure S5.1: The fabrication process flow of 4-inch wafer-scale silicon nitride nanopore chips fabrication. (a) Detailed fabrication process flow of silicon nitride solid-state nanopore. (b) The pattern of a 4-inch wafer includes apertures for the SiN_x membrane and dicing line. (c) The detailed design of the wafer backside. (d) The schematic image of the solid-state nanopore from the backside.

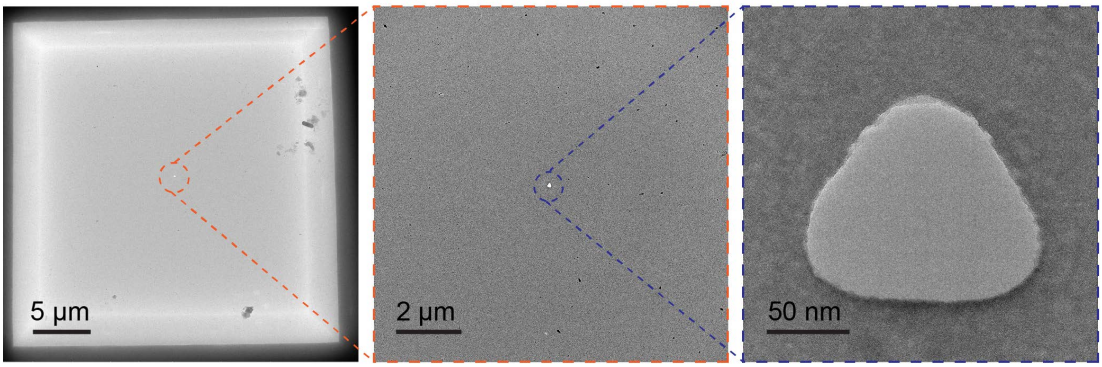

Figure S5.2: Bright-field TEM image of SiN_x membrane with an aperture (dotted circles) defined by e-beam lithography.[44]

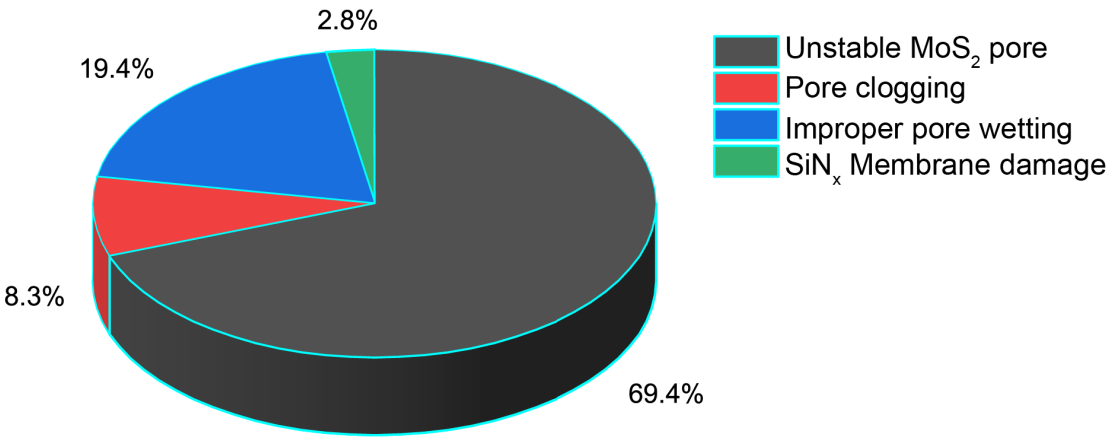

Figure S5.3: Challenges related to the MoS_2 nanopore devices (n =36) in aqueous ionic solution. The unstable pore is due to the delamination or 2D MoS_2 pore enlargement in the ionic solution.

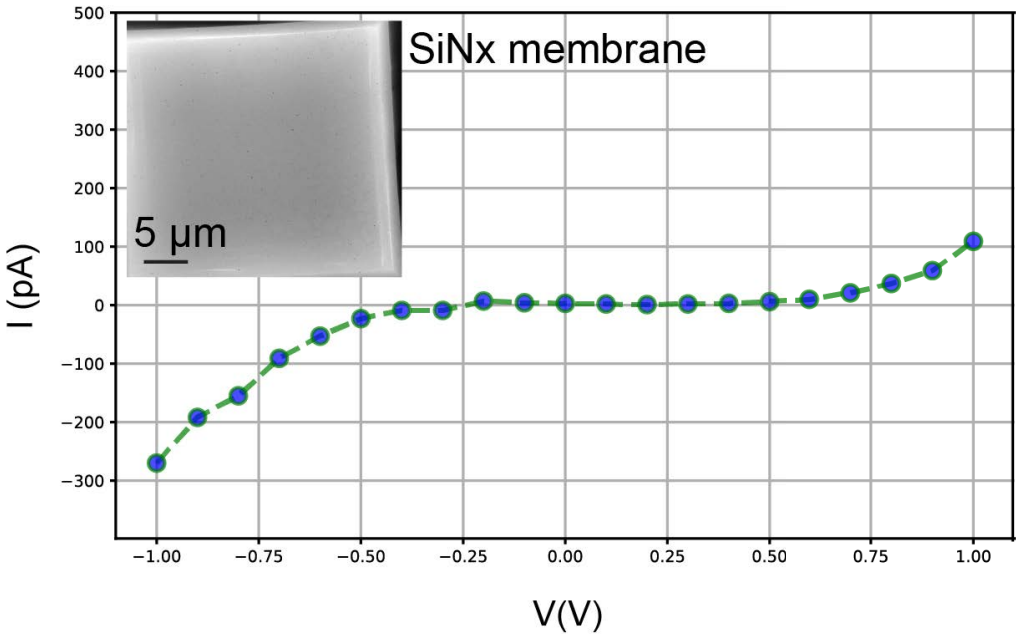

Figure S5.4: I-V characteristic of a SiN_x membrane (20 nm thin) in 1M KCl. The bare SiN_x membrane shows a low leakage of <300 pS at an applied bias voltage of 1V. The current was measured after 50s for each applied voltage (-1 V to 1 V) to reduce the capacitive charging effects of the membrane.

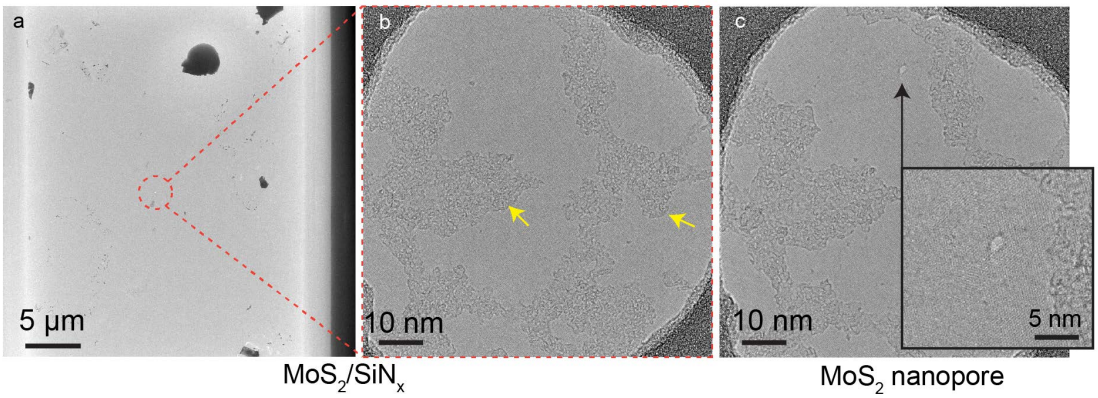

Figure S5.5: Bright-field TEM image of Device 2 (Fig. 2 in Main Text), imaged and drilled at 80 keV. (a) Monolayer MoS_2 is transferred on the SiN_x membrane. The aperture is marked with a dotted circle and a high-resolution image of free-standing MoS_2 is shown in (b). The residues are hydrocarbons and PMMA polymer residues originating from MoS_2 transfer (shown by yellow arrows). (c) A single nanopore is created using a focused ebeam drilled on a clean part of the membrane. Inset, zoomed image of the single nanopore (≈2.5 nm).

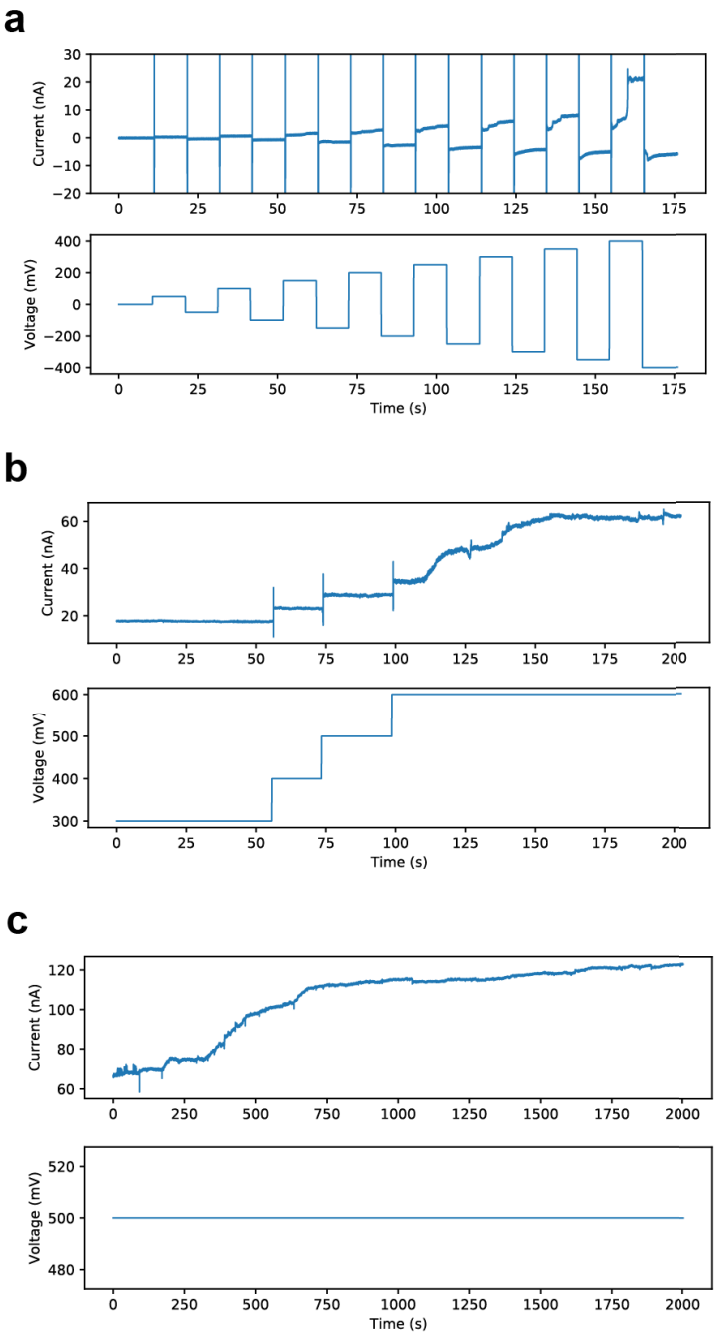

Figure S5.6: Examples of unstable ionic current from MoS_2 nanopore devices. The ionic current traces were measured in (a) 400 mM KCl (Device 1, in the Main Text), (b) 1M KCl, and (c) 3M KCl in Tris-EDTA buffer (pH 7).

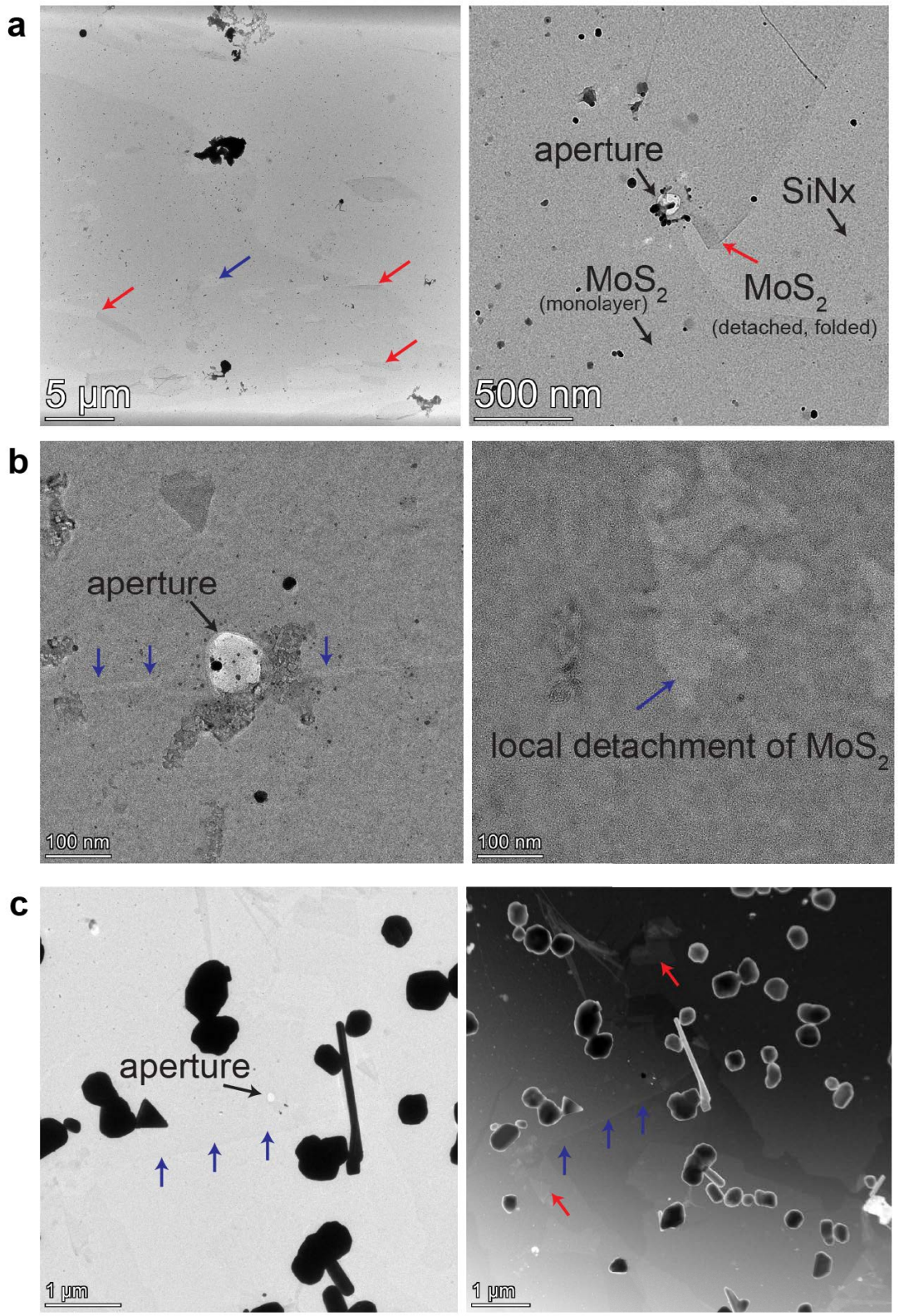

Figure S5.7: TEM images showing local detachment of monolayer MoS_2 post-experiment in ionic aqueous solution from three different devices (a-c). The images were taken in bright-field TEM mode while STEM mode helps identifying the detached monolayers in some cases as shown in second panel in (c). The SiN_x aperture is shown with black arrows, detachment/cracks with blue arrows, and folding of the monolayer is shown with red arrows.

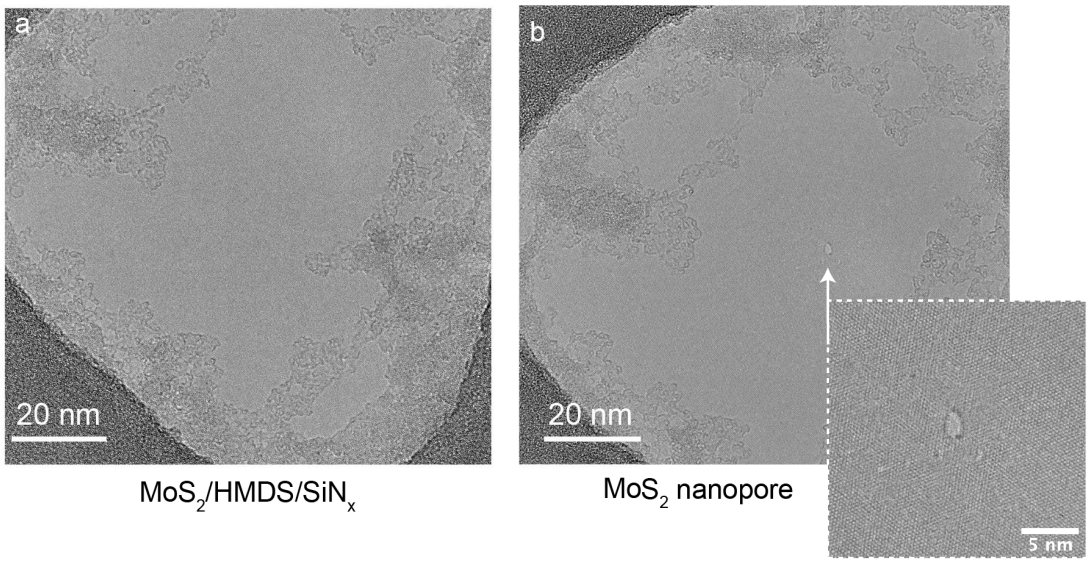

Figure S5.8: Bright-field TEM image of MoS_2/HMDS/SiN_x from Fig.5.3f. (a) TEM image of the free-standing MoS_2 membrane after transfer. The device level of cleanliness was comparable to devices without HMDS treatment. Also, during imaging we have not observed any e-beam induced deposition that typically occurs due to contaminant. (b) After drilling a nanopore in monolayer MoS_2. Inset, zoomed image of ≈3 nm MoS_2 nanopore.

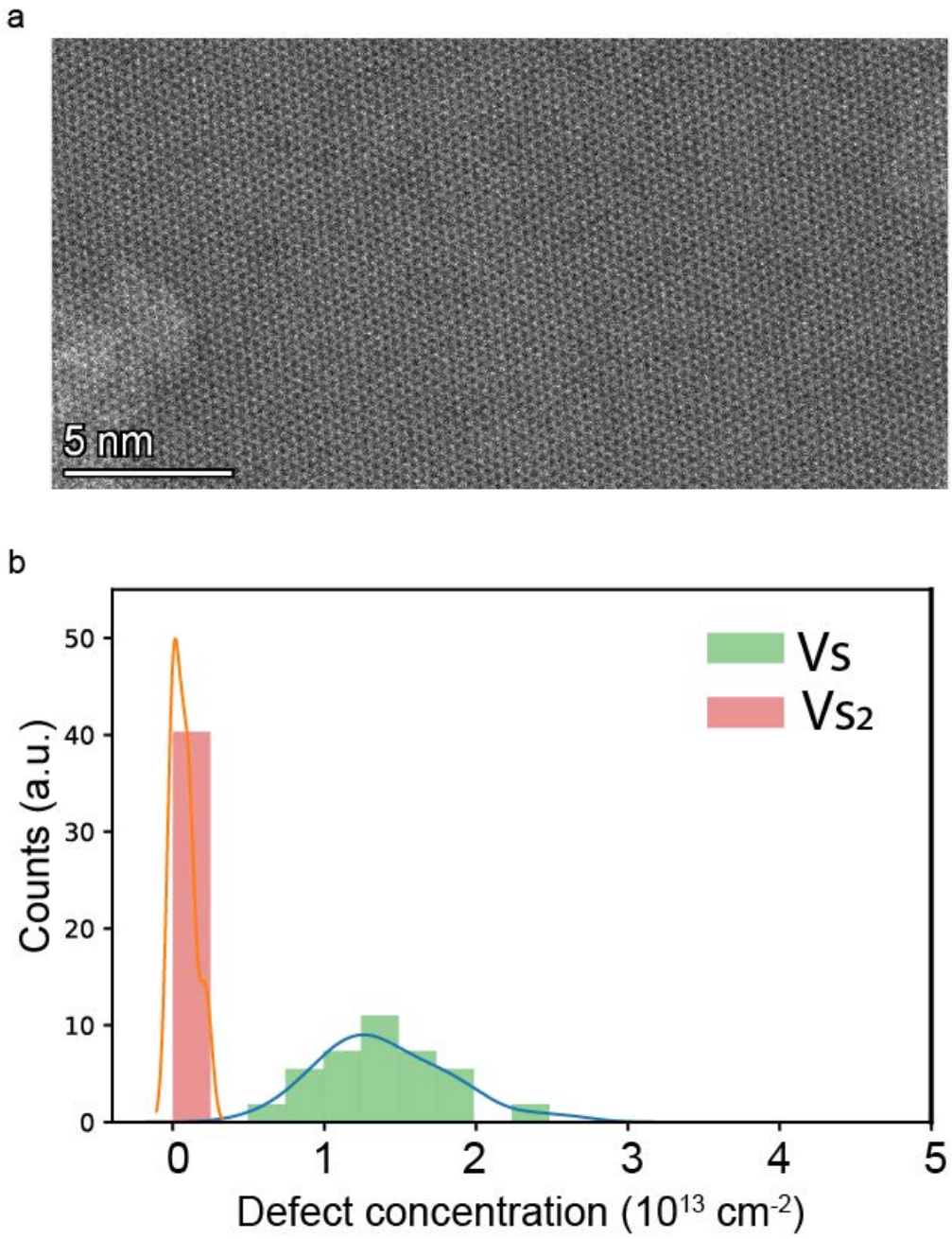

Figure S5.9: Inherent S defect density calculations. (a) Aberration-corrected ADF-STEM image of monolayer MOCVD grown large-area MoS_2 layer. (b) Histogram and kernel density estimation analysis shows the distribution of Vs and Vs2 defects.

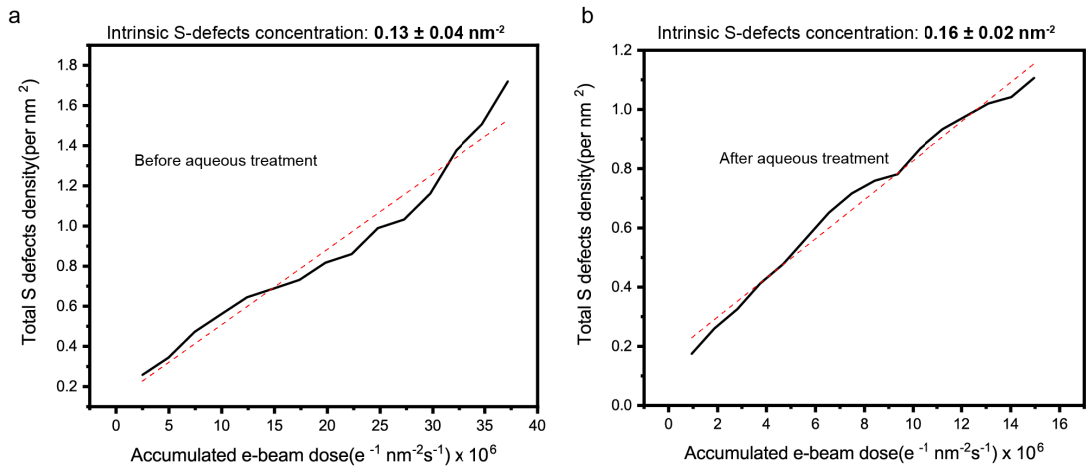

Figure S5.10: Initial S-defect density calculation for the monolayer MoS_2 sample. The measured defect densities (due to beam damage) are shown in black lines for different accumulated doses from an image series. A linear fit (dotted line) is used to extrapolate the total number of intrinsic S defects in the MoS_2 before the imaging. The total sulfur defects estimated are ≈1.3 x 10^{13} defects cm^{-2} (a) and ≈1.6 x 10^{13} defects cm^{-2} (b).

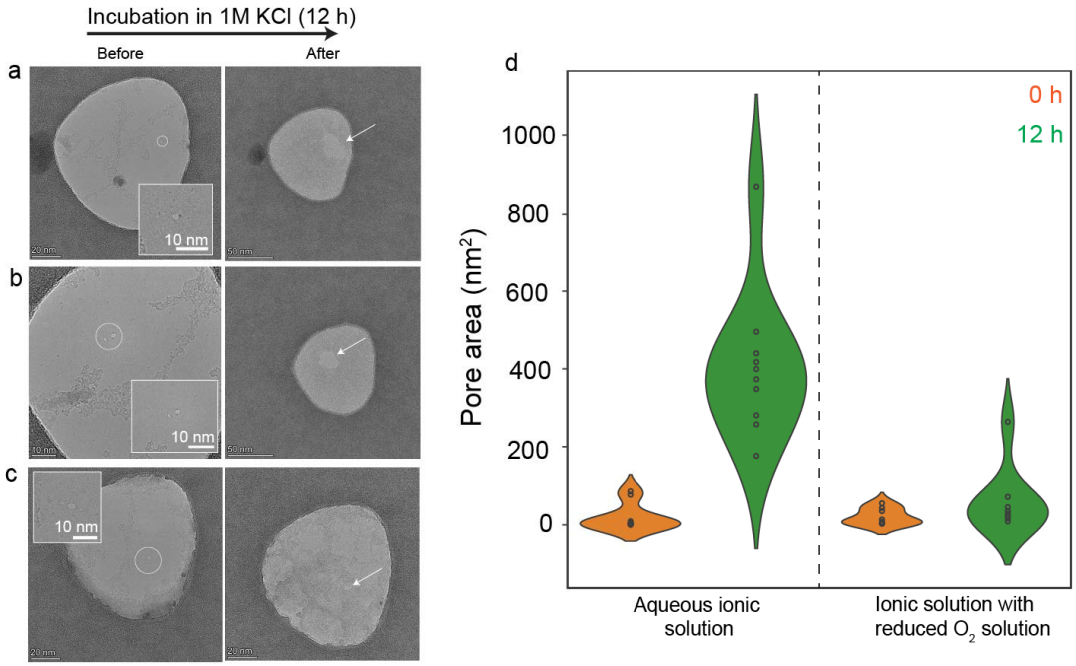

Figure S5.11: TEM images of nanopores before and after incubation in 1M KCl (12 h). (a,b) MoS_2 pores were incubated in a non-degassed buffer with a dissolved O_2 concentration of $\approx$ 8 mg L^{-1} and (c) in a reduced dissolved O_2 buffer (<1 mg L^{-1}). (d) Violin plots showing the distribution of calculated pore area for different pores before and after expansion in non-degassed (n = 10) and reduced O_2 buffer solution (n = 8). The open-pore area was calculated using Image J.

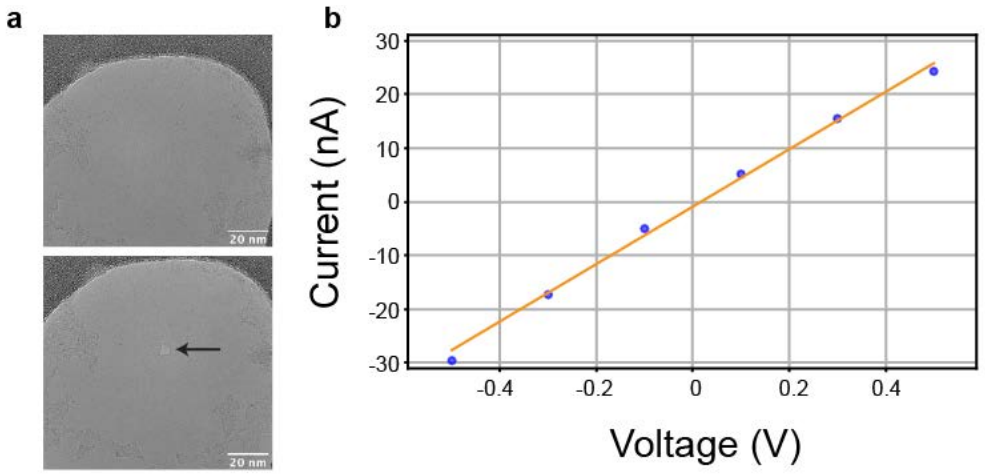

Figure S5.12: Device characteristics. (a) Bright-field TEM image of the device used in Figure 5.6 in the Main text for DNA translocations. The TEM images show free-standing clean monolayer MoS_2 on HMDS/SiN_x substrate before and after drilling a ≈6 nm pore using a focused e-beam in TEM at 80 kV. (b) I-V characteristics of the pore (-500 mV to +500 mV) with an open-pore conductance of ≈55 nS measured in 1M KCl Tris-EDTA buffer with reduced O_2 concentration (maintained below 1 mg/L).

6 Conclusions and Outlook

In conclusion to my thesis, I integrate my all-around efforts towards increasing the scalability efficiency and addressing practical bottlenecks of MoS_2 membranes and nanopores. Throughout my thesis, I worked on ways to improve the transfer quality of monolayer MoS_2 as cleanest as possible. In the latter half of my research work, I discovered that 2D nanopore membranes are vulnerable to delamination in an aqueous solution and that oxygen-rich aqueous environment often leads to unstable pore enlargement. Consequently, I demonstrate methods to address these undesirable effects that improve the durability of our devices in standard working conditions of a nanopore sensor.

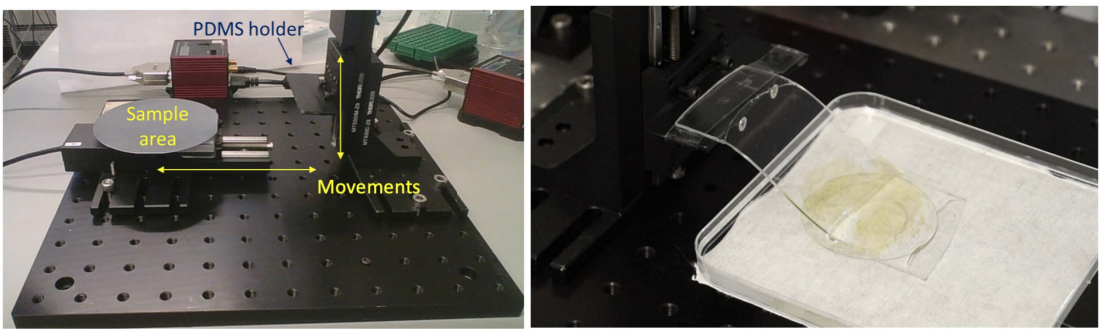

Figure 6.1: Wafer-scale transfer setup. Impression of wafer-scale transfer setup (left) and transfer in action (right) that I built for the wafer-scale transfer process. The setup is configured with LabVIEW and capable of transferring large-area MOCVD-grown MoS_2 wafers.

In chapter 3, I demonstrate two of the developed chip-scale transfer methods in the lab – PDMS polymer-assisted technique compatible with CVD-grown 2D materials and polymer-free transfer approach with just water as a medium. The technique works well with monolayer to even multi-layers. Our polymer-free transfer is perhaps the only technique where the lower face of the MoS_2 is exposed on the final device. Using this technique I also concluded that hydrocarbons that are persistent and unavoidable (with or without polymer support). They demand a major investigation since at the nanometer scale these are limiting factors

for device-to-device variation at least in nanofluidics. Nevertheless, our chip-scale transfer techniques can be useful across other materials science disciplines such as flexible substrates, and not merely restricted to flat surfaces or nanopores.

In chapter 4, after chip-scale methods, I was lucky that my colleague Dr. Macha, succeeded to achieve large-area growth of monolayer MoS_2 on 3-inch wafers I adapted our transfer technique to a wafer-scale approach using PDMS to batch fabricate nanopore devices. Using a controlled step-motor(Fig. 6.1) , I could show the one-step transfer of monolayer MoS_2 on a nanopore substrate with 128 devices with high transfer efficiency (>70%). Of course, in future experiments one could increase the density of nanopore chips on a larger scale. Furthermore, with a chip-scale stamp technique developed as shown in Chapter 3, one could also increase this efficiency in non-transferred areas (or voids), thus complementing the two techniques.

Moving on to the next issue I focused on, having survived the Covid-19 pandemic was the instability of the MoS_2 nanopores. In Chapter 5, I investigate the possible mechanisms that could cause the failure of our nanopore devices and low device yield (often < 10 %). Thanks to the CIME TEM facility at EPFL, I could always investigate and discover that the membrane (at a few hundred nanometer-scale) would delaminate in the aqueous salt solution which is an essential part of nanopore technology. This was a major reason that would increase the conductance of our nanopores more than expected. Further, I also learned that MoS_2 oxidizes over time and can lead to nanopore enlargement, although this was a slower process than the delamination effect.

Having investigated major reasons for the lack of nanopore stability, I address the delamination issue by chemically the SiN_x substrate with HMDS coating prior to transferring MoS_2 which strengthens MoS_2-SiN_x interfacial interaction. By comparing ionic current as well as TEM from the same devices, I found that the MoS_2 membrane remains stable for longer period (>5 h). I also studied the nanopore enlargement that is dependent on the dissolved oxygen concentration in an aqueous solution and can be considerably reduced in low dissolved oxygen in the solution. Owing to highly stable nanopore devices, we were able to demonstrate continuous DNA nanopore sensing at a high voltage on the same pore, which was not possible before on 2D nanopores. Stable and durable nanopore devices will serve as biophysical tools to study single biomolecules for a longer period and collect larger datasets.

In future, more specific chemically modified substrates with MoS_2 could serve better system for 2D membrane stabilized devices. Such stabilized nanopores could serve for long-term study and mimic ratchet system to control the residence time of DNA inside the nanopore as shown in Figure 6.2.

With stable nanopores, in future directions MoS_2 membrane being quite versatile and can be integrated with as a hybrid nanopore (for instance MspA in MoS_2 membrane) and can ratcheting studies can be performed for example, using helicase, Figure 6.3. Often, solid-state nanopores lack reproducibility in terms of size and geometry. Compared to biological nanopores the solid-state nanopores are more robust. Hybrid nanopore systems can offer

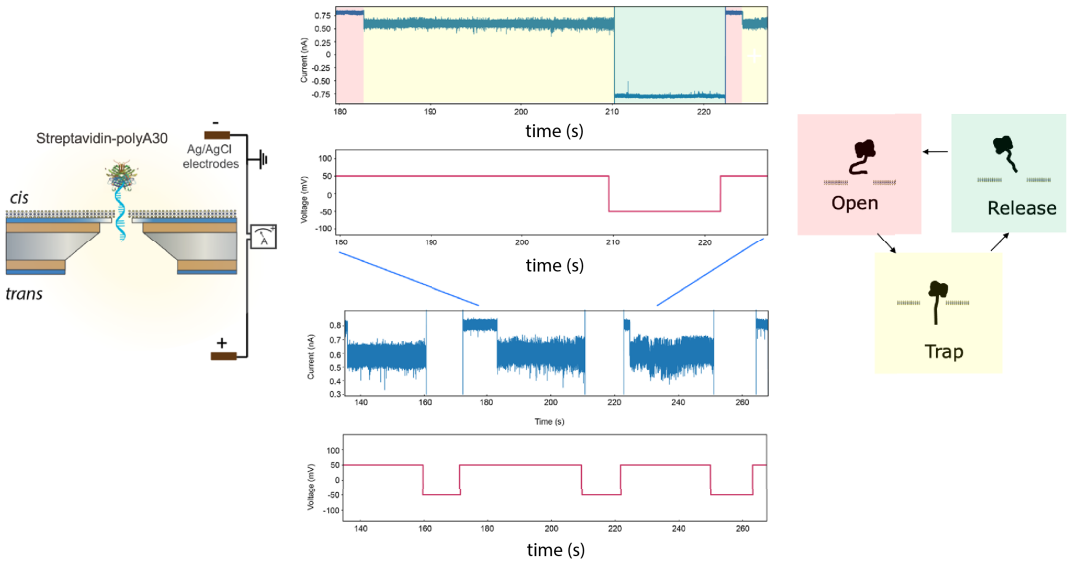

Figure 6.2: Schematic (left) showing MoS_2 nanopore for trapping ssDNA (poly-A30 homopolymer)] using streptavidin. An approach toward increasing the molecule resident time on the pore by docking and controlling the translocation of the DNA molecule. An example of docking (center) where a ssDNA on a MoS_2 nanopore and can be trapped/untrapped using a user-defined voltage control.

durability of solid-state nanopores and precise protein structure of a biological nanopore. 2D MoS_2 nanopores could aid as a support for biological proteins and address issues such as size and geometric specificity. Further, the biological proteins in such hybrid system can offer low noise platform for biosensing. Another such possibility is 2D MoS_2 membrane on a nanocapillary using our direct transfer approach. Such "all solid state" hybrid nanopore systems can be beneficial to study in terms low capacitance noise of glass capillaries and high sensitivity of atomically thin MoS_2 membranes.

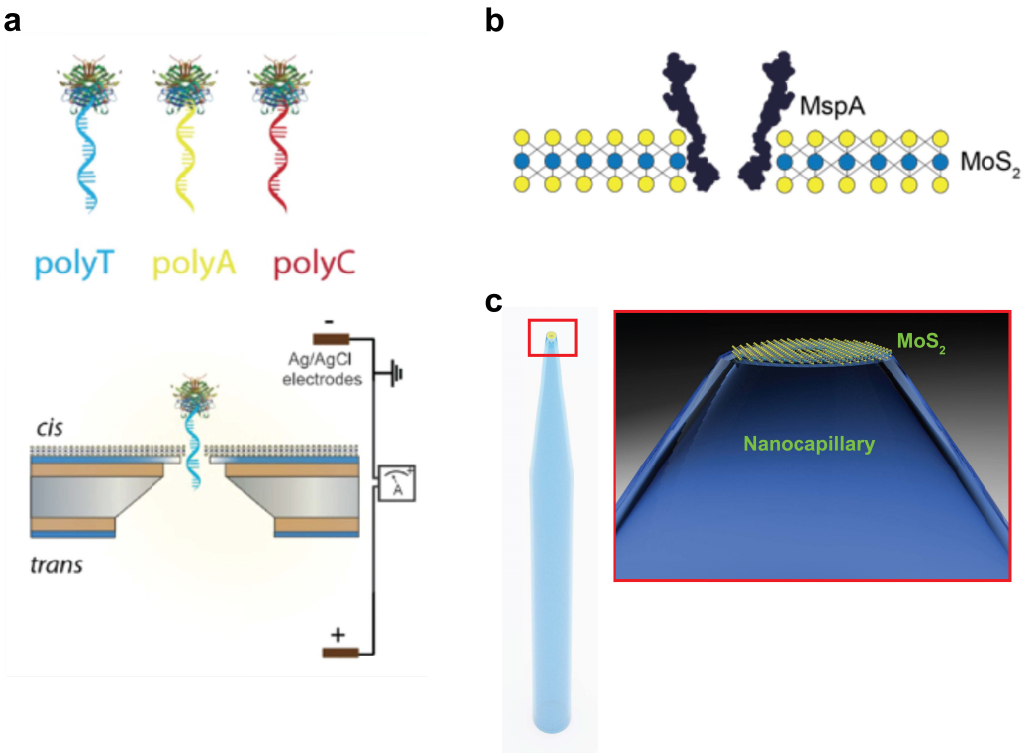

Figure 6.3: Biological and other 2D/solid-state nanopore hybrid system. (a) Trapping/release of streptavidin-tagged homopolymer DNA that can be used for enzyme-ratchet experiments on MoS_2. (b) Schematic of an MspA pore insertion in 2D MoS_2 membrane. (c) 2D nanopore on a glass nanocapillary hybrid system.

A Appendix

A.1 Materials

Following is a list of materials used for MoS_2 nanopore substrate fabrication, material transfer and nanopore measurements. The detailed list of protocols is given in Section A.2.

This section is based on the following publication:

> Michael Graf[1], Martina Lihter[1], **Mukeshchand Thakur**[1], Vasileia Georgiou, Juraj Topolancik, B. Robert Ilic, Ke Liu, Jiandong Feng, Yann Astier and Aleksandra Radenovic. Fabrication and Practical Applications of Molybdenum Disulfide Nanopores. Nature Protocols, 14 (2019).

M.G., M.L., and M.T. contributed equally.[1] K.L. and J.F. performed initial work on device fabrication, MoS_2 transfer and pore characterization. M.G., J.T., V.G., and B.R.I developed the substrate fabrication process, V.G. fabricated the substrates. Y.A. supervised the substrate fabrication process. J.F., K.L., and A.R. developed the ECR pore drilling method. M.G. built the transfer microscope set-up, M.G. and M.L. developed PMMA transfer method and optimized MoS_2 cleaning procedure, M.T. developed PDMS transfer method, M.L. and M.G. performed TEM characterization, M.L. and K.L. optimized the TEM pore drilling method. M.G. developed the translocation data acquisition and analysis software. M.G., M.L., and M.T. fabricated the devices. M.G. performed the translocation experiments presented. M.G., M.L., M.T., J.T., and A.R. wrote the manuscript.

A.1.1 List of Chemicals and Materials

- 4-inch double-side polished (DSP) silicon substrates (Doping: N-Type, Orientation: <100>, Resistivity: 1Ωcm - 20 Ωcm, Thickness: 400 ± 10 μm) (Nova Electronic Materials).

- PELCO ESD Safe SV Carbon Wafer Tweezers (Ted Pella, cat. no. 5048-SV).
- SPR 220 3.0 photoresist (MicroChem)AZ 300 MIF Developer (EMD Performance Materials Corp). ⚠ *It is a potential irritant and corrosive to metals. Wear proper eye protection and gloves while handling. It should be discarded in an appropriate waste disposal container.*
- ZEP 520A electron beam photoresist (ZEON). ⚠ *It is highly flammable liquid. Keep away from heat and static discharge. While handling, wear proper eye and face protection.*
- 45% Potassium hydroxide solution (Fisher Scientific, cat. no. SP236-500). ⚠ *It is highly corrosive and irritant. It should be handled with proper eye protection and gloves. It should be discarded in an appropriate waste disposal container.*
- 29% Ammonium hydroxide solution (Fisher Scientific, cat. no. NC1297835).⚠ *It is highly corrosive and irritant. It should be handled with proper eye protection and gloves. It should be discarded in an appropriate waste disposal container.*
- 30% Hydrogen peroxide (Fisher Scientific, cat. no. H325-4). ⚠ *It is highly corrosive and may cause severe burns. It should be handled with proper eye protection and gloves. It be discarded in an appropriate waste disposal container.*
- 49% Hydrofluoric Acid (Fisher Scientific, cat. no. 08-901-806). ⚠ *It is highly corrosive, toxic and fatal. It must be handled with face protection shields and neoprene gloves to prevent any exposure to skin. It must be handled within a laminar cabinet. It must be disposed in an appropriate waste disposal container.*
- Hydrochloric acid (Fisher Scientific, cat. no. 50-012-11). ⚠ *It is highly corrosive and irritant acid. It must be handled with face protection shields and neoprene gloves to prevent any exposure to skin. It must be handled within a laminar cabinet. It must be disposed in an appropriate waste disposal container.*
- Remover 1165 (MicroChem). ⚠ *It can cause eye, skin and respiratory irritation. It should be handled with proper eye protection and gloves within laminar cabinet It must be disposed in an appropriate waste disposal container.*
- Nanostrip (VWR, cat. no. 10135-756). ⚠ *It is highly corrosive, irritant and toxic. It must be handled with proper eye protection and gloves within laminar cabinet. It must be disposed in an appropriate waste disposal container.*
- ProTEK PS Primer (Brewer Science). ⚠ *It can cause irritation when in contact with eyes and skin. It should be handled with proper eye protection and gloves within laminar cabinet. It should be discarded in an appropriate waste disposal container.*
- ProTEK PSB-23 (Brewer Science). ⚠ *May cause drowsiness or dizziness. It should be handled with proper eye protection and gloves within laminar cabinet. It should be discarded in an appropriate waste disposal container.*

- Ethyl lactate (Sigma Aldrich, cat. no. W244015). ⚠ *It is flammable, oxidizing and corrosive. It can cause serious irritation when in contact with eyes and skin. It should be handled with proper eye protection and gloves within laminar cabinet. It should be discarded in an appropriate waste disposal container.*

- Hexyl acetate (Sigma Aldrich, cat. no. 108154).

- 2-Propanol (Fisher Scientific, cat. no. 50-012-02).⚠ *2-Propanol vapors can cause eye, skin and respiratory irritation. It should be handled with proper eye protection and gloves within laminar cabinet. It should be discarded in an appropriate waste disposal container.*

- Potassium chloride (KCl, 99.0%; Sigma-Aldrich, cat. no. P9333), for preparing the translocation buffer.

- Ethylenediaminetetraacetic acid solution (EDTA, pH8, Sigma-Aldrich, cat.no. 03690), for preparing the translocation buffer.

- Thermo Scientific NoLimits 2000 bp DNA Fragment (2 kbp, 0.5 μg/μL) in TE Buffer (10 mM Tris-HCl pH 7.6, 1 mM EDTA)Ambion 1M Tris (pH 8, Thermo Fisher Scientific, cat. No. AM9856), for preparing buffer for translocation experiments.

- RBSTM 25 solution (Sigma-Aldrich, cat. No. 83460), for cleaning the PMMA flow cells.CAUTION RBS 25 solution should be handled with proper eye protection and gloves since it can cause eye damage and skin irritation. It should be discarded in an appropriate waste disposal container.

- Poly(methyl methacrylate), PMMA, Mr=450, 8% in Anisol (Micro Resist Technology GmBH, Berlin, Germany).

- Sylgard 184 silicone base and a Sylgard curing agent.

- KWIK-CAST Silicone (World Precision Instruments).

- Milli-Q water (0.2 μm filtered).

- Ethanol (Thommen-Furler AG).

- Acetone (Thommen-Furler AG), for cleaning. ⚠ *Acetone is irritant for eyes and skin and can be hazardous if inhaled. It should be handled with proper eye protection and gloves within a laminar flow cabinet. It should be discarded in an appropriate waste disposal container.*

- Isopropanol (IPA, Thommen-Furler AG), for cleaning.

A.1.2 Clean room equipments

- RCA Wet Bench (Reynolds Tech).
- Silicon Etch Wet Bench (Reynolds Tech).
- LPCVD Furnace (Tystar Corp., model no. Mini-Tytan 4600).
- High-Purity Oxidation and Diffusion Furnace (Tystar Corp., Tytan).
- HMDS Vapor Prime System (Yield Engineering Systems).
- Spinner and Hotplate (Brewer Science, model no. CEE 100CB).
- Spinner (CEE Apogee).
- Laser Pattern Generator (Heidelberg, model no. DWL 2000).
- i-Line Stepper (ASML, model no. PAS5500/275D).
- Contact Aligner (Suss MicroTec MA8).
- Direct Write Electron Beam Lithography System (JEOL, model no. JBX 6300-FS).
- Reactive Ion Etcher (Unaxis 790).
- Deep Silicon Etcher (Unaxis Shuttleline DSEII).
- Spin Rinse Dryer (Semitool PSC-101).
- Backside LED illuminated Wet Etching Wafer Holder (AMMT).
- Ion Beam Sputtering Cluster Tool (4 Wave).
- Parametric Test Station (Keithley, model no. 4200 SCS).
- PDMS Dispenser (STANGL Semiconductor Equipment AG, Germany).
- Thinky Mixer (THINKY ARE 250, Japan).
- Hot-air oven (VWR VENTA-Line).
- Weighing pan (Scout^{TM} Pro).

A.1.3 Wet lab equipment

- Clean glass slides (Thermo Scientific)
- Clean-Room-Paper (VWR, Nonwoven Wipers)
- Hot-plate (CORNING PC-400D)

- Micropipettes (RAININ Pipet-Lite XLS)
- Microtips (VWR ZAP® SLIKTM Aerosol Tips)
- Tweezers (ideal-tek 1-259cf.SA), plastic tips
- Razor blades (Apollo Solingen Germany)
- Insulin Syringes U100 (1 ml, VWR, cat. no. CODA621640), for injection of the buffers into the flow cell
- Hypodermic Needle 26G (0.45 x 10 mm BD Microlance, VWR, cat. no. 613-5155), needle that fits into the flow cell
- Syringe Filters (Whatman Anotop 10 Plus 0.02 μm, Sigma-Aldrich, cat. no. WHA68093002), for filtering the buffer before injection into the flow cell

A.1.4 Other Materials

- Silver Wire (0.2 mm diameter, Advent Research Materials, cat. No. AG5488), for preparing Ag/AgCl electrodes.
- Teflon chucks.
- Flow cell.
- O-rings (2 mm inner diameter, 1 mm thickness, Kubo Tech AG, Effretikon, Switzerland, cat. No. 0101-001081).

A.1.5 Equipment

- Axopatch 200B (Molecular Devices, Inc. Sunnyvale, CA), for measuring the current (<100 kHz).
- Chimera VC100, for measuring the current (<2 MHz).
- FEMTO DLCPA-200, for measuring the current.
- NI-PXI-4461 (National Instruments, Austin TX, USA), to digitize the analog data from Axopatch 200B and FEMTO DLPCA-200.
- NI-PXI 8336 (National Instruments, Austin TX, USA), fiber optic interface to communicate with the computer.
- NI-PXI-1042Q (National Instruments, Austin TX, USA), chassis to hold NI-PXI-4461 and NI-PXI 8336.
- Simple Voltage Source for the chlorination of silver wire.

- Transmission Electron Microscope (FEI Talos, Hillsboro, OR, USA), for imaging and drilling nanopores.
- Custom made TEM holder.
- Furnace with argon and hydrogen gas flow.

A.1.6 Transfer Microscope Setup

- 5x Long working distance objective (LMPLFLN5x, Olympus, Tokyo, Japan).
- 50x Long working distance objective (LMPLFLN50x, Olympus, Tokyo, Japan).
- Halogen lamp power supply (TH4-200, Olympus, Tokyo, Japan).
- Halogen lamp (U-LH100L-3-7, Olympus, Tokyo, Japan).
- Microscope base (BXFM, Olympus, Tokyo, Japan).
- Camera (AVT PIKE F-505C, Allied Vision Technologies, Stadtroda, Germany).
- Vacuum and heating stage (taken from chip-to-chip bonder, Idonus, Neuchatel, Switzerland).
- Hypodermic Needle 26G (0.45x10mm BD Microlance, VWR, cat. no. 613-5155), screws onto the M4 screw of the sample holder post and provides connection to microcapillary.
- Laser based micropipette puller P-2000 (Sutter Instruments).
- Pulled microcapillary (Sutter Instruments P2000, Novato, CA, USA), for pulling microcapillaries. Alternatively, pre-pulled capillaries can be bought.
- XYZ Translation Stage with Standard Micrometers (Thorlabs, cat. no. PT3), for holding the needle.
- XY Stage (Thorlabs, cat. no. XRN25P-K1/M), for holding the sample.
- Post holder (Thorlabs, cat. no. PH1), for attaching the needle holder to the XYZ stage.
- Stainless steel post (Thorlabs, cat. no. TR2), acts as the needle holder in combination with a M4 screw.

A.1.7 Software

- Nanolithography Toolbox (Center for Nanoscale Science and Technology CNST, NIST).
- LabView 2017 (National Instruments, Austin TX, USA), to write the acquisition software.
- NIS-Elements Viewer.
- OpenNanopore.

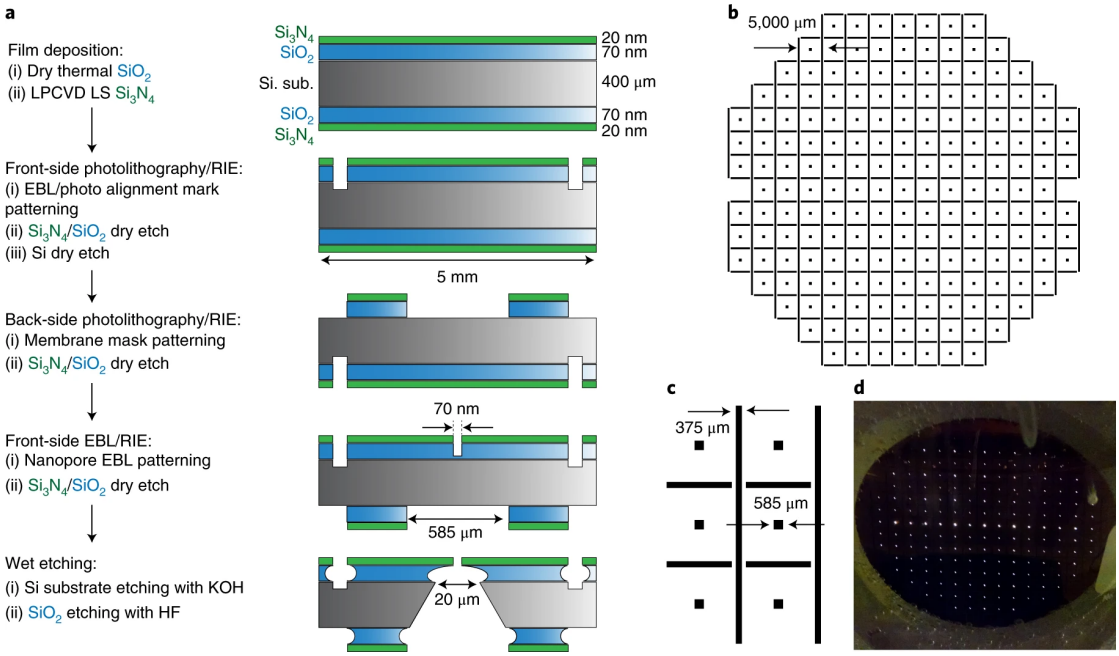

Figure A.1: Overview of the substrate fabrication. (a) Clean-room process flow. (b) Back-side-lithography design. (c) Dimensions of the membrane openings and the dicing lines. (d) Back-side illumination during KOH etching to verify membrane formation.

A.2 Procedures

A.2.1 Fabrication of silicon nitride substrates (Timing 2-3 days)

⚠ *Fabrication is performed in a clean room facility ISO 14644-1 Class 7. (Fig.A.1) summarizes an overview of the substrate fabrication process.* Following are step-by-step procedure for the fabrication of silicon nitride (SiN_x) substrates:

1. Generate the lithography patterns (alignment marks, membranes, and nanopores) with Nanolithography Toolbox and generate photolithography reticles with a laser pattern generator.

   ⚠ *Membrane pattern mask dimensions (585 × 585 µm) and the width of the trenches (375 µm) were chosen to generate ≈20 × 20-µm-square membranes and trenches etched 2/3 of the way into a 400-µm-thick silicon substrate upon completion of anisotropic KOH etching. This allows individual devices to be easily separated by cleaving the pieces from patterned arrays without the need for wafer scribing and dicing, thereby reducing sample handling during the fabrication process.*

2. Clean a batch of 4-inch silicon wafers using RCA clean. Clean the wafers at 80°C in H_2O : NH_4OH : H_2O_2 (5 : 1 : 1) for 10 min followed by a rinse in deionized water (DI). Clean the wafers at 80°C in H_2O : HCl : H_2O_2 (6 : 1 : 1) for 10 min followed by a rinse in DI water and spin dry.

3. Grow 70 nm of dry thermal SiO_2 at 1000°C in an oxidation and diffusion furnace and verify the SiO_2 film thickness using spectroscopic ellipsometry.

4. Deposit 20 nm of low-stress (LS) SiN_x on oxidized wafers and an additional silicon wafer monitor in a low-pressure chemical vapor deposition (LPCVD) furnace and verify the LS SiN_x film thickness on the monitor wafer using spectroscopic ellipsometry.

   ⚠ *Put aside one wafer in order to test the quality of the nitride membrane (Steps* **??***–35).*

5. Vapor prime the wafer in hexamethyldisilazane (HMDS) to improve photoresist adhesion.

6. Spin-coat one side of the wafer with positive photoresist SPR 220 3.0 at 3,000 rpm (1,000 rpm s^{-1} ramp-up rate) for 60 s, and soft-bake the wafer on a hot plate at 115°C for 90 s.

   ⚠ *Do not put the wafer directly on the vacuum chuck on the spinner as it could scratch the surface. Use a 4" wafer chuck to prevent surface damage. Clean all surfaces such as microscope stages, heating plates, wafer cooling plates on which the wafer is placed to avoid scratching the thin films. Handle the wafers only with ESD safe non-scratching tweezers.*

7. Expose the wafer in an i-line stepper at 200 mJ cm^{-2} to define stepper alignment marks.

8. Post-exposure soft-bake the wafer on a hot plate at 115°C for 90s.

9. Develop with MIF-300 AZ developer for 90 s, rinse it with DI water for 60 s, and dry with a nitrogen gun.

10. Descum in oxygen plasma (O_2 30 sccm, 40 mTorr, 100 W, 60 s).

11. Etch the LS SiN_x/SiO_2 layers using a reactive-ion etcher. Etch the 20-nm LS SiN_x first with CHF_3 30 s.c.c.m, O_2 2 s.c.c.m, 15 mTorr, 150 W, for 180 s. Consecutively, etch through 70-nm SiO_2 into silicon substrate with CF_4 30 sccm, 40 mTorr, 150 W, for 120 s. After etching, remove the photoresist with Remove 1165, rinse in DI water. The etched marks will be easily recognizable by stepper optics after the etch.

    ⚠ *Always clean the etch chamber and check the etch rates on monitor pieces.*

12. Repeat Step 5 - Step 11 to define electron-beam lithography (EBL) alignment marks. The local-alignment marks are positioned in the corners of the chips ((Fig.A.1a), outside of the area exposed to liquid when the sample is placed in the flow cell, to avoid current

leakage through the exposed substrate during ionic current and DNA translocation measurements.

13. Etch the LS SiN_x/SiO_2 layers, using a reactive-ion etcher. Etch the 20-nm LS SiN_x first with CHF_3 30 s.c.c.m., O_2 2 s.c.c.m., 15 mTorr, 150 W, for 180 s. Consecutively, etch through the 70-nm SiO_2 into the silicon substrate with CF_4 30 s.c.c.m., 40 mTorr, 150 W, for 120 s. After etching, remove the photoresist with Remover 1165, and rinse it in DI water. The etched marks will be easily recognizable by stepper optics after the etch.

14. Repeat Step 5 - Step 11 to define the membrane patterns and trenches (Fig.A.1b,c) at the back side of the wafer. Align the patterns to the stepper alignment marks at the front side of the wafer.

15. Spin-coat the front-side of the wafer (the side with alignment marks) with ZEP 520A EBL resist at 4,000 rpm (1,000 rpm sec^{-1} ramp up rate) for 60 s, and hard-bake the resist on a hot plate at 180°C for 15 min.

    ⚠ *It is recommended to filter the EBL resist to remove impurities that could create nanoscale pin-holes in LS SiN_x/SiO_2 during nanopore etching in Step19.*

16. Expose the wafer in electron beam at 1,000 μC cm^{-2} to define 70-nm nanopores into the resist. Use deep-etched EBL marks to locally align nanopore patterns to the center of the membrane.

17. Cold-develop at 4°C in hexyl acetate for 90 s, rinse in 2-propanol for 30 s, and dry the wafer with a nitrogen gun.

18. Descum in oxygen plasma (O_2 30 s.c.c.m, 40 mTorr, 100 W, 10 s).

19. Etch the nanopores into LS SiN_x with CF_4 30 s.c.c.m, 40 mTorr, 150 W, 9 loops, 60 s each. After etching, remove the photoresist with hot 100°C. Remover 1165, rinse in DI water and spin dry.

    ⚠ *Always clean the etching chamber and check the etching rates on monitor pieces. If nanopores are not open (Fig.A.2a) or only partially open (Fig.A.2b), increase the etching time or the number of loops.*

20. Remove the residual impurities by performing an RCA clean as described in Step 2.

21. Spin-coat the wafer with ProTEK Primer at 1,000 rpm (1,000 rpm s^{-1} ramp-up rate) for 60 s, bake the wafer on a hot plate at 110 °C for 60 s and then bake it on a hot plate at 220 °C for 5 min. Then spin-coat the wafer with ProTEK PSB-23 at 1,500 rpm (1,000 rpm s^{-1} ramp-up rate) for 60 s, and bake it on a hot plate at 110 °C for 120 s.

22. Expose the negative tone mask with the membrane array and trenches in a contact aligner at 500 mJ cm^{-2}.

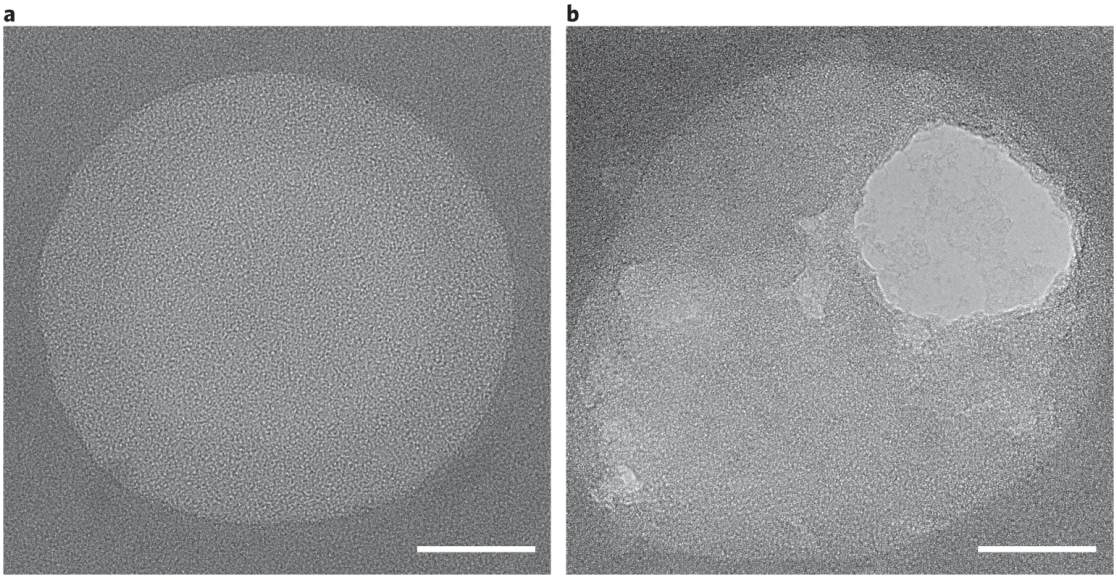

Figure A.2: Insufficient etching of the aperture (Step 19). (a) Unsuccessful etching ofSiN_x aperture. Scale bar, 20 nm. (b) MoS_2 monolayer transferred on incompletely etched SiN_x aperture. Scale bar, 20 nm.

23. Post exposure, soft-bake the wafer on a hot plate at 110 °C for 120 s.

24. Develop in ethylene lactate for 60 s.

25. Post development, hard-bake the wafer on a hot plate at 220 °C for 180 s.

26. Descum the wafer in oxygen plasma (O_2 30 s.c.c.m., 40 mTorr, 100 W, 155 s).

27. Mount the wafer protected with ProTeK into a holder so that the membrane patterns and trenches are facing outward and are exposed to the etching solutions. Etch the silicon substrate in 45% (wt/wt) KOH/DI-water (1:1) solution at 80 °C, constantly stirring the solution. Terminate the etching after 4 h 30 min, when the substrate becomes transparent to the back-side-illuminating LED light. Rinse the holder with the wafer in DI water. The back-side-illuminated wafer with released membranes in the etching solution is shown in Fig.A.1d.

   ⚠ *The thickness of the wafers varies, which requires adjustments to the etching time. It is important to know when to stop etching to get the desired membrane dimensions. A wafer holder with an LED-illuminated or a transparent back side that allows illumination of*

the wafer from the back while it is in the etching solution to see when the membranes become transparent is very useful.

28. Remove the wafer from the holder, dry it gently with a nitrogen gun and measure the membrane dimensions under a calibrated microscope with NIS-Elements Viewer to ensure that its dimensions are 20×20 μm.

    ⚠ *Handle the wafer with released membranes and etched trenches with extreme caution in this and the following steps as it is quite fragile. Never sonicate or spin-dry the wafers.*

29. Remove the ProTEK in hot Nanostrip, rinse in DI water and do an RCA clean as described in Step 2.

30. Etch the wafer in HF for 10 s to remove the remaining SiO_2 underlayer, rinse it with DI water and dry it gently with a nitrogen gun. Inspect the membrane with an optical microscope. Repeat RCA clean if impurities are present.

A.2.2 Optional: Fabrication of Test Wafer for Current Leakage Variation Analysis (Timing: 1-2 days)

31. Take one wafer from the batch prepared in Steps 1-4.

32. Perform lithography Step **??**, defining only membrane patterns and trenches.

33. Perform Steps **??**-26 to release the membranes.

34. Deposit 50 nm of gold by BTD at a 45° angle on both the membrane side and the back side of the wafer, using the sputtering cluster tool. The back side of the wafer is shown in (Fig.2.5a).

    ⚠ *The BTD technique traditionally used in fabrication of tunnel junctions is utilized to ensure good sidewall coverage in the KOH-etched vias and to prevent interface mixing and formation of defects in the SiN_x/SiO_2 layers.*

35. Separate the individual chips by carefully cleaving, effectively creating 180 large-area metal-insulator-metal (MIM) junctions shown in (Fig.2.5b).

    ⚠ *Handle the pieces with extreme caution with non-scratching tweezers while avoiding touching the metalized surfaces which can create defects in SiN_x/SiO_2 thin-film layers.*

36. Measure the voltage-current characteristics with parametric test station.

    ⚠ *Apply silver paint on the gold layer to avoid defect creation with electrical probes during measurements.*

A.2.3 Transfer

37. Transfer of MoS_2 to the SiN_x membrane can be achieved in two ways, as follows. Follow option A for transfer using PMMA and option B for transfer using PDMS.

    (A) Transfer of MoS_2 using PMMA (Timing: about 15 min per device, 8-12 h cleaning and annealing process)

    i Filter poly(methyl methacrylate) (PMMA, Mr=450, 8% in anisole) using 0.2 μm Millipore filter.

    ii Place the MoS_2/sapphire substrate on a spin-coater with vacuum suction and add ≈200-300 μL of PMMA followed by spin-coating at 2500 rpm for 1 min.

    ⚠ *It is ideal to perform this step-in a clean laminar flow cabinet to avoid any particulate contamination.*

    iii Place the PMMA/MoS_2/sapphire substrate on a hot-plate preheated at 180°C for 5 min.

    ⚠ *Keep it in clean dust-free environment. The best is to use it within a week.*

    iv Using a scalpel, manually scratch the spin-coated PMMA on the MoS_2/sapphire substrate orderly to leave behind small PMMA patches (c.a. 1 mm x 0.5 mm) covering the MoS_2.

    ⚠ *The scratching should be delicate and uniform. Unavoidably, scratching sometimes removes MoS_2 along with the PMMA layer leaving behind some defective monolayers at the edges of the patch. However, each PMMA patch harbors monolayer MoS_2 that can be used to transfer on SiN_x membranes.*

    v Place a drop of water (10 μL, 0.02 μm filtered) at the edge of a PMMA patch to be transferred.

    ⚠ *Do not put a large drop of water (>20 μL) as it will be difficult to track the detachment progress. If you accidentally put a larger volume of the drop, you can use a small clean-room paper to suck out the drop carefully and re-do the step with a smaller volume.*

    vi Using a microcapillary attached to a micromanipulator, approach one of the edges of the PMMA patch and slowly peel the edge of the patch so that the water starts to penetrate from below the patch.

    ⚠ *Slowly approach the edge of the patch. Larger forces might bend or break the microcapillary.*

    vii After approximately half of the patch is detached, slowly remove the microcapillary from below and re-align it on the top of the patch, press gently and slowly start detaching the rest of the patch from the substrate.

viii Once the entire patch is detached, it floats on the air-water interface. Slowly approach the microcapillary through the water-drop from the bottom of the floating PMMA/MoS_2 patch and lift it out of the water-drop.

⚠ *One can use bright-field illumination or dark-field mode under the optical microscope to search for the detached patch.*

ix Align the SiN_x membrane on which the MoS_2 is to be transferred and place a drop of water (10 μL, 0.02 μm filtered) c.a. 1-2 mm away from the membrane.

x Slowly approach the microcapillary with PMMA/MoS_2 patch from top of the water droplet so that it detaches from the microcapillary and unfolds on the drop (usually floating at the edge).

xi Slowly remove the microcapillary from below and re-align it on the top of the free-floating patch and press it gently on the PMMA/MoS_2 patch guiding it towards the membrane.

⚠ While maneuvering the PMMA/MoS_2 patch avoid direct contact of the microcapillary tip to the SiN_x membrane. This is to avoid the SiN_x membrane damage due to scratching by the microcapillary tip.

xii Carefully align the monolayer MoS_2 on top of the membrane and set the temperature of the sample holder to ca. 50°C without releasing the microcapillary. Let the water evaporate from the area between the patch and the membrane, thereby rendering MoS_2 attached to the membrane. Release the microcapillary from the patch and keep the substrate with freshly transferred MoS_2/PMMA patch on pre-heated hot-plate at 180°C for 5 min.

⚠ *It is important to check if the PMMA patch misaligns during the drying process.One can keep the samples in a dust-free environment for 24 h until it is cleaned. It is however advisable to clean the chips as soon as possible.*

xiii Place the chips in a Teflon chip's holder into closed beaker with acetone. Heat it to ≈ 60°C on a heat plate and leave it for 60 min. Quickly transfer the chips into the next beaker with hot acetone (≈60°C), leaving it on a hot plate for another 60 min. Repeat this once more but then turn off the heating and leave the chips in acetone until it cools down to ambient temperature (≈25°C). Continue the washing by transferring the chips into Isopropanol alcohol (IPA) and DI water (0.2 μm filtered) both at ambient temperature, for 30 min.

⚠ *Since membranes are very fragile avoid any abrupt temperature changes which could eventually cause cracking. Also avoid complete drying of the chips while transferring them from one beaker to another. This will prevent drying of the impurities on the membrane.*

xiv Carefully dry the chips with a very gentle nitrogen flow directed in parallel with the chip surface. While doing this hold the chip under 45° in respect to the ground so that the water droplet can easily flow away from the membrane toward the edges of the chip.

⚠ One can keep the samples in a dust-free environment for ca. 1 week until it is baked/annealed. It is, however, advisable to anneal the chips as soon as possible to successfully remove polymer residues.

xv Place the substrates in an alumina boat with MoS_2 facing the top and anneal it in a furnace at 400°C in Ar/H_2 flow (100 sccm/10 sccm) for 8 h.

⚠ One can keep the samples in a dust and moisture- free environment.

(B) Transfer of MoS_2 using PDMS (Timing: ≈ 10 min per device, preparation time ≈ 5-6 h)

i Preparation of PDMS and PDMS stamps: PDMS preparation should be performed in a clean room facility ISO 14644-1 Class 6 or Class 7. Using a PDMS dispenser, add Sylgard 184 silicone base and Sylgard curing agent in a ratio of 10:1 (wt/wt). 20 g of base and 2 g of curing agent are sufficient for making a thin layer of ≈1–1.5 mm of PDMS on a clean silicon wafer.

ii Mix the contents in a mixer (THINKY) for about 1 min at 2000 rpm and defoam for 2 min for about 2200 rpm.

⚠ It is important to mix the base and the curing agent homogenously to avoid any sticky residues or uncured PDMS base.

iii Degas the contents using a desiccator for about 30 min.

iv Place a clean silicon wafer in a Petri dish and pour degassed PDMS over it very slowly. One can degas again for 10 min to make sure that the PDMS is free of entrapped air bubbles. Bake the PDMS at 80 °C for 4 h.

⚠ *The baked PDMS can be kept at room temperature for a few weeks until used.*

v Cut small pieces of PDMS stamps (≈1-2 mm) using clean razor blades.

⚠ *Detach slowly to avoid PDMS breakage. Excessive force will introduce cracks on the PDMS.*

vi On a clean glass slide, dispense a small drop of uncured PDMS from step (iv) and place the flat PDMS stamp on it. Make sure that the side of the cured PDMS stamp that was facing the silicon wafer now is the top side. Bake the glass slide with PDMS at 80 °C for 20 min.

⚠ *Keep the PDMS stamps in a clean and dust-free environment. The PDMS stamps can be kept for weeks before use. They can be kept in a moisture-free environment.*

vii Transfer of MoS_2 using the PDMS stamp (steps (vii–xiv)). First, place the MoS_2 grown on a sapphire substrate under an optical microscope (facilitated with vacuum suction) and then place a PDMS stamp (attached to a glass slide) above the MoS_2, using a micromanipulator (xyz) and aligning it with the area of interest.

viii Using the micromanipulator stage, slowly bring down the PDMS stamp until it comes into contact with the MoS_2/sapphire surface.

⚠ *A slightly tilted glass-slide helps to interact with the MoS_2 surface. While using a micro-manipulator, try to make the PDMS stamp completely interact with the MoS_2 surface with least compression on PDMS stamp. Typically, higher pressure leads to cracks in the MoS_2 and potentially introduces a larger number of PDMS residues on the MoS_2 surface after transfer.*

ix Place a drop of Milli-Q water (5–10 μL) around the edges of the PDMS stamp, using a syringe needle or a small micropipette tip.

⚠ *If the PDMS stamp is too thin (<1 mm), the area will be inaccessible to a needle or micropipette tip, thereby making it inaccessible to a drop water around the PDMS/MoS_2 edge.*

x Using the micromanipulator, slowly lift the PDMS stamp, which enables the intercalation of water between the sapphire substrate and the MoS_2, facilitating the transfer of MoS_2 directly onto the stamp.

⚠ *If the water does not penetrate, use the micromanipulator to lower the stamp again and gently poke the edge of the water–PDMS stamp interface, so that the water penetrates from the edge.*

xi After the lift-off, focus on the area under the PDMS stamp to look for the MoS_2 triangle that is to be transferred to the target substrate.

xii Align the target substrate with a SiN_x membrane to the MoS_2 triangle and slowly lower the stamp, making sure that the triangle follows the vertical axis of the alignment with the membrane.

xiii After attachment of the MoS_2–PDMS stamp to the SiN_x membrane, slowly raise the stamp so that the desired MoS_2 is printed on the membrane.

xiv Confirm successful transfer, using an optical microscope with at least 50× magnification.

A.2.4 Nanopore Formation

38. For creating nanopores using TEM imaging and drilling, follow option A (TEM imaging and drilling) and for nanopore creation using ECR, follow option B (Nanopore formation using ECR drilling).

(A) TEM imaging and drilling (Timing ≈30 min)

⚠ *This section can be skipped in the case of pore generation through ECR.*

i Set the TEM to Bright field mode, lower the high tension to 80 kV.

⚠ *Imaging should be performed at low acceleration voltage and high vacuum to avoid damage to the sample.*

ii First, insert the holder containing the sample chip into the microscope stage. Then use the lowest magnification to find the membrane. Then zoom in to find the aperture in the SiN_x. If it is not visible, go out of focus to increase the contrast until you see it.

iii Set the beam spot size to 5 or 6 (first condenser lens or C1) and do the general alignment

iv Go to a higher magnification (SA mode, 630k), always spreading the beam and keeping the electron current density to < 0.05 pA/nm2, i.e., at 630k× magnification, the current should not exceed 300 pA.

v Perform the alignment of the electron beam away from the SiN_x aperture to avoid damage to the material.

vi Go to the suspended MoS_2 region and check the live fast Fourier transform (FFT) signal to make sure that there is an MoS_2 monolayer.

vii Correct the objective astigmatism and put the sample into the focal plane.

viii Find the clean MoS_2 region where you want to drill a hole and put it into the center of the field of view.

ix Quickly contract the beam to the smallest spot. If the layer is very clean, the damage will begin immediately. Slightly spread the beam to observe the pore growth.

⚠ *If the process of contracting the beam is too slow, the whole suspended area can get easily damaged.*

x Once the pore has reached a desired size, blank the beam.

xi Spread the beam again to reduce the electron current density and unblank it.

xii Take a high-resolution image of the created pore and remove the sample from the TEM.

xiii Precision painting under an optical microscope (Steps xiii–xvii). Dispense a small volume (50–100μL) of elastomer mix from a commercial kit (Kwik-Cast (WPI silicone elastomer)).

xiv Thoroughly mix both the elastomer contents for 30 s.

⚠ *The elastomer cures very quickly after mixing (≈3 min). Hence it is advised to use the elastomer mix quickly before it cures.*

xv Take a minimal amount of the mix onto a bristle attached to a micromanipulator holder.

xvi Place the chip under the optical microscope and start applying the elastomer mix, 'painting' around the membrane area using the elastomer mix on the bristle.

⚠ *While applying the elastomer mix, it is better to start far away from the SiNx membrane so that the mixture does not flow over the membrane.*

xvii Keep applying the elastomer mix quickly before it dries (3 min). If the elastomer dries before completion, prepare a fresh mixture and continue.

(B) Nanopore formation using ECR drilling (Timing ≈ 30 min per device)

i Perform precision painting as described in Option A (xiii–xvii).

ii Select a clean chip with transferred MoS_2 to be mounted in the PMMA flow cell.

iii Place an O-ring on one part of the flow cell, and carefully place the chip on top of the O-ring. Now, place a second O-ring on top of the chip. Carefully align the second piece of the flow cell and gently screw them together.

iv Prepare a single 10-cm Ag/AgCl electrode with both ends chlorinated (as described in the 'Experimental setup' section of the Introduction, under 'Electrodes') and insert the ends of the electrode through the top electrode outlet into each of the flow cell chambers.

⚠ *This step is vital to avoiding any electrical discharge into the MoS_2 membrane.*

v Prepare a Milli-Q water–EtOH (filtered with a 0.02-μm filter) mixture at a volumetric ratio of 1:1. Ultrasonicate the solution while degassing under vacuum for 40 min.

vi Inject a Milli-Q water–EtOH mixture (1:1, filtered with a 0.02-μm filter and degassed) from the liquid injection ports. Keep the flow cell for wetting.

vii Continuously inject the Milli-Q water–EtOH mixture from the liquid injection port.

⚠ *This step is essential to removing most of the air bubbles from the buffer solution.*

viii Using a syringe needle, steadily aspirate the wetting solution from both sides of the flow cell chambers via the liquid injection port and inject degassed buffer.

ix Prepare a pair of Ag/AgCl electrodes (≈10 cm) and insert the individual electrodes from the top electrodes/outlets into each of the PMMA chambers.

x In our geometry, the side with the transferred MoS_2 is defined as the 'cis side', the other side is referred to as the 'trans side'.

xi Connect the chlorinated Ag/AgCl electrodes on the cis side to the ground electrode; the trans side is connected to the active terminal to complete the circuit.

⚠ *Connect the ground lead first; the active lead should be connected afterward.*

xii The amplifier will short-circuit at this point due to the Ag/AgCl bridge still connecting the two chambers. Remove the bridge now, without removing the active and ground electrodes.

xiii Record the leakage current at a transmembrane voltage of 100 mV, using a Femto DLPCA-200 amplifier for 2 min.

xiv Increase the transmembrane voltage stepwise (100-mV steps, 10–25 s each) and notice the increase in the current.

xv Increase the voltage until there is a sudden increase in the current (typically at voltages >800 mV), which implies that one has reached a critical voltage.

xvi To check whether a nanopore has been formed, apply a lower transmembrane potential of 100 mV and compare the current with the previous leakage current recorded at Step (xiii).

xvii Record an I–V curve across a transmembrane potential of 0–800 mV at a step size of ≈50 mV with a dwell time of ≈10 s.

xviii Extract the conductance and linearity of the I–V curve and calculate the pore diameter.

⚠ *The acquisition software should be set up to show the conductance rather than the current. In such a way, the user can precalculate the target conductance for a given pore size and stop the process once that value is reached.*

A.2.5 DNA translocations (Timing 2–3 h, depending upon the experiment)

⚠ *Before starting the following steps, refer to the section avoid any discharge into the membrane.*

39. Prepare DNAbuffer mix by dissolving the DNA stock (e.g., 2 kb of dsDNA, 0.5 μg/μL) in 1 M KCl 10 mM Tris 1 mM EDTA buffer (filtered with a 0.02-μm filter and degassed, adjusted to pH 7.5) in a volumetric ratio of 1:50 in a PCR tube to reach a final DNA concentration of 10 ng/μL.

40. Incubate the DNA–buffer mix at 40 °C for 10 min on a PCR machine or block heater.

41. Use a micropipette to gently load the mixture into the cis chamber of the flow cell.

42. Set up the flow cell and apply a transmembrane voltage of 100–400 mV.

43. Acquire the data, using a custom-made LabVIEW program (as mentioned in the 'Data acquisition' section of the Introduction) and an amplifier (e.g., Axopatch 200B). For event detection and data analysis, we use a custom-made resource, OpenNanopore (MATLAB or Python-based).

A.3 Timing

Steps 1-30, Fabrication of SiN_x chips: 2-3 days

Steps 31-36, Fabrication of Test Wafer for Current Leakage Variation Analysis: ≈15 min

Steps 37A(i-xii), Transfer of MoS_2 using PMMA: ≈15 min

Steps 37A(xiii-xvi), Cleaning steps: ≈4 h

Steps 37B(i-vi), Preparation of PDMS and PDMS stamps: ≈ 5-6 h

Steps 37B(vii-xiv), Transfer of MoS_2 using PDMS stamp: ≈10 min per device

Step 38A(i–xii), TEM imaging and drilling: ≈ 30 min per device

Step 38A(xiii–xvii), Precision Painting, ≈ 10 min

Step 38B (i–xvii), nanopore formation using ECR drilling: ≈30 min per device

Steps 39–43, DNA translocations: ≈2–3 h, depending upon the experiment

Bibliography

(1) Coulter, W. H. Means for counting particles suspended in a fluid, US2656508A, 1953.

(2) Don, M. *JALA: Journal of the Association for Laboratory Automation* **2003**, *8*, 72–81.

(3) Kasianowicz, J. J.; Brandin, E.; Branton, D.; Deamer, D. W. *Proceedings of the National Academy of Sciences* **1996**, *93*, Publisher: Proceedings of the National Academy of Sciences, 13770–13773.

(4) Deamer, D.; Akeson, M.; Branton, D. *Nature Biotechnology* **2016**, *34*, Number: 5 Publisher: Nature Publishing Group, 518–524.

(5) Kasianowicz, J. J.; Bezrukov, S. M. *Biophysical Journal* **1995**, *69*, 94–105.

(6) NHGRI Seeks Next Generation of Sequencing Technologies, en.

(7) Cherf, G. M.; Lieberman, K. R.; Rashid, H.; Lam, C. E.; Karplus, K.; Akeson, M. *Nature Biotechnology* **2012**, *30*, Number: 4 Publisher: Nature Publishing Group, 344–348.

(8) Manrao, E. A.; Derrington, I. M.; Laszlo, A. H.; Langford, K. W.; Hopper, M. K.; Gillgren, N.; Pavlenok, M.; Niederweis, M.; Gundlach, J. H. *Nature Biotechnology* **2012**, *30*, Number: 4 Publisher: Nature Publishing Group, 349–353.

(9) Butler, T. Z.; Pavlenok, M.; Derrington, I. M.; Niederweis, M.; Gundlach, J. H. *Proceedings of the National Academy of Sciences* **2008**, *105*, Publisher: Proceedings of the National Academy of Sciences, 20647–20652.

(10) Lee, K.; Park, K.-B.; Kim, H.-J.; Yu, J.-S.; Chae, H.; Kim, H.-M.; Kim, K.-B. *Advanced Materials* **2018**, *30*, 1704680.

(11) Wanunu, M. *Physics of Life Reviews* **2012**, *9*, 125–158.

(12) Shi, W.; Friedman, A. K.; Baker, L. A. *Analytical Chemistry* **2017**, *89*, Publisher: American Chemical Society, 157–188.

(13) Xue, L.; Yamazaki, H.; Ren, R.; Wanunu, M.; Ivanov, A. P.; Edel, J. B. *Nature Reviews Materials* **2020**, *5*, Number: 12 Publisher: Nature Publishing Group, 931–951.

(14) Venkatesan, B. M.; Bashir, R. *Nature Nanotechnology* **2011**, *6*, Number: 10 Publisher: Nature Publishing Group, 615–624.

(15) Li, J.; Stein, D.; McMullan, C.; Branton, D.; Aziz, M. J.; Golovchenko, J. A. *Nature* **2001**, *412*, Number: 6843 Publisher: Nature Publishing Group, 166–169.

(16) Laszlo, A. H.; Derrington, I. M.; Ross, B. C.; Brinkerhoff, H.; Adey, A.; Nova, I. C.; Craig, J. M.; Langford, K. W.; Samson, J. M.; Daza, R., et al. *Nature biotechnology* **2014**, *32*, 829–833.

(17) Jain, M.; Olsen, H. E.; Paten, B.; Akeson, M. *Genome biology* **2016**, *17*, 1–11.

(18) Storm, A. J.; Chen, J. H.; Ling, X. S.; Zandbergen, H. W.; Dekker, C. *Nature Materials* **2003**, *2*, Number: 8 Publisher: Nature Publishing Group, 537–540.

(19) Yanagi, I.; Akahori, R.; Hatano, T.; Takeda, K.-i. *Scientific Reports* **2014**, *4*, Number: 1 Publisher: Nature Publishing Group, 5000.

(20) Fragasso, A.; Schmid, S.; Dekker, C. *ACS Nano* **2020**, *14*, Publisher: American Chemical Society, 1338–1349.

(21) Kwok, H.; Briggs, K.; Tabard-Cossa, V. *PLOS ONE* **2014**, *9*, Publisher: Public Library of Science, e92880.

(22) Van den Hout, M.; Hall, A. R.; Wu, M. Y.; Zandbergen, H. W.; Dekker, C.; Dekker, N. H. *Nanotechnology* **2010**, *21*, 115304.

(23) Gilboa, T.; Zrehen, A.; Girsault, A.; Meller, A. *Scientific reports* **2018**, *8*, 1–10.

(24) Yuan, Y.; Li, G.; Zaribafzadeh, H.; de la Mata, M.; Castro-Hartmann, P.; Zhang, Q.; Arbiol, J.; Xiong, Q. *arXiv preprint arXiv:1806.08172* **2018**.

(25) Drndić, M. *Nature Reviews Physics* **2021**, *3*, Number: 9 Publisher: Nature Publishing Group, 606–606.

(26) Skinner, G. M.; van den Hout, M.; Broekmans, O.; Dekker, C.; Dekker, N. H. *Nano Letters* **2009**, *9*, 2953–2960.

(27) Meller, A.; Nivon, L.; Brandin, E.; Golovchenko, J.; Branton, D. *Proceedings of the National Academy of Sciences* **2000**, *97*, 1079–1084.

(28) Storm, A. J.; Chen, J.; Zandbergen, H.; Dekker, C. *Physical review E* **2005**, *71*, 051903.

(29) Plesa, C.; Verschueren, D.; Pud, S.; Van Der Torre, J.; Ruitenberg, J. W.; Witteveen, M. J.; Jonsson, M. P.; Grosberg, A. Y.; Rabin, Y.; Dekker, C. *Nature nanotechnology* **2016**, *11*, 1093–1097.

(30) Plesa, C.; Kowalczyk, S. W.; Zinsmeester, R.; Grosberg, A. Y.; Rabin, Y.; Dekker, C. *Nano letters* **2013**, *13*, 658–663.

(31) Talaga, D. S.; Li, J. *Journal of the American Chemical Society* **2009**, *131*, 9287–9297.

(32) Li, J.; Fologea, D.; Rollings, R.; Ledden, B. *Protein and peptide letters* **2014**, *21*, 256–265.

(33) Si, W.; Aksimentiev, A. *ACS nano* **2017**, *11*, 7091–7100.

(34) Yusko, E. C.; Bruhn, B. R.; Eggenberger, O. M.; Houghtaling, J.; Rollings, R. C.; Walsh, N. C.; Nandivada, S.; Pindrus, M.; Hall, A. R.; Sept, D., et al. *Nature nanotechnology* **2017**, *12*, 360–367.

(35) Yang, J.; Ferranti, D. C.; Stern, L. A.; Sanford, C. A.; Huang, J.; Ren, Z.; Qin, L.-C.; Hall, A. R. *Nanotechnology* **2011**, *22*, Publisher: IOP Publishing, 285310.

(36) Chou, Y.-C.; Chen, J.; Lin, C.-Y.; Drndić, M. *The Journal of Chemical Physics* **2021**, *154*, 105102.

(37) Apel, P. Y.; Korchev, Y. E.; Siwy, Z.; Spohr, R.; Yoshida, M. *Nuclear Instruments and Methods in Physics Research Section B: Beam Interactions with Materials and Atoms* **2001**, *184*, 337–346.

(38) Siwy, Z. S.; Powell, M. R.; Petrov, A.; Kalman, E.; Trautmann, C.; Eisenberg, R. S. *Nano Letters* **2006**, *6*, Publisher: American Chemical Society, 1729–1734.

(39) Vlassiouk, I.; Apel, P. Y.; Dmitriev, S. N.; Healy, K.; Siwy, Z. S. *Proceedings of the National Academy of Sciences* **2009**, *106*, Publisher: Proceedings of the National Academy of Sciences, 21039–21044.

(40) Liu, K.; Pan, C.; Kuhn, A.; Nievergelt, A. P.; Fantner, G. E.; Milenkovic, O.; Radenovic, A. *Nature Communications* **2019**, *10*, Number: 1 Publisher: Nature Publishing Group, 3.

(41) Castellanos-Gomez, A.; Buscema, M.; Molenaar, R.; Singh, V.; Janssen, L.; Zant, H. S. J. v. d.; Steele, G. A. *2D Materials* **2014**, *1*, Publisher: IOP Publishing, 011002.

(42) Cun, H.; Macha, M.; Kim, H.; Liu, K.; Zhao, Y.; LaGrange, T.; Kis, A.; Radenovic, A. *Nano Research* **2019**, *12*, 2646–2652.

(43) Waduge, P.; Bilgin, I.; Larkin, J.; Henley, R. Y.; Goodfellow, K.; Graham, A. C.; Bell, D. C.; Vamivakas, N.; Kar, S.; Wanunu, M. *ACS Nano* **2015**, *9*, Publisher: American Chemical Society, 7352–7359.

(44) Graf, M.; Lihter, M.; Thakur, M.; Georgiou, V.; Topolancik, J.; Ilic, B. R.; Liu, K.; Feng, J.; Astier, Y.; Radenovic, A. *Nature Protocols* **2019**, *14*, Number: 4 Publisher: Nature Publishing Group, 1130–1168.

(45) Thakur, M.; Macha, M.; Chernev, A.; Graf, M.; Lihter, M.; Deen, J.; Tripathi, M.; Kis, A.; Radenovic, A. *Small Methods* **2020**, *4*, 2000072.

(46) Merchant, C. A.; Healy, K.; Wanunu, M.; Ray, V.; Peterman, N.; Bartel, J.; Fischbein, M. D.; Venta, K.; Luo, Z.; Johnson, A. C., et al. *Nano letters* **2010**, *10*, 2915–2921.

(47) Schneider, G. F.; Kowalczyk, S. W.; Calado, V. E.; Pandraud, G.; Zandbergen, H. W.; Vandersypen, L. M.; Dekker, C. *Nano letters* **2010**, *10*, 3163–3167.

(48) Garaj, S.; Hubbard, W.; Reina, A.; Kong, J.; Branton, D.; Golovchenko, J. *Nature* **2010**, *467*, 190–193.

(49) Hall, J. E. *The Journal of general physiology* **1975**, *66*, 531–532.

(50) Farimani, A. B.; Min, K.; Aluru, N. R. *ACS Nano* **2014**, *8*, Publisher: American Chemical Society, 7914–7922.

(51) Radisavljevic, B.; Radenovic, A.; Brivio, J.; Giacometti, V.; Kis, A. *Nature Nanotechnology* **2011**, *6*, Number: 3 Publisher: Nature Publishing Group, 147–150.

(52) Liu, K.; Feng, J.; Kis, A.; Radenovic, A. *ACS Nano* **2014**, *8*, Publisher: American Chemical Society, 2504–2511.

(53) Feng, J.; Liu, K.; Bulushev, R. D.; Khlybov, S.; Dumcenco, D.; Kis, A.; Radenovic, A. *Nature Nanotechnology* **2015**, *10*, Number: 12 Publisher: Nature Publishing Group, 1070–1076.

(54) Heiranian, M.; Farimani, A. B.; Aluru, N. R. *Nature communications* **2015**, *6*, 1–6.

(55) Feng, J.; Graf, M.; Liu, K.; Ovchinnikov, D.; Dumcenco, D.; Heiranian, M.; Nandigana, V.; Aluru, N. R.; Kis, A.; Radenovic, A. *Nature* **2016**, *536*, Number: 7615 Publisher: Nature Publishing Group, 197–200.

(56) Graf, M.; Lihter, M.; Altus, D.; Marion, S.; Radenovic, A. *Nano Letters* **2019**, *19*, Publisher: American Chemical Society, 9075–9083.

(57) Feng, J.; Liu, K.; Graf, M.; Lihter, M.; Bulushev, R. D.; Dumcenco, D.; Alexander, D. T.; Krasnozhon, D.; Vuletic, T.; Kis, A., et al. *Nano letters* **2015**, *15*, 3431–3438.

(58) Thiruraman, J. P.; Fujisawa, K.; Danda, G.; Das, P. M.; Zhang, T.; Bolotsky, A.; Perea-López, N.; Nicolaı, A.; Senet, P.; Terrones, M., et al. *Nano letters* **2018**, *18*, 1651–1659.

(59) Thiruraman, J. P.; Masih Das, P.; Drndic, M. *ACS nano* **2020**, *14*, 11831–11845.

(60) High-throughput nanopore fabrication and classification using FIB irradiation and automated pore edge analysis, Number: arXiv:2205.13661 arXiv:2205.13661 [cond-mat], 2022.

(61) Novoselov, K. S.; Geim, A. K.; Morozov, S. V.; Jiang, D.; Zhang, Y.; Dubonos, S. V.; Grigorieva, I. V.; Firsov, A. A. *Science* **2004**, *306*, Publisher: American Association for the Advancement of Science, 666–669.

(62) Schranghamer, T. F.; Sharma, M.; Singh, R.; Das, S. *Chemical Society Reviews* **2021**, *50*, Publisher: The Royal Society of Chemistry, 11032–11054.

(63) Dean, C. R.; Young, A. F.; Meric, I.; Lee, C.; Wang, L.; Sorgenfrei, S.; Watanabe, K.; Taniguchi, T.; Kim, P.; Shepard, K. L.; Hone, J. *Nature Nanotechnology* **2010**, *5*, 722–726.

(64) Frisenda, R.; Navarro-Moratalla, E.; Gant, P.; Lara, D. P. D.; Jarillo-Herrero, P.; Gorbachev, R. V.; Castellanos-Gomez, A. *Chemical Society Reviews* **2018**, *47*, Publisher: The Royal Society of Chemistry, 53–68.

(65) Schneider, G. F.; Calado, V. E.; Zandbergen, H.; Vandersypen, L. M. K.; Dekker, C. *Nano Letters* **2010**, *10*, Publisher: American Chemical Society, 1912–1916.

(66) Liang, J.; Xu, K.; Toncini, B.; Bersch, B.; Jariwala, B.; Lin, Y.-C.; Robinson, J.; Fullerton-Shirey, S. K. *Advanced Materials Interfaces* **2019**, *6*, 1801321.

(67) Woo, G.; Kim, H.-U.; Yoo, H.; Kim, T. *Nanotechnology* **2020**, *32*, Publisher: IOP Publishing, 045702.

(68) Lin, Z.; Zhao, Y.; Zhou, C.; Zhong, R.; Wang, X.; Tsang, Y. H.; Chai, Y. *Scientific Reports* **2015**, *5*, Number: 1 Publisher: Nature Publishing Group, 18596.

(69) Cho, H.-Y.; Nguyen, T. K.; Ullah, F.; Yun, J.-W.; Nguyen, C. K.; Kim, Y. S. *Physica B: Condensed Matter* **2018**, *532*, 84–89.

(70) Shinde, S. M.; Das, T.; Hoang, A. T.; Sharma, B. K.; Chen, X.; Ahn, J.-H. *Advanced Functional Materials* **2018**, *28*, 1706231.

(71) Phan, H. D.; Kim, Y.; Lee, J.; Liu, R.; Choi, Y.; Cho, J. H.; Lee, C. *Advanced Materials* **2017**, *29*, _eprint: https://onlinelibrary.wiley.com/doi/pdf/10.1002/adma.201603928, 1603928.

(72) Yu, H. et al. *ACS Nano* **2017**, *11*, Publisher: American Chemical Society, 12001–12007.

(73) Qiu, H.; Zhou, W.; Guo, W. *ACS nano* **2021**, *15*, 18848–18864.

(74) Carson, S.; Wanunu, M. *Nanotechnology* **2015**, *26*, Publisher: IOP Publishing, 074004.

(75) Shi, X.; Li, Q.; Gao, R.; Si, W.; Liu, S.-C.; Aksimentiev, A.; Long, Y.-T. *The Journal of Physical Chemistry Letters* **2018**, *9*, Publisher: American Chemical Society, 4686–4694.

(76) Leung, C.; Briggs, K.; Laberge, M.-P.; Peng, S.; Waugh, M.; Tabard-Cossa, V. *Nanotechnology* **2020**, *31*, 44LT01.

(77) Kc, S.; Longo, R. C.; Wallace, R. M.; Cho, K. *Journal of Applied Physics* **2015**, *117*, 135301.

(78) Pető, J.; Ollár, T.; Vancsó, P.; Popov, Z. I.; Magda, G. Z.; Dobrik, G.; Hwang, C.; Sorokin, P. B.; Tapasztó, L. *Nature chemistry* **2018**, *10*, 1246–1251.

(79) Marion, S.; Macha, M.; J. Davis, S.; Chernev, A.; Radenovic, A. *Physical Chemistry Chemical Physics* **2021**, *23*, Publisher: Royal Society of Chemistry, 4975–4987.

(80) Danda, G.; Masih Das, P.; Chou, Y.-C.; Mlack, J. T.; Parkin, W. M.; Naylor, C. H.; Fujisawa, K.; Zhang, T.; Fulton, L. B.; Terrones, M., et al. *ACS nano* **2017**, *11*, 1937–1945.

(81) Rosenstein, J. K.; Wanunu, M.; Merchant, C. A.; Drndic, M.; Shepard, K. L. *Nature methods* **2012**, *9*, 487–492.

(82) Wanunu, M.; Dadosh, T.; Ray, V.; Jin, J.; McReynolds, L.; Drndić, M. *Nature nanotechnology* **2010**, *5*, 807–814.

(83) Benameur, M.; Radisavljevic, B.; Héron, J.; Sahoo, S.; Berger, H.; Kis, A. *Nanotechnology* **2011**, *22*, 125706.

(84) Tabard-Cossa, V.; Trivedi, D.; Wiggin, M.; Jetha, N. N.; Marziali, A. *Nanotechnology* **2007**, *18*, 305505.

(85) Wen, C.; Zeng, S.; Arstila, K.; Sajavaara, T.; Zhu, Y.; Zhang, Z.; Zhang, S.-L. *ACS sensors* **2017**, *2*, 300–307.

(86) Smeets, R. M.; Keyser, U. F.; Dekker, N. H.; Dekker, C. *Proceedings of the National Academy of Sciences* **2008**, *105*, 417–421.

(87) Hoogerheide, D. P.; Garaj, S.; Golovchenko, J. A. *Physical review letters* **2009**, *102*, 256804.

(88) Smeets, R. M.; Keyser, U.; Wu, M.; Dekker, N.; Dekker, C. *Physical Review Letters* **2006**, *97*, 088101.

(89) Garaj, S.; Liu, S.; Golovchenko, J. A.; Branton, D. *Proceedings of the National Academy of Sciences* **2013**, *110*, 12192–12196.

(90) Arjmandi-Tash, H.; Belyaeva, L. A.; Schneider, G. F. *Chemical Society Reviews* **2016**, *45*, 476–493.

(91) Uram, J. D.; Ke, K.; Mayer, M. *ACS nano* **2008**, *2*, 857–872.

(92) Balan, A.; Machielse, B.; Niedzwiecki, D.; Lin, J.; Ong, P.; Engelke, R.; Shepard, K. L.; Drndić, M. *Nano letters* **2014**, *14*, 7215–7220.

(93) Balan, A.; Chien, C.-C.; Engelke, R.; Drndić, M. *Scientific reports* **2015**, *5*, 1–8.

(94) Waggoner, P. S.; Kuan, A. T.; Polonsky, S.; Peng, H.; Rossnagel, S. M. *Journal of Vacuum Science & Technology B, Nanotechnology and Microelectronics: Materials, Processing, Measurement, and Phenomena* **2011**, *29*, 032206.

(95) Matsui, K.; Goto, Y.; Yanagi, I.; Yanagawa, Y.; Ishige, Y.; Takeda, K.-i. *Japanese Journal of Applied Physics* **2018**, *57*, 046702.

(96) Dumcenco, D.; Ovchinnikov, D.; Marinov, K.; Lazić, P.; Gibertini, M.; Marzari, N.; Sanchez, O. L.; Kung, Y.-C.; Krasnozhon, D.; Chen, M.-W.; Bertolazzi, S.; Gillet, P.; Fontcuberta i Morral, A.; Radenovic, A.; Kis, A. *ACS Nano* **2015**, *9*, Publisher: American Chemical Society, 4611–4620.

(97) Li, J.; Östling, M. *Electronics* **2015**, *4*, 1033–1061.

(98) Kim, H.; Ovchinnikov, D.; Deiana, D.; Unuchek, D.; Kis, A. *Nano Letters* **2017**, *17*, Publisher: American Chemical Society, 5056–5063.

(99) Gurarslan, A.; Yu, Y.; Su, L.; Yu, Y.; Suarez, F.; Yao, S.; Zhu, Y.; Ozturk, M.; Zhang, Y.; Cao, L. *ACS nano* **2014**, *8*, 11522–11528.

(100) Li, H.; Wu, J.; Huang, X.; Yin, Z.; Liu, J.; Zhang, H. *ACS nano* **2014**, *8*, 6563–6570.

(101) Ma, X.; Liu, Q.; Xu, D.; Zhu, Y.; Kim, S.; Cui, Y.; Zhong, L.; Liu, M. *Nano letters* **2017**, *17*, 6961–6967.

(102) Lee, Y.-H.; Yu, L.; Wang, H.; Fang, W.; Ling, X.; Shi, Y.; Lin, C.-T.; Huang, J.-K.; Chang, M.-T.; Chang, C.-S., et al. *Nano letters* **2013**, *13*, 1852–1857.

(103) Garcia, A.; Raya, A. M.; Mariscal, M. M.; Esparza, R.; Herrera, M.; Molina, S. I.; Scavello, G.; Galindo, P. L.; Jose-Yacaman, M.; Ponce, A. *Ultramicroscopy* **2014**, *146*, 33–38.

(104) Park, H. J.; Ryu, G. H.; Lee, Z. *Applied Microscopy* **2015**, *45*, 107–114.

(105) Hong, J.; Hu, Z.; Probert, M.; Li, K.; Lv, D.; Yang, X.; Gu, L.; Mao, N.; Feng, Q.; Xie, L., et al. *Nature communications* **2015**, *6*, 1–8.

(106) Kuan, A. T.; Lu, B.; Xie, P.; Szalay, T.; Golovchenko, J. A. *Applied physics letters* **2015**, *106*, 203109.

(107) Kowalczyk, S. W.; Grosberg, A. Y.; Rabin, Y.; Dekker, C. *Nanotechnology* **2011**, *22*, 315101.

(108) Sahu, S.; Zwolak, M. *Physical Chemistry Chemical Physics* **2018**, *20*, 4646–4651.

(109) Carlsen, A. T.; Zahid, O. K.; Ruzicka, J.; Taylor, E. W.; Hall, A. R. *Acs Nano* **2014**, *8*, 4754–4760.

(110) Liu, K.; Lihter, M.; Sarathy, A.; Caneva, S.; Qiu, H.; Deiana, D.; Tileli, V.; Alexander, D. T. L.; Hofmann, S.; Dumcenco, D.; Kis, A.; Leburton, J.-P.; Radenovic, A. *Nano Letters* **2017**, *17*, Publisher: American Chemical Society, 4223–4230.

(111) Gadaleta, A.; Sempere, C.; Gravelle, S.; Siria, A.; Fulcrand, R.; Ybert, C.; Bocquet, L. *Physics of Fluids* **2014**, *26*, 012005.

(112) Moody, G.; Oke, R.; Thomas, J. *Analyst* **1969**, *94*, 803–804.

(113) Raillon, C.; Granjon, P.; Graf, M.; Steinbock, L.; Radenovic, A. *Nanoscale* **2012**, *4*, 4916–4924.

(114) Butler, S. Z.; Hollen, S. M.; Cao, L.; Cui, Y.; Gupta, J. A.; Gutiérrez, H. R.; Heinz, T. F.; Hong, S. S.; Huang, J.; Ismach, A. F., et al. *ACS nano* **2013**, *7*, 2898–2926.

(115) Lin, Y.-C.; Zhang, W.; Huang, J.-K.; Liu, K.-K.; Lee, Y.-H.; Liang, C.-T.; Chu, C.-W.; Li, L.-J. *Nanoscale* **2012**, *4*, 6637–6641.

(116) Wang, X.; Feng, H.; Wu, Y.; Jiao, L. *Journal of the American Chemical Society* **2013**, *135*, 5304–5307.

(117) Zrehen, A.; Gilboa, T.; Meller, A. *Nanoscale* **2017**, *9*, 16437–16445.

(118) Drndić, M. *Nature Nanotechnology* **2014**, *9*, 743–743.

(119) Branton, D.; Deamer, D. W.; Marziali, A.; Bayley, H.; Benner, S. A.; Butler, T.; Di Ventra, M.; Garaj, S.; Hibbs, A.; Huang, X., et al. *Nature biotechnology* **2008**, *26*, 1146–1153.

(120) Yu, H.; Liao, M.; Zhao, W.; Liu, G.; Zhou, X.; Wei, Z.; Xu, X.; Liu, K.; Hu, Z.; Deng, K., et al. *ACS nano* **2017**, *11*, 12001–12007.

(121) Wanunu, M.; Morrison, W.; Rabin, Y.; Grosberg, A. Y.; Meller, A. *Nature nanotechnology* **2010**, *5*, 160–165.

(122) Haque, F.; Li, J.; Wu, H.-C.; Liang, X.-J.; Guo, P. *Nano Today* **2013**, *8*, 56–74.

(123) Hernández-Ainsa, S.; Keyser, U. F. *Nanomedicine* **2013**, *8*, 1551–1554.

(124) Lu, H.; Giordano, F.; Ning, Z. *Genomics, Proteomics & Bioinformatics* **2016**, *14*, 265–279.

(125) Danda, G.; Drndić, M. *Current opinion in biotechnology* **2019**, *55*, 124–133.

(126) Kozubek, R.; Tripathi, M.; Ghorbani-Asl, M.; Kretschmer, S.; Madauß, L.; Pollmann, E.; O'Brien, M.; McEvoy, N.; Ludacka, U.; Susi, T.; Duesberg, G. S.; Wilhelm, R. A.; Krasheninnikov, A. V.; Kotakoski, J.; Schleberger, M. *The Journal of Physical Chemistry Letters* **2019**, *10*, Publisher: American Chemical Society, 904–910.

(127) Thiruraman, J. P.; Masih Das, P.; Drndić, M. *Advanced Functional Materials* **2019**, *29*, _eprint: https://onlinelibrary.wiley.com/doi/pdf/10.1002/adfm.201904668, 1904668.

(128) Ke, J.-A.; Garaj, S.; Gradečak, S. *ACS Applied Materials & Interfaces* **2019**, *11*, Publisher: American Chemical Society, 26228–26234.

(129) Macha, M.; Marion, S.; Nandigana, V. V. R.; Radenovic, A. *Nature Reviews Materials* **2019**, *4*, Number: 9 Publisher: Nature Publishing Group, 588–605.

(130) Graf, M.; Lihter, M.; Unuchek, D.; Sarathy, A.; Leburton, J.-P.; Kis, A.; Radenovic, A. *Joule* **2019**, *3*, 1549–1564.

(131) Kang, K.; Xie, S.; Huang, L.; Han, Y.; Huang, P. Y.; Mak, K. F.; Kim, C.-J.; Muller, D.; Park, J. *Nature* **2015**, *520*, 656–660.

(132) Boandoh, S.; Choi, S. H.; Park, J.-H.; Park, S. Y.; Bang, S.; Jeong, M. S.; Lee, J. S.; Kim, H. J.; Yang, W.; Choi, J.-Y.; Kim, S. M.; Kim, K. K. *Small* **2017**, *13*, _eprint: https://onlinelibrary.wiley.com/doi/pdf/10.1002/smll.201701306, 1701306.

(133) Zhou, J. et al. *Nature* **2018**, *556*, Number: 7701 Publisher: Nature Publishing Group, 355–359.

(134) Lu, Z.; Sun, L.; Xu, G.; Zheng, J.; Zhang, Q.; Wang, J.; Jiao, L. *ACS nano* **2016**, *10*, 5237–5242.

(135) Meitl, M. A.; Zhu, Z.-T.; Kumar, V.; Lee, K. J.; Feng, X.; Huang, Y. Y.; Adesida, I.; Nuzzo, R. G.; Rogers, J. A. *Nature materials* **2006**, *5*, 33–38.

(136) Thi, Q. H.; Kim, H.; Zhao, J.; Ly, T. H. *npj 2D Materials and Applications* **2018**, *2*, 1–7.

(137) Kwon, K. C.; Choi, S.; Hong, K.; Moon, C. W.; Shim, Y.-S.; Kim, T.; Sohn, W.; Jeon, J.-M.; Lee, C.-H.; Nam, K. T., et al. *Energy & Environmental Science* **2016**, *9*, 2240–2248.

(138) Mlack, J. T.; Masih Das, P.; Danda, G.; Chou, Y.-C.; Naylor, C. H.; Lin, Z.; López, N. P.; Zhang, T.; Terrones, M.; Johnson, A., et al. *Scientific reports* **2017**, *7*, 1–8.

(139) Zhang, K.; Bersch, B. M.; Zhang, F.; Briggs, N. C.; Subramanian, S.; Xu, K.; Chubarov, M.; Wang, K.; Lerach, J. O.; Redwing, J. M., et al. *ACS applied materials & interfaces* **2018**, *10*, 40831–40837.

(140) Lee, J.-U.; Kim, K.; Cheong, H. *2D Materials* **2015**, *2*, 044003.

(141) Chakraborty, B.; Bera, A.; Muthu, D.; Bhowmick, S.; Waghmare, U. V.; Sood, A. *Physical Review B* **2012**, *85*, 161403.

(142) Zhou, W.; Zou, X.; Najmaei, S.; Liu, Z.; Shi, Y.; Kong, J.; Lou, J.; Ajayan, P. M.; Yakobson, B. I.; Idrobo, J.-C. *Nano letters* **2013**, *13*, 2615–2622.

(143) Komsa, H.-P.; Kotakoski, J.; Kurasch, S.; Lehtinen, O.; Kaiser, U.; Krasheninnikov, A. V. *Physical review letters* **2012**, *109*, 035503.

(144) Yang, J.; Choi, M. K.; Sheng, Y.; Jung, J.; Bustillo, K.; Chen, T.; Lee, S.-W.; Ercius, P.; Kim, J. H.; Warner, J. H., et al. *Nano letters* **2019**, *19*, 1788–1795.

(145) Holroyd, C.; Horn, A. B.; Casiraghi, C.; Koehler, S. P. *Carbon* **2017**, *117*, 473–475.

(146) Jain, A.; Bharadwaj, P.; Heeg, S.; Parzefall, M.; Taniguchi, T.; Watanabe, K.; Novotny, L. *Nanotechnology* **2018**, *29*, 265203.

(147) Khalkhali, M.; Zhang, H.; Liu, Q. *The Journal of Physical Chemistry C* **2018**, *122*, 6737–6747.

(148) Kozbial, A.; Gong, X.; Liu, H.; Li, L. *Langmuir* **2015**, *31*, 8429–8435.

(149) Verschueren, D. V.; Yang, W.; Dekker, C. *Nanotechnology* **2018**, *29*, 145302.

(150) Dela Torre, R.; Larkin, J.; Singer, A.; Meller, A. *Nanotechnology* **2012**, *23*, 385308.

(151) Pérez, M. D. B.; Nicolaı, A.; Delarue, P.; Meunier, V.; Drndić, M.; Senet, P. *Applied Physics Letters* **2019**, *114*, 023107.

(152) Heerema, S.; Schneider, G.; Rozemuller, M.; Vicarelli, L.; Zandbergen, H.; Dekker, C. *Nanotechnology* **2015**, *26*, 074001.

(153) Gu, Z.; Ying, Y.-L.; Cao, C.; He, P.; Long, Y.-T. *Analytical chemistry* **2015**, *87*, 907–913.

(154) Carson, S.; Wilson, J.; Aksimentiev, A.; Wanunu, M. *Biophysical journal* **2014**, *107*, 2381–2393.

(155) Zhu, C.; Zeng, Z.; Li, H.; Li, F.; Fan, C.; Zhang, H. *Journal of the American Chemical Society* **2013**, *135*, 5998–6001.

(156) Lu, C.; Liu, Y.; Ying, Y.; Liu, J. *Langmuir* **2017**, *33*, 630–637.

(157) Vovusha, H.; Sanyal, B. *RSC advances* **2015**, *5*, 67427–67434.

(158) Lee, W.; Liu, Y.; Lee, Y.; Sharma, B. K.; Shinde, S. M.; Kim, S. D.; Nan, K.; Yan, Z.; Han, M.; Huang, Y., et al. *Nature communications* **2018**, *9*, 1–9.

(159) Chen, X.; Park, Y. J.; Kang, M.; Kang, S.-K.; Koo, J.; Shinde, S. M.; Shin, J.; Jeon, S.; Park, G.; Yan, Y., et al. *Nature communications* **2018**, *9*, 1–12.

(160) Singh, E.; Singh, P.; Kim, K. S.; Yeom, G. Y.; Nalwa, H. S. *ACS applied materials & interfaces* **2019**, *11*, 11061–11105.

(161) Fanget, A.; Traversi, F.; Khlybov, S.; Granjon, P.; Magrez, A.; Forró, L.; Radenovic, A. *Nano letters* **2014**, *14*, 244–249.

(162) Puster, M.; Rodrıguez-Manzo, J. A.; Balan, A.; Drndic, M. *ACS nano* **2013**, *7*, 11283–11289.

(163) Krivanek, O. L.; Chisholm, M. F.; Nicolosi, V.; Pennycook, T. J.; Corbin, G. J.; Dellby, N.; Murfitt, M. F.; Own, C. S.; Szilagyi, Z. S.; Oxley, M. P., et al. *Nature* **2010**, *464*, 571–574.

(164) Zhou, Z.; Hu, Y.; Wang, H.; Xu, Z.; Wang, W.; Bai, X.; Shan, X.; Lu, X. *Scientific reports* **2013**, *3*, 1–5.

(165) Rueden, C. T.; Eliceiri, K. W. *Microscopy and microanalysis* **2019**, *25*, 142–143.

(166) Jiang, X.; Zhao, C.; Noh, Y.; Xu, Y.; Chen, Y.; Chen, F.; Ma, L.; Ren, W.; Aluru, N. R.; Feng, J. *Science advances* **2022**, *8*, eabj2510.

(167) Thiruraman, J. P.; Dar, S. A.; Masih Das, P.; Hassani, N.; Neek-Amal, M.; Keerthi, A.; Drndić, M.; Radha, B. *Science Advances* **2020**, *6*, eabc7927.

(168) Mojtabavi, M.; Tsai, W.-Y.; VahidMohammadi, A.; Zhang, T.; Gogotsi, Y.; Balke, N.; Wanunu, M. *Small* **2022**, *18*, 2105857.

(169) Mojtabavi, M.; VahidMohammadi, A.; Liang, W.; Beidaghi, M.; Wanunu, M. *ACS nano* **2019**, *13*, 3042–3053.

(170) Cohen-Tanugi, D.; Grossman, J. C. *Nano letters* **2012**, *12*, 3602–3608.

(171) Li, W.; Yang, Y.; Weber, J. K.; Zhang, G.; Zhou, R. *ACS nano* **2016**, *10*, 1829–1835.

(172) Cheng, C.; Iyengar, S. A.; Karnik, R. *Nature Nanotechnology* **2021**, *16*, 989–995.

(173) Chen, K.; Kong, J.; Zhu, J.; Ermann, N.; Predki, P.; Keyser, U. F. *Nano letters* **2018**, *19*, 1210–1215.

(174) Hu, R.; Tong, X.; Zhao, Q. *Advanced healthcare materials* **2020**, *9*, 2000933.

(175) Lanza, M.; Smets, Q.; Huyghebaert, C.; Li, L.-J. *Nature communications* **2020**, *11*, 1–5.

(176) Chou, Y.-C.; Masih Das, P.; Monos, D. S.; Drndić, M. *ACS nano* **2020**, *14*, 6715–6728.

(177) Loessberg-Zahl, J.; De Bruijn, D. S.; Van Den Beld, W. T.; Dollekamp, E.; Grady, E.; Keerthi, A.; Bomer, J.; Radha, B.; Zandvliet, H.; Bol, A. A., et al. *The Journal of Physical Chemistry C* **2019**, *124*, 430–435.

(178) Gao, J.; Li, B.; Tan, J.; Chow, P.; Lu, T.-M.; Koratkar, N. *ACS nano* **2016**, *10*, 2628–2635.

(179) Mirabelli, G.; McGeough, C.; Schmidt, M.; McCarthy, E. K.; Monaghan, S.; Povey, I. M.; McCarthy, M.; Gity, F.; Nagle, R.; Hughes, G., et al. *Journal of Applied Physics* **2016**, *120*, 125102.

(180) Kc, S.; Longo, R. C.; Wallace, R. M.; Cho, K. *Journal of Applied Physics* **2015**, *117*, Publisher: American Institute of Physics, 135301.

(181) Chhowalla, M.; Shin, H. S.; Eda, G.; Li, L.-J.; Loh, K. P.; Zhang, H. *Nature Chemistry* **2013**, *5*, Number: 4 Publisher: Nature Publishing Group, 263–275.

(182) Ghulinyan, M.; Bernard, M.; Bartali, R.; Pucker, G. *Applied Surface Science* **2015**, *359*, 679–686.

(183) Gao, J.; Li, B.; Tan, J.; Chow, P.; Lu, T.-M.; Koratkar, N. *ACS Nano* **2016**, *10*, Publisher: American Chemical Society, 2628–2635.

(184) Mak, K. F.; He, K.; Lee, C.; Lee, G. H.; Hone, J.; Heinz, T. F.; Shan, J. *Nature Materials* **2013**, *12*, Number: 3 Publisher: Nature Publishing Group, 207–211.

(185) Oh, H. M.; Han, G. H.; Kim, H.; Bae, J. J.; Jeong, M. S.; Lee, Y. H. *ACS Nano* **2016**, *10*, Publisher: American Chemical Society, 5230–5236.

(186) Ardekani, H.; Younts, R.; Yu, Y.; Cao, L.; Gundogdu, K. *ACS Applied Materials & Interfaces* **2019**, *11*, Publisher: American Chemical Society, 38240–38246.

(187) Wang, Z.; von dem Bussche, A.; Qiu, Y.; Valentin, T. M.; Gion, K.; Kane, A. B.; Hurt, R. H. *Environmental Science & Technology* **2016**, *50*, Publisher: American Chemical Society, 7208–7217.

(188) Larkin, J.; Henley, R.; Bell, D. C.; Cohen-Karni, T.; Rosenstein, J. K.; Wanunu, M. *ACS Nano* **2013**, *7*, Publisher: American Chemical Society, 10121–10128.

(189) Chen, W.; Zhao, J.; Zhang, J.; Gu, L.; Yang, Z.; Li, X.; Yu, H.; Zhu, X.; Yang, R.; Shi, D.; Lin, X.; Guo, J.; Bai, X.; Zhang, G. *Journal of the American Chemical Society* **2015**, *137*, Publisher: American Chemical Society, 15632–15635.

(190) Shree, S.; George, A.; Lehnert, T.; Neumann, C.; Benelajla, M.; Robert, C.; Marie, X.; Watanabe, K.; Taniguchi, T.; Kaiser, U.; Urbaszek, B.; Turchanin, A. *2D Materials* **2019**, *7*, Publisher: IOP Publishing, 015011.

Doctoral candidate

Mukeshchand THAKUR

✉ *mukeshchandthakur@yahoo.com*
mukeshchandthakur
thakurwid2hands
mukeshchandthakur

Bioengineer specialized in biophysics, nanotechnology and nanopore sensor technology with aspiration to work in affordable healthcare industry

Education

2018–2022 **Doctoral Assistant (Microsystems and Microelectronics)**, *Laboratory of Nanoscale Biology*, École polytechnique fédérale de Lausanne (EPFL),Switzerland,

2013–2015 **Master in Technology (Biotechnology)**, *School of Biotechnology and Bioinformatics*, D.Y. Patil University, India,

2008–2012 **Bachelor in Technology (Biotechnology)**, *School of Biotechnology and Bioinformatics*, D.Y. Patil University, India,

Ph.D. Thesis

thesis title *MoS_2 Nanopores: Wafer-scale Fabrication and Monolayer Stability for Long-term Single-Molecule Biosensing*

supervisor Prof. **Aleksandra Radenovic** at École polytechnique fédérale de Lausanne (EPFL)

description Worked on solid-state nanopore devices as single-molecular level DNA biosensors. My work focused on addressing current commercial bottlenecks in the nanopore field such as device scalability, atomic thin 2D material transfer and stability issues in nanopore devices.

Master thesis

thesis title *Multi-Fluorescent Carbon Nanoparticle and its Lipid Nanohybrid thereof as Bio-labeling Probe*

supervisor Prof. **Rohit Srivastava** at Indian Institute of Technology (IIT) Bombay

description I chemically synthesised fluorescent quantum dots (using chemical or green synthesis approach) and prepared lipid-hybrids for biomedical applications such as cell imaging. I was particular focusing on development of near-infrared fluorescent nanoparticles for therapy of in-vitro cancer cells.

Research Experience

2015–2017 **Project Assistant**, *IIT Bombay*, Dept. of Biosciences and Bioengineering, India
Project on graphene-based 2D materials and quantum dots for biomedical applications.

June 2015 **Taiwan International Graduate Program-International Internship Program (TIGP-IIP) Fellowship**, *Taipei*, Academia Sinica, Taiwan
Principal Investigator: Prof. Yit-Tsong Chen. On Two-Dimensional Materials for FET-Based Biosensors at Nanoscale Materials and Bio-analytical Chemistry Laboratory, Institute of Atomic and Molecular Sciences, Academia Sinica, Taiwan.

2014–2015 **IITB Research Internship Award Fellowship**, *IIT Bombay*, Department of Biosciences and Bioengineering, India
Worked on theranostic Applications of Fluorescent Nanoparticle-Lipid Nanohybrids.

2012–2013 **Junior Research Assistant**, *N.S.N. Research Center for Nanotechnology and Bionanotechnology*, Ambernath, Maharashtra
Worked on metallic nanoparticle synthesis (gold, silver, platinum), their separation and purification for the application in cancer phototherapy.

Publications

[1] Mukeshchand Thakur, Michal Macha, Andrey Chernev, Michael Graf, Martina Lihter, Jochem Deen, Mukesh Tripathi, Andras Kis, and Aleksandra Radenovic. Wafer-scale fabrication of nanopore devices for single-molecule dna biosensing using mos_2. *Small Methods*, page 2000072, 2020.

[2] Michal Macha, Sanjin Marion, Mukesh Tripathi, Mukeshchand Thakur, Martina Lihter, Andras Kis, Alex Smolyanitsky, and Aleksandra Radenovic. High-throughput nanopore fabrication and classification using fib irradiation and automated pore edge analysis. *arXiv preprint arXiv:2205.13661*, 2022.

[3] Michael Graf, Martina Lihter, Mukeshchand Thakur, Vasileia Georgiou, Juraj Topolancik, B Robert Ilic, Ke Liu, Jiandong Feng, Yann Astier, and Aleksandra Radenovic. Fabrication and practical applications of molybdenum disulfide nanopores. *Nature Protocols*, 14:1130–1168, 2019.

[4] Evgenii Glushkov, Anna Archetti, Anton Stroganov, Jean Comtet, Mukeshchand Thakur, Vytautas Navikas, Martina Lihter, Juan Francisco Gonzalez Marin, Vitaliy Babenko, Stephan Hofmann, et al. Waveguide-based platform for large-fov imaging of optically-active defects in 2d materials. *ACS Photonics*, 2019.

[5] Mukesh Kumar Kumawat, Mukeshchand Thakur, Raju B Gurung, and Rohit Srivastava. Graphene quantum dots for cell proliferation, nucleus imaging, and photoluminescent sensing applications. *Scientific Reports*, 7:15858, 2017.

[6] Jaya R Lakkakula, Deepika Divakaran, Mukeshchand Thakur, Mukesh Kumar Kumawat, and Rohit Srivastava. Cyclodextrin-stabilized gold nanoclusters for bioimaging and selective label-free intracellular sensing of co 2+ ions. *Sensors and Actuators B: Chemical*, 262:270–281, 2018.

for the complete list refer my Google Schlolar

Patents *(Granted)*

[1] Liponions as a multi-colour fluorescent biolabelling probe. Aravind Kumar, **Mukeshchand Thakur** and Rohit Srivastava. IPA No. 2368/MUM/2015

[2] Cyclodextrin functionalized inorganic nanostructures: synthesis and applications thereof. Jaya Raju Lakkakula, Deepika Divakaran Tharayil, **Mukeshchand Thakur**, Mukesh Kumar Kumawat and Rohit Srivastava. IPA No. 201721016954

Teaching

2019–2012 **Optical Tweezers**, *Advanced Bioengineering Methods Laboratory*, Masters course, EPFL

2020–2021 **Nanopores**, *Developed this new module*, Masters course, EPFL

2018–2019 **Brownian Motion**, *Advanced Bioengineering Methods Laboratory*, Masters course, EPFL

Conferences

June 11-18, 2022 **Solid-state to Biophysics X**, *Poster presentation*, Cavtat, Croatia

February 4-7, 2019 **Dead Sea Workshop on Wafer Filtration**, *Poster presentation*, Ein Gedi, Israel

June 16-23, 2018 **Solid-state to Biophysics IX**, *Poster presentation*, Cavtat, Croatia

In-silico skills

Programming Python, Matlab

Office Microsoft: Word, Excel, Powerpoint, Keynote

3D Blender, BioRender

Imaging Image J/Fiji, Adobe Illustrator, Photoshop, Inkscape

Video Adobe Premiere Pro

Documents MS Office, LaTeX

Technical skills

Clean room Photolithography, electron-beam lithography, wet and dry etching, mask writing, mask alignment, ellipsometry, nanoparticles, 2D material transfer, nanopore drilling

Analytical Ion current measurements, UV-Vis-Fluorescence spectroscopy, DLS, AFM, Raman spectroscopy

Imaging Scanning and Transmission electron microscopy, optical and fluorescent microscopy

Wet lab Electrophoresis, DNA/protein purification, nanoparticle synthesis, PCR

Co-Curricular and management

President **YUVA-Indians at EPFL and UNIL**, *EPFL*, Switzerland, 2020-2021
Managing and organizing Indian cultural events for the ex-pat students within the EPFL/UNIL campus. Collaborated with other major organizations like Indian embassy to organize social events for cultural exchange and social awareness

Treasurer & Logistics Manager **YUVA-Indians at EPFL and UNIL**, *EPFL*, Switzerland, 2018-2020
Experience in managing logistics for the cultural events (both online and offline) at EPFL and UNIL

Language

English Full proficiency

Hindi Native proficiency

Marathi Native proficiency

Kumaoni Native proficiency

Nepali Native proficiency

French Elementary